Top Quark Produced Through the Electroweak Force: Discovery Using the Matrix Element Analysis and Search for Heavy Gauge Bosons Using Boosted Decision Trees

by

Monica Pangilinan

B.A., Cornell University, 2003
M.A., Boston University 2006

Thesis

Submitted in partial fulfillment of the requirements for
the Degree of Doctor of Philosophy
in the Department of Physics at Brown University

Providence, Rhode Island
May 2010

Abstract of " Top Quark Produced Through the Electroweak Force: Discovery Using the Matrix Element Analysis and Search for Heavy Gauge Bosons Using Boosted Decision Trees" by Monica Pangilinan, Ph.D., Brown University, May 2010

The top quark produced through the electroweak channel provides a direct measurement of the V_{tb} element in the CKM matrix which can be viewed as a transition rate of a top quark to a bottom quark. This production channel of top quark is also sensitive to different theories beyond the Standard Model such as heavy charged gauged bosons termed W'.

This thesis measures the cross section of the electroweak produced top quark using a technique based on using the matrix elements of the processes under consideration. The technique is applied to 2.3 fb^{-1} of data from the DØ detector. From a comparison of the matrix element discriminants between data and the signal and background model using Bayesian statistics, we measure the cross section of the top quark produced through the electroweak mechanism

$$\sigma\left(p\bar{p}\rightarrow tb+X, tqb+X\right) \quad = 4.30^{+0.98}_{-1.20} \text{ pb}$$

The measured result corresponds to a 4.9σ Gaussian-equivalent significance. By combining this analysis with other analyses based on the Bayesian Neural Network (BNN) and Boosted Decision Tree (BDT) method, the measured cross section is 3.94 ± 0.88 pb with a significance of 5.0σ, resulting in the discovery of electroweak produced top quarks. Using this measured cross section and constraining $|V_{tb}| < 1$, the 95% confidence level (C.L.) lower limit is $|V_{tb}| > 0.78$.

Additionally, a search is made for the production of W' using the same samples from the electroweak produced top quark. An analysis based on the BDT method is used to separate the signal from expected backgrounds. No significant excess is found and 95% C.L. upper limits on the production cross section are set for W' with masses within 600 - 950 GeV. For four general models of W' boson production using decay channel $W' \rightarrow t\bar{b}$, the lower mass limits are the following: M(W'_L with SM couplings) $>$ 840 GeV; M(W'_R) $>$ 880 GeV or 890 GeV if the right-handed neutrino is lighter or heavier than W'_R; and M(W'_{L+R}) $>$ 915 GeV.

This dissertation by Monica Pangilinan is accepted in its present form by
the Department of Physics as satisfying the
dissertation requirement for the degree of
Doctor of Philosophy

Date..... .....
Meenakshi Narain, Advisor

Recommended to the Graduate Council

Date..... .....
David Cutts, reader

Date..... .....
Anastasia Volovich, reader

Approved by the Graduate Council

Date..... .....
Sheila Bonde
Dean of the Graduate School

Preface and Acknowledgments

I would like to thank everyone that helped make this thesis possible. First, I would like to thank my adviser Meenakshi Narain for helping me become a better physicist. Thank you for asking all the hard questions, for showing me that the right way may not always be the shortest way, for making sure that I was never lost, and for always being understanding. Your dedication to the field and to research while balancing a family shows me that all things are possible and what it means to be a good physicist regardless of gender.

I would also like to thank the conveners of the single top group, Reinhard, Ann and Cecilia, who were instrumental in making the single top discovery a reality. I would also like to thank Stefan, Marc, and Remi for helping me understand the CTT and how important detector work is and for showing me that carrying the pager isn't all that bad. I would especially like to thank Norik for helping me with the DFEA2 boards and helping me getting tuned in the CTT group.

Great thanks especially to the postdocs I have worked with. First, to Shabnam for helping me understand how to script, for being patient with all my questions and taking the time to answer them, for the late night jobs and getting the BNN pulled through, and for being a great friend and colleague who always had an encouraging word if I needed it. Second, to Yuji who was a major help in pulling through the ME analysis and always had an insightful comment on how to better the analysis or what other things I could look into. I hope to emulate both of you as a postdoc.

For the people I have worked with in the singletop group, Jorge, Andres, and Dag. Thanks for all the great times outside of the group meetings and for helping me whenever I had asked and for surviving through with me and keeping me sane throughout the analysis from start to finish. I would also like to thank Tutanon, Erin, and David for pushing through and completing the jobs necessary to finish the W′ analysis.

I would also like to thank all the friends I have made along in grad school. First to the BU kids who helped me find life in Boston, kept me entertained throughout all the problem sets we had to do, and who showed me that not all physicists are bad. I would especially like to thank Marco, the Mikes, Ron, Silvia, Diego, Chris, Fanny, Leyla, and Marc. Next, I would like to thank the Chitown

gang, especially the Carpool who made the rides enjoyable to and from Fermilab. Thanks for being such great friends and keeping me together through all our ridiculous times together.

Finally, I would like to thank my family, from San Diego to all corners of the world. Thank you for teaching me the importance of an education and of each other and for opening your homes to me as my home away from home. I would especially like to thank my parents and my brother and sister whose untiring love and support I hope to repay. Without you, I would be nothing and could do nothing. You have made me who I am and have taught me to be independent, to work hard for what I want, and most importantly that love comes without any conditions and knows no bounds.

Contents

List of Tables

List of Figures

Chapter 1

Introduction

Physics aims to understand how the universe works based on a fundamental set of relationships. This is done by studying the interactions between objects, which can range from something as large as whole galaxies to the smallest building blocks of matter such as quarks. The fundamental interactions between quarks and other elementary particles that form everything we see today is described by particle physics. As of now, the Standard Model (SM), a theory that describes these elementary particle interactions, has been very successful due to results of high energy experiments which have thoroughly verified the accuracy of the SM. However, this theory is incomplete as, for example, gravity is not accounted for, and inconsistencies have been found such as massive neutrinos which are massless in the SM. Furthermore, the theory is believed to be an effective theory that may break down at energies that can be probed by the Large Hadron Collider (LHC), which successfully started high energy collisions this year. To address the man shortcomings of the SM, a new theory is expected to emerge beyond the SM which the LHC will hopefully find via a new particle whose properties will filter out the many theoretical candidates. This is truly an exciting time in particle physics!

This thesis provides an experimental test to the SM, namely through the top quark, and also sets constraints on theories beyond the SM. The top quark is an interesting quark in that it has many peculiar features that distinguish it from other quarks, namely its large mass and its decay

through the electroweak force rather than the strong force. This thesis looks in particular at the electroweak production of top quarks, where one can test theoretical assumptions directly such as that the SM has three generations and that the top quark can be produced through the electroweak force much like the other quarks. Furthermore, the top quark produced through this channel can be used as a probe into physics beyond the SM, particularly heavy charged gauge bosons, if any discrepancies arise from the experimental verification of this SM cross section. All of this will be discussed and answered in this thesis which will be broken up into two parts: the discovery of the top quark produced via the electroweak channel and new theoretical constraints put on heavy charged gauge bosons predicted by theories beyond the SM.

For the first part, the chapters are arranged in the following way: Chapter 2 is a general theoretical overview of the SM and beyond, which can be probed through the electroweak top quark production channel; Chapter 3 describes the experimental facilities of the Tevatron and $D\emptyset$ detector which is the only place so far that produces top quarks; Chapter 4 looks at how the Monte Carlo (MC) used to model data is created and also how both the data and MC reconstruct detector objects into physics objects; Chapter 5 gives the MC corrections to model data well and the event selection cuts and b-tagging algorithm to reduce the background while maximizing the signal; Chapter 6 looks at the Matrix Element (ME) analysis used to further optimally separate signal and background; and Chapter 7 gives an overview on how the cross section is calculated with the ME results. For the second part, Chapter 8 gives a simple overview of how the MC is generated for charged heavy gauge bosons which will be referred to as W' and looks at the multivariate technique of Boosted Decision Trees (BDT) that is used to derive limits on the parameters of W'. Lastly, Chapter 9 gives an overview of both analyses.

Chapter 2

Theory

Particle physics tries to understand interactions at the subatomic level and has been successful through the formulation of the SM. However, the SM has many faults that make it far from being a complete theory. In particular, gravity is not accounted for nor has the mechanism for mass generation been discovered. Thus, finding and measuring the SM cross section of a top quark produced through the electroweak channel helps either to verify or to discount the consistency of this theory. Additionally, by finding or ruling out heavy charged gauge bosons that decay like the SM charged gauge bosons W, theories beyond the SM can be confirmed or further constrained. This chapter will give an overview of the Standard Model and possible extensions to the SM, and will explain why the top quark, specifically when produced through the electroweak channel, is an interesting sector to probe the SM and beyond.

2.1 Standard Model

The Standard Model (SM) [2] [1] is a theory that uses three of the four fundamental forces to describe interactions of elementary particles. These forces are the electromagnetic, weak, and strong force with the missing force being gravity. The SM is a gauge theory that uses the gauge group $SU(3) \times SU(2) \times U(1)$, where $SU(3)$ corresponds to the strong force and can be described by quantum chromodynamics, and $SU(2) \times U(1)$ corresponds to the electromagnetic and weak force

which become unified at high energies. Additionally, electromagnetic interactions can be described by quantum electrodynamics. However, before one can delve into how these forces interact, one needs to understand what exactly these elementary particles are and the properties they have.

2.1.1 Elementary Particles

The elementary particles that form the SM can be divided into fermions, gauge bosons, and the Higgs boson where each type of particles play different roles in the theory. The properties of these particles except the Higgs boson can be found in Fig. 2.1

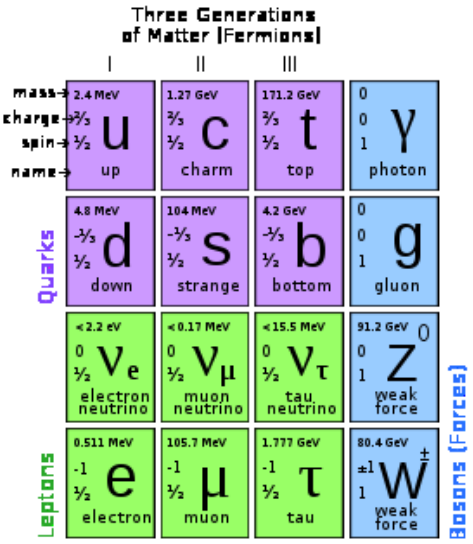

Figure 2.1: The properties of the elementary particles is organized much like the periodic table. The properties of these particles such as mass, charge, and intrinsic spin can be found on the left-hand side of each particle box. The only missing elementary particle from this table is the Higgs boson

Fermions

Fermions are spin-1/2 particles that follow Fermi-Dirac statistics, mainly the Pauli Exclusion Principle which states that two identical fermions cannot occupy the same quantum state simultaneously. In other words, the total wave function must be anti-symmetric for these two identical fermions. In total, there are 12 fermions, six quarks and six leptons, where the defining property that separates the two are the ability of quarks to carry color charge and thus interact through the strong

force. Additionally, there are antiquarks and antileptons which have the same properties as the corresponding quarks and leptons except they carry the opposite charge.

The six quarks are the up, down, charm, strange, bottom and top quark. Quarks have an electric charge of either +2/3 or -1/3 of the electron and thus also interact through the electroweak force. Quarks are always found in bound states due to color confinement which will be discussed in further detail. This means they are either found in "colorless" composites which can either be mesons which are composed of a quark and antiquark with a color and anticolor charge or in baryons which are composed of three quarks that have three different color or three different anticolor charges.

The six leptons are the electron, muon, tau, electron neutrino, muon neutrino, and tau neutrino. The neutrinos have no charge and can only interact through the weak force; however, the electron, muon, and tau have -1 electric charge and thus can interact electromagnetically and also through the weak force.

The quarks and leptons mentioned above can be divided into three generations where each member of a greater generation has a higher mass than the previous generation. Each generation is built of four particles, a quark with +2/3 and one with -1/3 charge which are termed up-type and down-type respectively, and a lepton with -1 charge and no charge (neutrino). The higher generations can decay to a lower generation but the first generation is stable and ultimately form the electrons and atomic nuclei that are the building blocks of macroscopic matter. As for the second and third generation particles, these are only observed in very high-energy environments that were present during the very early universe or in high-energy particle experiments. Upon creation, the higher generations will decay quickly into the first generation particles.

Gauge Bosons

Gauge bosons are what mediate interactions between matter particles. The two matter particles will feel a force, the gauge boson relaying the force from one particle to the other. Gauge bosons are spin 1 particles and thus do not follow the Pauli Exclusion Principle.

For the electromagnetic force, the photon is the gauge boson that mediates interactions between

charged particles. The photon is massless and has two polarizations. The interactions between charged particles via photons are well described by quantum electrodynamics which will be discussed further.

For the weak force, there are three gauge bosons: W^+, W^-, and Z. These bosons act as the mediator of the weak force and are massive with the W's at 80.390 GeV and the Z at 91.187 GeV [1]. At high energies where the W and Z can be produced, the electromagnetic and weak interactions have the same coupling strength and can be thought of as a unified force known as the electroweak force. The three gauge bosons mediate between particles of different flavors where the W carries either a $\pm$ 1 charge and acts only on left-handed particles and right-handed antiparticles and the Z has no charge and interacts with both left-handed particles and antiparticles. The W boson can produce either leptons of different generations or quarks of different generations as long as the two differ by a charge of 1; however, no lepton and quark have been produced by a W experimentally. As for the Z boson, there have been no flavor changing neutral currents discovered [1].

For the strong force, there are eight massless gauge bosons known as gluons that mediate interactions between the color charged particles, the quarks. The gluons carry a color charge of either red, green, or blue and anticolor charge of either antired, antigreen, and antiblue. There are nine possibilities but one of the combinations actually forms a color singlet which has no net color charge and thus cannot play a role of a gluon which carries color charge from one quark to another. Because the gluons carry color charge, they can self interact. Gluons and their interactions with other gluons and quarks is described by quantum chromodynamics which will be discussed more in detail.

Higgs Boson

The Higgs Boson is a massive scalar elementary particle with spin 0. The Higgs boson is what gives mass to the other elementary particles and explains why photons are massless while the weak bosons are massive. This is due to the Higgs mechanism which will be described in a subsequent section. Due to the mass differences between the weak bosons and the photon, the Higgs is responsible for electroweak symmetry breaking. As of yet, the Higgs boson has not been discovered and is predicted

to have a mass range of 115 - 190 GeV [1].

2.1.2 Quantum Electrodynamics

Quantum electrodynamics is a relativistic quantum field theory of electrodynamics that describes how light and charged particles interact. This is a perturbation theory of the electromagnetic quantum vacuum that has a Lagrangian which controls the dynamics and kinematics of the theory:

$$L_{QED} = \overline{\psi}(i\gamma^{\mu}D_{\mu} - m)\psi - \frac{1}{4}F_{\mu\nu}F^{\mu\nu} + \text{H.c.} \tag{2.1}$$

where γ^{μ} are the Dirac matrices, ψ is a bispinor field of spin-1/2 particles, D_{μ} is the gauge covariant derivative, and $F_{\mu\nu}$ is the electromagnetic field tensor and is given by $F_{\mu\nu} = \partial_{\mu}A_{\nu} - \partial_{\nu}A_{\mu}$. The $F_{\mu\nu}$ terms can be thought of as the kinetic terms of the photon field which when written in this manner is gauge invariant. For $D_{\mu} = \partial_{\mu} + ieA_{\mu}$, e is the electric charge of the bispinor field, and A_{μ} is the covariant four-potential of the electromagnetic field generated by the bispinor field. The Lagrangian for a free particle can be used to generate the equations of motion:

$$L_{freeparticle} = \overline{\psi}(i\gamma^{\mu}\partial_{\mu} - m)\psi \tag{2.2}$$

From the Lagrangian, the equations of motion are described by the Dirac equation:

$$\overline{\psi}(i\gamma^{\mu}\partial_{\mu} + m) = 0 \tag{2.3}$$

$$(i\gamma^{\mu}\partial_{\mu} - m)\psi = 0 \tag{2.4}$$

Furthermore, the additional terms from the gauge covariant derivative form new interactions, namely in this case a spin-1/2 particle and its antiparticle with a photon.

Cross section calculations, which will be discussed later, can be done at all energy ranges since the interactions are of order α_{EM} which is 1/137 and well within the calculational limits of perturbation theory.

2.1.3 Quantum Chromodynamics

With the success of quantum electrodynamics, the same principles of building a Lagrangian that is invariant under Lorentz transformations was attempted to describe color charge. The end result is quantum chromodynamics (QCD), a non-Abelian gauge theory based on the symmetry group $SU(3)$. However, the calculational abilities of QCD extends to only the high energy regime as the QCD coupling (α_s), dependent on the energy of the process, decreases as the energy increases:

$$\alpha_s(Q^2) = \frac{12\pi}{(33 - 2n_f)\log(Q^2/\lambda^2)} \tag{2.5}$$

where Q^2 is the squared momentum of the virtual propagator, n_f is the number of flavors, and λ is the energy scale at which the effective coupling will become large. This behavior of the "running coupling constant" results in two interesting things. First, since the coupling is small enough at high energies ($Q^2 >> \lambda^2$), perturbation theory can be used where the quarks can be thought of as "asymptotically free," meaning that quarks can be thought of as unbound and thus free particles. λ is ≈ 0.1 to 0.5 GeV and the Q^2 value where α_s is of order 0.1 and perturbation theory can be used safely is $(30\ GeV)^2$. Second, the force between quarks does not diminish the further apart they are. In fact, the force actually increases the further the quarks are separated, so much so that a $q\bar{q}$ pair is produced as this takes less energy than to separate the quarks further apart. This is why quarks are always found in a bound state.

The QCD Lagrangian is the following:

$$L_{QCD} = \overline{\psi_i}(i\gamma^\mu\partial_\mu - m)\psi_i - gG^a_\mu\overline{\psi_i}\gamma^\mu T^a_{ij}\psi_j - \frac{1}{4}G^a_{\mu\nu}G^{\mu\nu}_a + \text{hermitean conjugate} \tag{2.6}$$

where ψ_i is the quark field, G^a_μ are the gluon fields, T^a_{ij} are the generators where the representation commonly used is the Gell-Mann matrices, and $G^a_{\mu\nu}$ is analogous to the electromagnetic field strength tensor and is given by $G_{\mu\nu} = \partial_\mu G^a_\nu - \partial_\nu G^a_\mu - gf^{abc}G^b_\mu G^c_\nu$. Here, f^{abc} are the structure constants of $SU(3)$ and the last term in $G_{\mu\nu}$ leads to gluon self interactions. From the above Lagrangian, Feynman diagrams can be made with quark-antiquark-gluon interactions and cubic or quartic gluon

self-interactions.

2.1.4 Higgs Mechanism

Photons and gluons are required to be massless since the presence of mass terms for gauge fields destroys the gauge invariance of the Lagrangian. However, W's and Z's are massive and so there must be a way to introduce mass without breaking gauge invariance. This is done using spontaneous symmetry breaking described below.

Consider a complex scalar field $\phi = (\phi_1 + i\phi_2)/\sqrt{2}$ described by the Lagrangian:

$$L_{scalar} = (\partial_\mu \phi)^*(\partial^\mu \phi) - (\mu^2 \phi^* \phi + \lambda(\phi^* \phi)^2) \tag{2.7}$$

which is invariant under the transformation $\phi \rightarrow e^{i\alpha}\phi$. If $\mu^2 < 0$ and $\lambda > 0$, the mass term has the wrong sign for field ϕ and the potential (the last two terms of the Lagrangian) has minima that satisfies the following equation:

$$\frac{\partial V}{\partial \phi} = \phi^*(\mu^2 + 2\lambda\phi^*\phi) = 0 \tag{2.8}$$

Thus, by substituting for ϕ with ϕ_1 and ϕ_2, $\phi_1^2 + \phi_2^2 = v^2$ with $v^2 = -\mu^2/\lambda$

Perturbative calculations need to be expanded around the minima since $\phi = 0$ is an unstable point and would lead to the perturbation series to diverge. The minima then correspond to any point in a circle of radius v in ϕ_1 and ϕ_2 space. One can choose the point $\phi_1 = v$ and $\phi_2 = 0$ and $\phi(x) = [v + \eta(x) + i\xi(x)]/\sqrt{2}$ where $\eta(x) + i\xi(x)$ are quantum fluctuations about the stable vacuum $\phi_1 = v$. The Lagrangian can now be expressed as

$$L_{scalar} = \frac{1}{2}(\partial_\mu \xi)^2 + \frac{1}{2}(\partial_\mu \eta)^2 - \frac{1}{2}(-2\mu^2\eta^2) + \text{const.} + \text{cubic and quartic terms in } \eta,\ \xi \tag{2.9}$$

Field η has a mass $\sqrt{-2\mu^2}$ but ξ has no mass. This massless scalar ξ is a Goldstone boson. Also, since we have chosen a particle ground state in (ϕ_1, ϕ_2), a continuous symmetry has been

spontaneously broken, resulting in a massless scalar. This is Goldstone's theorem.

However, if one looks at spontaneously breaking a local gauge symmetry, the massless scalar will get "eaten" by the massive gauge boson. First consider the $U(1)$ gauge symmetry where $\phi \rightarrow e^{i\alpha(x)}\phi$. Then, ∂_μ is replaced by the covariant derivative:

$$D_\mu = \partial_\mu - ieA_\mu \tag{2.10}$$

where the gauge field transforms as

$$A_\mu \rightarrow A_\mu + \frac{1}{e}\partial_\mu \alpha \tag{2.11}$$

The gauge invariant Lagrangian becomes

$$L_{scalar} = (\partial^\mu + ieA^\mu)\phi^*(\partial_\mu - ieA_\mu)\phi - (\mu^2\phi^*\phi + \lambda(\phi^*\phi)^2) - \frac{1}{4}F_{\mu\nu}F^{\mu\nu} \tag{2.12}$$

Again one takes $\mu^2 < 0$ and translating to the minima of the potential, the Lagrangian becomes

$$L_{scalar} = \frac{1}{2}(\partial_\mu \xi)^2 + \frac{1}{2}(\partial_\mu \eta)^2 - v^2\lambda\eta^2 + \frac{1}{2}e^2v^2A_\mu A^\mu - evA_\mu\partial^\mu\xi - \frac{1}{4}F_{\mu\nu}F^{\mu\nu} + \text{interaction terms}$$

However, there now is an off diagonal term $A_\mu\partial^\mu\xi$, indicating that A_μ has an extra degree of polarization in the longitudinal direction which should not happen when translating field variables. This means that the fields in the Lagrangian are unphysical and so a particular gauge must be chosen:

$$\phi \rightarrow \frac{1}{\sqrt{2}}(v + h(x))e^{i\theta(x)/v} \tag{2.13}$$

$$A_\mu \rightarrow A_\mu + \frac{1}{ev}\partial_\mu\theta \tag{2.14}$$

where $\theta(x)$ is chosen so that h is real.

The new Lagrangian is now

$$L_{scalar} = \frac{1}{2}(\partial_\mu h)^2 - v^2\lambda h^2 + \frac{1}{2}e^2v^2A_\mu A^\mu - \lambda v h^3 - \frac{1}{4}\lambda h^4 + \frac{1}{2}e^2A_\mu^2h^2 + ve^2A_\mu^2h - \frac{1}{4}F_{\mu\nu}F^{\mu\nu} \quad (2.15)$$

where now the Goldstone boson ξ has been absorbed by the vector gauge boson A_μ as a longitudinal polarization of this particle and h is a massive scalar particle called the Higgs particle. This is the "Higgs mechanism."

This same procedure can also be applied to the $SU(2)$ gauge symmetry where ϕ is an $SU(2)$ doublet of complex scalar fields:

$$\phi = \begin{pmatrix} \phi_\alpha \\ \\ \phi_\beta \end{pmatrix} = \frac{1}{\sqrt{2}} \begin{pmatrix} \phi_1 + i\phi_2 \\ \\ \phi_3 + i\phi_4 \end{pmatrix} \quad (2.16)$$

and ϕ is invariant by the $SU(2)$ transformation:

$$\phi \rightarrow \phi' = e^{i\alpha_a\tau_a/2}\phi \quad (2.17)$$

where τ_α are the Pauli matrices. The covariant derivative is

$$D_\mu = \partial_\mu + ig\frac{\tau_a}{2}W_\mu^a \quad (2.18)$$

and W_μ^a are gauge fields where a =1,2,3. The gauge fields transform as follows:

$$W_\mu^a \rightarrow W_\mu^a - \frac{1}{g}\partial_\mu\alpha - \alpha \times W_\mu^a \quad (2.19)$$

The Lagrangian then becomes

$$L_{scalar} = (\partial_\mu\phi + ig\frac{1}{2}\tau \cdot W_\mu\phi)^\dagger(\partial^\mu\phi + ig\frac{1}{2}\tau \cdot W^\mu\phi) - V(\phi) - \frac{1}{4}W_{\mu\nu}W^{\mu\nu} \quad (2.20)$$

where

$$V(\phi) = \mu^2\phi^\dagger\phi + \lambda(\phi^\dagger\phi)^2 \tag{2.21}$$

and the kinetic energy of the gauge fields is given by

$$W_{\mu\nu} = \partial_\mu W_\nu - \partial_\nu W_\mu - gW_\mu \times W_\nu \tag{2.22}$$

Again we look at $\mu^2 < 0$ and $\lambda > 0$ and look for where the minimum of the potential occurs with respect to $|\phi|$, leading to this relation:

$$\phi^\dagger\phi = \frac{1}{2}(\phi_1^2 + \phi_2^2 + \phi_3^2 + \phi_4^2) = -\frac{\mu^2}{2\lambda} \tag{2.23}$$

The symmetry is spontaneously broken when we expand at a particular vacuum described by

$$\phi_1 = \phi_2 = \phi_4 = 0, \quad \phi_3 = -\frac{\mu^2}{\lambda} = \mathrm{v}^2 \tag{2.24}$$

We can then pick a particular gauge where

$$\phi(x) \equiv \frac{1}{\sqrt{2}} \begin{pmatrix} 0 \\ \\ v + h(x) \end{pmatrix} \tag{2.25}$$

and $\phi(x)$ transforms as follows:

$$\phi'(x) \to e^{i\tau\cdot\theta(x)/v}\phi(x) \tag{2.26}$$

where the massless Goldstone boson fields θ_1, θ_2, θ_3 have been "eaten" by the gauge fields and h is the Higgs boson. The gauge bosons W_μ^a have mass terms from the vacuum expectation value and

come from the following Lagrangian term:

$$\left| ig\frac{1}{2}\tau \cdot W_\mu \phi \right|^2 = \frac{g^2}{8}\left| \begin{pmatrix} W_\mu^3 & W_\mu^1 - iW_\mu^2 \\ W_\mu^1 + iW_\mu^2 & -W_\mu^3 \end{pmatrix} \begin{pmatrix} 0 \\ v \end{pmatrix} \right|^2 = \frac{g^2 v^2}{8}[(W_\mu^1)^2 + (W_\mu^2)^2 + (W_\mu^3)^2] \quad (2.27)$$

where the gauge bosons W_μ^a mass is $\frac{1}{2}gv$

2.1.5 Cabibbo-Kobayashi-Maskawa (CKM) Quark-Mixing Matrix

The masses and mixings of quarks arise from interactions of quarks with the Higgs boson which will be described in the next section. In order to do calculations for electroweak interactions, one needs to rotate the weak eigenstates $\begin{pmatrix} d' \\ s' \\ b' \end{pmatrix}$ to that of the mass eigenstates $\begin{pmatrix} d \\ s \\ b \end{pmatrix}$. This rotation between different states is done through the CKM matrix:

$$\begin{pmatrix} d' \\ s' \\ b' \end{pmatrix} = \begin{pmatrix} V_{ud} & V_{us} & V_{ub} \\ V_{cd} & V_{cs} & V_{cb} \\ V_{td} & V_{ts} & V_{tb} \end{pmatrix} \begin{pmatrix} d \\ s \\ b \end{pmatrix} \quad (2.28)$$

which can be parameterized by three mixing angles and a CP-violating phase. The different components of the CKM matrix can also be viewed as the probability for quarks to transition from one state to another. Furthermore, the CKM matrix assumes that there are three generations and that the matrix must be unitary. A direct measurement of the different terms constrains the three mixing angles and most importantly the CP-violating phase. It can also answer whether the matrix is unitary or must be expanded if more than three generations exist.

2.1.6 The Electroweak Force

At high energies, the electromagnetic and weak force can be merged into one unified force, the electroweak force. This uses the gauge group $SU(2)_L \times U(1)_Y$ with gauge bosons W_μ^i where $i = 1, 2, 3$

and B_μ for the $SU(2)$ and $U(1)$ factors, respectively, and has gauge couplings g and g'. The basic interactions are an isotriplet of weak currents J_μ coupled to three vector bosons W^μ and a weak hypercharge coupled to vector boson B^μ and can be described by the following:

$$-igJ_\mu \cdot W^\mu - i\frac{g'}{2} j_\mu^Y B^\mu = -ig\overline{\chi_L}\gamma_\mu T \cdot W^\mu \chi_L - ig'\overline{\psi}\gamma_\mu \frac{Y}{2}\psi B^\mu \tag{2.29}$$

Here, $\mathbf{T}$ and Y are the generators of the $SU(2)_L \times U(1)_Y$ respectively. The fermions then transform as follows:

$$\chi_L \rightarrow \chi'_L = e^{i\alpha(x)\cdot\mathbf{T}+i\beta(x)Y}\chi_L \tag{2.30}$$

$$\psi_R \rightarrow \psi'_R = e^{i\beta(x)Y}\psi_R \tag{2.31}$$

where χ_L is an isospin doublet and ψ_R is an isospin singlet.

For leptons, the doublet and singlet are defined as

$$\chi_L = \begin{pmatrix} \nu_l \\ l^- \end{pmatrix}_L \quad \text{with T} = 1/2 \text{ and Y} = -1 \tag{2.32}$$

$$\psi_R = l_R^- \quad \text{with T} = 0 \text{ and Y} = -2 \tag{2.33}$$

since the neutrino is massless in this theory. For quarks, the doublet and singlet are defined as

$$\chi_L = \begin{pmatrix} u \\ d \end{pmatrix}_L \tag{2.34}$$

$$\psi_R = u_R, d_R \tag{2.35}$$

since the quarks are massive and the relation above can be expanded to the higher quark generations where the up-like quark is the charm and top quark and the down-like quark is the strange and bottom quark for the second and third generations respectively.

The electromagnetic interactions are formed by the electromagnetic current with charge Q from

a combination of the neutral currents J^3_μ and j^3_μ defined as follows:

$$j^{em}_\mu = J^3_\mu + \frac{1}{2} j^Y_\mu, \quad Q = T^3 + \frac{Y}{2} \tag{2.36}$$

The basic interactions from Eq. 2.29 lead to the following interactions for gauge bosons A^μ and Z^μ:

$$-i\left[g \sin\theta_W J^3_\mu + g' \cos\theta_W \frac{j^Y_\mu}{2}\right] A^\mu - i\left[g \cos\theta_W J^3_\mu + g' \sin\theta_W \frac{j^Y_\mu}{2}\right] Z^\mu \tag{2.37}$$

where θ_W corresponds to the Weinberg or weak mixing angle and electric charge, e, can be given by $e = g \sin\theta_W = g' \cos\theta_W$.

The Lagrangian that describes the electroweak force can be described by the following:

$$L_{EW} = \overline{\chi_L}\gamma^\mu \left[i\partial_\mu - g\frac{1}{2}\tau \cdot W_\mu - g'\left(\frac{Y_L}{2}\right)B_\mu\right]\chi_L + \overline{\psi_R}\gamma^\mu \left[i\partial_\mu - g'\left(\frac{Y_R}{2}\right)B_\mu\right]\psi_R$$
$$-\frac{1}{4}W_{\mu\nu} \cdot W^{\mu\nu} - \frac{1}{4}B_{\mu\nu}B^{\mu\nu}$$

where the kinetic term for W_μ was defined earlier and the kinetic term for B_μ is defined as $B_{\mu\nu} = \partial_\mu B_\nu - \partial_\nu B_\mu$

The Higgs mechanism can now be used. Four real scalar fields ϕ_i are introduced whose interactions are governed by the following Lagrangian:

$$L_{EW,scalar} = \left|\left(i\partial_\mu - gT \cdot W_\mu - g'\frac{Y}{2}B_\mu\right)\phi\right|^2 - V(\phi) \tag{2.38}$$

where $V(\phi)$ is defined in Eq. 2.21. A gauge invariant ϕ for $SU(2) \times U(1)$ can be defined as follows:

$$\phi = \begin{pmatrix} \phi^+ \\ \phi^0 \end{pmatrix} \quad \text{with } \phi^+ \equiv (\phi_1 + \mathrm{i}\phi_2)/\sqrt{2} \text{ and } \phi^0 \equiv (\phi_3 + \mathrm{i}\phi_4)/\sqrt{2} \tag{2.39}$$

and with weak hypercharge $Y = 1$. Again, $\mu^2 < 0$ and $\lambda > 0$ and the vacuum ϕ_0 that is chosen is that described for the Higgs mechanism that breaks $SU(2)$. ϕ_0 is chosen to be a neutral scalar with

$T = 1/2$, $T^3 = -1/2$, and $Y = 1$ and so the transformation of $\phi_0 \rightarrow \phi_0'$ is invariant for all $\alpha(x)$ values because $Q = T^3 + \dfrac{Y}{2} = 0$. The vacuum remains invariant under $U(1)_{EM}$ transformations and the photon remains massless.

The other gauge bosons acquire mass by substituting the vacuum expectation value ϕ_0 for $\phi(x)$ in $L_{EW,scalar}$

$$\begin{aligned}
\left|\left(ig\frac{1}{2}\tau\cdot W_\mu - i\frac{g'}{2}B_\mu\right)\phi\right|^2 &= \frac{1}{8}\left|\begin{pmatrix} gW_\mu^3 + g'B_\mu & g(W_\mu^1 - iW_\mu^2) \\ g(W_\mu^1 + iW_\mu^2) & -gW_\mu^3 + g'B_\mu \end{pmatrix}\begin{pmatrix} 0 \\ v \end{pmatrix}\right|^2 \\
&= \frac{g^2v^2}{8}\left[(W_\mu^1)^2 + (W_\mu^2)^2\right] + \frac{v^2}{8}(g'B_\mu - gW_\mu^3)(g'B^\mu - gW^{3\mu}) \\
&= \left(\frac{vg}{2}\right)^2 W_\mu^+ W^{-\mu} + \frac{v^2}{8}\begin{pmatrix} W_\mu^3 & B_\mu \end{pmatrix}\begin{pmatrix} g^2 & -gg' \\ -gg' & g'^2 \end{pmatrix}\begin{pmatrix} W^{3\mu} \\ B^\mu \end{pmatrix}
\end{aligned}$$

where $W^\pm = (W^1 \mp iW^2)/\sqrt{2}$ with masses $\dfrac{1}{2}gv$.

As for the last term, diagonalizing the matrix, the eigenvalues are $\dfrac{v^2}{8}$ and 0, yielding eigenvectors $[gW_\mu^3 - g'B_\mu]^2$ and $[g'W_\mu^3 + gB_\mu]^2$ respectively. which corresponds to $\dfrac{1}{2}M_Z^2 Z_\mu^2 + \dfrac{1}{2}M_A^2 A_\mu^2$ for physical fields Z_μ and A_μ. This leads to

$$A_\mu = \frac{g'W_\mu^3 + gB_\mu}{\sqrt{g^2 + g'^2}} \quad \text{with } \mathrm{M_A} = 0, \tag{2.40}$$

$$Z_\mu = \frac{gW_\mu^3 - g'B_\mu}{\sqrt{g^2 + g'^2}} \quad \text{with } \mathrm{M_Z} = \frac{\mathrm{v}\sqrt{\mathrm{g}^2 + \mathrm{g}'^2}}{2} \tag{2.41}$$

The Higgs doublet also generates fermion masses by adding the following Lagrangian for leptons:

$$L_{leptons,scalar} = -G_l\begin{pmatrix} \overline{\nu_l} & \bar{l} \end{pmatrix}_L \begin{pmatrix} \phi^+ \\ \phi^0 \end{pmatrix} l_R + \overline{l_R}\begin{pmatrix} \phi^- & \overline{\phi^0} \end{pmatrix}\begin{pmatrix} \overline{\nu_l} \\ \bar{l} \end{pmatrix}_L \tag{2.42}$$

The symmetry is spontaneously broken when

$$\phi = \frac{1}{\sqrt{2}} \begin{pmatrix} 0 \\ \\ v + h(x) \end{pmatrix}$$

where $h(x)$ is the neutral Higgs field and ϕ_i has been gauged away. The Lagrangian, upon this substitution of ϕ becomes:

$$L_{leptons,scalar} = -\frac{G_l}{\sqrt{2}} v(\overline{l_L} l_R + \overline{l_R} l_L) - \frac{G_e}{\sqrt{2}} (\overline{l_L} l_R + \overline{l_R} l_L) h \tag{2.43}$$

Here, the first term is the mass term where the lepton's mass is

$$m_l = \frac{G_l v}{\sqrt{2}} \tag{2.44}$$

and the last term is a new interaction that involves a hl^+l^- which has a coupling strength proportional to the mass of the lepton l.

As for quarks, the down-like quarks are generated in the same way as the leptons. For up-like quarks, a new Higgs doublet must be used:

$$\phi_c = -i\tau_2 \phi^* = \begin{pmatrix} -\overline{\phi^0} \\ \\ \phi^- \end{pmatrix} \tag{2.45}$$

The symmetry is then spontaneously broken and ϕ_c becomes

$$\phi = \frac{1}{\sqrt{2}} \begin{pmatrix} v + h(x) \\ \\ 0 \end{pmatrix} \tag{2.46}$$

which transforms like ϕ but has a weak hypercharge of $Y = -1$.

The Lagrangian for both up- and down-like quarks becomes:

$$L_{quarks,scalar} = -G_d^{ij}\begin{pmatrix}\overline{u_i} & \overline{d_i'}\end{pmatrix}_L\begin{pmatrix}\phi^+\\ \phi^0\end{pmatrix}d_{jR} - G_u^{ij}\begin{pmatrix}\overline{u_i} & \overline{d_i'}\end{pmatrix}_L\begin{pmatrix}-\overline{\phi^0}\\ \phi^-\end{pmatrix}u_{jR} + \text{ hermitean conjugate} \tag{2.47}$$

with $i, j = 1, ..., N$ where N is the number of quark doublets. The Lagrangian can be rewritten in a diagonal form by converting the flavor eigenstates denoted by d' to mass eigenstates d using the CKM matrix:

$$-m_d^i\overline{d_i}d_i\left(1+\frac{h}{v}\right) - m_u^i\overline{u_i}u_i\left(1+\frac{h}{v}\right) \tag{2.48}$$

where the coupling of the quarks to the Higgs boson depends on the mass of the quark.

By adding all the interactions together mentioned above, the electroweak Lagrangian is

$$\begin{aligned} L_{EW} = &-\frac{1}{4}W_{\mu\nu}\cdot W^{\mu\nu} - \frac{1}{4}B_{\mu\nu}\cdot B^{\mu\nu} \\ &+\overline{f_L}\gamma^\mu\left(i\partial_\mu - g\frac{1}{2}\tau\cdot W_\mu - g'\frac{Y}{2}B_\mu\right)f_L + \overline{f_R}\gamma^\mu\left(i\partial_\mu - g'\frac{Y}{2}B_\mu\right)f_R \\ &+\left|\left(i\partial_\mu - g\frac{1}{2}\tau\cdot W_\mu - g'\frac{Y}{2}B_\mu\right)\phi\right|^2 - V(\phi) \\ &-(G_1\overline{f_L}\phi f_R + G_2\overline{f_L}\phi_c f_R + \text{ hermitean conjugate}) \end{aligned}$$

The first two terms correspond to the $W^\pm$, Z, γ kinetic energies and self interactions. The next two terms correspond to the fermion f kinetic energies and interactions with the electroweak gauge bosons. The following two terms correspond to the gauge bosons and Higgs boson masses and couplings. The last set of terms correspond to the fermion masses and coupling to the Higgs boson.

2.1.7 Cross Section Calculations

Cross section calculations can be done using Feynman diagrams, a pictorial representation that uses these new interactions from the above Lagrangians to describe a particular initial and final state. The diagrams represent mathematical relations that arise from the Lagrangian and form the invariant amplitude needed for cross section calculations. The differential cross section for a particular initial

and final state can be described by the following equation:

$$d\sigma = \frac{|M|^2}{F} dQ \tag{2.49}$$

where M is the invariant amplitude that is computed from all Feynman diagrams that describe a particular initial and final state, F is the flux factor, and dQ is the Lorentz invariant phase space factor.

The flux factor is the incident flux in the lab and given by the following for a general collinear collision between particle A and particle B:

$$F = |v_A - v_B| \cdot 2E_A \cdot 2E_B \tag{2.50}$$

where $v_{A(B)}$ is the velocity of particle A (B) and $E_{A(B)}$ is the energy of particle A (B).

The Lorentz invariant phase space factor depends on the number of initial and final particles and can be given for the interaction AB $\rightarrow$ CD as the following:

$$dQ = (2\pi)^4 \delta^{(4)}(p_C + p_D - p_A - p_B) \frac{d^3 p_C}{(2\pi)^3 2E_C} \frac{d^3 p_D}{(2\pi)^3 2E_D} \tag{2.51}$$

This phase space factor imposes momentum conservation and when calculating the cross section, integrates over all of the phase space of the final state particles.

The cross section can be thought of as the effective area over which a set of initial state particles interact to produce a particular set of final state particles. By calculating the cross section and multiplying this with the luminosity, which can be thought of as the number of times a collision with a particular initial state occurs, one can calculate how often a certain process should occur. This is how experiment verifies theory: within error, the number of events for a particular initial and final state predicted by the theoretical cross section should match the number of events seen in experiment with event signatures that match the final state after processes that mimic the same final state are accounted for. If this does not match, then the theory is not correct.

2.2 Top quark

Hypothesized together with the bottom quark in 1973 by Makoto Kobayashi and Toshihide Maskawa to explain CP violations in kaon decay, the top quark was not discovered until 1995 at Fermilab by both DØ and CDF via the strong interaction [3] [4]. It would take another 14 years before the electroweak produced top quark was discovered and again by both Fermilab collaborations [5] [6] . During these 14 years, experimental results confirmed that the top quark is an up-like quark in the third generation and thus has an electric charge of $+2e/3$. It is a fermion with spin-1/2. It is also the most massive of quarks at $173.1 \pm 0.6(\text{stat}) \pm 1.1(\text{syst})$ GeV/c^2 [7], the next heaviest quark (bottom) being at 4 GeV/c^2 [1]. As a result, the top quark couples very strongly to the Higgs boson as the coupling strength is proportional to the quark's mass.

The top quark is produced primarily through the strong interaction but can also be made via the electroweak channel which is the focus of this thesis and described in further detail in the next section. For strong interactions, a gluon produces a top and antitop quark and is commonly know as top pairs. The cross section for this production mode is $7.91^{+0.61}_{-1.01}$ pb^{-1} for a top mass at 170 GeV/c^2 [8]. The Feynman diagram for top pairs at leading order can be found in Fig. 2.2.

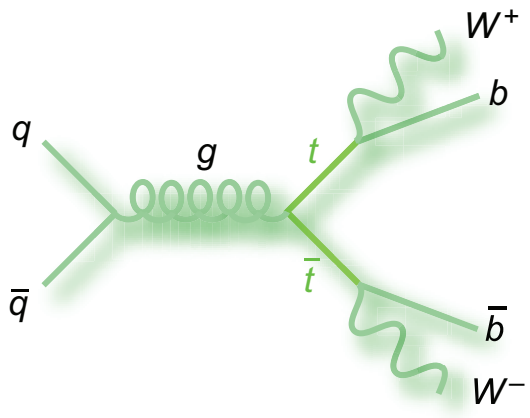

Figure 2.2: The top pair is produced by a quark and antiquark annihilating to form a gluon which has enough energy to produce a top and antitop quark.

The top quark has a lifetime of 5×10^{-25}s which is 20 times shorter than the timescale for strong interactions. As a result, the top quark will decay into a W and a down-type quark rather than

hadronize like all the other quarks. The dominant decay is to Wb since this occurs 99% of the time. As for the W, it has many decay modes which are summarized in Table 2.1 [1].

W^+ decay modes	Branching Fraction (%)
$l^+\nu$	10.80 ± 0.09
$e^+\nu$	10.75 ± 0.13
$\mu^+\nu$	10.57 ± 0.15
$\tau^+\nu$	11.25 ± 0.20
hadrons	67.60 ± 0.27

Table 2.1: The branching fractions for all possible W decay modes are listed in this table [1].

For the top pair, the different decay modes can be found in Fig. 2.3

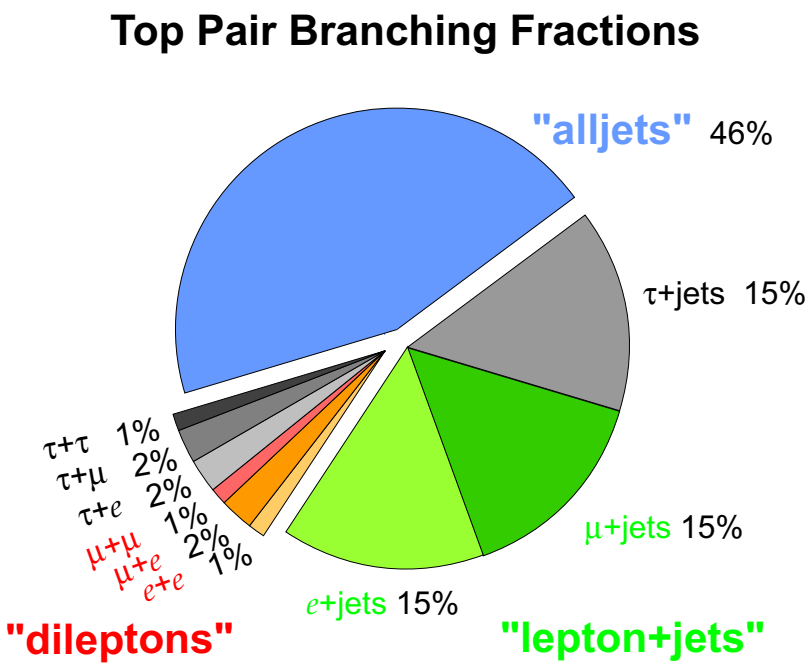

Figure 2.3: The top pair branching fractions for all possible decay modes: alljets, dileptons, and lepton+jets.

Electroweak Production of the top quark

The top quark produced by the electroweak channel can occur through three different Feynman diagrams: s-channel, t-channel, and associated W production. For the s-channel, the top quark is produced by $q\bar{q}$ annihilation into a virtual time-like W boson that then decays into a t and $\bar{b}$ quark

or $\bar{t}$ and b quark. At NLO, the s-channel cross section is 1.12 ± 0.05 pb [9]. For the t-channel, a quark and gluon scatter, resulting in a virtual space-like W produced by a light and bottom quark exchange and producing a forward scattered light quark and a top quark. At NLO, the t-channel cross section is 2.34 ± 0.13 pb[9] . For associated W production, the top quark is created in association with an on-shell W boson; however, it has a negligible cross section of 0.28 ± 0.06 pb [9] at the Tevatron and will most likely be found at the LHC.

Fig. 2.4 shows the Feynman diagrams for top quarks produced singly through the electroweak channel.

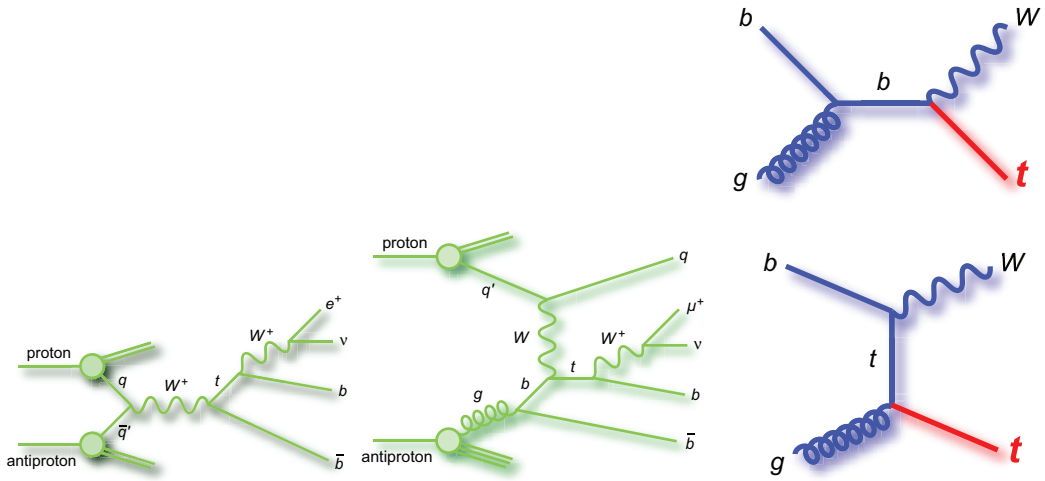

Figure 2.4: The Feynman diagrams for electroweak produced top quarks for s-channel production (left), t-channel production (center), and associated W production (right).

The top quark produced in this way, sometimes referred to as single top since only one top quark is found in the final state, can be used to study many interesting properties that are enhanced in this particular top quark production channel. First, it provides a direct measurement of V_{tb} without any assumptions on the necessity of unitarity and three generations. Without a direct measurement of this process, $|V_{tb}|$ is measured by comparing the branching fractions B of $t \to Wb$ and $t \to Wq$:

$$\frac{B(t \to Wb)}{B(t \to Wq)} = \frac{|V_{tb}|^2}{\sum_q |V_{tq}|^2} = |V_{tb}|^2 \tag{2.52}$$

where q are the b, s, and d quarks. By assuming unitarity and a three generation model,

$$|V_{ub}|^2 + |V_{cb}|^2 + |V_{tb}|^2 = 1 \tag{2.53}$$

and the precise measurements of $|V_{ub}|$ and $|V_{cb}|$ then constrain $|V_{tb}|$ to the following [1]:

$$0.991 < |V_{tb}| < 0.9994 \tag{2.54}$$

However, without these assumptions, $|V_{tb}|$ has a larger range [11]:

$$0.06 < |V_{tb}| < 0.9994 \tag{2.55}$$

Thus, a direct measurement could provide clear evidence for four or more generations, if $|V_{tb}|$ differs greatly from 0.99.

Second, the top quark produced through the electroweak channel is highly polarized and this polarization can be measured cleanly because the top quark does not hadronize [10] [11]. The polarization of the top quark is transferred to the W and b quark since the SM Wtb vertex is entirely left-handed. Since the W's decay into left-handed light fermions, the W polarization information is passed to its decay products which, for this case, are a lepton and neutrino. As a result, the original top quark's polarization can be measured from the final decay products that we measure.

The SM demands W to be either longitudinal or left-handed since right-handed W bosons are heavily suppressed due to the small mass of the b quark relative to the top quark and W boson mass. Furthermore, the b quark mass is much less than the energy it gets from the top quark decay and the left-handed chirality of the Wtb vertex translates into left-handed helicity for the b. As for the W bosons, the longitudinal W bosons are emitted preferentially in the same direction as the top quark spin, whereas the transverse Ws prefer the backwards direction relative to the top quark spin axis. This comes from angular momentum conservation and the SM $V - A$ coupling, which is characterized by $1 - \gamma^5$ couplings, between the W and quarks. If the W boson is emitted along the

top quark spin axis, the spin of the b quark points in the same direction as the spin of the original top quark and we must have zero spin projection for the W boson, corresponding to the longitudinal mode of the W. The charged lepton will be in the same direction as the W and so it will be in the direction of the top spin axis. On the other hand, when the W is emitted in the backwards direction, the spin of the b quark is in the opposite direction of the spin of the parent top quark. W must have left-handed helicity in order to conserve angular momentum and when it decays, the charged lepton must also be right-handed so it will prefer to move against the W direction and so will also be in the same direction as the top quark spin.

In both cases, if the SM is correct, the charged lepton is maximally correlated with the top quark spin and the angular distribution between the charged lepton and the spin axis of the top quark in its rest frame must follow the following distribution:

$$\frac{1}{\Gamma}\frac{d\Gamma}{dcos\theta} = \frac{1}{2}(1 + cos\theta) \tag{2.56}$$

where θ is the angle between the direction of the charged lepton and the top quark polarization, in the top quark rest frame, and Γ is the partial width for semi-leptonic top decay in SM.

Third, this production mode of the top quark is a sensitive probe into physics beyond the SM, especially if one looks at the s- and t-channel processes separately [11]. For t-channel processes, models that produce anomalous couplings or flavor changing neutral currents contribute new diagrams to this channel. As for the s-channel, models with a new intermediate particle such as strong dynamics, a charged top-pion, Kaluza-Klein modes of the W, or a W$'$ gauge boson would open new production modes in this channel. This thesis will also look at W$'$ gauge bosons that decay much like the SM W bosons and will also set limits on theories that predict W' bosons. Diagrams from beyond the SM models can be found in Fig. 2.5. Additionally, the top quark produced in the electroweak channel is a background when searching for the SM Higgs boson, the last particle discovery needed to confirm the SM.

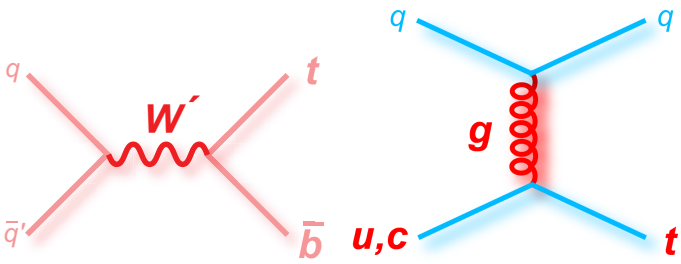

Figure 2.5: Physics beyond the SM can be probed by the s-channel and t-channel production of top quarks produced through the electroweak channel. For s-channel production (left), a heavy gauge boson W' can contribute additional diagrams whereas for the t-channel production (right), flavor changing neutral currents where the t can produce a c quark and a gauge boson such as the Z, γ, or gluon can contribute additional diagrams.

Chapter 3

The Tevatron and the DØ Detector

Located near Chicago, Fermilab remains at the cutting edge of high energy particle physics research and is currently the only place where top quarks can be produced. Producing these high energy collisions of protons and antiprotons is an amazing feat in itself and requires a series of accelerators that rely on the basic physics of electricity and magnetism applied in extraordinary ways. The detectors located at these collision points need to disentangle all the particles that are produced and need to do this every 396 ns, keeping only those events that mark "interesting physics," the anomalies. Not only do we need to understand what type of particles we expect and how often they should be produced, but we also need to know how these particles will interact in different environments so we can build detectors in ways that we can distinguish the difference between the types of particles produced. Until we can be fairly confident in how the detector works and its different idiosyncrasies that need to be calibrated and understood, we cannot make any interesting connections with what theory tells us.

3.1 Tevatron

The Tevatron is, for the time being, the world's most powerful particle beam collider and the only place that top quarks can be produced. The Tevatron makes protons and antiprotons and then accelerates these particles to high energies and to a velocity nearly that of the speed of light before

they collide with one another [12] [13]. These high energy collisions act like a large magnifying glass, probing interactions that occur over very small distances, interactions like the W boson producing a top and anti-bottom quark or vice versa. The protons and antiprotons are accelerated to 980 GeV through a series of accelerators outlined in Figure 3.1.

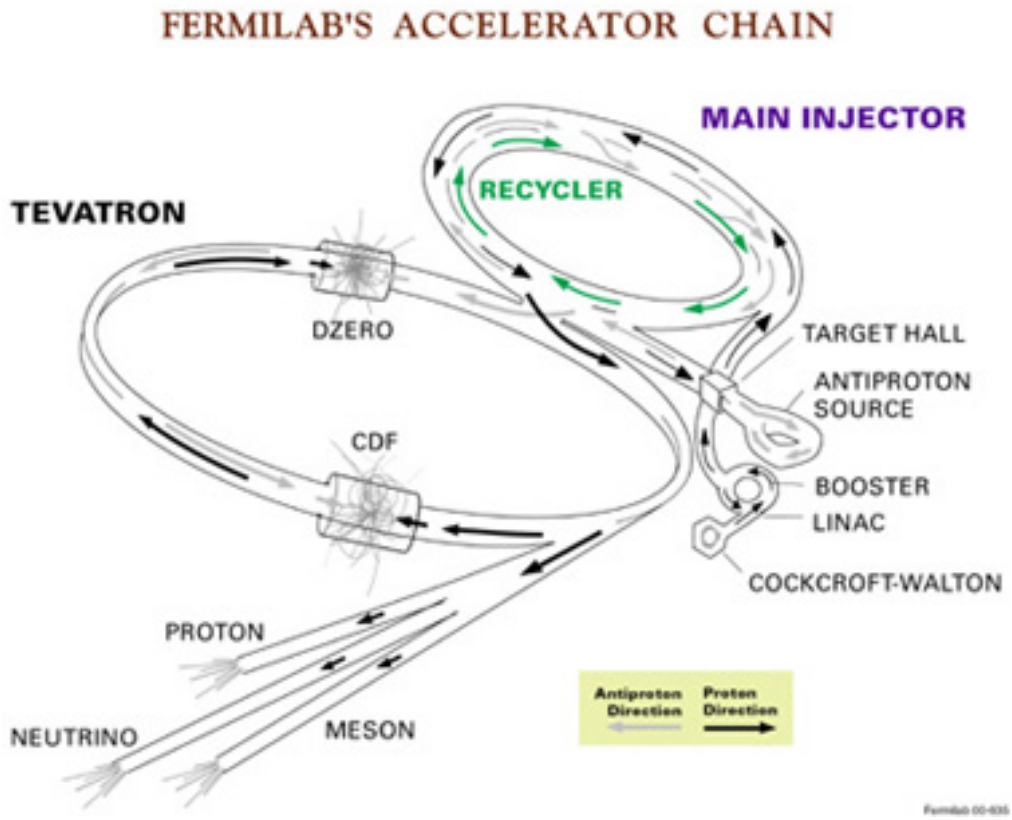

Figure 3.1: The proton is accelerated through many different types of accelerators, starting from the Cockcroft-Walton pre-accelerator to the linear accelerator, composed of drift tubes and side coupled cavities, to a series of synchrotrons known as the Booster, the Main Injector and finally to the Tevatron. The antiprotons come from protons in the Main Injector which collide with a nickel target and are stored in the Accumulator rings until there is enough to collide with the protons in the Tevatron [12].

The whole process starts with a small bottle of hydrogen at the Cockcroft-Walton pre-accelerator. The hydrogen gas is ionized, creating negative ions when an electron combines with the gas using a magnetron. These negative ions are accelerated by a positive voltage to an energy of 750 keV using the Cockcroft-Walton pre-accelerator. This pre-accelerator is a voltage multiplier ladder network of capacitors and diodes that converts 75 keV AC to a higher DC voltage level of -750 keV.

The ions then enter a linear accelerator through a 750 keV transfer line. Using an Electrostatic Chopper, the 750 keV transfer line separates the continuous flow of ions into 42 μs long pulses, the frequency of the linear accelerator. Each pulse goes through a Buncher to make the pulse into a bunch before entering the linear accelerator. A Buncher makes a bunch by slowing down particles arriving early in the radio-frequency (RF) cycle using a decelerating voltage, and speeding up particles arriving later using an accelerating voltage.

The linear accelerator (Linac) is approximately 500 feet long and accelerates particles using drift tubes and side-coupled cavities. The first portion is the Drift Tube Linac (DTL) which uses five drift tubes, accelerating the ions from 750 keV to 116 MeV. Each time the particles traverse the gap between the drift tubes, they get a boost in energy and velocity that comes from a RF system that drives the appropriate cavity fields in the drift tubes to the increased level and phase necessary for these ions to gain energy and thus be accelerated to 116 MeV.

The ions then enter the Side-Coupled Linac (SCL) which is composed of seven side coupled cavities. Each side-coupled cavity module consists of four sections with each section containing 16 accelerating cells and 15 coupling cells. Each individual cell accelerates the bunches in such a way that the bunches enter the cells when the field is in the accelerating direction and then moves to another cell when the field changes direction to the decelerating direction at a specified RF used by the SCL. The accelerating gradient for each side-couple cavity module is about 7.5 MV/m, three times that of the Drift-Tube Linac (DTL). In this case, the beam pulses travel 8 cells apart in the SCL where there can be up to two pulses in a section and eight pulses in one module.

The next stage is the Booster, where the ions enter through the 400 MeV transfer line, and are stripped of their electrons by passing through carbon foil. The Booster is a synchrotron which is a circular accelerator that uses magnets to bend the beam of protons to follow a circular trajectory. The Booster consists of an injection and extraction system as well as high and low level RF acceleration systems consisting of 19 cavities. The RF cavity operates by using a time varying electric field which is moved along the cavities much in the same manner as the SCL described above. In order for the protons to follow a circular path, bending magnets are necessary. There are also focusing magnets

to keep the bunches from spreading out. The protons circle the Booster 20,000 times, picking up more energy every revolution until they reach 8 GeV.

The protons then enter the Main Injector, which is another synchrotron but with a larger radius. The protons enter the Main Injector through the 8 GeV Injection line. The Main Injector has four functions: accelerating protons from 8 to 150 GeV, making 120 GeV protons which are used to make antiprotons, receiving antiprotons from the Antiproton Source and increasing their energy to 150 GeV, and injecting both protons and antiprotons into the Tevatron.

Antiprotons are made from the protons that come from the Main Injector. When they collide with a nickel target, the collisions produce many secondary particles, including antiprotons. For every 200,000 protons hitting the target, only one antiproton is produced. The antiprotons enter the Antiproton Debuncher and Accumulator rings where they are collected, focused and then stored until a sufficient amount is produced. Once this occurs the antiprotons are sent to the Main Injector for acceleration and injection into the Tevatron. The Main Injector tunnel also has an Antiproton Recycler that stores antiprotons that return from a trip through the Tevatron and can later be re-injected.

The Tevatron then accelerates 36 bunches of protons and antiprotons to 980 GeV in the same ring but the bunches travel in opposite directions due the charge difference between protons and antiprotons. The beams cross at two interaction points, CDF and DØ, every 396 ns with a center of mass energy of 1.96 TeV. The Tevatron currently can reach instantaneous luminosities well above $10^{32}\ cm^{-2}s^{-1}$ and produces very exciting physics results that are starting to probe the limits of where the Standard Model should breakdown.

3.2 DØ Detector

Proposed in 1983, the *DØ* experiment has had two successful run periods from 1992 - 1996, during which the top quark was discovered via strong interactions, and from 2001 - present day, during which the electroweak production mechanism of the top quark was discovered which is the focus of this thesis. The remnants of the proton-antiproton collisions travel through different detector parts

that are tailored to specific particle interactions with matter where specific detector components show the particles' trajectories and measure their energy and momentum. The DØ detector [14], which is the focus of the remaining sections of this chapter, is composed of three parts: the silicon and fiber tracker in a 2 Tesla superconducting solenoidal magnet, a liquid argon/uranium calorimeter, and a muon system in 1.8 Tesla toroidal magnetic field. From these subdetectors, events must be selected and then written to tape for further analysis. Fig.3.2 shows the DØ detector will all its subdetectors.

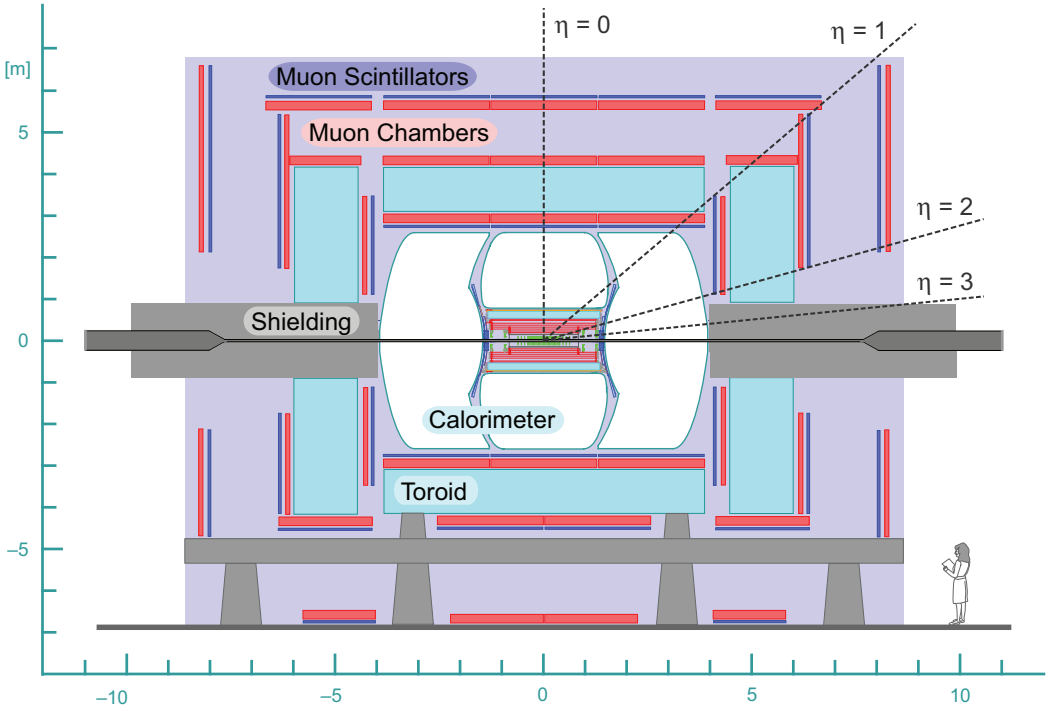

Figure 3.2: The DØ detector [14] is pictured here with all its subdetectors which will be discussed in detail in the coming sections.

3.2.1 DØ Coordinate System

The *DØ* coordinate system uses a right-handed Cartesian coordinates (x,y,z) where the center of the detector is the origin of the coordinate system. The positive values for the z-axis are along the proton direction, for the y-axis are upward, and for the x-axis are away from the Tevatron

center. The transverse plane corresponds to the (x,y) plane or the plane perpendicular to the beam pipe. The spherical (r,θ,ϕ) are also used where the angles ϕ and θ are the azimuthal and polar angles respectively and $\theta = 0$ is along the proton beam direction. The r-coordinate denotes the perpendicular distance from the beam axes. As for θ, it can be described also by the Lorentz invariant pseudorapidity η:

$$\eta \equiv -\ln(\tan(\theta/2)) \tag{3.1}$$

which approximates the true rapidity y:

$$y = \frac{1}{2}\ln\left(\frac{\mathrm{E} + \mathrm{p_z}}{\mathrm{E} - \mathrm{p_z}}\right) \tag{3.2}$$

for finite angles in the limit that $(m/E) \to 0$.

3.2.2 Central Tracking System

The central tracking system, shown in Fig. 3.3 consists of the silicon microstrip tracker (SMT) and the central fiber tracker (CFT) in a 2 Tesla superconducting solenoidal magnet. Surrounding the beryllium beam pipe, which has a wall thickness of 0.508 mm, an outer diameter of 38.1 mm, and a length of 2.37 m, the central tracking system locates the primary interaction vertex with a resolution of 35 μm along the beamline and also secondary vertices for b-tagging with an impact parameter resolution of better than 15μm in $r - \phi$ for particles with $p_T >$ 10 GeV/c at $|\eta| = 0$. The central tracking system improves measurements of the lepton p_T, jet transverse energy (E_T), and missing transverse energy $\not\!\!E_T$. The electromagnetic calorimeter can also be calibrated using the E/p of electrons which comes from the tracking system since it is defined to measure the momentum (p) and the charge of a charged particle that passes through it.

Silicon Microstrip Tracker

The SMT, as seen in Fig. 3.4, covers nearly the full η range of the calorimeter and muon systems and provides tracking information close to the collision point of DØ. This information is important

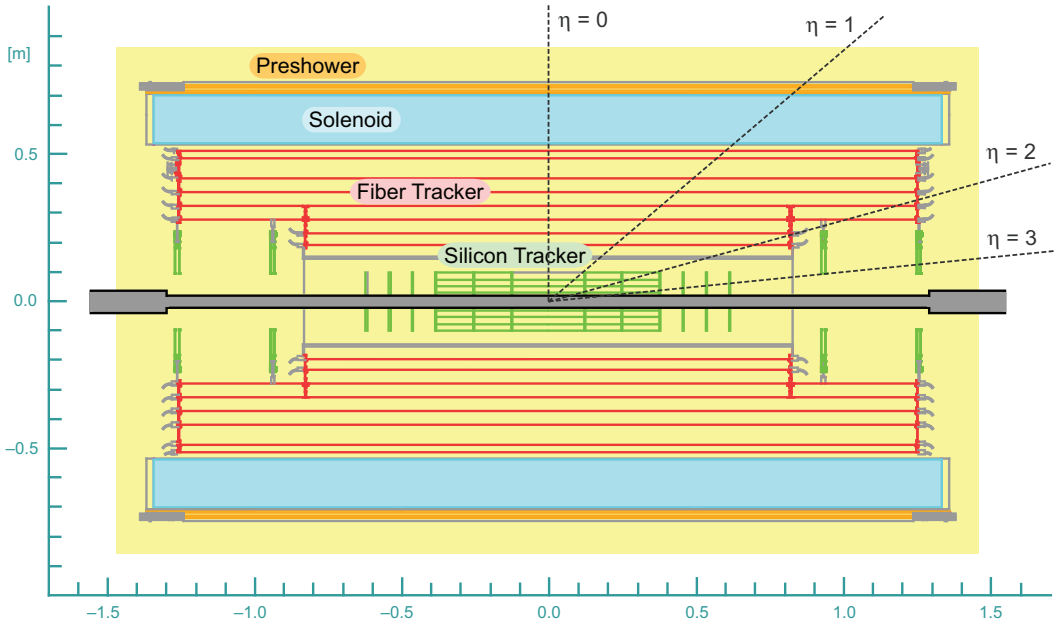

Figure 3.3: The central tracking system is pictured here [14] and is composed of two subdetectors: the SMT and CFT.

for finding secondary vertices needed for tagging jets as coming from the b-quark. The center of the SMT has barrel modules that are interspersed with disks. As for the forward region, it contains assemblies of disks only. The barrel detectors measure the r-ϕ coordinate and the disk detectors measure r-z and r-ϕ of a particle. Both detectors are made from doped silicon and have a reverse voltage applied to them. A charged particle that passes through the silicon will then create an electron-hole pair which forms an electric current that can be readout.

The SMT has six barrels in the central region where each barrel has four silicon readout layers called "ladders". Layers 1 and 2 have 12 ladders each while layers 3 and 4 have double that with 24. In the high $|z|$ region, the barrels are capped with 12 double-sided wedge detectors called F-disks. After the barrels, there are three more F-disks and two large H-disks. An H-disk is made of 24 wedges, where each wedge has two back to back single-sided "half" wedges. Each side of a wedge is read out independently, resulting in 912 readout modules.

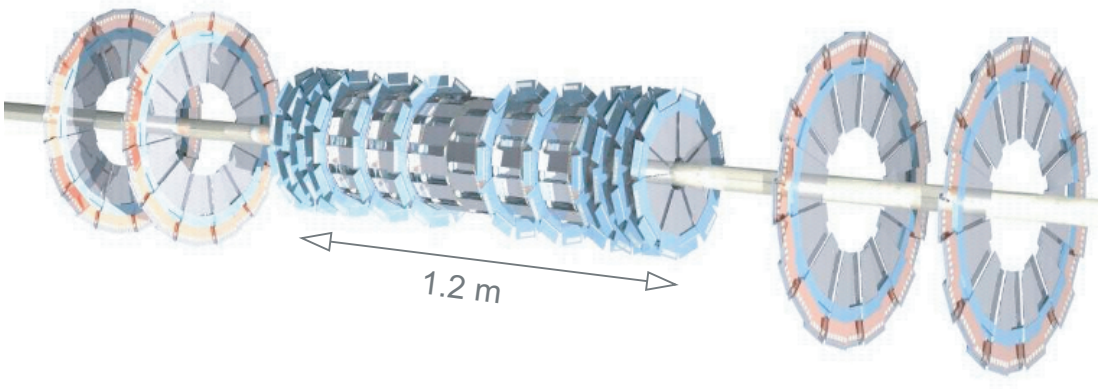

Figure 3.4: The SMT subdetector is pictured here and has barrel modules interspersed with disks at the center of the subdetector and assemblies of disks in the forward region [14].

Central Fiber Tracker

The Central Fiber Tracker (CFT) provides more tracking information as a charged particle traverses the detector. These tracks can point to whether the particle comes from the primary vertex or a secondary vertex and also the curvature of the tracks can be used to measure the track's momentum and charge. The CFT occupies 20 - 53 cm in radial space from the center of the beam pipe and is composed of 80,000 1 mm fibers. These fibers are distributed over eight doublet layers. A doublet layer has two sublayers of fiber where one of the sublayers is along the beam direction and the other is at a stereo angle in ϕ of $\pm\ 3\,^{\circ}$. The CFT is divided into 80 sectors where each sector covers 4.5° in azimuth.

As a particle traverses the CFT, it interacts with the fibers as energy deposited into the scintillating fibers. This energy is converted into photons whose wavelengths are then shifted from 340nm to 530nm which is in the visible spectrum. The Visible Light Photon Counters (VLPCs) convert this light into an electrical signal.

3.2.3 Solenoid Magnet

The superconducting solenoidal magnet that encloses the tracking system bends the trajectories of the charged particles, resulting in momentum and charge measurements based on the hits found

in the central tracking system. The dimensions of the magnet are 2.73 m in length and 1.42 m in diameter and are based on the available space in the central calorimeter vacuum vessel. The magnet produces a central field of 2T in the z direction and has an overall thickness of approximately one radiation length at $\eta = 0$.

3.2.4 Preshower Detectors

The preshower detectors help in identifying electrons and photons since these particles should shower in these detectors, which have a 2 X_0 radiation length, prior to entering the calorimeter. They also serve as tracking detectors because it provides another spatial point for matching tracks to calorimeter showers. The central preshower detector (CPS) covers $|\eta| < 1.3$ and is located between the solenoid and the central calorimeter. The two forward preshower detectors (FPS) span $1.5 < |\eta| < 2.5$ and are attached to the faces of the end calorimeters. These detectors are made from triangular strips of scintillator with no dead space between the strips. At the center of each of the strip is a wavelength-shifting fiber that collects and carries the light produced as a charged particle passes through it to the end of the detector. These fibers are connected to clear light-guide fibers which transmit the light to VLPC cassettes for readout.

For the CPS, there are three concentric cylindrical layers of triangular scintillator strips which are arranged in an axial-u-v geometry where the u stereo angle is set at 23.774° and the v stereo angle is set at 24.016°.

For the FPS detectors, there are two layers at different z composed of scintillator strips separated by a 2 X_0-thick lead-stainless-steel absorber. The upstream layers are known as the minimum ionizing particle (MIP) layers, and it is in these layers that charged particles leave minimum ionizing signals that provide coordinates in η, ϕ, and z of the track. The MIP layers and the absorber cover the η region from $1.65 < |\eta| < 2.5$. The downstream layers behind the absorber are called shower layers due to the clusters of energy found from electrons and other heavier charged particles showering in the absorber. The shower layers cover $1.5 < |\eta| < 2.5$.

Each FPS detector has MIP u and v and shower u and v measuring planes. These planes are

constructed from two layers, each with eight 22.5° wedges of active material separated by eight wedges of inactive material. The active material has two sublayers of nested scintillator strips at a stereo angle of 22.5° from each other. Wavelength shifting fibers connected to clear waveguides collect light from the strips and transport it to the VLPC cassettes. The absorber is divided into 48 wedge-shaped segments that each subtends 7.5° in ϕ and is comprised of two lead absorber elements epoxied to each side of a 1/8“ - thick stainless-steel plate.

3.2.5 Calorimeter

The DØ calorimeter system has three sampling calorimeters and an intercryostat detector. The calorimeters measure the energy of electrons, photons, and jets which can then be used to calculate the missing transverse energy ($\not\!\!E_T$) required by energy conservation. These physics objects can also be identified based on which calorimeter they shower in. The calorimeter can be divided into the following sections: the central calorimeter (CC) which covers $|\eta| \lesssim 1$ and the two end calorimeters, ECN (north) and ECS (south) which extend coverage to $|\eta| \approx 4$. Fig. 3.5 shows the entire calorimeter system.

Each sampling calorimeter has an electromagnetic section which is closest to the interaction region and is followed by fine and coarse hadronic sections. A sampling calorimeter consists of an active medium which generates signal and a passive medium which acts as an absorber. For the EM section, when a high energy electron or photon is incident on a thick absorber, it makes an electromagnetic cascade by pair production and bremsstrahlung until a critical energy is reached. At this energy, the electrons or photons can only lose energy through ionization and excitation.

For the hadronic sections, the charged particles that enter contain very little electrons or photons as they are mostly contained in the EM sections. For inelastic hadronic collisions, a significant fraction of the energy is removed due to the production of secondary π^0's and η's which then decay to produce photons that generate EM cascades. Charged secondaries such as $\pi^{\pm}$, p, etc. deposit energy through ionization and excitation but can also interact with nuclei. The charged collision products as well as the showering γ-rays from the prompt de-excitation of highly excited nuclei

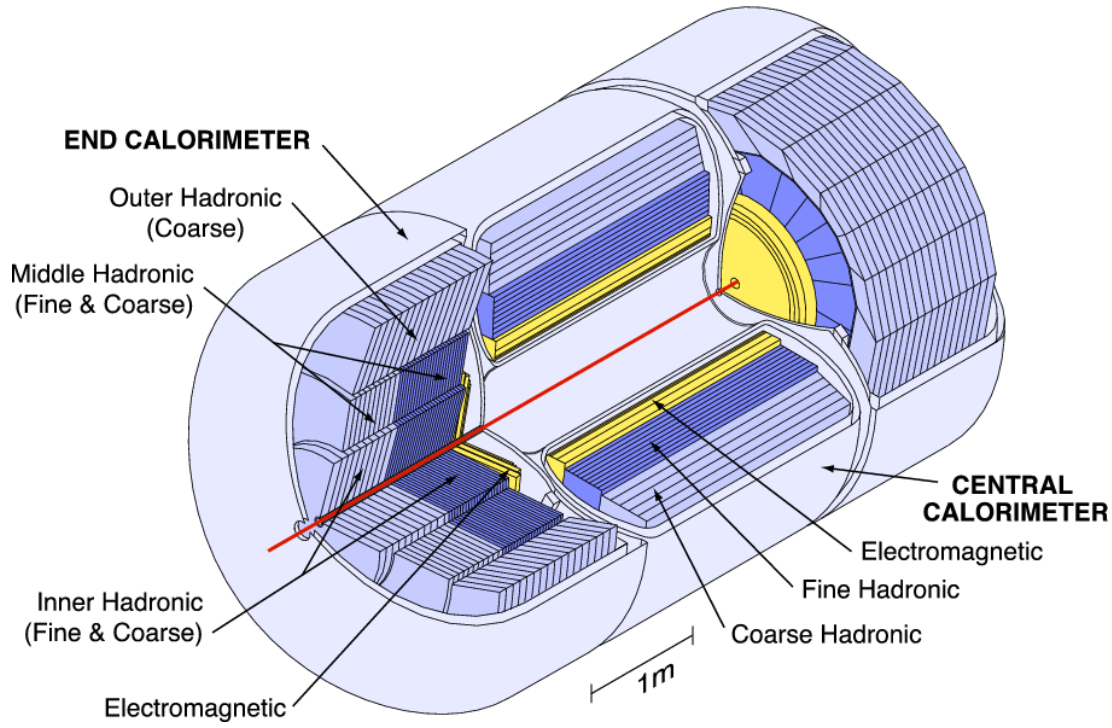

Figure 3.5: The calorimeter system is pictured here, showing the CC and two EC regions [14].

produce detectable ionization.

For both sections, the active medium used is liquid argon which when charged particles enter, cause ionization that can be collected as signal in the detector. As for the absorbers, the electromagnetic sections (EM) have thin plates at 3 or 4 mm depending on the calorimeter section made of nearly pure depleted uranium. The fine hadronic sections are made from 6-mm-thick uranium-niobium alloy. The coarse hadronic modules have 46.5 mm plates of copper in the CC and stainless steel in the EC.

A typical calorimeter cell consists of absorber plates with liquid argon gaps. An electric field is established by grounding the metal absorber plates and connecting the resistive surfaces of the signal boards to positive high voltage that is around 2.0 kV. The electron drift time across the 2.3 mm liquid argon gap is approximately 450 ns. The surfaces of the signal boards have G-10 sheets whose epoxied surfaces facing the liquid argon gap serve as high voltage electrodes for the gap while the other surface is used for segmented readout. Several such surfaces at approximately the same η and

ϕ are ganged together in depth to form a readout cell. These readout cells form pseudo-projective towers as seen in Fig. 3.6 since the centers of cells of increasing shower depth lie on rays projecting from the center of the interaction region but the cell boundaries are aligned perpendicular to the absorber plates.

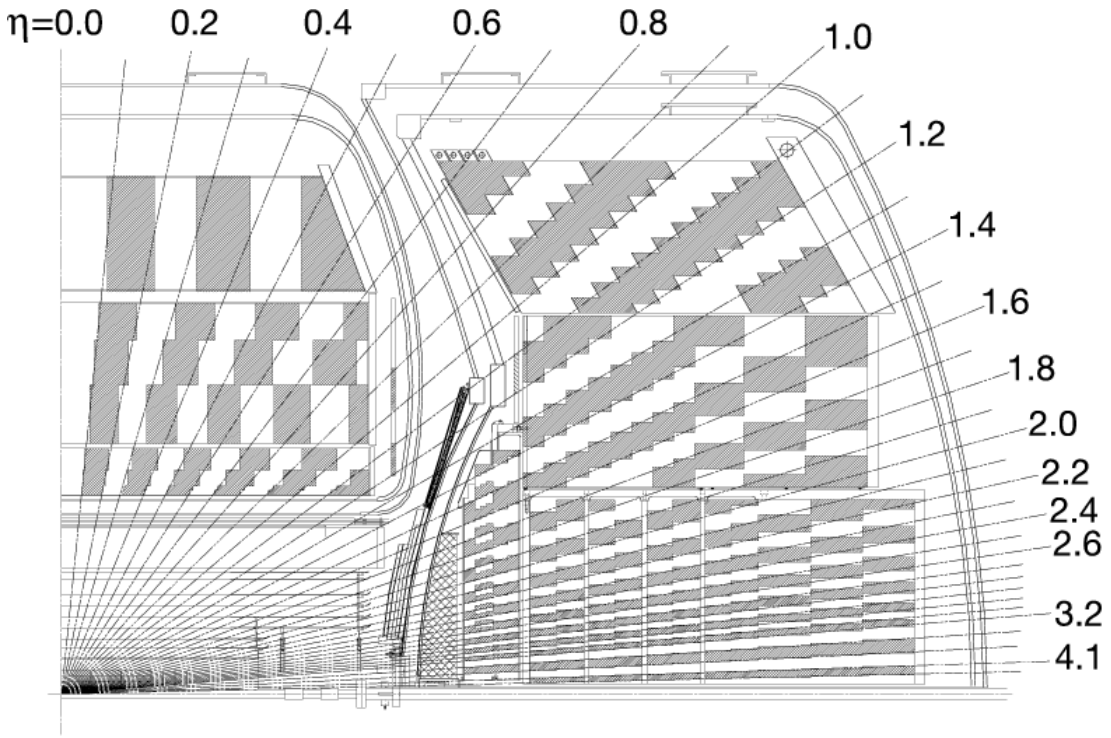

Figure 3.6: A schematic view of the DØ calorimeter showing the pseudo-projective towers formed by the readout cells [14]. The shading pattern are groups of cells ganged together for signal readout. The rays indicate η regions from the center of the detector.

The transverse sizes of the readout cells are similar to the transverse sizes of the showers: 1-2 cm for EM showers and 10 cm for hadronic showers. Towers in both modules are $\Delta\eta$=0.1 and $\Delta\phi$=0.1. The third layer of the EM modules is segmented twice as finely in both η and ϕ for precise location of EM shower centroids since this layer is where the EM shower is maximal. Cell sizes also increase in η and ϕ at larger η. In total, the calorimeter has 55,296 channels to be readout.

The intercryostat detector (ICD) provides scintillator sampling at the ends of the cryostats and covers the region from $1.1 < |\eta| < 1.4$. This detector is a series of $0.5''$-thick scintillating tiles

enclosed in light-tight aluminum boxes where each tile covers an area of $\Delta\eta \times \Delta\phi \approx 0.3 \times 0.4$ and is further divided into twelve subtiles of $\Delta\eta \times \Delta\phi \approx 0.1 \times 0.1$. Each subtile is readout using two wavelength shifting fibers connected to clear optical fibers that terminate at a photomultiplier tube.

3.2.6 Muon Detector

The muon system is located after the calorimeter system which removes almost all of the EM and hadronic particles. The only particles that are left that pass into this detector are neutrinos, which does not interact with any of the detectors, and muons which are detected using drift tubes and scintillator counters. The drift tubes provide the muon's track segments and the scintillator counters provide the muon's timing information. The drift tube and scintillator detectors for the entire system are shown in Figs. 3.7 and 3.8 respectively.

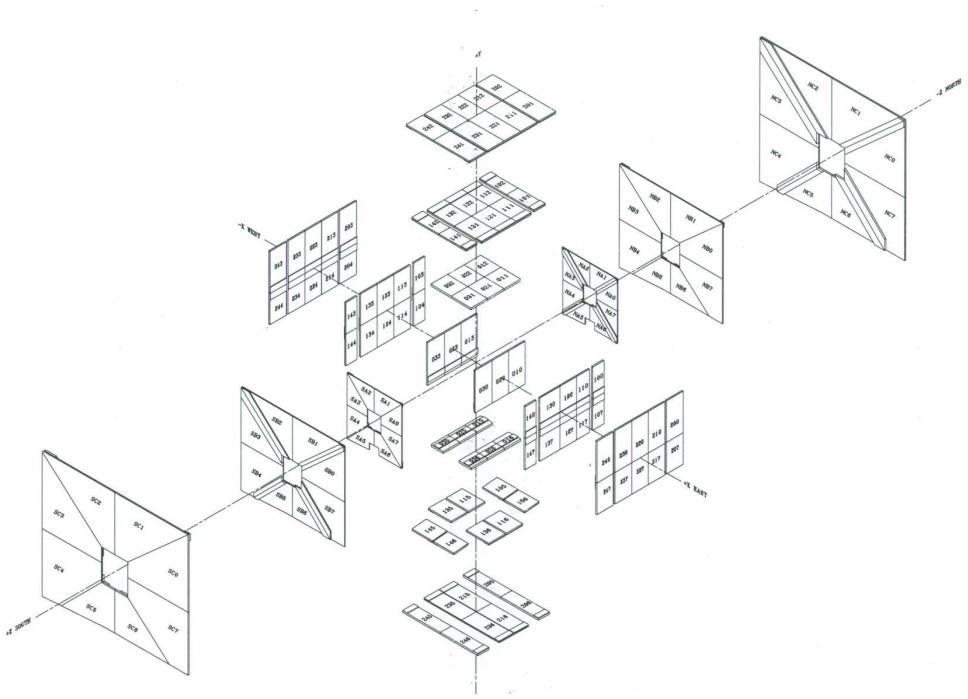

Figure 3.7: A complete view of the muon wire chambers used in the muon system [14].

The drift tube works based on the ionization that occurs from a charged particle losing energy in the gas in the chamber. This cases the creation of ions and electrons which drift through the gas, sometimes causing further ionization, towards the positive electrode. As the ionization cluster

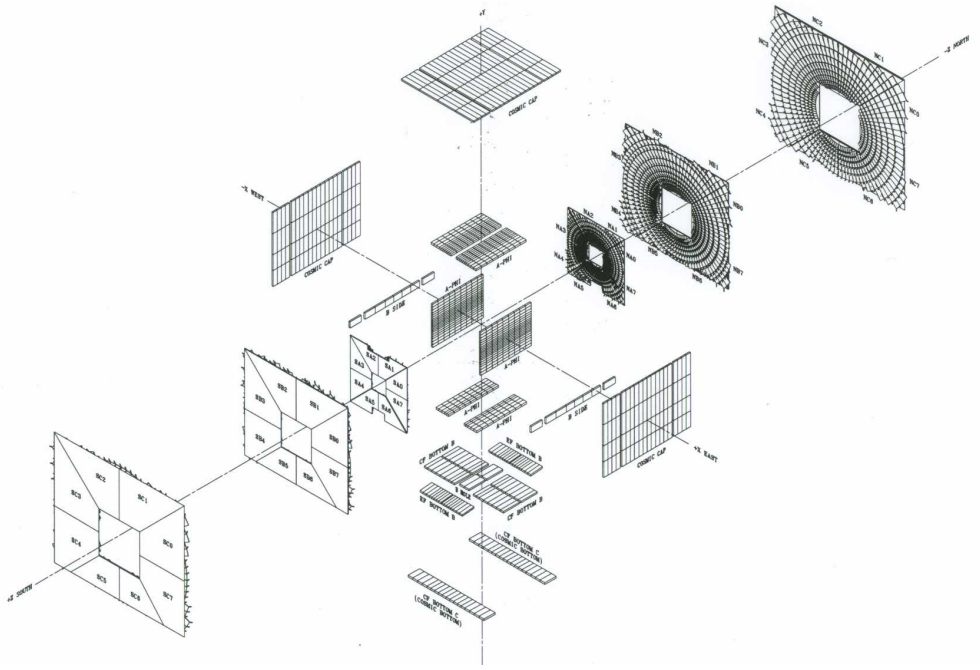

Figure 3.8: A complete view of the muon wire chambers used in the muon system [14].

reaches the anode, which is typically a cylindrical wire, the electrons feel a strong electric field once they are close to the anode, energizing the electrons enough to cause further ionization where the new electrons formed can also ionize the gas, causing an avalanche that will be registered as a signal once it reaches the positive electrode. The electron usually drifts at a constant velocity due to the competing processes of collision with the gas particles and acceleration by the electric field and so from the time measured, the distance the electron drifts can be determined. As for the scintillator counters, they operate much like the scintillator fibers mentioned earlier.

The muon system can be divided into two portions: the central muon system and the forward muon system. The central system is composed of proportional drift tubes (PDTs), toroidal magnets, and scintillation counters and covers the η range from $|\eta| < 1.0$. The forward muon system uses mini drift tubes (MDTs), trigger scintillation counters, and beam pipe shielding and extends the η range to 2.0.

The torodial magnets for the muon system are used for momentum measurements as the muon's trajectory will bend at a curvature that depends on its momentum. The central toroid is a square

annulus 109 cm thick whose inner surface is about 318 cm from the beamline, covering the η region from $|\eta| < 1.0$. The magnets are operated in series at a current of 1500 A and produces a little under 2T field in the z-direction..

Central Muon System

The central muon system covers $|\eta| < 1.0$ and consists of a torodial magnet, drift chambers, the cosmic cap and bottom scintillation counters, and the Aϕ scintillation counters. The drift chambers have three layers denoted as A, B, or C where each layer can be located either inside (A layer) or outside of the central toroidal magnet (B and C layer). For each layer, there are three or four decks of drift cells where each drift cell is composed of an anode wire at the center and vernier cathode pads above and below the wires. The operating voltage is 2.3 kV for the pads and 4.7 kV for the wires. The drift velocity is approximately 10 cm/μs, resulting in a maximum drift time of about 500 ns which is based on the gas mixture: 84% argon, 8% methane, and 8% CF_4. The hit position is provided by an anode wire at the center of each cell and the vernier cathode pads above and below the wires provide additional information on the hit position along the wire. The wires are read out by electronics at one end of each chamber.

For each PDT hit, the electron drift time, the difference ΔT in the arrival time of the signal pulse at the end of the hit cell's wire and at the end of its readout partner's wire, and the charge deposition on the inner and outer vernier pads are recorded. The ΔT and the charge deposition are used to determine the hit position along the wire and also limit the drift distance resolution to $\sigma \equiv 1$ mm. The resolution of ΔT varies from 10 to 50 cm, depending on the cell that the muon passes in relation to the electronics. The pad signal resolution is about 5 mm. The A-layer pads are fully instrumented with electronics but only about 10% of the B- and C-layer pads are instrumented, resulting in the "muon hole" at $|\eta| < 1.25$ and $4.25 < \phi < 5.15$.

The cosmic cap and bottom counters cover the top, sides and bottom of the outer layer of the central muon PDTs. The counters are made from scintillator tiles and wave-shifting fibers. In total, there are 240 counters, each 25 inches wide, and 81.5 - 113 inches long. The counters are positioned

with their width along z and length along ϕ. The fibers are then read out using phototubes mounted on the counters. As for the cosmic bottom, there are 132 counters where the 48 outside of the center bottom B layer are similar to those in the cosmic cap, and the 68 on the undersides of the remaining B and C layers are also similar to those in the cosmic cap except they have fewer fibers. These counters are also read out using photomultiplier tubes. The bottom counters are positioned with their narrow dimension along ϕ and their long dimension along η

The Aϕ scintillation counters cover the A-layer PDTs that are mounted between the calorimeter and the torodial magnet. A total of 630 Aϕ counters are used. These counters are very similar to the cosmic bottom counters in that they are composed of a scintillator with embedded fibers that are attached to a photomultiplier tube. Using cosmic rays, the average muon signal corresponds to 50-60 photoelectrons.

Forward Muon System

The forward muon system extends from $1.0 < |\eta| < 2.0$. This system consists of end torodial magnets, three layers of mini drift tubes (MDTs) for muon track reconstruction, three layers of scintillation counters for triggering on events with muons, and shielding around the beam pipe. The MDTs are arranged in three layers from A, B, and C where A is closest to the interaction region. Each layer has three (B- or C-layer) or four planes (A-layer) of tubes mounted along magnetic field lines. A MDT tube consists of eight cells, each with a 50 μm W-Au wire in the center of the cell. In total, there are 48,640 wires in the MDT system. The gas used in this system is $CF_4 - CH_4$, resulting in a maximum drift time of 40 ns for tracks that are perpendicular to the detector plane and 60 ns for tracks inclined at 45°. Negative high voltage at 3.2kV is applied to the cathode and the anode wire is grounded.

The scintillator counters are both inside (A-layer) and outside (B- or C-layer) of the torodial magnet. Each layer has ninety-six counters. The counter is made from a scintillator plate cut in a trapezoidal shape with WLS bars attached to the two sides of the plate for light collection that is then transmitted to a 1 inch phototube.

Shielding is needed to prevent non-muon backgrounds from interacting with the muon system. These backgrounds come from scattered proton and antiproton fragments that interact with the end of the calorimeter or with the beampipe, proton and antiproton fragments interacting with the Tevatron low-beta quadrupole magnets, and beam halo interactions from the tunnel. The shielding consists of layers of iron, polyethylene, and lead in a steel structure surrounding the beam pipe and low-beta quadrupole magnets. The iron acts as a hadronic and electromagnetic absorber due to its short interaction length of 16.8 cm and radiation lengths of 1.76 cm. The polyethylene is a good absorber of neutrons and the lead is a good absorber of gamma rays. The shielding provides a factor of 50 - 100 reduction in the energy deposition in the muon detector and provides almost background-free muon triggering and reconstruction.

3.2.7 Luminosity monitor

The luminosity monitor (LM) detects inelastic $p\bar{p}$ collisions to determine the luminosity at the DØ interaction region. The LM can also measure beam halo rates and the z coordinate of the interaction vertex. The LM consists of two arrays of 24 plastic scintillation counters with PMT readout located at z = ±140 cm. The arrays are in front of the end calorimeters and occupy the radial region between the beam pipe and the FPS. The counters are 15 cm long and cover the pseudorapidty range $2.7 < |\eta| < 4.4$. PMTs, mounted on the faces of the scintillators with their axes parallel to the z axis, detect the scintillation light.

The luminosity L is determined from the average number of inelastic collisions per beam crossing $\overline{N}_{LM}$ measured by the LM:

$$L = \frac{f\overline{N}_{LM}}{\sigma_{LM}} \tag{3.3}$$

Here, f is the beam crossing frequency and σ_{LM} is the effective cross section for the LM based on the acceptance and efficiency of the LM detector. Due to multiple $p\bar{p}$ collisions in a single beam crossing, the fraction of beam crossings with no collisions and Poisson statistics are used to determine $\overline{N}_{LM}$. Precise time-of-flight measurements of particles from the $p\bar{p}$ interaction are needed in order to make

an estimate of the z position z_v of the interaction vertex:

$$z_v = \frac{c}{2}(t_- - t_+) \tag{3.4}$$

where t_+ and t_- are the times-of-flight measured for particles hitting the LM detectors at $\pm$ 140 cm. Measurements with $|z_v| < 100$ cm are used since collisions outside of this range come from beam halo particles. A luminosity block number, where the luminosity block is the fundamental unit of time for the luminosity measurement and is 60 seconds, is incremented every run or store transition. It is assumed that for each block, the luminosity is effectively constant and so the luminosity calculations, particularly the integrated luminosity for a data set, use an average luminosity value for each luminosity block.

3.2.8 Triggering

The trigger system is a three stage system that cuts down events at each stage from a starting rate of 1.7 MHz to 100 Hz which is the maximum rate that can be written to tape. The first stage or Level 1 (L1) is made up of hardware trigger elements that provide a trigger accept rate of 2 kHz. The second stage or Level 2 (L2) has a global processor to make a trigger decision based on individual objects and object correlations made from specific subdetectors. This reduces the rate to 1 kHz. The last stage or Level 3 (L3) consists of microprocessors that use sophisticated algorithms to reduce the rate to 100 Hz which are recorded for offline reconstruction. Each event that satisfies the successive L1 and L2 triggers is fully digitized and transferred to a single commodity processor in the L3 farm. The overall coordination and control of DØ triggering is handled by the COOR package, which interacts directly with the trigger framework for L1 and L2 triggers and with the data acquisition (DAQ) supervising systems.

Level 1 trigger

The Level 1 trigger looks at specific subdetectors for interesting features that should be further investigated. The calorimeter trigger (L1Cal) looks for energy deposition patterns exceeding pro-

grammed limits on transverse energy deposits. The central track trigger (L1CTT) reconstructs the trajectories of charged particles as they traverse the central fiber tracker and the central and forward preshower detectors and is discussed in further detail in Appendix A. The level 1 muon (L1Muon) trigger looks for patterns consistent with muons using hits from muon wire chambers, muon scintillation counters, and tracks from the L1CTT. The L1 trigger decision must arrive at the trigger framework in 3.5 μs or less.

Level 2 trigger

The Level 2 trigger has preprocessors for each subdetector that collect data from the subdetector and the L1 trigger system to form physics objects. The L2Global, which is the global processor, selects which algorithms to run on the data from the preprocessors and decides whether to accept the event or not for further processing at Level 3. It also looks at data from multiple detectors to form higher quality physics objects and to provide event-wide correlations amongst these objects.

For L2Cal, jets and electrons/photons are identified and the event $\not\!\!E_T$ is calculated. For L2Muon, the quality of the muon candidates is improved through the use of calibration information and more precise timing information. These candidates now contain the track p_T, η and ϕ coordinates, and quality and timing information. For L2PS, CPS and FPS axial clusters are given η and ϕ coordinates and are matched to CFT tracks, resulting in electron (matched) or photon (unmatched) identification. For the L2CTT, track information from either the L1CTT or the SMT barrels are used to find the track's isolation, the azimuthal angle with respect to the beamline, and the azimuthal angle at the third layer of the EM calorimeter. The L2STT reconstructs charged particle tracks found in the CFT at L1 and adds increased precision by using SMT hit information. It also measures the impact parameter of the track with respect to the beam which is precise enough to tag the decays of long-lived particles, particularly B hadrons.

Level 3 trigger

The Level 3 trigger is a software trigger that performs a limited reconstruction of events at a much more sophisticated level than at L2. The reconstruction is done at a rate of 15ms for each event.

About 235 ms/event is available for unpacking, reconstruction, and filtering. The L3 trigger decisions are based on complete physics objects as well as relationships between objects. This is done using object-specific software algorithms known as filter tools. These algorithms unpack raw data, locate hits, form clusters, apply calibrations, and reconstruct electrons, muons, taus, jets, vertices, and $\not\!\!E_T$. Algorithm parameters are given to the tools by the trigger list and these parameters define the physics objects precisely. All tools cache their results and once all filters are satisfied, the events are sent to the host cluster to be recorded.

3.2.9 Data acquisition systems

The primary data acquisition system (L3DAQ) transports subdetector data from the VME readout crates to L3 trigger filtering processing nodes. The COOR program is responsible for overall coordination and control of triggering and data acquisition. The L3DAQ system has a bandwidth of 250 MB/s, corresponding to an event size of about 200 kB at a L2 trigger accept rate of 1 kHz. All nodes in the system are based on commodity computers where there are currently 252 L3 nodes. Up to 63 VME crates are read out for each event where each crate contains 1-20 kB of data. A SBC, or single-board computer, in each VME crate reads out the VME modules and sends the data to one or more farm nodes. An event builder (EVB) process on each farm node builds a complete event from the event fragments and makes it available for L3 trigger filters. The final repository for the raw event data is tape. Data is transmitted to each tape drive at approximately 10 MB/s. This raw data now needs to be reconstructed into physics objects, taking into account the detector conditions and different subdetector effects.

Chapter 4

Event and Object Reconstruction

After understanding how the detector works, the information from the detector can be reconstructed with confidence into physics objects that can be matched with theory. The various hits in the silicon detector can pinpoint the primary vertex of the interaction and also secondary vertices that hint at heavy flavored jets. The central tracking information can be used to determine the momentum of charged particles and can be matched with jets found in the calorimeter, where the showers can give the energy of the jet, and the locations of the showers can determine the nature of the jet. The muon system can then give the momentum and trajectory of muon-like objects. Finally, using energy and momentum conservation, characteristics of the neutrino, whose signature is the missing energy of the event, can be found. These objects are the necessary tools to definitively test the Standard Model or determine the validity of new theories beyond the scope of the Standard Model.

4.1 Event Reconstruction

The *DØ* event data model has an event class that represents the results of a single beam crossing. This acts as a container for all the data associated with a single crossing: the raw output of the detector, the results of trigger processing, and the results of many different reconstruction tasks. Multiple instances of single algorithms with different parameters can be run on these events.

The *DØ*RECO program is responsible for offline reconstruction of both recorded data and MC

events. Events are organized in blocks called chunks. These chunks that are inputs to DØRECO contain the raw detector signals. First, detector unpackers process individual detector data blocks and match electronics channels with physical detector elements, applying detector specific calibration constants. Clusters and hits are then reconstructed and given physical positions in space. The next step reconstructs global tracks from hits in the CFT and SMT using several different tracking algorithms. These tracks are used to find primary vertex candidates and secondary vertex candidates, which are important for b-tagging purposes. Once the vertices are defined, particles such as electrons, photons, muons, neutrinos, and jets can be reconstructed and identified using a multitude of different algorithms. The output of DØRECO contains these additional chunks associated with each reconstructed object. These files are then stored on tape and available for physics analysis. The reconstruction algorithms used will be discussed in further detail in the subsequent sections.

4.2 Tracks

Charged particles traversing through the central tracking system leave hits in the SMT and CFT that can be reconstructed into tracks. The final set of tracks in an event are found through a two step process: first, two algorithms, the histogramming track finder (HTF) and the alternative algorithm (AA), are used to preselect tracks; second, the tracks that pass this preselection become inputs to the global track reconstruction (GTR) which uses a Kalman filter to combine, refit, and smooth these tracks. The output of the Kalman filter are the final tracks of an event.

A Kalman filter [15] is a recursive filter that estimates the state of a system which is represented as a vector of real numbers. The state of the system is modified using a linear operator applied to the current state to generate the new state where some noise is mixed in and optionally some information from the controls on the system if they are known. It estimates a process by using a form of feedback control. This is done by first projecting the state and the error covariance forward for the next time step. Then by looking at the new state, the projected estimate is adjusted by measurements in the new state, particularly the *a posteriori* error covariance. This is repeated with the previous *a posteriori* estimates to predict the new *a priori* estimates. Kalman filters [16] are

used in the final step of track finding and also in subsequent steps of the two algorithms used to preselect tracks.

The HTF algorithm [17] starts from track trajectories that can be defined by three parameters: the track curvature ρ defined by qB/p_T where q is the charge of the particle, B is the magnetic field, and p_T is the transverse momentum; the impact parameter d_0; and the direction of the track at the impact parameter ϕ. All hits go through a Hough transformation that transforms a hit in coordinate space (x,y) to a line in the parameter space (ρ,ϕ). Under this transformation, for n hits that define a track with trajectory parameters ρ_0 and ϕ_0, there will be n lines in (ρ,ϕ) that will intersect at the point (ρ_0,ϕ_0). Therefore, when one looks at the number of hits at point (ρ_0,ϕ_0), there should be n hits. Fig. 4.1 shows the steps for the Hough transformation.

Once all hits go through a Hough transformation, the parameter space ρ and ϕ can be divided into cells that span from -ρ_{min} to ρ_{min} which is set by p_{Tmin} the tracks must have and from 0 to 2π respectively. Cells are discarded if they do not have enough hits and the remaining cells become candidates for further filtering. These are converted into templates which are a set of hits organized into measuring planes and a set of trajectory parameters. A 2D Kalman filter is then applied for each template where all three parameters are fit, accounting for the material interactions, such as multiple scattering and energy loss. Another Hough transformation is then applied from the r, z coordinate space to the parameter space of the track origin's position along the z axis and the track inclination in r, z defined by dz/dr. Afterwards, looking from η, increasing or decreasing from 0, the hits from the detectors which can be crossed by the tracks hypothesized are kept. The templates are now composed of hits that are well aligned. The 3D Kalman filter can now be used to build tracks either in the SMT or CFT which are then extrapolated to the other detector to build complete tracks.

As for AA [18], it is an iterative algorithm that adds a hit to an existing track which is then used to generate a new track unless its χ^2 is too large. The detector can then be described as a series of non-intersecting surfaces where all hits are assigned to a particular surface that must contain the next set of hits. Paths can then be defined as an ordered list of surfaces crossed by a track. Thus,

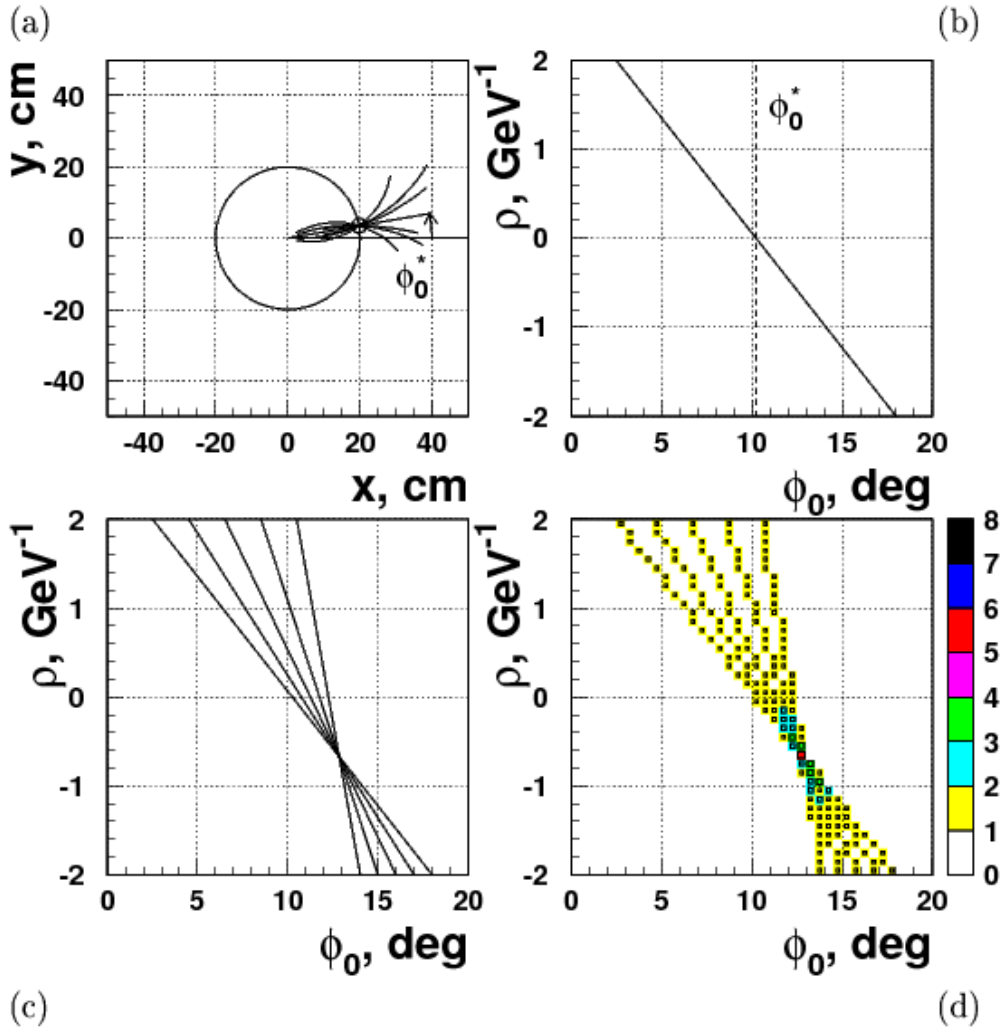

Figure 4.1: The Hough transformation is applied for a single muon 1.5 GeV muon track composed of 5 hits. (a) A set of trajectories are shown which contain a given hit. (b) A hit in coordinate space (x,y) is converted to a line in the parameter space (ρ,ϕ). (c) The curves from different hits intersect at one point in (ρ,ϕ), corresponding to the track parameters. (d) The intersection has 5 hits which correspond to the 5 hits that make up the track [17].

a track is then just a list of hits with given paths and can be fitted to obtain the most likely set of kinematical track parameters, their error matrix, and χ^2. However, in order to predict a hit from a track, one needs to propagate that track to the associated surface and only include hits nearby the surface. The fitting is done using a Kalman filter with inputs from the track parameters and error matrix and then adds the information from an additional hit to generate a new set of track parameters and error matrix.

4.3 Primary Vertex

The primary vertex (PV) of the event is the three-dimensional location of the hard scatter. It is found using the adaptive primary vertex algorithm [19]. This is a two step process: vertex finding and vertex fitting.

The algorithm starts by looking for tracks and then clustering sets of tracks together. A track must have a $p_T > 0.5 GeV/c^2$ and two or more SMT hits if it is in the SMT fiducial region or where $|z| < 36$ cm. Outside of this region, no minimal number of SMT hits is required. By having these two regions, a higher vertex reconstruction efficiency is achieved because the poorly reconstructed tracks are no longer used in the fit within the SMT fiducial region and in the forward region which is outside the SMT's capacity, tracks generally discarded can be used to pinpoint further the location of the primary vertex. The track is then clustered with other tracks that are within 2 cm of each other. For each of these z-clusters, the location and width of the beam is determined by fitting all tracks to a common vertex using a Kalman Filter vertex fitting algorithm where the tracks with the highest χ^2 contribution to the vertex is removed until the total vertex χ^2 per degree of freedom is smaller than 10. After this, the tracks in each cluster are pre-selected according to their distance of closest approach to the previously calculated beam spot where the distance must be smaller than 5σ. After the tracks have been selected, the Adaptive vertex filter algorithm finds a common vertex.

All primary vertex track candidates are fitted using the Kalman Filter algorithm where each

track is weighted according to $w(\chi^2)$:

$$w_i = \frac{1}{1 + e^{(\chi_i^2 - \chi_{cutoff}^2)/2T}} \tag{4.1}$$

where χ_i^2 is the χ^2 contribution of track i to the vertex, χ_{cutoff}^2 is the distance where the weight function drops to 0.5, and T controls the sharpness of the function. Thus, the secondary vertex contributions are accounted for by re-weighting track errors since T is allowed to be greater than 0 and so the secondary vertex track may contribute to both the primary and secondary vertices with a weight smaller than 1. This way tracks can contribute to the primary vertex with a weight based on how close it is to this vertex. The optimized parameters found were a χ_{cutoff}^2 at 4 and a T value of 1 based on studies using $Z \rightarrow b\bar{b}$ events in the SMT fiducial region with the purpose of finding parameters that would yield a pull width closest to 1. Initially each track weight is set to 1.0 and after k iterations, the weight of the track will depend on the distance to the vertex at the previous iteration. For each track used in the fit, its weight is recomputed according to the χ^2 distance to the new fitted vertex unless $w(\chi^2) < 1 \times 10^{-6}$ at which point the track's weight is set to 0. This is repeated until the maximum change in track weights from the previous iteration is $< 1 \times 10^{-4}$ or the number of iterations is 100.

From this list, one of the PV is chosen as having come from the hard scatter while the rest come from minimum bias (MB) events [20]. For each vertex, all tracks within some distance around it are used to compute that probability that the vertex comes from a MB interaction. This probability is based on the p_T of the tracks since tracks from MB interactions tend to have lower p_Ts than if the tracks came from the PV. For each track, the probability $P(p_T)$ that it comes from a MB interaction is given by:

$$P(p_T) = \frac{\int_{log_{10}(p_T)}^{\infty} F(p_T) dp_T}{\int_{log_{10}(0.5)}^{\infty} F(p_T) dp_T} \tag{4.2}$$

where $F(p_T)$ is the MB track $log_{10}(p_T)$ spectrum distribution obtained from MC and the lower limit for the integral in the denominator comes from the fact that only tracks with $p_T > 0.5$ GeV were

used. The probability that a vertex comes from a MB interaction (PMB) is then given by:

$$PMB = \prod \sum_{k=0}^{N-1} \frac{-ln \prod}{k!} \tag{4.3}$$

where $\prod$ is the product of the individual track probabilities for N tracks associated with a particular vertex. The vertex with the smallest probability is then chosen as the PV.

4.4 Calorimeter Objects

The DØ calorimeter has a large number of cells that pick up signal from electronic noise and uranium decay. The average of a pedestal distribution is set as zero in the hardware and so the cell can have negative or positive energy from noise in the calorimeter. A cell, however, will only be read out if its absolute value of its energy is above a certain threshold which is set to $1.5\sigma_{ped}$ or 1.5 times above the root mean square (RMS) of the pedestal distribution. This is known as zero suppression. The T42 algorithm [21] is then used to determine which cells to use for further reconstruction. This algorithm looks for cells above $4\sigma_{ped}$ and then includes neighboring cells with energy above $2.5\sigma_{ped}$. The transverse energy can then be calculated based on the cells energy and the direction determined by the cell's location and the reconstructed hard scatter PV.

4.4.1 Electrons

Electrons are reconstructed using the clusters of energy depositions in the electromagnetic section of the calorimeter which must have a shower shape consistent with an electromagnetic object [22] [23]. The clustering algorithm starts from preclusters that are formed from seed towers in the EM calorimeter which have $p_T > 500$ MeV. Neighboring towers are then added if they have $p_T > 50$ MeV and if they are within $\Delta R < 0.3$ of the seed tower in the central region of the detector, or within a cone of radius of 10 cm in the third layer of the EM calorimeter in the end caps. The final clusters start from these preclusters if they have an energy above 1 GeV and any EM tower within $\Delta R < 0.4$ is

added to the nearby precluster where

$$R = \sqrt{\Delta\eta^2 + \Delta\phi^2}. \tag{4.4}$$

The final clusters have their centers determined by the energy weighted mean of its cells in the third layer of the EM calorimeter. An EM cluster is thus defined as a group of towers in a cone of radius $R = 0.2$ around the highest energy tower where most of the energy will be deposited in the EM layers of the calorimeter. Thus, the EM fraction f_{EM}, which is E_{EM}/E_{tot}, should be large. As for the isolation in the calorimeter, a variable known as the isolation fraction can be determined where

$$f_{iso} = \frac{E_{tot}(R < 0.4) - E_{EM}(R < 0.2)}{E_{EM}(R < 0.2)}. \tag{4.5}$$

This is generally small for electrons since there is not much calorimeter energy in a halo around the EM cluster. Furthermore, because an electron is charged, a track from central tracking should match with an EM cluster and can also be matched with a hit from the Central PreShower (CPS).

As for the shower shape, the showers must develop with a longitudinal and lateral shape comparable to that of an electron. This is determined using the H-Matrix which has seven parameters that compare the values of the energy deposited in each layer of the EM calormeter and the total shower energy with the average distributions obtained in MC. A χ^2 value is assigned to this H-Matrix which tend to be small for electrons.

A likelihood [24] can also be constructed using f_{EM}, χ^2 of the H-Matrix, E_T/p_T, $\chi^2_{spatial}$, distance of closest approach (dca), the number of tracks in a R < 0.05 cone around the candidate track, the total track p_T in a R < 0.4 around the track except of that of the candidate track, and CPSstripmax. The $\chi^2_{spatial}$ is defined as

$$\chi^2_{spatial} = \left(\frac{\delta\phi}{\sigma_\phi}\right)^2 + \left(\frac{\delta z}{\sigma_z}\right)^2 \tag{4.6}$$

where $\delta\phi$ is the difference in ϕ between the extrapolated track impact at the EM3 floor of the

calorimeter and the cluster position in the EM3 floor and δz is the difference between the vertex position calculated from the track and that calculated from the EM cluster. The dca is the shortest distance of the selected track to the line parallel to the z-axis which passes through the primary vertex position. Finally, the CPSstripmax is the total number of strips in a 3D cluster that has the largest number of strips in its single layer cluster out of all 3D clusters within a 20 cm radius from the EM object over the EM energy. For each distribution a probability is assigned for either background or signal and the likelihood is thus

$$L = \frac{P(sig)}{P(sig) + P(bkg)} \tag{4.7}$$

The electrons used in this analysis must be in the central calorimeter, or $|\eta^{det}| < 1.1$, and there are three different types based on isolation: loose isolated electrons, tight isolated electrons, and ultraloose electrons. A loose isolated electron has an electron ID=10, $\pm$ 11 and use version 3 of the EM ID for loose electrons which means that the following requirements must be met: 90% of the energy of the cluster must be in the electromagnetic portion of the calorimeter and the χ^2 from the 7×7 H-matrix must be less than 50. The energy deposition in the calorimeter must be matched with $\chi^2 > 0$ to a charged particle track from the tracking detectors with $p_T > 5$ GeV and z(track, primary vertex) < 1 cm. The isolation requirement is $f_{iso} < 0.15$ and $p_T > 15$ GeV. A tight isolated electron has the same requirements as the loose isolated electron and must have the seven-variable EM-likelihood L > 0.85.

The ultraloose electron has $f_{EM} > 0.9$, H-matrix $\chi^2 < 50$, $f_{iso} < 0.15$, and $p_T > 15$ GeV. The ultraloose electron has no requirements for a matching track.

4.4.2 Jets

Jets come from hadronization of quarks which produce many particles that deposit energy in the hadronic calorimeter. Jets are reconstructed by a clustering algorithm that assigns particles or calorimeter towers to jets [26] [27]. The jets are clustered using the Run II Midpoint Algorithm [28] [29]. The jet centroid is defined as (y_{jet}, ϕ_{jet}) and objects are clustered together if their distance

relative to the jet axis defined as $\Delta R = \sqrt{(y - y_{jet})^2 + (\phi - \phi_{jet})^2}$ is less than R_{cone} where R_{cone} is the cone radius which is set to 0.5. The process begins with pseudo-projective calorimeter towers ($\Delta\eta \times \Delta\phi = 0.1 \times 0.1$) that are reconstructed by adding the four-momentum of the cells above threshold where each cell is treated as massless. The momentum for each cell is defined with respect to the interaction vertex reconstructed by the tracking system. Next the calorimeter towers with $p_T \geq 1$ GeV are seeds for finding pre-clusters which are comprised of the neighboring towers within $\Delta R < 0.3$ of the seed towers. A cone of radius R_{cone} is formed around each pre-cluster centered at its centroid and a new jet center is computed using the E-scheme defined as follows:

$$p_{jet} = (E_{jet}, p_{jet}) = \sum_i (E_i, p_i) \tag{4.8}$$

$$y_{jet} = \frac{1}{2} \ln\left(\frac{\mathrm{E_{jet}} + \mathrm{p_{zjet}}}{\mathrm{E_{jet}} - \mathrm{p_{zjet}}}\right) \tag{4.9}$$

$$\phi_{jet} = \tan^{-1}\left(\frac{p_{yjet}}{p_{xjet}}\right) \tag{4.10}$$

$$p_{Tjet} = \sqrt{p_{xjet}^2 + p_{yjet}^2} \tag{4.11}$$

where the sums are over all towers in the cone. This procedure is repeated iteratively for all the seeds, using this same E-scheme, until the jet center is stable. These stable solutions are called proto-jets. From these proto-jets, midpoints between proto-jets are found which provide seeds where preclusters are formed. A cone of radius R_{cone} is made around each pre-cluster and a new jet center is computed until a stable center is found. By using this midpoint algorithm, sensitivity to soft radiation is reduced since soft radiation between two jets will no longer merge these two jets into a single jet. Finally overlapping proto-jets will be split or merged depending on how much p_T is contained in the overlap region. Overlap is defined when two proto-jets are separated by less than $2R_{cone}$. The two proto-jets are then merged into a single jet if more than 50% of the p_T of the lower-energy jet is contained in the overlap region. Otherwise the energy of each cell in the overlap region is assigned to the jet nearest to the cell. Once this is done, the four-momentum is recalculated using the E-scheme and only jets with $p_T > 6$ GeV are kept.

Afterwards, the jet energies need to be converted from reconstructed to particle-level energies which uses the jet energy scale corrections. The main purpose of the jet energy scale (JES) corrections [30] [31] are to correct the calorimeter jet energy back to the stable-particle jet level prior to interaction with the detector. These corrections are estimated separately for data and MC.

First, the energy not associated with the hard scatter is subtracted out. This energy can come from electronic and uranium noise, multiple collisions in the same bunch crossing, beam remnants, multiple parton interactions, and pile-ups from previous collisions. This is the "Offset correction" and is measured by looking at the per-tower energy density in MB events which in this case are events triggered by the luminosity monitor. The energy densities are added up for a specified jet cone size, giving the offset energy correction for the jet. This is done for different η regions and for different primary vertex multiplicities as the number of primary vertices depends on the instantaneous luminosity.

Next, the response of the calorimeter is energy calibrated as a function of the jet η and is known as the "Relative response correction." The calorimeter is fairly uniform in the CC and EC; however the gaps between the two regions is not as uniformly instrumented. This correction uses the Missing Transverse Energy Projection Fraction (MPF) method on photon+jet and dijet events. This method tags an object which must be in the CC and has a probe which can have different η values. At the particle level, the tag particle's (photon for photon+jet events and a jet for dijet events) p_T should directly cancel that of the hadron jet since these particles are chosen to be back to back. However, at the detector level, there is $\not\!\!E_T$ projected in the tag object direction which gives the response correction R_{had} and is described by the following:

$$\vec{p}_{T,tag} + R_{had}\ \vec{p}_{T,probe} = -\vec{\not\!\!E}_T \text{ where } \quad \mathrm{R_{had}} = 1 + \frac{\tilde{\not\!\!E}_T \cdot \tilde{\mathrm{p}}_{\mathrm{T,tag}}}{\tilde{\mathrm{p}}^2_{\mathrm{T,tag}}} \tag{4.12}$$

The two samples are combined and each sample dominates in different p_T regions, the photon+jet events in the low p_T region and the dijets in the high p_T region.

The "Absolute response correction" follows and accounts for energy loss from uninstrumented detector regions and lower calorimeter response to hadrons compared to electrons or photons. This is

measured by applying the MPF method to selected photon+jet events after the first two corrections mentioned above are applied. Stringent cuts are applied to the photon since it is the tag particle and the photon and jet are required to be back to back. The corrections are the same for different η regions and can be attributed to the application of the "Relative response correction."

The last correction, the "Showering correction," comes from energy leaking outside (inside) the calorimeter jet cone from particles inside (outside) of the particle jet due to shower development that comes from instrumental effects. Photon+1-jet events with only one PV are used. For a given bin of estimated jet energy and η, the jet energy density profile from calorimeter towers is computed as a function of radial distance in (η,ϕ) to the jet axis. After removing energy unrelated to the hard scatter, the MC ratio of the energy within a jet cone radius to the total energy from a larger cone radius is compared to the same MC ratio for MC that did not go through the detector simulation. The first ratio gives the showering correction that comes from the detector and physics effects whereas the latter gives the showering correction from physics effects only. The ratio of the two gives the showering correction due to instrumental effects.

An additional correction for jets that contain a "medium-nseg3" muon (which will be discussed in the next section) within $\Delta R(\mu, \text{jet-axis}) < 0.5$ is applied for the momentum carried away by the muon and the neutrino. The jets used in this analysis have a $p_T > 15$ GeV and are within $|\eta| < 3.4$.

4.4.3 B Jets

B jets are jets that originate from b-quarks. These jets must first be deemed taggable, meaning they must satisfy quality requirements that reject different tracking efficiencies, badly reconstructed jets, and detector effects. Once this is satisfied, the jets can be tagged by the tagging algorithm directly or by a parameterization called a tag-rate function (TRF). The tagging algorithm will be discussed more in detail in the next chapter.

Taggable Jets

Taggability [32] is defined as the probability that a jet is taggable. Taggability requirements on jets are used to reject badly reconstructed jets and tracks, and detector effects, and to provide a stable basis for reconstructing b-jets. A jet is taggable if the jet is a calorimeter jet that is matched within $\Delta R < 0.5$ of a track jet. The track jet consists of at least two tracks, where the tracks must have $\Delta R < 0.5$ between them, and each track used to form the track jet has to have at least one SMT hit on it and at least one of the tracks must have a $p_T > 1$ GeV.

4.4.4 $\not\!\!E_T$

The $\not\!\!E_T$ in an event comes from the noninteracting particle that does not interact with the detector and is ascribed to the neutrino. The $\not\!\!E_T$ in the event is determined from momentum conservation and is the negative sum of the transverse momenta of all particles observed in the detector. This is done by adding up vectorially the transverse energies in all cells of the electromagnetic and fine hadronic calorimeters and only cells that form a good jet in the coarse hadronic calorimeter after the T42 algorithm is applied. This quantity is then corrected for by the energy corrections applied to the reconstructed objects and for the momentum of all muons in the event which suffer energy losses in the calorimeter.

4.5 Muons

Muons are identified [33] [34] in three independent detector subsystems. The muon detector is a three layer system that provides muon identification with a momentum measurement. A track from the central tracking system can also be used to match to a local muon found in the muon detector. The calorimeter can also be used to find a minimum ionizing particle (MIP) signature but this signature is less effective than that mentioned previously.

Muons are defined by quality and type. The type of muon used in this analysis is a nseg 3 muon, meaning that a local muon with hits in the A-layer and the B-layer or C-layer is matched

to a central track. A muon track is matched to a central track if the muon track fit converged, otherwise the central track is matched to a muon. The $\delta\eta$ and $\delta\phi$ between the minimum ionizing particle (MIP) and the central track extrapolated to the calorimeter must be matched. As for muon quality, "Medium" was used in this analysis, meaning that there are at least two A layer wire hits, at least one A layer scintillator hit, at least two BC layer wire hits, and at least one BC scintillator hit (except for central muons with less than four BC wire hits). A "Loose" muon has the same criteria as the "Medium" muon except that one of the criteria fails and the A wire and scintillator requirements are treated as one criteria.

There are also loose cosmic ray rejection timing requirements: $|\Delta t$(A layer scintillator, $t_0)| < 10$ ns and $|\Delta t$(BC layer scintillator, $t_0)| < 10$ ns. The track reconstructed in the muon system must match a track reconstructed in the central tracker with track quality "medium" and track match "medium." Furthermore, $|dca| < 0.2$ cm and if there is an SMT hit, this cut is tightened to 0.02 cm. The χ^2 per degrees of freedom of the central track fit must also be smaller than 4. The track must be close to the primary vertex: z(track,PV) < 1 cm. The muon also must have $p_T > 15$ GeV, and it must not be in a jet which is imposed by Δ R(μ,jet) > 0.5, rejecting heavy flavored mesons. The event is rejected if another muon is found with the same requirements except that second muon's p_T cut is lowered to 4 GeV which is mostly caused by punchthrough muons.

The isolation requirements are used to separate $W \rightarrow \mu\nu$ from heavy flavor background. The isolation used is TopScaledLoose which is defined by two parameters: Scaled Track Halo and Scaled Calorimeter Halo. The Calorimeter Halo is the energy deposited in an annular cone of radius 0.1 $< R <$ 0.4 around the muon direction and the Track Halo is the momenta of all the tracks in a cone of radius R < 0.5 around the muon direction except the track matched to the muon. The Scaled Track Halo and Scaled Calorimeter Halo comes from dividing these variables by the muon p_T which helps removes the luminosity dependence as seen in **??** when comparing with isolation points that use Calorimeter Halo and Track Halo. For the TopScaledLoose isolation point, these scaled variables must be < 0.2.

Chapter 5

Data Sample and Event Selection

Once everything is reconstructed both in data and Monte Carlo (MC), one needs to make sure the MC correctly models not only what theory expects but also how it will be modified by detector effects. Cuts then need to be applied to keep as much signal as possible while at the same time trying to minimize physics processes that can mimic the signal event signature. These two competing goals can be measured by using the signal to background ratio. However, even with these cuts, the signal to background ratio is about 1:250. Jets are tagged as b-jets in order to further reduce this ratio to 1:20 for one b-tag events and 1:15 for two b-tag events. The MC generation and corrections needed to properly model the DØ data is discussed in this chapter. Additionally, the different procedures used to reduce the signal to background ratio aside from the multivariate technique are examined. The multivariate technique will be discussed in the next chapter.

5.1 Data Sample

The data sample used in this analysis was collected from August 2002 to August 2007, corresponding to an integrated luminosity of 2.3 fb^{-1} with 1.1 fb^{-1} from Run IIa and 1.2 fb^{-1} from Run IIb where Run IIa and Run IIb are separated by a major upgrade of the DØ detector. Data collected from Run IIa corresponds roughly from August 2002 to February 2006 and Run IIb corresponds roughly from June 2006 to August 2007.

		Integrated Luminosity[pb^{-1}]		
Channel	Trigger Version	Delivered	Recorded	Good Quality
Run IIa electron (e)	v8.00 – v14.93	1,312	1,206	1,043
Run IIa muon (mu)	v8.00 – v14.93	1,349	1,240	1,055
Run IIb e and mu	v15.00 – v15.80	1,497	1,343	1,216
Total Run II Integrated Luminosity				**2.3 fb^{-1}**

Table 5.1: Integrated luminosities for the datasets used in this analysis.

The luminosity L is calculated by measuring the counting rate of inelastic proton-antiproton collisions recorded by the LM described in Chapter 2:

$$L = \frac{1}{\sigma_{eff}} \frac{dN}{dt} \tag{5.1}$$

where σ_{eff} is the effective inelastic cross section seen by the LM which is $60.7 \pm 2.4mb$ multiplied by the geometric acceptance and efficiency for registering inelastic events, both of which are determined using MC simulated inelastic events run through the LM detector simulation and response [35].

In practice, the luminosity L is calculated by inverting the following expression:

$$P(0) = e^{-\sigma_{eff}L/f} \times (2e^{(-\sigma_{SS}/2f)L} - e^{-\sigma_{SS}L/f}) \tag{5.2}$$

where $P(0)$ is the probability that a bunch crossing does not produce a coincidence of in-time hits recorded in the two LM arrays, σ_{SS} is the effective cross section for only one of the arrays to fire, and f is the crossing frequency for a given beam bunch. $P(0)$ is measured for each of the 36 bunch crossings by counting the number of events that occur in 1 minute and the terms in parenthesis comes from multiple interactions per bunch crossing that can produce hits in both arrays from two or more interactions that each fire a single array although there are no proton-antiproton interactions. These interactions come from beam halo interactions which are generated from beam-gas interactions, intra-beam scattering, and particle diffusion.

MC events were generated for diffractive and non-diffractive events with the non-diffractive MC weighted so that it best matches the zero-bias data sample. The following values of σ were found:

$\sigma_{eff} = 48.0$ mb and $\sigma_{SS} = 9.4$ mb. Using the instantaneous luminosity profiles, the integrated luminosity is obtained by integrating this profile distribution which essentially adds up the instantaneous luminosity for a 1 minute block $\times$ total 1 minute time blocks used in the data set.

5.1.1 Triggers

Data is required to pass any reasonable trigger where a reasonable trigger is any trigger except b-tagging, gap, and forward proton triggers and in the case of the muon channel, an EM trigger and in the case of the electron channel, a muon trigger. In total, 788 triggers for the Run IIa electron channel, 358 triggers for the Run II a muon channel, 492 triggers for the Run IIb electron channel, and 303 triggers for the Run IIb muon channel were used and the ORing of all these triggers is known as the Mega-OR where the Single-Lepton-OR is a subset of the Mega-OR. The Single-Lepton-OR is defined as any trigger that finds either a single muon or electron in the event and is modeled using turn-on curves that give the efficiency of an event to pass the trigger requirements at all 3 levels parameterized in p_T, ϕ, or η. Since a large number of triggers were used, the trigger efficiency was assumed to be 100%. This was verified by comparing two ratios: first, the ratio of Single-Lepton-OR selected data to Mega-OR selected data, and second, the ratio of MC simulation that has the Single-Lepton-OR turn-on curves applied to MC simulation that is 100% efficient. If the ratio of the two ratios is around one, then assuming that the Single-Lepton-OR is modeled correctly, the Mega-OR trigger efficiency is 100%. Figure 5.1 shows an example of these ratios as a function of a topological variable sensitive to the trigger selection: Jet1 p_T which is the leading jet's transverse momentum.

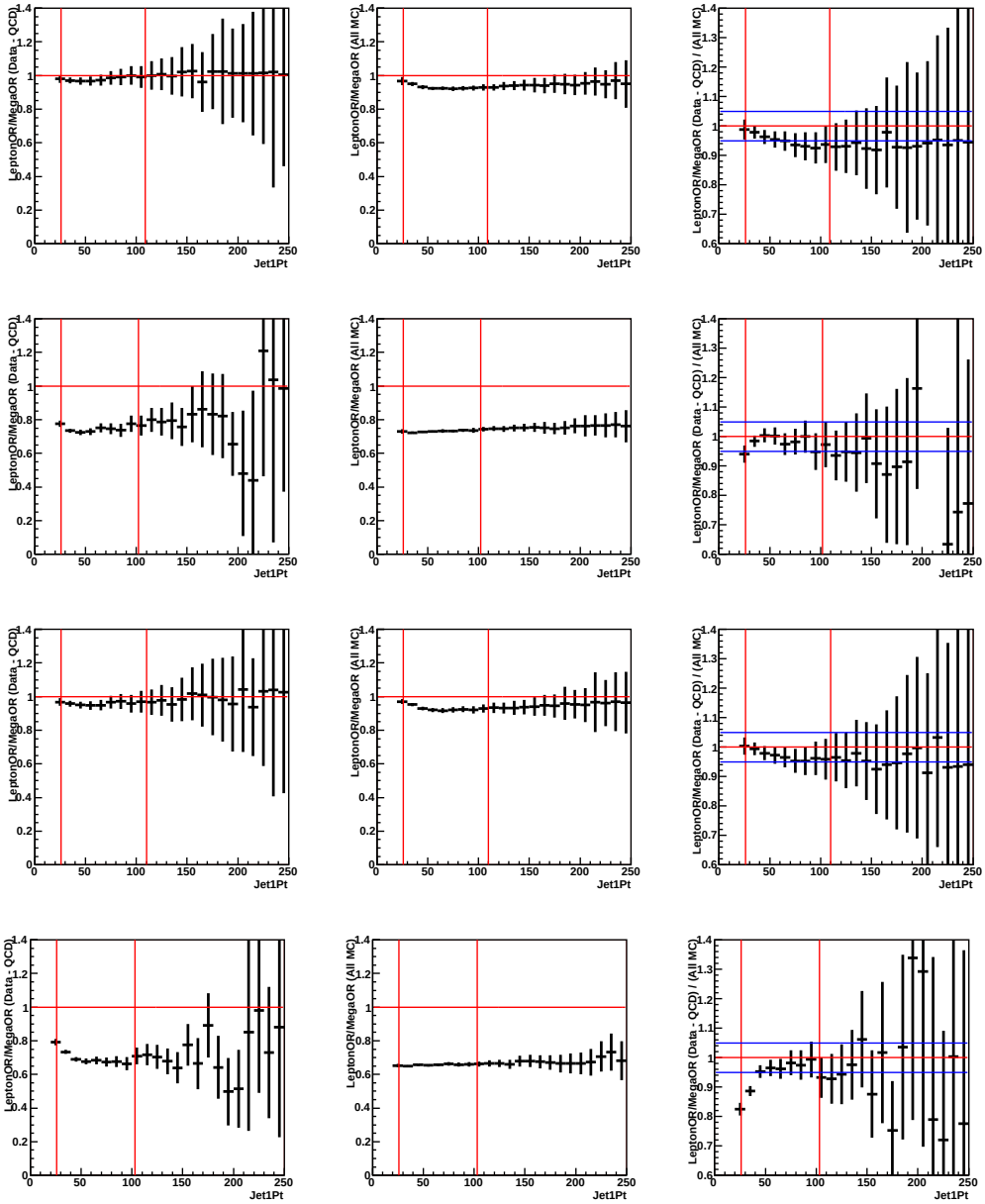

Figure 5.1: Ratio of Single-Lepton-OR to Mega-OR in data-minus-multijets (left column); ratio of Single-Lepton-OR to 100% in the sum of MC backgrounds (center column); ratio of these "efficiencies" in data to MC (right column) as a function of Jet1 p_T. The rows correspond to Run IIa electrons, Run IIa muons, Run IIb electrons, and Run IIb muons.

5.1.2 Background Processes

For this analysis, we focus only on events with singly produced top quarks, also known as single top, that decay to a W boson and a b quark where the W boson decays to a lepton and a neutrino rather than two quarks. As a result, the single top quark event signature is an isolated high p_T lepton, large $\not\!\!E_T$ that corresponds to a neutrino, and two or more jets where at least one of them is b-tagged. This signature can be mimicked by the other processes discussed below.

W+jets

W+jets is the largest background prior to b-tagging but still has a high contribution in the two jet bin. W$b\bar{b}$ has the same event signature as single top events if there is initial state or final state radiation; however, Wjj and W$c\bar{c}$ can also mimic the signal if one of the jets is mistagged as a b-jet. Wjj corresponds to light partons or a gluon, u, d, or s quark which hadronize into jets.

$t\bar{t}$

Events from $t\bar{t}$ come into play in higher jet multiplicity bins. In this, a $t\bar{t}$ that decays into leptons and jets has the same signature as single top quark events with initial or final state radiation. However, for $t\bar{t}$ that decays into dileptons, one of the leptons produced by the W bosons is not reconstructed.

Multijet

Multijet events are an instrumental background where these events have a jet reconstructed incorrectly as a lepton, and as a result, can produce an energy mis-measurement of the event that leads to a significant amount of $\not\!\!E_T$.

Z+jets

The Z+jets events are similar to the W+jets background but in order to mimic a singly produced top, one of the leptons is lost or not reconstructed. However, if the Z decays into $\tau\tau$, the taus can decay in the following manner: $\tau \to l\bar{\nu}_l\nu_\tau$ or to a $\tau \to qq'\nu_T$. This $\tau\tau$ decay looks like a W+jets

event, with the ν_T either partially or fully responsible for the $\not\!\!E_T$ in the event, depending on how the W boson decays.

Diboson

Diboson events are events that contain two gauge bosons. For WW and WZ, the single top event signature can be mimicked by one of the bosons decaying leptonically and the other decaying hadronically. As for ZZ, one of the Zs can decay leptonically with one of the leptons either being lost or not reconstructed and the other decaying hadronically. There is also the possibility that the Z can decay into taus, producing an off-shell W boson.

Figure 5.2 shows the Feynman diagrams for the background processes mentioned above.

5.2 Monte Carlo Generation

For MC, the first step is the simulation of a $p\bar{p}$ collision producing a particular final state using an event generator. GEANT v3.21 [36] is used to trace the particles through the $D\emptyset$ detector, determine where their paths intersect active areas, and simulate their energy deposition and secondary interactions. $D\emptyset$GSTAR [37] reads these files produced and puts it in the $D\emptyset$OM format. The $D\emptyset$SIM program modifies the MC to simulate detector effects such as detector inefficiencies and noise from the detector itself or the readout electronics or multiple interactions that can occur from a beam crossing. The trigger electronics and the effects of the trigger on the data selection is applied using $D\emptyset$TRIGSIM for L1 and the filtering code which is used at L2 and L3. The output from this is the same as that from the $D\emptyset$ data acquisition system but additional MC information is kept to show correlations between the detector data and the original generator output. The event generators and the settings used are defined below for all signal and background processes modeled by MC.

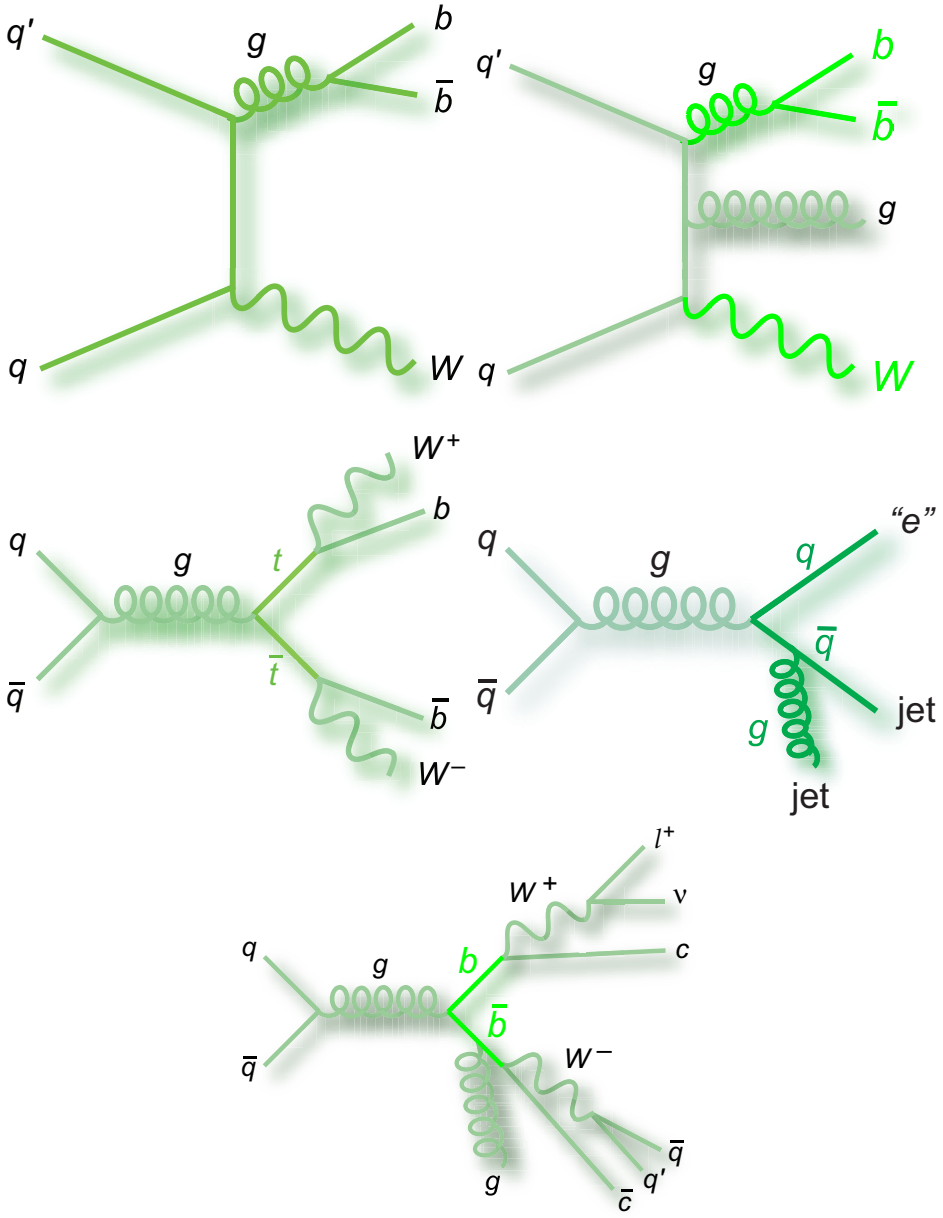

Figure 5.2: Background processes that mimic top quarks produced through the electroweak channel. The first row corresponds to W$b\bar{b}$ events where the right figure has final state radiation. The gluon can also make $c\bar{c}$ or other lighter quark pairs. Z+jets events look similar to these diagrams except the neutrino is replaced by a lost lepton. The second row corresponds to $t\bar{t}$ events (left) where one of the leptons is not reconstructed from the W decay and multijet events (right) where a jet is reconstructed incorrectly as a lepton. The last row corresponds to WW events where the W has to decay leptonically and hadronically.

5.2.1 Monte Carlo Event Samples

Signal MC Event Generation

The electroweak produced top quark event samples are generated with the CompHEP-SINGLETOP [38] Monte Carlo event generator using NLO calculations for the kinematic distributions. CompHEP-SINGLETOP first simulates events at the parton level for the final particles and then inputs these events into the PYTHIA 6.409 [39] which simulates initial state and final state radiation as well as hadronization and multiple interaction effects. TAUOLA [40] was used to decay tau leptons and EVTGEN [41] to decay b hadrons. Afterwards it goes through the detector simulation where the events keep all spin correlations from the initial particles in the final state particles.

The settings used by CompHEP-SINGLETOP are a top quark mass at 170 GeV, s-channel factorization scaled at m_t^2 and t-channel factorization scaled at $(m_t/2)^2$, and CTEQ6M [42] PDFs. The PDFs are the parton distribution functions which are determined from global fits to deep inelastic scattering, Drell Yan and jet production data. The Alta Parisi equation then evolves the parton distribution function from one factorization scale to another. These functions can be thought of as how much of the proton or antiproton's momentum is assigned to different constituents of the proton or antiproton.

For the s-channel processes, NLO results coincide with LO results but differ by K factor that accounts for the NLO contributions to the LO results. As a result, $p\bar{p} \rightarrow t\bar{b}$ and $p\bar{p} \rightarrow \bar{t}b$ events are generated with NLO CTEQ6M PDFs. Afterwards, the distributions are normalized to the NLO total cross section.

As for t-channel processes, the NLO distributions are generated in the following manner: a) for events where the additional b quark $p_T > 10$ GeV, events for $p\bar{p} \rightarrow tjb$ are calculated using COMPHEP b) for events where the additional b quark $p_T < 10$ GeV, events for $p\bar{p} \rightarrow tj$ are generated and multiplied by a K factor that ensures the cross sections are the same for when the additional b quark $p_T = 10$ GeV. The b quark is then added by using the initial state radiation mechanism in PYTHIA.

Background MC Event Generation

ALPGEN 2.11 [43] with the jet-matching algorithm following the MLM prescription [44] is used to generate the W+jets, Z+jets, and $t\bar{t}$ samples. The MLM prescription matches the partons from the matrix element calculation to the jets reconstructed after the perturbative shower. These parton-level events can have a minimum E_T requirement for the partons and a minimum separation between the jets. Starting from the color-flow extracted from the matrix element calculations, the events are showered and afterwards jets are formed with a specified cone size and minimum E_T. Starting from the hardest parton, the jet which is closest to this parton in (η,ϕ) is selected. If the distance is smaller than R_{min} from the parton to jet centroid, then the jet and parton are matched. The jet is then removed from the list and the rest of the partons are matched to the remaining jets. Events are kept if the event has equal numbers of jets and partons and each parton has a matched jet. For all samples generated with ALPGEN, the parton-matching cluster threshold is set to 8 GeV and the parton-matching cluster radius size is set to R=0.4.

For W+jets, CTEQ6L1 PDFs were used with a factorization scale at $m_W^2 + \sum_{alljets} m_T^2$ where m_T, the transverse mass, is defined as $m_T^2 = m^2 + p_T^2$ and extends to all final state partons excluding the W decay products. Furthermore, the W+light-parton (Wlp) jet samples, as defined below, have additional parton-level cuts on the light partons (lp), such as $p_T(lp) > 8\ GeV$ and $\Delta\ R(lp, lp) > 0.4$ for all massless partons. This is done to avoid divergences in the cross section.

The final W+jets samples that were generated are the following:

- Wlp: $W + Nlp \rightarrow l\nu + Nlp$ where N can be 0, 1, 2, 3, 4, or 5 and lp are light partons which can be gluons or massless u, d, s, or c quarks. This sample is further divided to Wcj meaning $Wc + (N-1)lp \rightarrow l\nu c + (N-1)lp$ and Wjj which has no c quarks.

- Wbb: $W +_N lp \rightarrow l\nu + Nlp$ where the b quarks are massive and N can be 0, 1, 2, or 3.

- Wcc: $Wc\bar{c} + Nlp \rightarrow l\nu c\bar{c} + Nlp$ where the c quarks are massive and N can be 0, 1, 2, or 3.

The Z+jets samples follow the same prescription as the W+jets samples.

For the $t\bar{t}$ samples, the settings used are a top quark mass at 170 GeV, CTEQ6L1 PDFs, and a

factorization scale at $m_t^2 + \sum p_t^2(jets)$.

The final $t\bar{t}$ samples that were generated are the following:

- $t\bar{t}$ -lepjets: t+$Nlp \rightarrow l\nu bb + Nlp$ where N can be 0, 1, or 2.
- $t\bar{t}$ -dilepton: t+$Nlp \rightarrow ll\nu\nu bb + Nlp$ where N can be 0, 1, or 2.

The diboson samples were generated with PYTHIA with inclusive decays. The samples generated are WW, WZ, and ZZ. All these MC samples have the duplicate events removed. Once the events have been generated, they are processed through the GEANT simulation of the DØ detector or "*DØgstar*" and then the events are reconstructed. The cross sections, branching fractions, and statistics for each sample can be found in Table 5.2

	The Monte Carlo Event Sets			
Event Type	Cross Section [pb]	Branching Fraction	No. of RunII a Events	No. of RunII b Events
Signals				
$tb \rightarrow \ell$+jets	$1.12^{+0.05}_{-0.12}$	0.3240 ± 0.0032	0.6M	0.8M
$tqb \rightarrow \ell$+jets	$2.34^{+0.13}_{-0.17}$	0.3240 ± 0.0032	0.5M	0.8M
Signal total	$\mathbf{3.46^{+0.18}_{-0.29}}$	$\mathbf{0.3240 \pm 0.0032}$	**1.1M**	**1.6M**
Backgrounds				
t$\rightarrow \ell$+jets	$7.91^{+0.61}_{-1.01}$	0.4380 ± 0.0044	2.6M	1.3M
t$\rightarrow \ell\ell$	$7.91^{+0.61}_{-1.01}$	0.1050 ± 0.0010	1.3M	0.9M
Top pairs total	$\mathbf{7.91^{+0.61}_{-1.01}}$	$\mathbf{0.5430 \pm 0.0054}$	**3.9M**	**2.2M**
$Wb\bar{b} \rightarrow \ell\nu bb$	93.8	0.3240 ± 0.0032	2.3M	2.5M
$Wc\bar{c} \rightarrow \ell\nu cc$	266	0.3240 ± 0.0032	2.3M	3.0M
$Wjj \rightarrow \ell\nu jj$	24,844	0.3240 ± 0.0032	21.0M	18.3M
W+jets total	**25,205**	$\mathbf{0.3240 \pm 0.0032}$	**25.6M**	**23.8M**
$Zb\bar{b} \rightarrow \ell\ell bb$	43.0	0.10098 ± 0.00006	1.0M	1.0M
$Zc\bar{c} \rightarrow \ell\ell cc$	114	0.10098 ± 0.00006	0.2M	1.0M
$Zjj \rightarrow \ell\ell jj$	7,466	0.10098 ± 0.00006	3.9M	7.0M
Z+jets total	**7,624**	$\mathbf{0.10098 \pm 0.00006}$	**5.1M**	**9.0M**
$WW \rightarrow$ anything	12.0 ± 0.7	1.0 ± 0.0	2.9M	0.7M
$WZ \rightarrow$ anything	3.68 ± 0.25	1.0 ± 0.0	0.9M	0.6M
$ZZ \rightarrow$ anything	1.42 ± 0.08	1.0 ± 0.0	0.9M	0.5M
Diboson total	$\mathbf{17.1 \pm 1.0}$	$\mathbf{1.0 \pm 0.0}$	**4.7M**	**1.8M**

Table 5.2: The cross sections, branching fractions, and initial numbers of events in the Monte Carlo event samples. The symbol ℓ stands for electron plus muon plus tau decays.

5.2.2 Event Selection Cuts

Common selection for both electron and muon channels

- Good quality (for data) which means that the tracking, calorimeter, and muon systems are working properly and that there is not excessive noise in the calorimeter.
- Fire at least one of the many triggers in the Mega-OR set
- Good primary vertex defined as $|z_{\rm PV}| < 60$ cm with at least three tracks attached
- Two, three, or four good jets where a good jet is defined as the following:
  - the fraction of the jet's p_T contained in the CH layers of the calorimeter < 0.4 and if it is > 0.1 then the fraction of total towers needed to contain 90% of the jet's p_T needs to be $<$ (80%$-$ half the CH fraction)
  - the fraction of the jet's p_T contained in the EM layers of the calorimeter must be between 5% and 95%
  - the ratio of the hottest cell to that in the second hottest cell < 10
  - the minimum number of towers needed to contain 90% of the jet's p_T has to be > 1.
  - the jets must have $p_{\rm T} > 15$ GeV and $|\eta^{det}| < 3.4$
- The leading jet is required to have $p_{\rm T} > 25$ GeV
- Jet triangle cut $|\Delta\phi(\text{leading jet}, \not\!\!E_T)|$ vs. $\not\!\!E_T$:
  - $|\Delta\phi|$ from 1.5 to π rad when $\not\!\!E_T = 0$ GeV, and $\not\!\!E_T$ from 0 to 35 GeV when $|\Delta\phi| = \pi$ rad
- Missing transverse energy
  - $20 < \not\!\!E_T < 200$ GeV in events with exactly two good jets
  - $25 < \not\!\!E_T < 200$ GeV in events with three or more good jets

Electron channel selection

- Only one tight electron with $|\eta^{det}| < 1.1$ and $p_{\rm T} > 15$ (20) GeV in events with 2 (3 or more) good jets
- No additional loose electron with $p_{\rm T} > 15$ GeV

- No tight isolated muon with $p_{\mathrm{T}} > 15$ GeV and within $|\eta^{det}| < 2.0$
- Electron coming from the primary vertex: $|\Delta z(e, \mathrm{PV})| < 1$ cm
- Electron triangle cuts which are used to reduce the multijet background to $< 5\%$. The cuts are determined by looking at two-dimensional distributions in $\Delta\phi$ and $\not\!\!E_T$ for multijets and signal such as those found in Figs. 5.3 and 5.4 and cutting out areas with high multijets events while avoiding areas with high signal density.

  $|\Delta\phi(e, \not\!\!E_T)|$ vs. $\not\!\!E_T$:

  - $|\Delta\phi|$ from 2 to 0 rad when $\not\!\!E_T = 0$ GeV, and $\not\!\!E_T$ from 0 to 40 GeV when $|\Delta\phi| = 0$ rad
  - $|\Delta\phi|$ from 1.5 to 0 rad when $\not\!\!E_T = 0$ GeV, and $\not\!\!E_T$ from 0 to 50 GeV when $|\Delta\phi| = 0$ rad
  - $|\Delta\phi|$ from 2 to π rad when $\not\!\!E_T = 0$ GeV, and $\not\!\!E_T$ from 0 to 24 GeV when $|\Delta\phi| = \pi$ rad

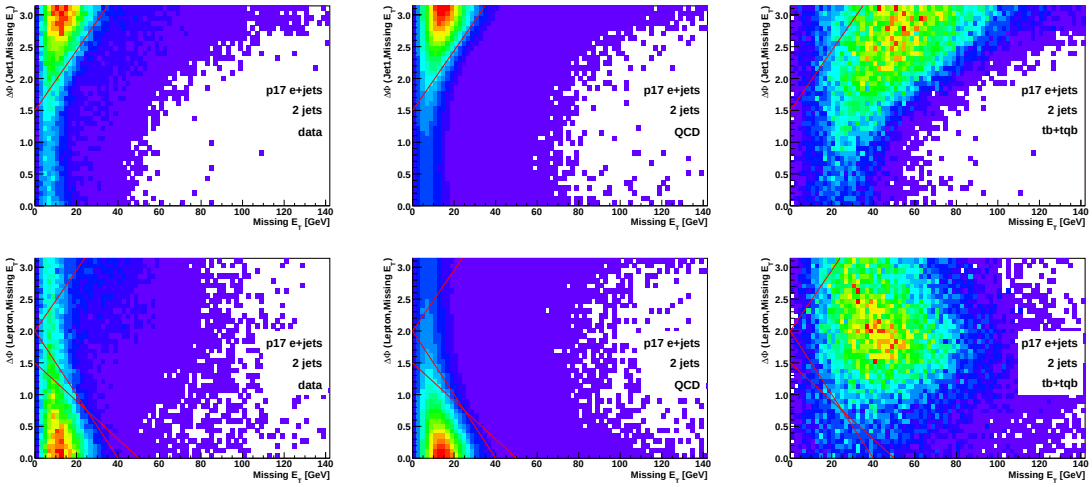

Figure 5.3: $\Delta\phi$(jet1,$\not\!\!E_T$) versus $\not\!\!E_T$ (up) and $\Delta\phi$(lepton,$\not\!\!E_T$) versus $\not\!\!E_T$ (down) two-dimensional distributions for data (left), multijets (center) and tb+tqb signal (right), in the electron channel in Run IIa data.

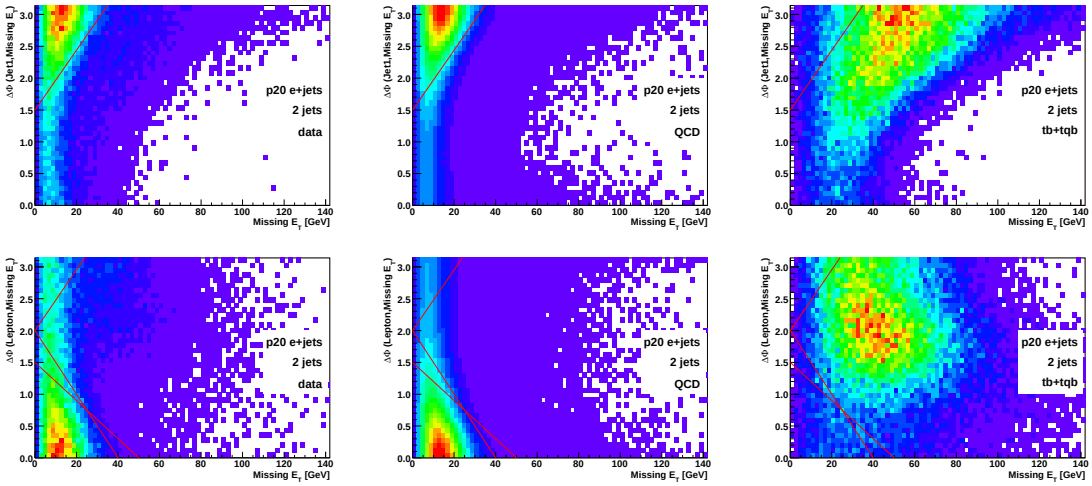

Figure 5.4: $\Delta\phi$(jet1,$\not\!\!E_T$) versus $\not\!\!E_T$ (up) and $\Delta\phi$(lepton,$\not\!\!E_T$) versus $\not\!\!E_T$ (down) two-dimensional distributions for data (left), multijets (center) and tb+tqb signal (right), in the electron channel in Run IIb data.

- Scalar sum of the transverse energies of all good jets, the electron transverse momentum, and the missing transverse energy (H_T). This cut is used to help reduce the multijet background to $< 5\%$ by cutting the low H_T where most of the multijets background lies as can be see in Figure 5.5.
  - $H_T(\text{alljets}, e, \not\!\!E_T) > 120$ GeV in events with exactly two good jets
  - $H_T(\text{alljets}, e, \not\!\!E_T) > 140$ GeV in events with exactly three good jets
  - $H_T(\text{alljets}, e, \not\!\!E_T) > 160$ GeV in events with exactly four good jets

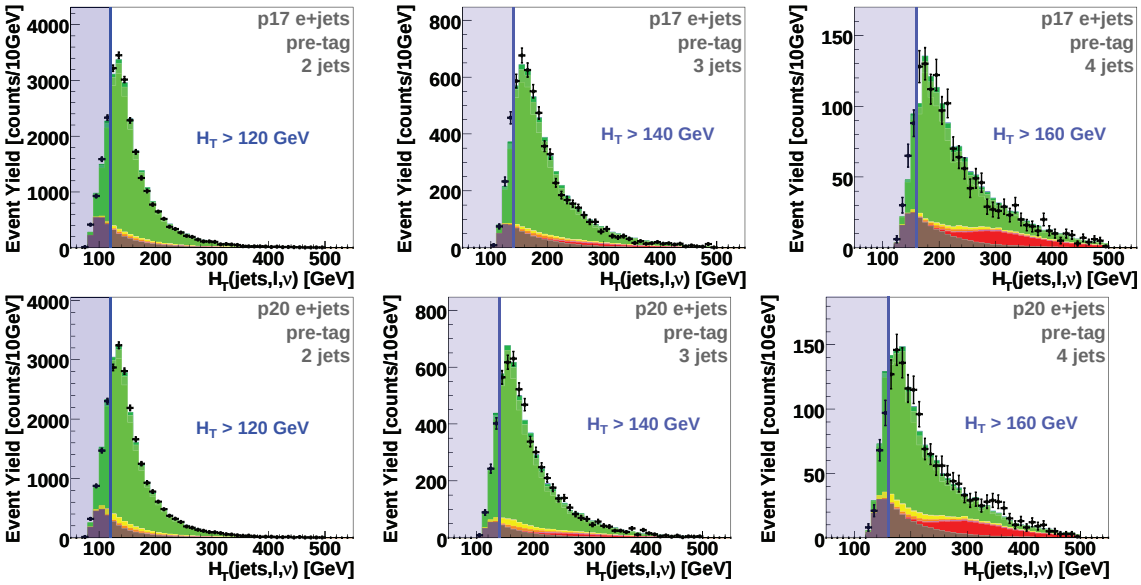

Figure 5.5: Pretagged distributions in the electron channel for 2-jet (left column), 3-jet (middle), and 4-jet events (right), for p17 and p20 (alternate rows), for $H_T(\text{lepton}, \not\!\!E_T, \text{alljets})$ before the H_T cuts.

Muon channel selection

- Only one tight muon with $p_{\mathrm{T}} > 15$ GeV and $|\eta^{det}| < 2.0$
- No additional loose muons with $p_{\mathrm{T}} > 4$ GeV.
- No loose electron with $p_{\mathrm{T}} > 15$ GeV and within $|\eta^{det}| < 2.5$
- Muon coming from the primary vertex: $|\Delta z(\mu, \mathrm{PV})| < 1$ cm
- Muon triangle cuts $|\Delta\phi(\mu, \not\!\!E_T)|$ vs. $\not\!\!E_T$ which are used to reduce the multijets background to $< 5\%$. The cuts are determined by looking at two-dimensional distributions in $\Delta\phi$ and $\not\!\!E_T$ for multijets and signal such as those found in Figs. 5.6 and 5.7 and cutting out areas with high multijets events while avoiding areas with high signal density:
    - $|\Delta\phi|$ from 1.2 to 0 rad when $\not\!\!E_T = 0$ GeV, and $\not\!\!E_T$ from 0 to 85 GeV when $|\Delta\phi| = 0$ rad
    - $|\Delta\phi|$ from 2.5 to π rad when $\not\!\!E_T = 0$ GeV, and $\not\!\!E_T$ from 0 to 30 GeV when $|\Delta\phi| = \pi$ rad

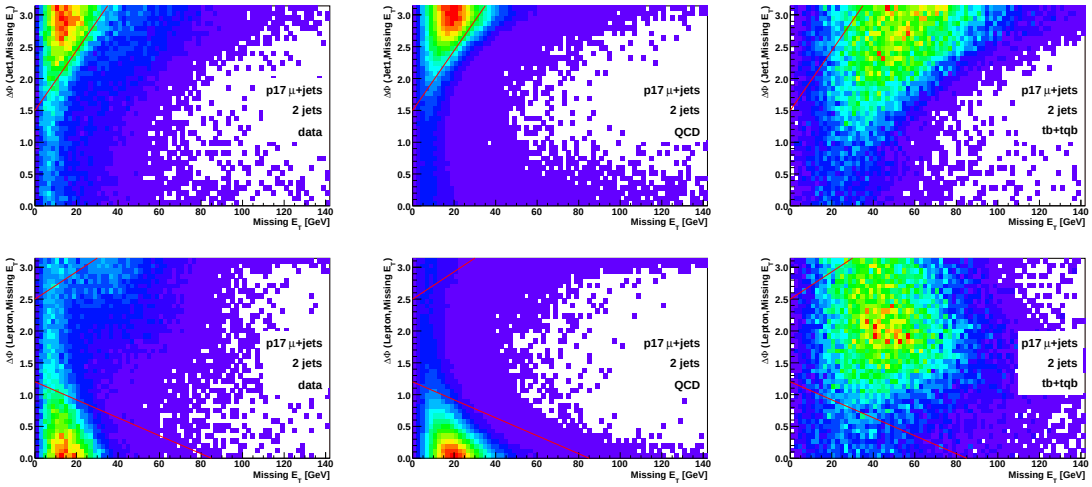

Figure 5.6: $\Delta\phi$(jet1,$\not\!\!E_T$) versus $\not\!\!E_T$ (up) and $\Delta\phi$(lepton,$\not\!\!E_T$) versus $\not\!\!E_T$ (down) two-dimensional distributions for data (left), multijets (center) and tb+tqb signal (right), in the muon channel in Run IIa data.

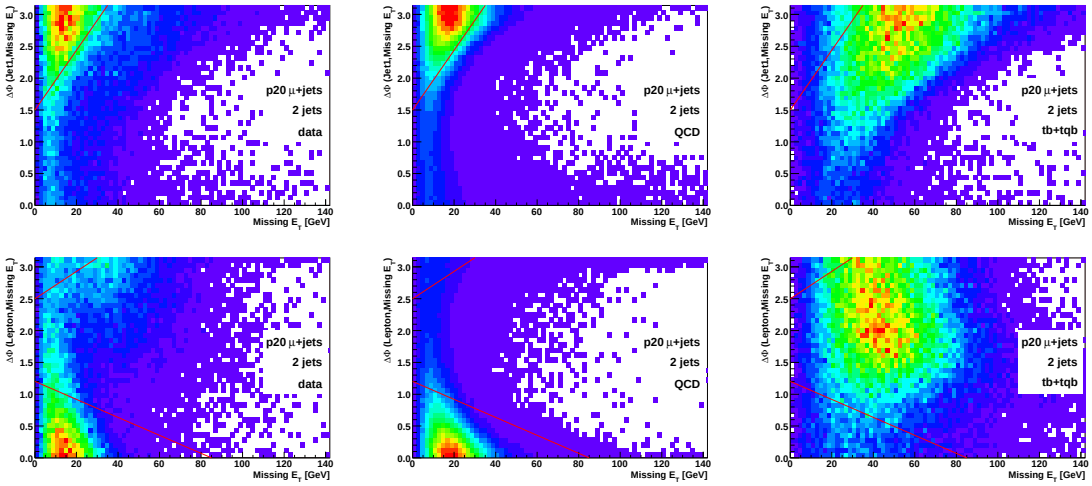

Figure 5.7: $\Delta\phi$(jet1,$\not\!\!E_T$) versus $\not\!\!E_T$ (up) and $\Delta\phi$(lepton,$\not\!\!E_T$) versus $\not\!\!E_T$ (down) two-dimensional distributions for data (left), multijets (center) and tb+tqb signal (right), in the muon channel in Run IIb data.

- Muon track curvature significance cuts |TrackCurvSig| vs. $|\Delta\phi(\mu, \not\!\!E_T)|$, where |TrackCurvSig| = $|\frac{q/p_{\mathrm{T}}}{\sigma(1/p_{\mathrm{T}})}|$, and q and p_T are the charge and transverse momentum of the charged track associated with the muon
  - $|\Delta\phi|$ from 0.875π to π rad when |TrackCurvSig| = 0, and |TrackCurvSig| from 0 to 4 (6) when $|\Delta\phi| = \pi$ rad for Run IIa (Run IIb) period
  - $|\Delta\phi|$ from 2 to π rad when |TrackCurvSig| = 0, and |TrackCurvSig| from 0 to 2 (3) when $|\Delta\phi| = \pi$ rad for Run IIa (Run IIb) period

  These cuts are needed to reject events with poorly measured muons that cause an excess in data over background model in the $\Delta\phi$ distributions.

- Transverse momentum of the leading jet within the ICD region of the detector: leading jet $p_T >$ 30 GeV when $1.0 <$ |leading jet $\eta^{det}| < 1.5$

- Scalar sum of the transverse energies of all good jets, the electron transverse momentum, and the missing transverse energy. This cut is used to help reduce the multijet background to $< 5\%$ by cutting the low H_T where most of the multijets background lies as can be see in Figure 5.8
  - $H_T(\text{alljets}, \mu, \not\!\!E_T) > 110$ GeV in events with exactly two good jets
  - $H_T(\text{alljets}, \mu, \not\!\!E_T) > 130$ GeV in events with exactly three good jets
  - $H_T(\text{alljets}, \mu, \not\!\!E_T) > 160$ GeV in events with exactly four good jets

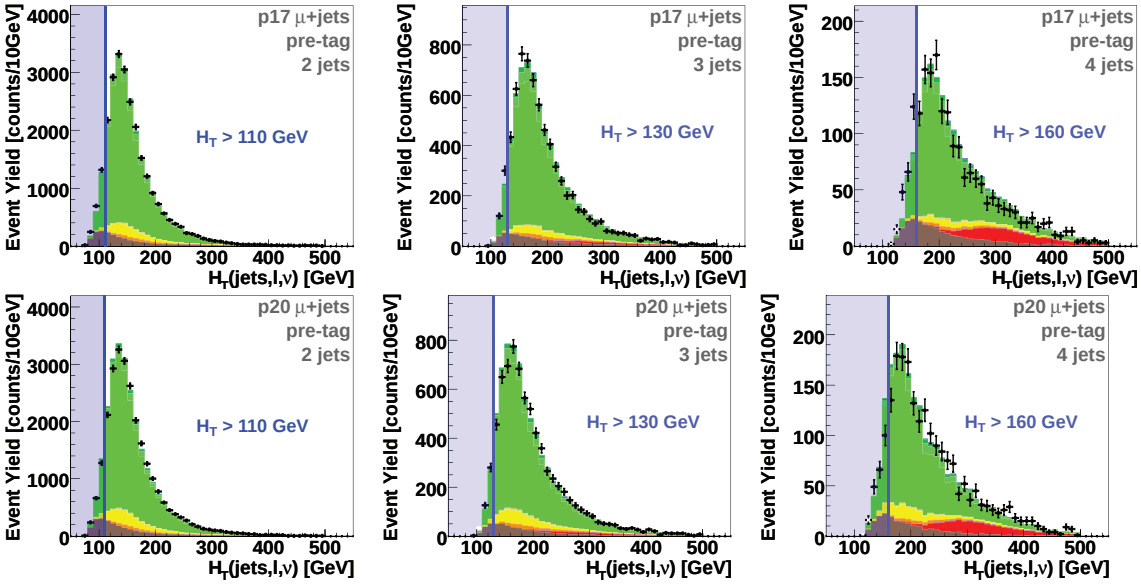

Figure 5.8: Pretagged distributions in the muon channel for 2-jet (left column), 3-jet (middle), and 4-jet events (right), for p17 and p20 (alternate rows), for $H_T(\text{lepton}, \not\!\!E_T, \text{alljets})$ before the H_T cuts.

Multijets Background

This is an orthogonal sample where all the selection cuts listed above are kept except for the lepton requirements, which are replaced with the following:

Electron channel

- Only one ultraloose electron that fails the seven-variable EM-likelihood cut (i.e. it satisfies $L < 0.85$) and also is not required to have a matching track.
- No second ultraloose electron is allowed in any $|\eta^{det}|$ region.

The purpose of using these ultraloose electrons is to increase the statistics ten-fold in order to smooth out discrete distributions due to low statistics and to adequately use the multijets background in the multivariate analyses. However, by increasing the statistics, differences in shape for some variable distributions were introduced, resulting in a need to reweight the events using the fake-electron probability. This fake-electron probability comes from the "matrix method"of normalization [45] defined by two equations:

$$\begin{aligned} N_{\text{uloose}} &= N_{\text{uloose}}^{\text{fake}-e} + N_{\text{uloose}}^{\text{real}-e} \\ N_{\text{tight}} &= N_{\text{tight}}^{\text{fake}-e} + N_{\text{tight}}^{\text{real}-e} = \varepsilon_{\text{fake}-e}\, N_{\text{uloose}}^{\text{fake}-e} + \varepsilon_{\text{real}-e}\, N_{\text{uloose}}^{\text{real}-e} \end{aligned}$$

where N_{uloose} is the number of events with ultraloose electrons which is comprised of events with fake electrons which come from the multijets background ($N_{\text{uloose}}^{\text{fake}-e}$) and real electrons that come from W+jets and $t\bar{t}$ events that pass the ultraloose requirements ($N_{\text{uloose}}^{\text{real}-e}$). Those in the tight electron sample are again comprised of events with fake and real electrons that pass the tight electron requirements but really these are a subset of the ultraloose events defined by the efficiency (ϵ) that a ultraloose electron passes the tight electron selection whether they are real ($\varepsilon_{\text{real}-e}$) or not ($\varepsilon_{\text{fake}-e}$). Rewriting these equations yields

$$N_{\text{tight}}^{\text{fake}-e} = \frac{\varepsilon_{\text{fake}-e}}{1-\varepsilon_{\text{fake}-e}}\, N_{\text{uloose}-\text{tight}} - \frac{\varepsilon_{\text{fake}-e}}{1-\varepsilon_{\text{fake}-e}}\,\frac{1-\varepsilon_{\text{real}-e}}{\varepsilon_{\text{real}-e}}\, N_{\text{tight}}^{\text{real}-e} \tag{5.3}$$

However, the second term is less than 1 % than the first term and so the correction factor $\frac{\varepsilon_{\text{fake}-e}}{1-\varepsilon_{\text{fake}-e}}$ is what is used to reweight the orthogonal dataset before using it to model the multijets background. $\varepsilon_{\text{fake}-e}$ is measured using data that pass all the selection cuts mentioned previously but in the $\not\!\!E_T$ region below 10 GeV which is dominated by the multijet events. $\varepsilon_{\text{fake}-e}$ is the ratio of events in this region that pass the tight electron requirements over the total amount of events in this region. This efficiency is dependent on the lepton p_T and since there is no jet dependence, events with at least two jets were used. The fake rate can be seen in Figure 5.9 as a function of lepton p_T and used to determine the correction factor applied to the orthogonal data sample based on the p_T of the lepton in each event.

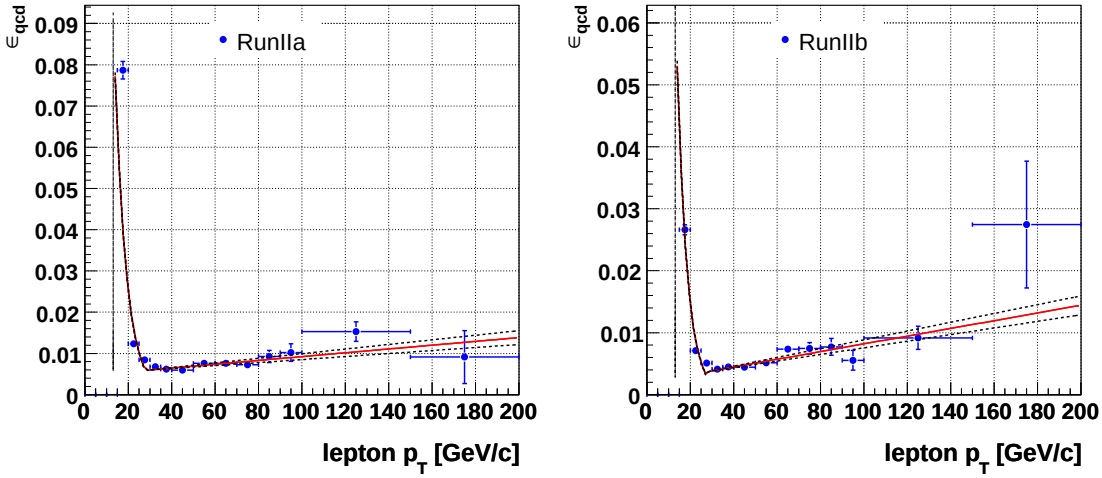

Figure 5.9: $\varepsilon_{\text{fake}-e}$ as a function of electron p_T for Run IIa (p17) (left) and Run IIb (p20) data (right).

Muon channel

- The $\Delta R(\mu, \text{jet}) > 0.5$ isolation requirement is dropped. This increases the statistics again by ten-fold
- Events with a tight isolated muon are rejected. This ensures orthogonality.
- Jets near the muon are removed and the $\not\!\!E_T$ of the event is corrected accordingly.

The shapes of the muon multijets sample where one removes the $\Delta R(\mu, \text{jet}) > 0.5$ cut and the jets near the muon are similar to the sample with loose muons with the $\Delta R(\mu, \text{jet}) > 0.5$ cut applied.

The removal of the cut and the jet near the muon has the added benefit of more statistics as seen in Figure 5.10.

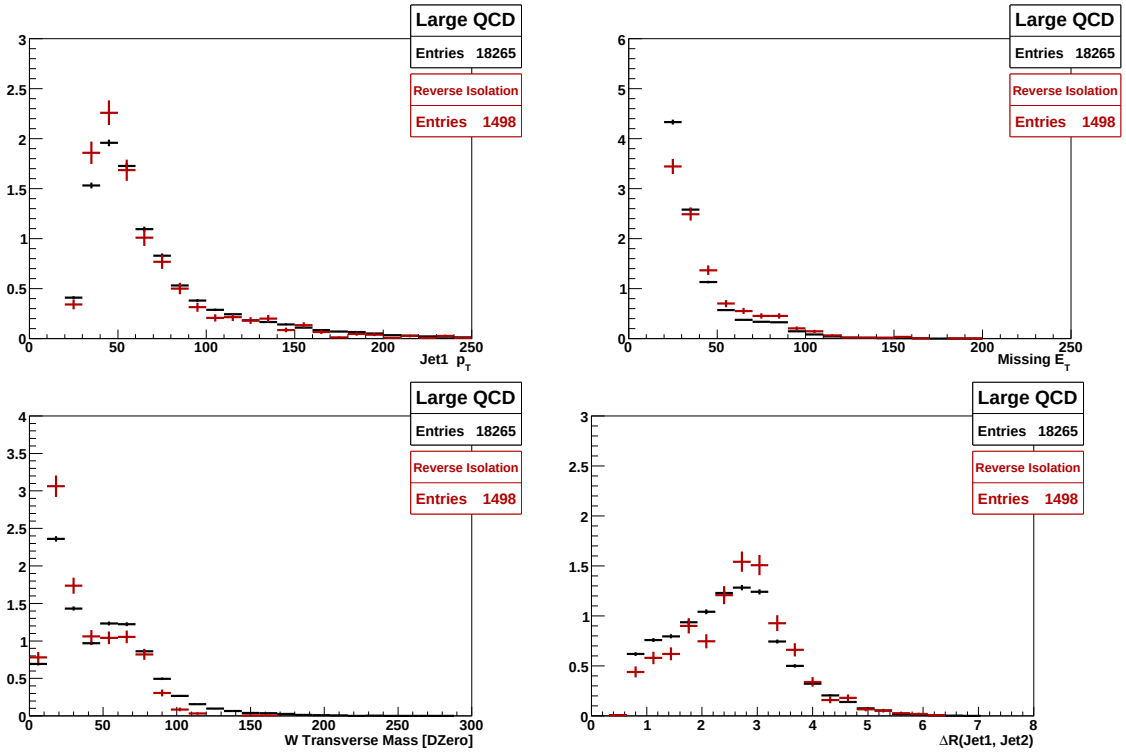

Figure 5.10: Kinematic distributions comparing the old (red points) and new (black points) multijets background models. Upper row, p_T(jet1) and $\not\!\!E_T$, lower row, $M_T(W)$ and ΔR(jet1, jet2).

5.2.3 MC Correction Factors

The Monte Carlo files generated need to be corrected with scale factors that make the MC reconstruction and selection efficiencies match those found in data.

- **Theory Cross Section Normalization**

  The MC samples for signal, $t\bar{t}$, and dibosons are normalized to match the number of events based on the theoretical cross sections and branching fractions expected at 2.3 fb^{-1}. The cross sections and branching fractions can be found in Table 5.2. The theoretical cross sections for signal and $t\bar{t}$ are derived in these papers, [9] and [8]. The theoretical diboson cross section is calculated using the NLO event generator MCFM [46]

- **Primary vertex position reweighting**

  The position of the primary vertices along the beamline in z is reweighted to make the distribution in MC events match data.

- **Instantaneous luminosity reweighting**

  The instantaneous luminosity distributions of the MC events is reweighted to to match those in Run IIa and Run IIb data. These luminosity profiles are generated from the luminosity of the zero-bias data overlay events

- Z p_T **distribution reweighting**

  The Z p_T spectrum generated with ALPGEN is reweighted to match the theory model at NLO. The reweighting depends on the true Z p_T and the jet multiplicity [47].

- **EM ID efficiency correction factor**

  This scale factor accounts for differences in electron cluster finding and the efficiency of identifying electrons [22] [23]. There are two sets of scale factors, those relating to general electron quality definitions such as ID, electromagnetic fraction and isolation and those relating to a particular electron quality definition such as H-matrix cut, track-matching requirements, and the likelihood cut. The first set is parameterized in η^{det} and is denoted as preselection. The latter set is parameterized by both η^{det} and ϕ and is denoted as post-preselection. These scale factors are derived using $Z \rightarrow ee$ data and simulated events using the tag and probe method where the tag electron has stringent cuts to ensure that a $Z \rightarrow ee$ event is selected and then looser electron cuts on the probe electron which will be used to measure the efficiencies needed for the correction factor. Additionally signal contamination is removed by making a signal and background hypothesis based on a fit of the Z mass from 80 GeV/c^2 to 100 GeV/c^2 and subtracting this background hypothesis. Furthermore, contamination from QCD multijets and W+jets is accounted for by subtracting the yield numbers based on same sign and opposite sign EM objects found in the event. The efficiencies from data and MC then come from how many events pass the reconstruction cuts divided by the total number of events.

This correction factor is defined as

$$\varepsilon_{e-\mathrm{ID}} = \frac{\varepsilon^{\mathrm{Data}}_{\mathrm{Presel}}}{\varepsilon^{\mathrm{MC}}_{\mathrm{Presel}}} \times \frac{\varepsilon^{\mathrm{Data}}_{\mathrm{PostPresel}}}{\varepsilon^{\mathrm{MC}}_{\mathrm{PostPresel}}} \tag{5.4}$$

$$\tag{5.5}$$

where ε is the efficiency which can be derived for the data or MC sample and for the preselection or post-preselection scale factors.

- **Muon ID efficiency correction factor**

  The muon correction factor depends on the muon ID efficiency [33] [34], which is parameterized in η^{det} and ϕ, the track match, which is parameterized in track-z and η_{CFT}, and the isolation, which is parameterized in η. These efficiencies are derived from $Z \rightarrow \mu\mu$ using the "tag and probe" method.

  For the muon ID efficiency, the tag and probe method tags a muon which is used as a control and then uses the other muon as the probe. The control muon has more stringent selection requirements to ensure that the events selected are really $Z \rightarrow \mu\mu$ events, especially in data, resulting in a strong belief that the other object used to test muon id requirements is really a muon. As for the probe muon, it has looser selection requirements and is then matched (either using reconstruction central matching algorithm or $\Delta R < 0.5$) to muon id objects to estimate the muon reconstruction efficiency. On average, for MediumNSeg3 muons, the average muon id efficiency is 80.2% and a correction factor between data and MC of 0.97.

  For the tracking efficiency, the tag and probe method is again implemented with different selection criteria. The tracking efficiency depends on the SMT hit efficiency which varies as a function of η, where the SMT is very inefficient at small $|\eta|$ since the SMT cannot detect charged particles transverse to its surface, and also z. The SMT hit efficiency is luminosity dependent due to the beam shape change in z which widens with decreasing luminosity and is time dependent due to the upgrades in the detector such as HDI recoveries, sharper beam, and improved SMT firmware. On average, the tracking efficiency is 91.0% for medium tracks.

As for the correction between data and MC, this is a scale factor of 0.93 on average.

For the isolation efficiency, the tag and probe method is used with similar requirements as that used for the tracking efficiency. The control muon must also have TrackHalo < 3.5 GeV and CalorimeterHalo < 2.5 GeV to remove possible heavy flavor backgrounds and the control and tag muon must have an invariant mass consistent with the Z decay ($70 < M_{\mu\mu} < 110$ GeV).

The overall muon correction factor is thus

$$\varepsilon_{\mu-\mathrm{ID}} = \frac{\varepsilon^{\mathrm{Data}}_{\mathrm{MediumID}}}{\varepsilon^{\mathrm{MC}}_{\mathrm{MediumID}}} \times \frac{\varepsilon^{\mathrm{Data}}_{\mathrm{TrackMatch}}}{\varepsilon^{\mathrm{MC}}_{\mathrm{TrackMatch}}} \times \frac{\varepsilon^{\mathrm{Data}}_{\mathrm{TightIsol}}}{\varepsilon^{\mathrm{MC}}_{\mathrm{TightIsol}}} \tag{5.6}$$

$$\tag{5.7}$$

where ε corresponds to the efficiencies calculated for either data or MC and for either medium quality muons, track matching of muons, or the tight isolation point for muons.

5.2.4 W+jets Reweighting

Due to ALPGEN Monte Carlo W+jets samples unable to properly model data, these events need to be reweighted. This reweighting is done prior to b-tagging. For example, in the Run IIa and Run IIb electron channel in the two-jet bin, the shapes of the data sample and all the background samples added do not match. The data has a wider distribution then the background samples as seen in the first row of Figure 5.11. As a result, the distributions are reweighted in the following order as long as the variable exists in a particular jet multiplicity : $\eta(\mathrm{jet1}), \eta(\mathrm{jet2}), \Delta\phi(\mathrm{jet1}, \mathrm{jet2}), \Delta\eta(\mathrm{jet1}, \mathrm{jet2})$, and $\eta(\mathrm{jet3}), \eta(\mathrm{jet4})$. This reweighting function is determined for each variable by subtracting out the non W+jets background from the data sample and dividing this data histogram by the W+jets sample histogram for each bin. This is illustrated in the last two rows of Figure 5.11.

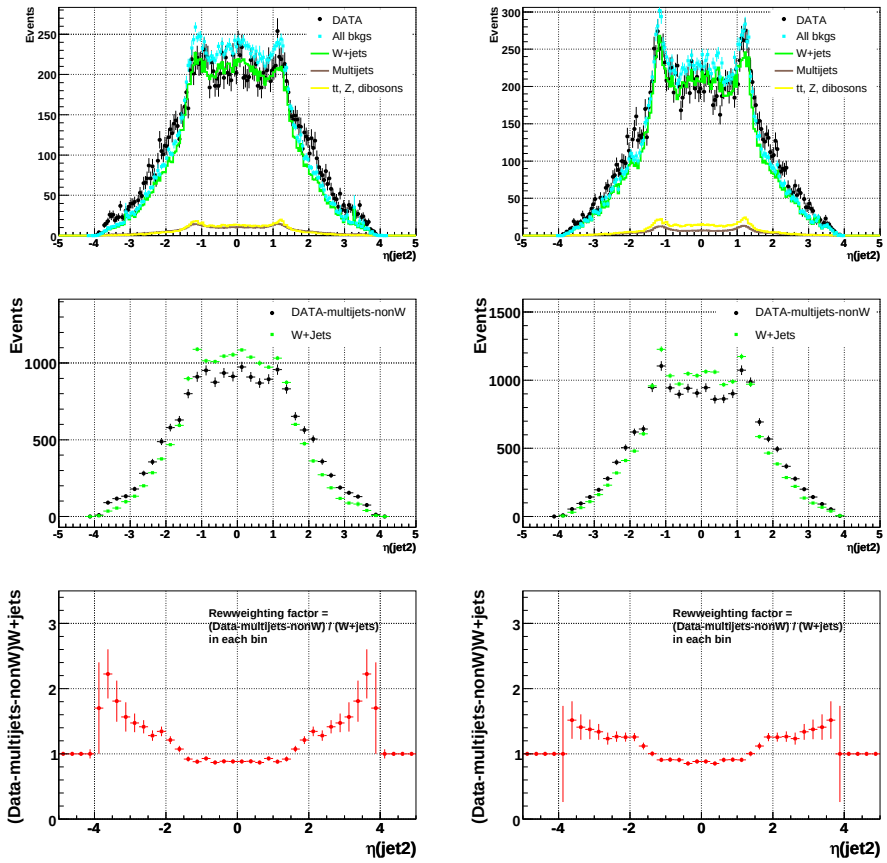

Figure 5.11: An example of how the ALPGEN W+jets reweighting factors for jets are calculated (Run IIa left, RunIIb right). See text above for a description.

The electron and muon channels are combined when doing this reweighting since the mismodeling of jet quantities in ALPGEN W+jets samples should be independent of lepton flavor. This is in fact what is seen as the reweighting function is very similar for both leptons.

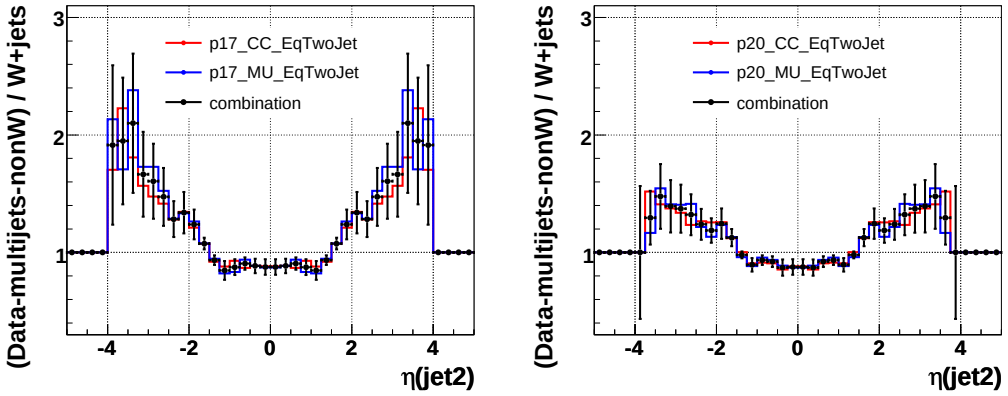

Figure 5.12: Reweighting factors for η(jet2) from an electron and muon channel and their combination for Run IIa (left) and Run IIb (right).

The combination for this is done bin by bin using a weighted average where the weights are determined by $1/\sigma^2_{i,\text{channel}}$ where $\sigma_{i,}$ is the uncertainty of the reweighting histogram for bin i and a particular channel. There is also no significant differences between the reweighting functions determined for different jet multiplicities separately so each jet bin is combined. However, the reweighting factors are treated separately for Run IIa and Run IIb and the final reweighting factors can be seen in Figs. 5.13 and 5.14 respectively.

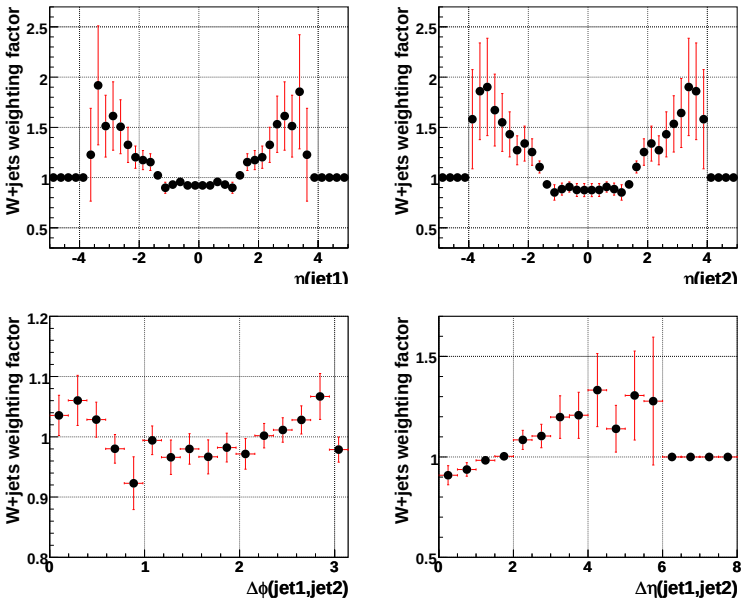

Figure 5.13: The Run IIa (p17) $\eta(\text{jet1}), \eta(\text{jet2}), \Delta\phi(\text{jet1}, \text{jet2})$, and $\Delta\eta(\text{jet1}, \text{jet2})$ ALPGEN W+jets reweighting factors.

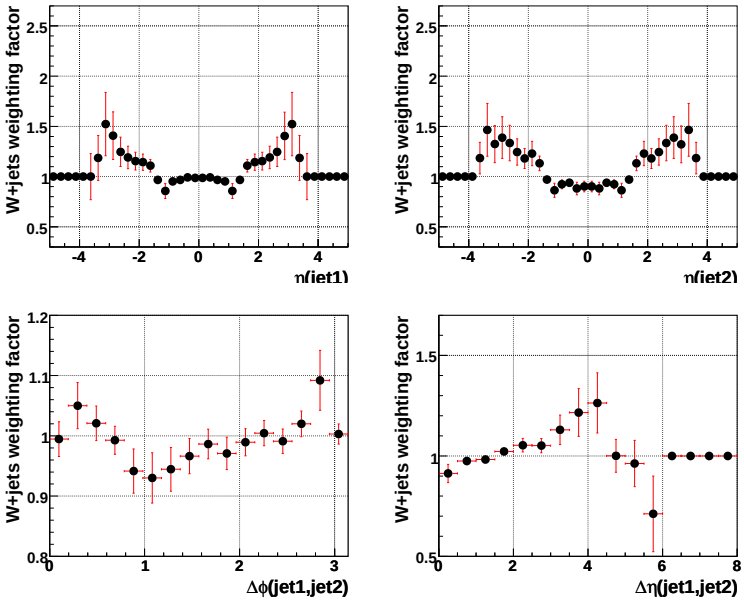

Figure 5.14: The Run IIb (p20) $\eta(\text{jet1}), \eta(\text{jet2}), \Delta\phi(\text{jet1}, \text{jet2})$, and $\Delta\eta(\text{jet1}, \text{jet2})$ ALPGEN W+jets reweighting factors.

Additionally, the muon detector pseudorapidity $\eta^{det}(\mu)$ had to be reweighted to get good background-data agreement. Another reweighting was done for the instantaneous luminosity which is applied to all MC samples and was derived for Run IIa and Run IIb aside from the one mentioned above. This can clearly be seen in Figure 5.2.4 since the zero bias data used to make the luminosity reweighting profiles still do not yield good data and background agreement.

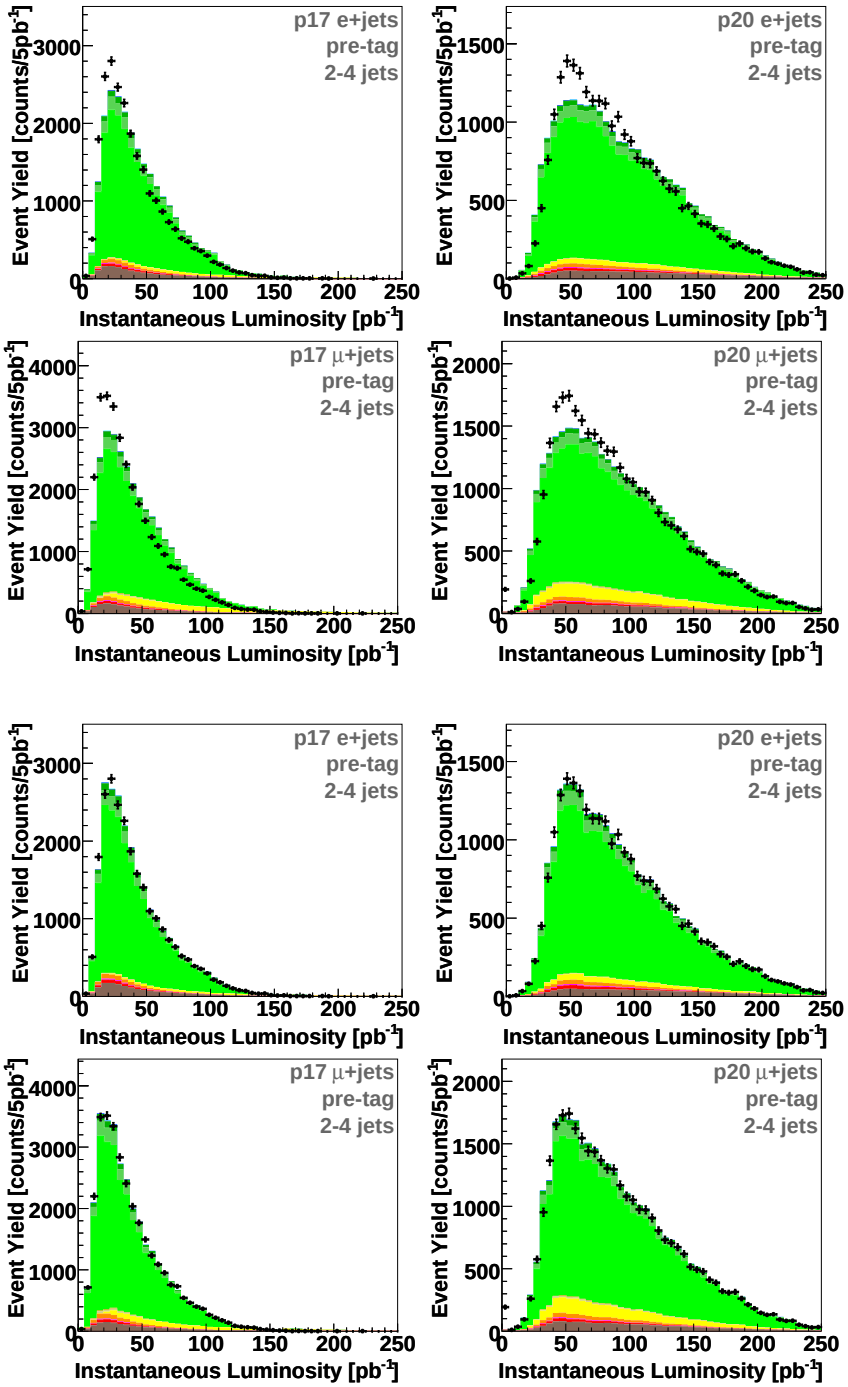

Figure 5.15: Instantaneous luminosity distributions for Run IIa (left) and Run IIb (right) before reweighting in this variable (upper two rows) and after (lower two rows).

In sum, the reweightings are applied in the following order, instantaneous luminosity (all MC samples), $\eta^{det}(\mu)$, η(jet1), η(jet2), $\Delta\phi$(jet1,jet2), $\Delta\eta$(jet1,jet2), η(jet3), and η(jet4). This is because the instantaneous luminosity was derived prior to any W+jets reweighting. As for the angular distributions, they are derived in the following order: η(jet1), η(jet2), $\Delta\phi$(jet1,jet2), $\Delta\eta$(jet1,jet2), η(jet3), and η(jet4). Thus, they must be applied in that same order. The $\eta^{det}(\mu)$, although derived last, should not affect the distributions whether it is applied prior or after the angular distributions reweighting functions.

5.2.5 W+jets + Multijets Normalization

The sum of the W+jets and multijets backgrounds is normalized to the pretagged data using the following equation:

$$Y_{\text{pretagged data}} = S_{W+\text{jets}} * Y_{W+\text{jets}}^{\text{before}-\text{IKS}} + Y_{\text{all other MC}} + S_{\text{multijets}} * Y_{\text{multijets}}^{\text{before}-\text{IKS}}, \qquad (5.8)$$

where Y_{sample} is the event yield in that sample after all the corrections and reweightings have been applied including the MC efficiency correction factors, samples scaled by integrated luminosity, ALPGEN leading-log cross sections which includes the branching fractions, and the theory K' and K'_{HF}-factors to account for higher order effects. $S_{W+\text{jets}}$ and $S_{\text{multijets}}$ is determined simultaneously by using the iterative KS-test normalization (IKS) method described below:

1. Select a kinematic variable (var1) that has different distributions for W+jets and multijets events, and is thus sensitive to their relative normalization.
2. Start with $S_{W+\text{jets}} = 1.0$ and calculate a corresponding $S_{\text{multijets}}$ using Eq. 5.8.
3. Do a Kolomogorov-Smirnov test (KS-test) [48] between data and background distributions of the variable var1 and record the KS-test value. The KS-test calculates an empirical distribution function, E_N, for both data and the background distributions and is defined as follows: $E_N(Y_i) = n(i)/N$ where N is the number of ordered data points Y_1,Y_2,..,Y_N and

$n(i)$ is the number of points less than data point value Y_i. The largest difference between the two empirical distribution functions is the KS-test statistic. The probability of this test is then calculated where a value much less than 1 means that the two histograms are not compatible.

4. Increase $S_{W+\text{jets}}$ by 0.001.
5. Repeat the above three steps until $S_{W+\text{jets}}$ reaches 4.0 or $S_{\text{multijets}}$ becomes negative.
6. Select a set of $S_{W+\text{jets}}$ and $S_{\text{multijets}}$ which gives the maximum KS-test value (KS_{max})
7. Repeat the procedure for a group of varN kinematic variables.

The final $S_{W+\text{jets}}$ and $S_{\text{multijets}}$ is determined by:

$$S_{W+\text{jets}} = \frac{\sum_{i=\text{var1}}^{\text{varN}} S^i_{W+\text{jets}} * \text{KS}^i_{\text{max}}}{\sum_{i=\text{var1}}^{\text{varN}} \text{KS}^i_{\text{max}}} \tag{5.9}$$

$$S_{\text{multijets}} = \frac{\sum_{i=\text{var1}}^{\text{varN}} S^i_{\text{multijets}} * \text{KS}^i_{\text{max}}}{\sum_{i=\text{var1}}^{\text{varN}} \text{KS}^i_{\text{max}}} \tag{5.10}$$

The variables chosen for this method are $p_T(\ell)$, $\not\!\!E_T$, and $M_T(W)$ and is done for each jet multiplicity. The final scale factors for W+jets and multijets are listed in Table 5.3.

IKS Normalization Scale Factors

	$S_{W+\text{jets}}$				$S_{\text{multijets}}$			
	Run IIa (p17)		Run IIb (p20)		Run IIa (p17)		Run IIb (p20)	
	e	μ	e	μ	e	μ	e	μ
2 jets	1.51	1.30	1.41	1.23	0.348	0.0490	0.388	0.0639
3 jets	1.92	1.79	1.75	1.57	0.291	0.0291	0.308	0.0410
4 jets	2.29	2.06	1.81	1.92	0.189	0.0244	0.424	0.0333

Table 5.3: W+jets and multijets scale factors from the iterative KS-test normalization method.

5.2.6 Heavy Flavor Fraction

The ALPGEN leading-log cross section calculations for W+jets are very sensitive to the renormalization and factorization scales. By comparing the LL and NLO calculations, K' and K'_{HF} scale factors have been determined for both W+jets and Z+jets [49].

NLO/LL K' and K'_{HF} Factors for W+Jets and Z+Jets Cross Sections

	Wjj	Wcj	$Wc\bar{c}$	$Wb\bar{b}$	Zjj	$Zc\bar{c}$	$Zb\bar{b}$
Run IIa	1.30	1.80	1.30×1.47	1.30×1.47	1.346	1.346×1.25	1.346×1.25
Run IIb	1.30	1.80	1.30×1.47	1.30×1.47	1.30	1.30×1.67	1.30×1.52

Table 5.4: Theoretical K'-factors used to scale the boson+jets backgrounds. When a product of two numbers is shown, the first one, K', is for the ratio of NLO to LL for all events and the second one is the heavy-flavor scale factor K'_{HF}.

In addition to these theoretical K'-factors, a further heavy-flavor scale factor correction S_{HF} is needed to adjust W$b\bar{b}$ and W$c\bar{c}$ [50] to achieve good data-background agreement. This factor is determined in a sample with a certain b-tagging requirement and good data-background agreement. Then, looking at a sample orthogonal to this sample, we want to try to keep the data background agreement. As a result,

$$S_{HF} = \frac{W'(D'' - X'') - W'' * (D' - X')}{B''(D' - X') - B' * (D'' - X'')} \tag{5.11}$$

where D is the data yield, W is the W+light-jets yield, B is the W+heavy-flavor yield and X is the other backgrounds plus the signal for the sample that pass the b-tagging requirement ($'$) and the one orthogonal to it ($''$). The S_{HF} is generated by solving the two equations below where S is a necessary scale factor to keep the normalization agreement needed before b-tagging.

$$D' = X' + S \times (W' + S_{HF} \times B') \tag{5.12}$$

$$D'' = X'' + S \times (W'' + S_{HF} \times B'') \tag{5.13}$$

The samples used to calculate S_{HF} is from the two-jet bin since a bias is introduced from the $t\bar{t}$ background which is more abundant at jet multiplicities above two. Table 5.5 shows the heavy-flavor scale factor corrections derived for the two Run periods and lepton types and their combinations.

Heavy-Flavor Scale Factor Corrections S_{HF} for W+Jets Events

	Run IIa		Run IIb		
	e	μ	e	μ	
1 tag	1.04 ± 0.19	1.15 ± 0.20	0.95 ± 0.20	0.65 ± 0.18	
2 tags	0.84 ± 0.30	0.70 ± 0.29	1.23 ± 0.40	1.17 ± 0.40	
	Run IIa+b		$e + \mu$		Run IIa+b
	e	μ	Run IIa	Run IIb	$e + \mu$
1 tag	1.00 ± 0.14	0.90 ± 0.13	1.10 ± 0.14	0.79 ± 0.13	0.95 ± 0.10
2 tags	1.02 ± 0.25	0.91 ± 0.17	0.77 ± 0.21	1.20 ± 0.28	0.97 ± 0.17

Table 5.5: Heavy-flavor scale factor corrections for the two run periods and lepton types and combinations of each, calculated using two-jet events.

The final S_{HF} used is the weighted average of the two entries in the last column of the lower row of Table 5.5. Thus,

$$S_{HF} = 0.946 \pm 0.082 \text{ (stat)}$$

5.3 B-tagging

Tagging b-jets reduces the signal to background ratio even more after event selection cuts since the single top event signature requires at least one b-tagged jet. In order to apply b-tagging, jets are required to be "*taggable*" and then are directly "*tagged*" if the sample is from data or have tag-rate functions (TRFs) applied to them if the sample is from Monte Carlo. The tagger used in this analysis is the Neural Network tagger which will be discussed in detail in this section whereas what constitutes a taggable jet was discussed in the previous chapter.

5.3.1 Neural-Network (NN) Tagger

The NN tagger [51] [52] uses a neural network to separate out jets that originate from a b quark rather than from other quarks. The neural network tagger relies on a mixture of variables from previous b-tagging methods and are listed in order of separation power.

Neural Network Variables

- Decay length significance of the Secondary Vertex Tagger (SVT) [53]

  The Secondary Vertex Tagger relies on the fact that a B-meson decays a distance, L_{xy}, of ≈ 3 mm in the transverse plane from the PV and that 70% of events with $L_{xy} > 1$ mm have at least 2 tracks with $\text{dca}/\sigma(dca) > 3.0$. This variable is defined as $|L_{xy}|/\sigma_{L_{xy}}$.

- Weighted combination of the tracks' impact parameter (IP) significances [54]

  This variable relies on the fact that tracks produced by charged decay products of long-lived b-hadrons have a non-zero IP with respect to the primary vertex (PV). The sign of the impact parameter is given by the sign of the impact parameter projection on

the jet axis. Impact parameter significance is then the impact parameter divided by its uncertainty which is determined by the track finding algorithm. The neural network needs continuous variable distributions to operate optimally so a weighted combination is made from variables relating to the tracks' IP significances. These variables are CSIP3s, the number of tracks with a decay length significance greater than 3; CSIP2s, the number of tracks with a decay length significance greater than 2; CSIP3w, the number of tracks with a negative decay length significance greater than 3 and $d\phi < 1.15$ with respect to the jet; and CSIP2w, the number of tracks with a negative decay length significance greater than 2 and $d\phi < 1.15$ with respect to the jet. The weighted combination made from these variables is the following:

$$CSIP\ Comb = 6 \times 3s + 4 \times 2s + 3 \times 3w + 2 \times 2w \tag{5.14}$$

- JLIP probability (that the jet originates from the Primary Vertex (PV)) [55]

  Jets from light quark fragmentation make a flat distribution from 0 to 1 in P_{jet}, which is the probability that all tracks in a jet originate from the primary interaction point. This is due to isotropic effects such as smearing from the SMT resolution, tracks with wrong hits assignments, multiple scattering, secondary interactions in the detector material or decays in flight. For heavy flavored jets, there is a peak at very low P_{jet} values due to the secondary vertex where these jets start fragmenting. Using the negative part of the impact parameter significance distribution, $P_{trk}(S_{IP})$ is defined as the following:

$$P_{trk}(S_{IP}) = \frac{\int_{-50}^{-|S_{IP}|} R(s)ds}{\int_{-50}^{0} R(s)ds} \tag{5.15}$$

  where

$$S_{IP} = \frac{S_{IP}^{raw}}{pull(p_{scat}, i, N_{PV})} \tag{5.16}$$

$$S_{IP}^{raw} = \frac{IP}{\sigma_{IP}^{raw}} \tag{5.17}$$

S_{IP}^{raw} is the signed IP value divided by its error. The pull is the error from the fit to a Gaussian of the IP as a function of p_{scat} for different criteria regarding CFT hits and SMT hits and also the number of tracks at the primary vertex. p_{scat} is defined as

$$p_{scat} = p(sin\theta)^{3/2} \tag{5.18}$$

where p is the momentum of the particle and θ is the polar angle relative to the beam axis and is proportional to the smearing of p due to multiple scattering. $R(S_{IP})$ is the negative part of the IP significance distribution which is used since the distribution is affected mostly by detector or reconstruction effects and is less affected by long lived light quark particles that can mimic b-jet characteristics. $R(S_{IP})$ is known as the impact parameter resolution function. The jet lifetime probability with either a positive or negative IP significance is thus

$$P_{jet}^{\pm} = \prod^{\pm} \times \sum_{j=0}^{N_{trk}^{\pm}-1} \frac{(-log \prod^{\pm})^j}{j!} \text{ with } \prod^{\pm} = \prod_{\mathrm{i=1}}^{\mathrm{N_{trk}^{\pm}}} \mathrm{P_{trk}(S_{IP<0}^{IP>0})} \tag{5.19}$$

- χ^2 per degree of freedom of the SVT secondary vertex
  This is $\dfrac{\chi^2}{(N_{Tracks} - 3)}$
- number of tracks used to reconstruct the secondary vertex
- mass of the secondary vertex
- number of secondary vertices found inside the jet

NN Architecture

The neural network used is a simple feed-forward network which consists of a layer of input nodes, hidden nodes and one layer of output nodes. The previous layer nodes are connected to each of the nodes in the consecutive layers by links that have a weight w_j and bias w_0 representing the strength of the signal between the two nodes. The node j of the hidden

output layer computes a linear combination x_j of the nodes in the previous layer y_i with a bias w_0 as seen in the following equation:

$$x_j = w_{0j} + \sum_i w_{ij} y_i \tag{5.20}$$

The output y_j of the node j is a function of input x_j by either $y_j = x_j$ or $y_j = \frac{1}{1+e^{-x_j}}$

The basic neural network structure is $N_{input} : N_{hidden} : N_{output}$ where the number of output nodes is 1 and the number of input nodes is the number of variables used which in this case is 7. Only two hidden layers were used in order to keep the NN as simple as possible and also to constrain the output from 0 to 1. For the first hidden layer, there are 24 hidden nodes which was ascertained by finding the lowest fake rate at fixed signal efficiencies of 75%, 70%, 60% and 50%. The last hidden layer has one node in order to constrain the NN output from 0 to 1 and is found to have no effect on the fake rate and b-tagging efficiencies.

NN Samples

The following data samples are used for making the NN and calculating the efficiencies [58] [59] described in the next section:

- EM - $\not\!\!E_T$ < 10 GeV, EMF < 0.8 applied to remove EM biased jets, 1 electron with $p_T > 4GeV$.
- JETQCD - jet triggers
- BID - one loose μ $p_T > 4GeV$ inside a 0.7 cone jet.
- 3JET - greater than or equal three jets. This is only used for Run IIb

MC used are QCD samples for $q\bar{q}$, $c\bar{c}$ and $b\bar{b}$ with different p_T ranges, $t\bar{t}$, $Z \to b\bar{b}$, $Z \to b\bar{b}(+\mu)$, $Z \to c\bar{c}$, $Z \to c\bar{c}(+\mu)$, $Z \to q\bar{q}$, $Z \to q\bar{q}(+\mu)$. For Run IIb, additional samples of $b\bar{b}$ and $c\bar{c}$ at different p_T ranges, and SUSY Higgs were also used.

The event selection requires the following criteria:

- Primary vertex reconstructed from 4 or more tracks with $|z| < 60$ cm
- Track jets formed from tracks found with $dr < 0.5$ of a seed track where these tracks must have at least 2 SMT hits and the seed track must have $p_T > 1.0\ GeV$. A track jet must consist of at least two tracks of $p_T > 0.5\ GeV$.
- Calorimeter jets reconstructed must be taggable with corrected $p_T > 15 GeV$ and at least two jets per event. The jet flavor is determined based on the hadrons found within $dR < 0.5$ of the jet. The jet is a b-jet if a b-hadron is found, a c-jet if a c-hadron is found but no b-hadron, and a fake jet or (uds)-jets if no heavy flavor is present in the jet which can also include jets originating from minimum bias vertices.
- Medium muons with $p_T > 4\ GeV/c$, a global $\chi^2 < 100$ and matched to a good jet within $\Delta R < 0.5$.
- Triggers used must not have a heavy-flavor bias

For the samples used, the following cuts were applied: SVT_{sl} decay length significance > 2.5, JLIP Probability > 0.02, and CSIP Combination > 8.

b-jet Efficiencies

The b-jet efficiency is measured on data using the System8 Method (S8) [56]. This has eight equations with eight unknowns using the number of tags found by two different tagging methods on two different samples. In order to solve for the efficiencies of the two tagging methods, the two taggers need to be uncorrelated with different b-efficiencies and the two data samples need to have different b-contents. The two taggers used are the NN and SLT tagger. The SLT tag is defined as a muonic jet where the muon satisfies a p_{TRel} cut of 0.6 GeV for Run IIa and 0.5 GeV for Run IIb with respect to the jet axis. This tagging method relies on the fact that the B hadron decays semileptonically to the final state of muon +X with the branching fraction of 10.95% while the probability for light quarks to decay to a muon is much smaller. Therefore, a muon near a jet is most likely produced from a b-quark. The p_{TRel} cut ensures

that NN b-efficiency differs from the SLT b-efficiency for all NN operating points. The two data samples used were the BID muonic jet sample and a b-enriched subset consisting of muonic jets with an away tagged jet passing NN L2 criteria.

The S8 equations are defined as

$$n = n_b + n_{udsc} \tag{5.21}$$

$$p = p_b + p_{udsc} \tag{5.22}$$

$$n^{SLT} = \epsilon_b^{SLT} n_b + \epsilon_{udsc}^{SLT} n_{udsc} \tag{5.23}$$

$$p^{SLT} = \epsilon_b^{SLT} p_b + \epsilon_{udsc}^{SLT} p_{udsc} \tag{5.24}$$

$$n^{NN} = \epsilon_b^{NN} n_b + \epsilon_{udsc}^{NN} n_{udsc} \tag{5.25}$$

$$p^{NN} = \beta\epsilon_b^{NN} p_b + \alpha\epsilon_{udsc}^{NN} p_{udsc} \tag{5.26}$$

$$n^{SLT,NN} = \kappa_b \epsilon_b^{SLT} \epsilon_b^{NN} n_b + \kappa_{udsc} \epsilon_{udsc}^{SLT} \epsilon_{udsc}^{NN} n_{udsc} \tag{5.27}$$

$$p^{SLT,NN} = \kappa_b \beta \epsilon_b^{SLT} \epsilon_b^{NN} p_b + \kappa_{udsc} \alpha \epsilon_{udsc}^{SLT} \epsilon_{udsc}^{NN} p_{udsc} \tag{5.28}$$

where n is the number of jets in the muonic jet samples, p is the number in the b-enriched sample, and ϵ is the efficiency of the tagger. The superscripts refer to which tagger is used and the subscripts refer to the jet flavor.

The other coefficients are the correlation coefficients which are measured using MC samples.

- α - Ratio of the udsc-tagging efficiencies in the two samples. This is calculated using the inclusive MC QCD sample but with the b-jets rejected.
- β - Ratio of the b-tagging efficiencies in the two samples. This is calculated from the ratio of the muonic b-jet to the muonic b-jet with an away tag tagging efficiencies. This is determined from the combined $b \to \mu$ MC sample.
- κ_b - Correlations between the NN tagger and the SLT tagger on b-jets. This is defined as

$$\kappa_{b,udsc} = \frac{\epsilon_{b,udsc}^{N} N \times \epsilon_{b,udsc}^{SLT}}{\epsilon_{b,udsc}^{NN\&SLT}} \tag{5.29}$$

where ϵ corresponds to the efficiency, the subscripts refer to the jet flavor, and the superscript refers to the taggers where & corresponds to both tags being present. This is measured using the $b \rightarrow \mu$ MC sample. A straight line is used to model this coefficient due to a linear dependence in p_T

κ_{udsc} - Correlations between the NN tagger and the SLT tagger on udsc-jets. Using the equation above, this coefficient is measured using the $c \rightarrow \mu$ MC sample. There is also a linear dependence in p_T and so a straight line fit is used.

p_{TRel} - Ratio of the SLT tagging efficiencies on c and uds-jets. The S8 efficiencies were calculated at different SLT operating points from 0.3 to 0.7 GeV/c to see if there was any dependence on p_{TRel}. The only affected efficiencies are κ_b and κ_{udsc}

With these correlation coefficients, the S8 equations can now be solved using Minuit [57] to determine the b-jet efficiencies. The same game can be played to determine c-jet efficiencies by using c-jet samples. The efficiency is determined as a function of p_T for different η regions. For the muonic b-jet, efficiencies in p_T are parameterized using $\epsilon(p_T) = \frac{c}{1 + ae^{-bp_T}}$ determined up to jet p_T=60 GeV For b and c-jet, efficiencies in p_T are parameterized as follows:

$$\epsilon(p_T) = a + bln(p_T) + c(ln(p_T))^2 + d(ln(p_T))^3 \tag{5.30}$$

For the η parametrization, it is defined as

$$\epsilon(|\eta|) = e + f|\eta| + g|\eta|^2 + h|\eta|^3 + i|\eta|^4 + j|\eta|^5 + k|\eta|^6 + l|\eta|^7 \tag{5.31}$$

These distributions are then scaled by the relative change in the efficiency as a function of η:

$$\epsilon(p_T, \eta) = \epsilon(p_T)_{R_\eta} \times \frac{\epsilon(\eta)}{\epsilon_{R_\eta}} \tag{5.32}$$

where ϵ_{R_η} is the total efficiency calculated in each η region, R_η.

As for the light jet efficiencies, this is determined using EM and QCD skims and is also parameterized in p_T for different η regions. The negative tag rate (NTR) is used to approximate the positive tag fake rate but needs to be corrected for due to the c and b-quark contribution and an asymmetry in the distribution from long lifetime udsg-jets. For the NN tagger, a negative tag result is defined as the output from the NN when all the NN inputs from the corresponding input taggers are from the negative tag results for the jet. The CSIP and JLIP negative tag variables are calculated from tracks which have a negative IP significance with respect to the primary vertex. The SVT variables are calculated from secondary vertices which have a negative decay length and a $\Delta R < 0.5$ with respect to the jet.

The fake tag rate (FTR) is defined as follows:

$$FTR = SF_{hf} \times SF_{ll} \times NTR \tag{5.33}$$

where SF_{hf} is the ratio of the light jet NTR to the total NTR and SF_{ll} is the ratio between the light jet positive tag rate and the light jet NTR. These scale factors depend on the p_T in the three η regions and hence the FTR parameterization is in both p_T and η.

5.3.2 Tag-Rate Function (TRF)

The Tag-Rate Function (TRF) is the probability to tag a jet of flavor α and is a function of the taggability and tagging efficiency:

$$P_\alpha(p_T, \eta, z_{PV}) = P^{\text{taggable}}(p_T, \eta, z_{PV}) \times \varepsilon_\alpha(p_T, \eta) \tag{5.34}$$

The TRF must be applied on Monte Carlo events in order to properly account for detector effects. For the probability to tag a jet of flavor α, a data/MC scale factor must be used which is measured from Data muonic b-efficiency/MC muonic b-efficiency in order to accurately account for detector effects that lower the tagging efficiency of b-jets.

As for the taggability, the detector effects is parameterized in jet p_T, jet η, and primary vertex z zones and are derived using data samples that have all the single top selection cuts applied except that the lepton isolation is kept loose. The loose lepton isolation is to ensure that there is enough statistics to make stable taggability rate functions. The functions are split into muon or electron and Run IIa or Run IIb. In order to validate that the taggability derived with loose data samples can be used on the tight data samples, the observed taggability is measured with the tight data samples and then compared with the taggability rate function value for the same tight events.

Additionally, the TRFs are used in the Matrix Element analysis discussed in the next chapter.

Application of B-tagging

The neural network has 12 different operating points which depend on the neural network output cut that is applied. For this analysis, the TIGHT operating point is used for the single-tagged channels which requires the NN output to be greater than 0.775 and OLDLOOSE is used for double-tagged channels which requires the NN output to be greater than 0.5. The single and double tagged channels are made orthogonal to each other by vetoing single tagged events with another jet that has a NN output greater than 0.5. The average fake rates for the TIGHT/OLDLOOSE operating points are 0.82%/2.5% for data jets in the central calorimeter and the average b-tagging efficiencies on data are 49%/61% for jets up to $|\eta| = 2.5$. The different tagging efficiencies for the analysis with and without taggability requirements can be found in Table 5.6 and 5.7

We can now get probability values for an event to be single-tagged, double-tagged or untagged from the b-tagging efficiencies used in this analysis.

b-Tagging Efficiencies

	Run IIa					
	OLDLOOSE			TIGHT		
Taggability	*b*-jets	*c*-jets	light jets	*b*-jets	*c*-jets	light jets
Without	58%	17%	1.5%	48%	10%	0.42
With	50%	14%	1.2%	41%	8.6%	0.35

Table 5.6: *b*-tagging efficiencies for the OLDLOOSE and TIGHT operating points measured by averaging the tag rate function values for Run IIa. The upper row shows values without taking into account taggability and the lower row shows values including it.

b-Tagging Efficiencies

	Run IIb					
	OLDLOOSE			TIGHT		
Taggability	*b*-jets	*c*-jets	light jets	*b*-jets	*c*-jets	light jets
Without	57%	18%	2.1%	46%	11%	0.63%
With	48%	15%	1.7%	39%	8.9%	0.52%

Table 5.7: *b*-tagging efficiencies for the OLDLOOSE and TIGHT operating points measured by averaging the tag rate function values in Run IIb. The upper row shows values without taking into account taggability and the lower row shows values including it.

$$
\begin{aligned}
P_{\text{event}}(1\text{ tag}) &= \sum_j P_{\alpha_j}^{\text{TIGHT}}(p_{Tj},\eta_j)\prod_{i\neq j}(1-P_{\alpha_i}^{\text{OLDLOOSE}}(p_{Ti},\eta_i)) \\
P_{\text{event}}(2\text{ tags}) &= \sum_{j,i\neq j} P_{\alpha_j}^{\text{OLDLOOSE}}(p_{Tj},\eta_j)P_{\alpha_i}^{\text{OLDLOOSE}}(p_{Ti},\eta_i)\times \\
&\quad \prod_{k\neq j\neq i}(1-P_{\alpha_k}^{\text{OLDLOOSE}}(p_{Tk},\eta_k))
\end{aligned}
$$

Using these equations, Monte Carlo events are permuted where each jet in the event is defined as b-tagged or not b-tagged and the corresponding probability assigned to that jet is then multiplied through with the other jets which are also defined as b-tagged or not b-tagged and also given a corresponding probability which depends on the characteristics of the jet. This is done for all the different combinations which depend on the jet multiplicity and also on the number of b-tagged jets. As a result, for each event, the sum of the new event weights for no b-tags, 1 b-tag and 2-btags must equal the original event weight prior to applying the TRFs

5.4 Event Yields

After applying the proper corrections, reweighting, and normalizations, the yields or the number of events of the signal or background is shown for the 2.3 fb^{-1} data analyzed prior to b-tagging in Tables 5.8 - 5.10.

Pretagged Event Yields

	Run IIa					
	Electron Channel			Muon Channel		
	2 jets	3 jets	4 jets	2 jets	3 jets	4 jets
Signals						
tb	23	8.2	2.2	27	11	2.8
tqb	43	17	5.8	51	23	7.0
tb+tqb	67	26	8.0	77	33	10
Backgrounds						
t→ll	60	37	12	57	41	13
t→l+jets	41	136	158	32	143	196
$Wb\bar{b}$	479	160	45	530	211	57
$Wc\bar{c}$	1,041	356	101	1,196	485	125
Wcj	1,338	315	65	1,514	389	81
Wjj	13,847	3,309	722	17,028	4,612	984
$Zb\bar{b}$	18	7.1	3.5	70	22	6.6
$Zc\bar{c}$	33	12	4.2	151	46	13
Zjj	461	125	40	1,309	348	84
Dibosons	339	98	24	457	142	34
Multijets	923	278	74	896	235	69
Background Sum	18,582	4,834	1,246	23,243	6,675	1,663
Data	18,582	4,834	1,246	23,243	6,675	1,663

Table 5.8: Yields after selection and before b-tagging for Run IIa.

Tables 5.11 and 5.14 show the event yields for all signals and backgrounds after b tagging, separated by data taking period, lepton flavor and jet multiplicity within each table

Pretagged Event Yields

	Run IIb					
	Electron Channel			Muon Channel		
	2 jets	3 jets	4 jets	2 jets	3 jets	4 jets
Signals						
tb	24	8.4	2.3	26	11	3.3
tqb	43	19	6.3	49	24	7.9
tb+tqb	67	27	8.6	75	35	11
Backgrounds						
t→ll	65	42	13	61	46	14
t→l+jets	43	141	168	33	145	198
$Wb\bar{b}$	458	161	42	499	200	61
$Wc\bar{c}$	1,006	351	94	1,126	453	137
Wcj	1,327	316	70	1,442	377	96
Wjj	14,166	3,489	795	16,941	4,710	1,137
$Zb\bar{b}$	19	8.2	3.4	70	26	7.4
$Zc\bar{c}$	35	15	5.9	152	54	14
Zjj	596	167	55	1,833	507	118
Dibosons	343	103	26	445	145	37
Multijets	987	294	188	1,369	377	108
Background Sum	19,048	5,087	1,460	23,972	7,040	1,927
Data	19,048	5,087	1,460	23,972	7,040	1,927

Table 5.9: Yields after selection and before b-tagging for Run IIb.

Pretagged Event Yields for Combined Signals and Backgrounds

	Electron+Muon, Run IIa+Run IIb			
	2 jets	3 jets	4 jets	All Channels
Signal				
tb+tqb	286	121	37	444
Backgrounds				
t	392 (0.5%)	731 (3%)	772 (12%)	1,895 (2%)
W+jets	73,938 (87%)	19,894 (84%)	4,612 (73%)	98,444 (86%)
Z+jets & dibosons	6,331 (7%)	1,825 (8%)	475 (8%)	8,631 (8%)
Multijets	4,175 (5%)	1,184 (5%)	439 (7%)	5,798 (5%)
Background Sum	84,845	23,636	6,296	114,777
Data	84,845	23,636	6,296	114,777
$S:B$	1:297	1:195	1:170	1:259

Table 5.10: Yields after selection but before b-tagging for the analysis channels and backgrounds combined. The percentages are of the total background for each component.

Single-Tagged Event Yields

	Run IIa					
	Electron Channel			Muon Channel		
	2 jets	3 jets	4 jets	2 jets	3 jets	4 jets
Signals						
tb	9.1	3.1	0.82	10.2	3.9	1.0
tqb	17.4	6.6	2.1	20.5	8.6	3.6
tb+tqb	26.4	9.7	3.0	30.7	12.5	3.6
Backgrounds						
t→ll	23.6	14.2	4.3	22.1	15.6	4.8
t→l+jets	16.3	52.0	57.0	12.5	54.3	69.8
$Wb\bar{b}$	135.4	44.2	12.0	146.4	57.1	16.0
$Wc\bar{c}$	66.0	24.8	8.1	73.9	33.4	9.9
Wcj	98.3	24.0	5.0	112.1	30.2	6.3
Wjj	73.6	21.9	6.1	87.0	30.1	8.1
$Zb\bar{b}$	6.5	2.8	0.89	26.8	7.9	2.5
$Zc\bar{c}$	2.7	1.2	0.55	13.3	4.6	1.5
Zjj	5.4	1.8	0.63	12.7	4.3	1.1
Dibosons	16.2	5.3	1.4	22.3	7.8	2.1
Multijets	28.0	10.3	3.0	51.5	17.2	7.3
Background Sum	472.1	202.4	99.0	580.6	262.5	129.4
Bkgds+Signals	498.5	212.2	101.8	611.3	275.0	134.6
Data	508	202	103	627	259	131

Table 5.11: Yields after selection for events with exactly one b-tagged jet for Run IIa.

Single-Tagged Event Yields

	Run IIb					
	Electron Channel			Muon Channel		
	2 jets	3 jets	4 jets	2 jets	3 jets	4 jets
Signals						
tb	9.5	3.3	0.91	9.9	4.3	1.2
tqb	16.9	7.2	2.5	18.5	8.7	3.0
tb+tqb	26.4	10.5	3.4	28.4	13.0	4.2
Backgrounds						
t→ll	25.6	16.1	4.9	23.5	17.0	5.0
t→l+jets	16.4	53.8	61.5	12.2	53.6	70.6
$Wb\bar{b}$	129.5	44.3	11.6	136.0	53.4	16.8
$Wc\bar{c}$	68.6	26.2	7.6	72.4	32.6	10.9
Wcj	106.1	25.8	5.4	111.9	29.7	6.6
Wjj	114.4	35.4	9.6	128.3	46.5	14.5
$Zb\bar{b}$	5.0	2.4	1.0	20.1	7.7	2.2
$Zc\bar{c}$	2.1	1.1	0.57	10.7	4.3	1.2
Zjj	6.0	2.1	0.79	13.9	5.0	1.3
Dibosons	17.4	5.8	1.7	22.7	8.4	2.4
Multijets	31.0	10.1	7.1	73.5	28.2	9.0
Background Sum	522.1	223.2	111.6	625.3	286.5	140.5
Bkgds+Signals	548.5	233.6	115.2	653.6	299.4	144.7
Data	547	207	124	595	290	142

Table 5.12: Yields after selection for events with exactly one b-tagged jet for Run IIb.

Double-Tagged Event Yields

	Run IIa					
	Electron Channel			Muon Channel		
	2 jets	3 jets	4 jets	2 jets	3 jets	4 jets
Signals						
tb	5.69	2.12	0.58	6.66	2.75	0.75
tqb	0.81	1.61	0.90	0.92	2.15	1.07
tb+tqb	6.50	3.72	1.49	7.59	4.90	1.82
Backgrounds						
t→ll	13.91	9.70	3.12	14.09	11.22	3.58
t→l+jets	4.32	28.63	43.16	3.51	32.18	55.38
$Wb\bar{b}$	33.96	12.34	3.69	35.64	15.71	4.77
$Wc\bar{c}$	5.12	2.75	1.28	5.62	3.56	1.50
Wcj	1.44	0.68	0.19	1.62	0.83	0.26
Wjj	1.45	0.86	0.34	1.70	1.20	0.46
$Zb\bar{b}$	0.88	0.74	0.31	6.14	2.60	0.91
$Zc\bar{c}$	0.15	0.13	0.10	1.05	0.54	0.25
Zjj	0.14	0.09	0.05	0.31	0.20	0.07
Dibosons	2.05	0.85	0.28	3.06	1.37	0.46
Multijets	1.90	1.10	0.48	3.28	1.98	0.93
Background Sum	65.33	57.88	53.00	76.03	71.40	68.57
Bkgds+Signals	71.82	61.59	54.48	83.60	76.29	70.40
Data	67	61	37	71	62	56

Table 5.13: Yields after selection for events with exactly two b-tagged jets for Run IIa.

Double-Tagged Event Yields

	Run IIb					
	Electron Channel			Muon Channel		
	2 jets	3 jets	4 jets	2 jets	3 jets	4 jets
Signals						
tb	5.26	2.00	0.58	5.61	2.59	0.78
tqb	0.94	1.89	1.01	0.99	2.22	1.21
tb+tqb	6.20	3.89	1.58	6.60	4.80	1.99
Backgrounds						
t→ll	13.58	9.99	3.17	12.95	10.79	3.33
t→l+jets	4.07	27.71	43.44	3.11	29.00	51.06
$Wb\bar{b}$	30.54	12.19	3.43	30.84	14.42	5.07
$Wc\bar{c}$	5.55	3.15	1.17	5.60	3.72	1.67
Wcj	2.04	0.96	0.28	2.07	1.04	0.33
Wjj	2.81	1.66	0.64	3.21	2.20	0.98
$Zb\bar{b}$	0.69	0.60	0.34	4.34	2.07	0.70
$Zc\bar{c}$	0.14	0.14	0.10	0.86	0.53	0.19
Zjj	0.16	0.11	0.06	0.34	0.24	0.09
Dibosons	1.96	0.91	0.30	2.98	1.38	0.46
Multijets	2.25	1.37	1.13	4.92	3.12	0.97
Background Sum	63.78	58.80	54.06	71.22	68.50	64.85
Bkgds+Signals	69.99	62.68	55.64	77.81	73.31	66.85
Data	79	56	51	85	79	80

Table 5.14: Yields after selection for events with exactly two b-tagged jets for Run IIb.

Table 5.15 shows a condensed version of the same information. The numbers in parentheses in the tables are the percentage of the total background for each component.

Tagged Event Yields for Combined Signals and Backgrounds

	Electron+Muon, Run IIa+Run IIb			
	2 jets	3 jets	4 jets	All Channels
Signals				
tb+tqb	139±18	63±9.6	21±4.6	223±30
Backgrounds				
$t\bar{t}$	222±35	436±66	484±71	1,142±168
W+jets	1,829±161	637±61	180±18	2,647±241
Z+jets & dibosons	229±38	85±17	26±6.7	340±61
Multijets	196±50	73±17	30±6.4	300±52
Background Sum	2,476±183	1,231±102	721±78	4,429±336
Backgrounds+Signals	2,615±192	1,294±107	742±80	4,652±352
Data	2,579	1,216	724	4,519
$S:B$	1:18	1:20	1:34	1:20

Table 5.15: Yields after selection for the analysis channels and backgrounds combined.

Table 5.16 and 5.17 summarizes the signals, summed backgrounds, and data from each channel, showing the uncertainties on the signals and backgrounds, and the signal:background ratios for single and double tag events respectively.

Tagged Event Yields for Each Channel and Signal:Background Ratios

	Single-Tagged		
	2 jets	3 jets	4 jets
Electron Channel for Run IIa Data (p17)			
Signal Sum	26.4 ± 2.8	9.7 ± 1.3	3.0 ± 0.6
Background Sum	472.1 ± 38.4	202.4 ± 16.9	99.0 ± 10.0
Data	508	202	103
$S : B$	1:18	1:21	1:33
Electron Channel for Run IIb Data (p20)			
Signal Sum	26.4 ± 2.8	10.5 ± 1.4	3.4 ± 0.7
Background Sum	522.1 ± 44.8	223.2 ± 19.0	111.6 ± 11.0
Data	547	207	124
$S : B$	1:20	1:21	1:33
Muon Channel for Run IIa Data (p17)			
Signal Sum	30.7 ± 3.2	12.5 ± 1.6	3.6 ± 0.8
Background Sum	580.6 ± 47.2	262.5 ± 21.0	129.5 ± 12.6
Data	627	259	131
$S : B$	1:19	1:21	1:36
Muon Channel for Run IIb Data (p20)			
Signal Sum	28.4 ± 3.4	13.0 ± 1.8	4.2 ± 0.9
Background Sum	625.3 ± 59.4	286.5 ± 25.8	140.5 ± 14.1
Data	595	290	142
$S : B$	1:22	1:22	1:33
Electron and Muon Channels for Runs IIa+IIb			
Signal Sum	112.0 ± 14.5	45.7 ± 7.0	14.2 ± 3.2
Background Sum	$2,200.1 \pm 153,4$	974.5 ± 72.3	480.6 ± 45.4
Data	2,277	958	500
$S : B$	1:20	1:21	1:34

Table 5.16: Summed signal and background yields after selection with total uncertainties, the numbers of data events, and the signal:background ratio in each analysis channel, and for electron and muon p17 and p20 channels combined for single-tagged events .

Tagged Event Yields for Each Channel and Signal:Background Ratios

	Double-Tagged		
	2 jets	3 jets	4 jets
Electron Channel for Run IIa Data (p17)			
Signal Sum	6.5 ± 1.0	3.7 ± 0.6	1.5 ± 0.3
Background Sum	65.3 ± 9.5	57.9 ± 8.6	53.0 ± 8.5
Data	67	61	37
$S : B$	1:10	1:16	1:36
Electron Channel for Run IIb Data (p20)			
Signal Sum	6.2 ± 0.9	3.9 ± 0.6	1.6 ± 0.3
Background Sum	63.8 ± 9.4	58.8 ± 8.7	54.1 ± 8.5
Data	79	56	51
$S : B$	1:10	1:15	1:34
Muon Channel for Run IIa Data (p17)			
Signal Sum	7.6 ± 1.1	4.9 ± 0.8	1.8 ± 0.4
Background Sum	76.0 ± 10.6	71.4 ± 10.2	68.6 ± 10.8
Data	71	62	56
$S : B$	1:10	1:14	1:37
Muon Channel for Run IIb Data (p20)			
Signal Sum	6.6 ± 1.0	4.8 ± 0.8	2.0 ± 0.4
Background Sum	71.2 ± 10.2	68.5 ± 10.1	64.9 ± 10.4
Data	85	79	80
$S : B$	1:11	1:14	1:32
Electron and Muon Channels for Runs IIa+IIb			
Signal Sum	26.9 ± 4.0	17.3 ± 2.8	6.9 ± 1.5
Background Sum	276.4 ± 32.8	256.6 ± 32.3	240.5 ± 34.1
Data	302	258	224
$S : B$	1:10	1:15	1:34

Table 5.17: Summed signal and background yields after selection with total uncertainties, the numbers of data events, and the signal:background ratio in each analysis channel, and for electron and muon p17 and p20 channels combined for double-tagged events .

Figure 5.16 shows the color scheme used in the plots in this thesis.

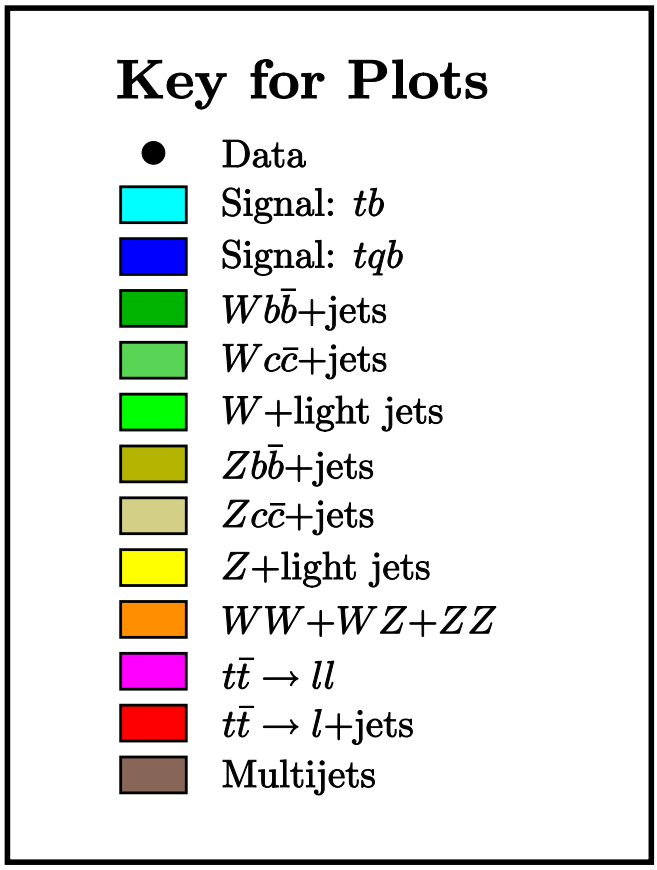

Figure 5.16: Illustration of the color scheme used in plots of signals and backgrounds in the single top analyses.

Figure 5.17 illustrates the proportions of the signal and background components in the datasets divided by number of jets and number of b-tagged jets.

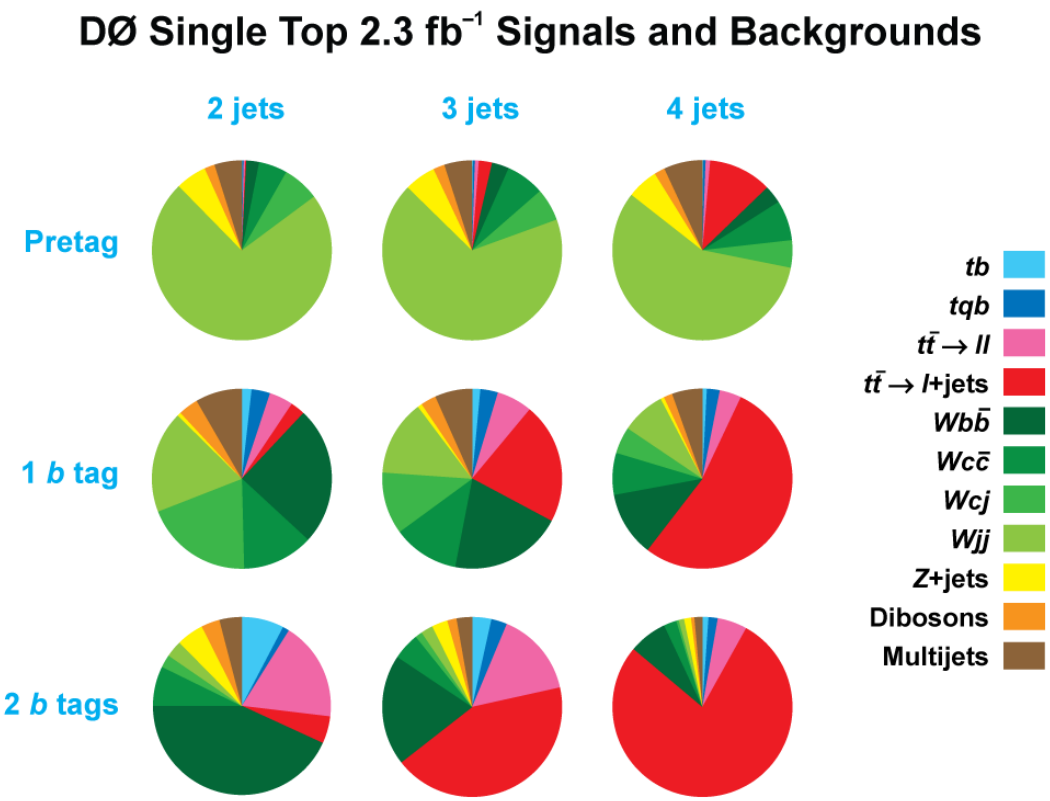

Figure 5.17: Illustration of the composition of the datasets as a function of number of jets and number of b tags.

5.5 Event Distributions

Figures 5.18 to 5.29 show various kinematic distributions in the pretagged and tagged final samples. Each figure has one column for each jet multiplicity and the following rows for run period and b-tag multiplicity: p17-PreTag, p20-PreTag, p17-EqOneTag, p20-EqOneTag, p17-EqTwoTag, p20-EqTwoTag. These figures show distributions of jet, lepton, and $\not\!\!E_T$ properties which need to be well modeled in order to properly apply the multivariate technique, the Matrix Element (ME) analysis. The data MC agreement show that the MC is correctly generated and the detector effects are well understood.

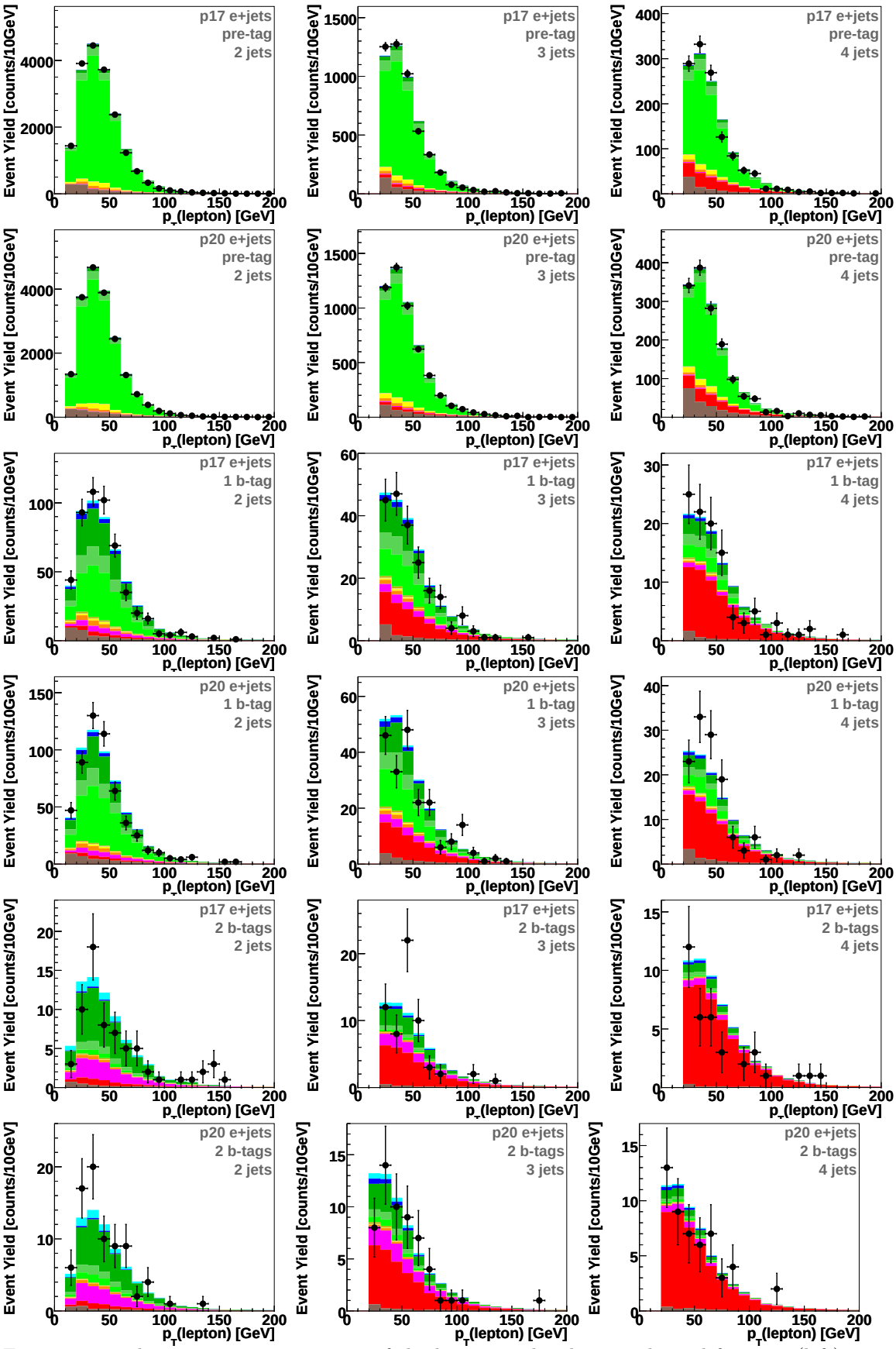

Figure 5.18: The transverse momentum of the lepton in the electron channel for 2-jet (left), 3-jet (middle), and 4-jet events (right), for p17 and p20, pretagged, single-tagged, and double-tagged events.

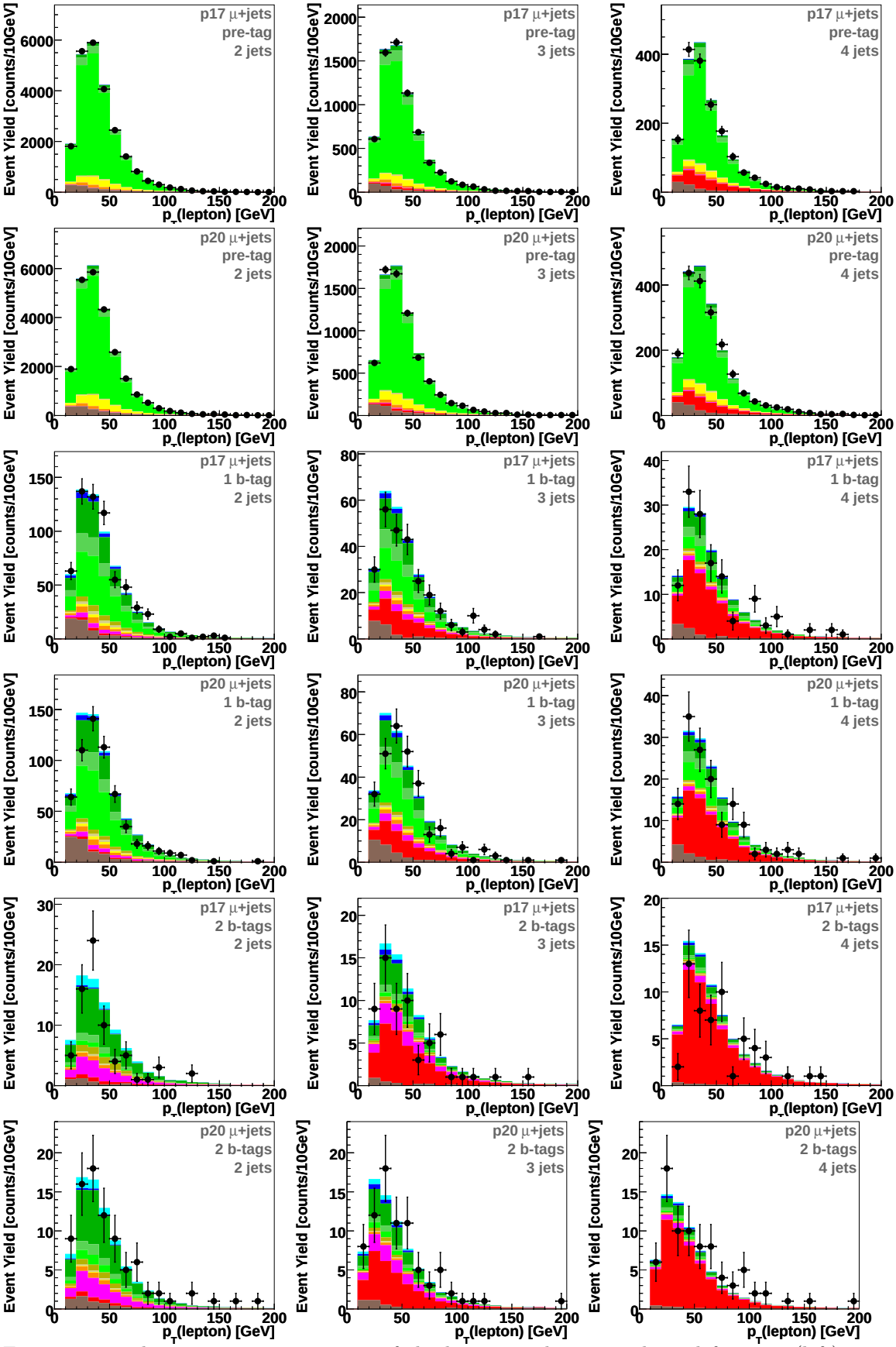

Figure 5.19: The transverse momentum of the lepton in the muon channel for 2-jet (left), 3-jet (middle), and 4-jet events (right), for p17 and p20, pretagged, single-tagged, and double-tagged events.

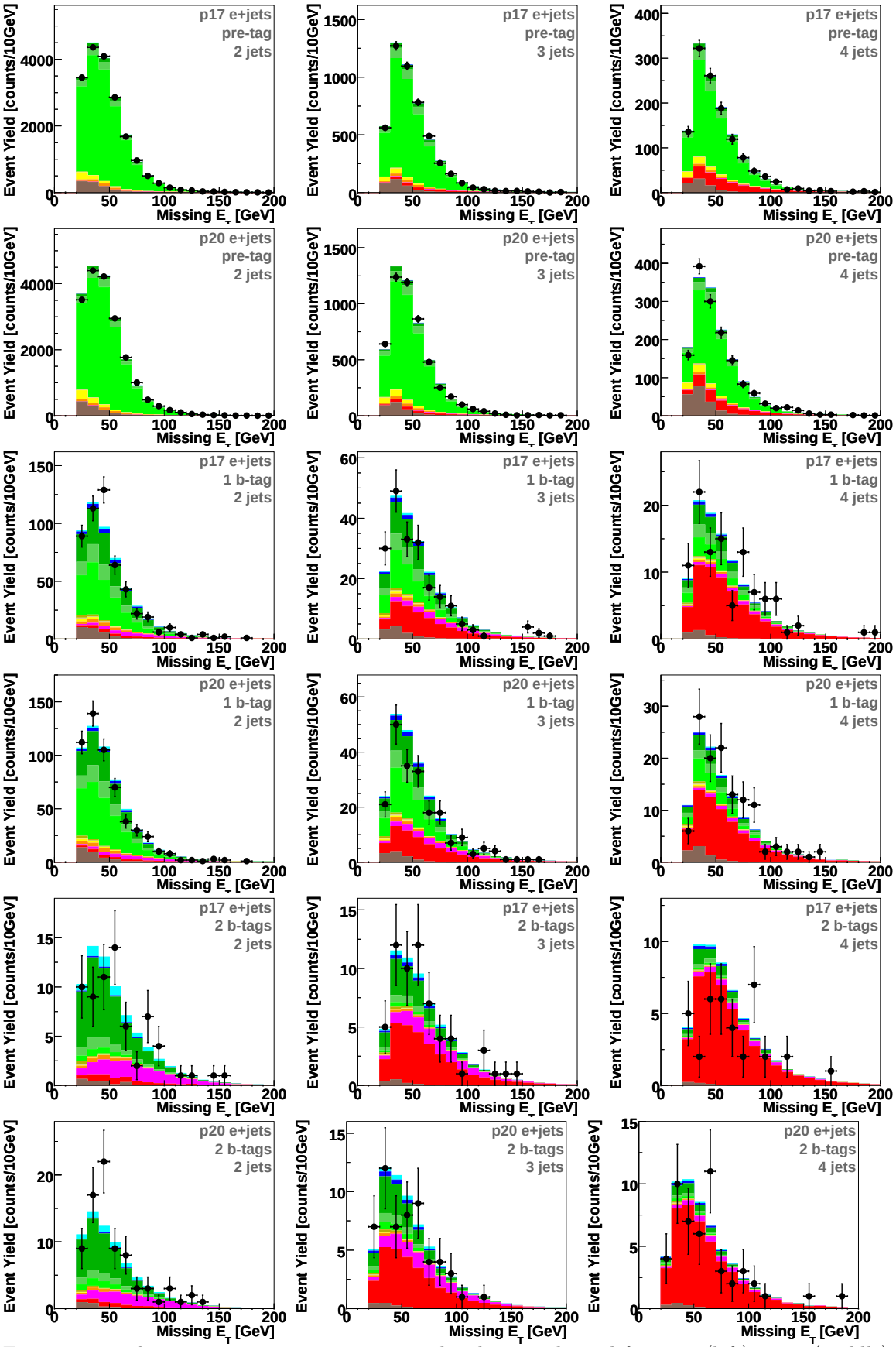

Figure 5.20: The missing transverse energy in the electron channel for 2-jet (left), 3-jet (middle), and 4-jet events (right), for p17 and p20, pretagged, single-tagged, and double-tagged events.

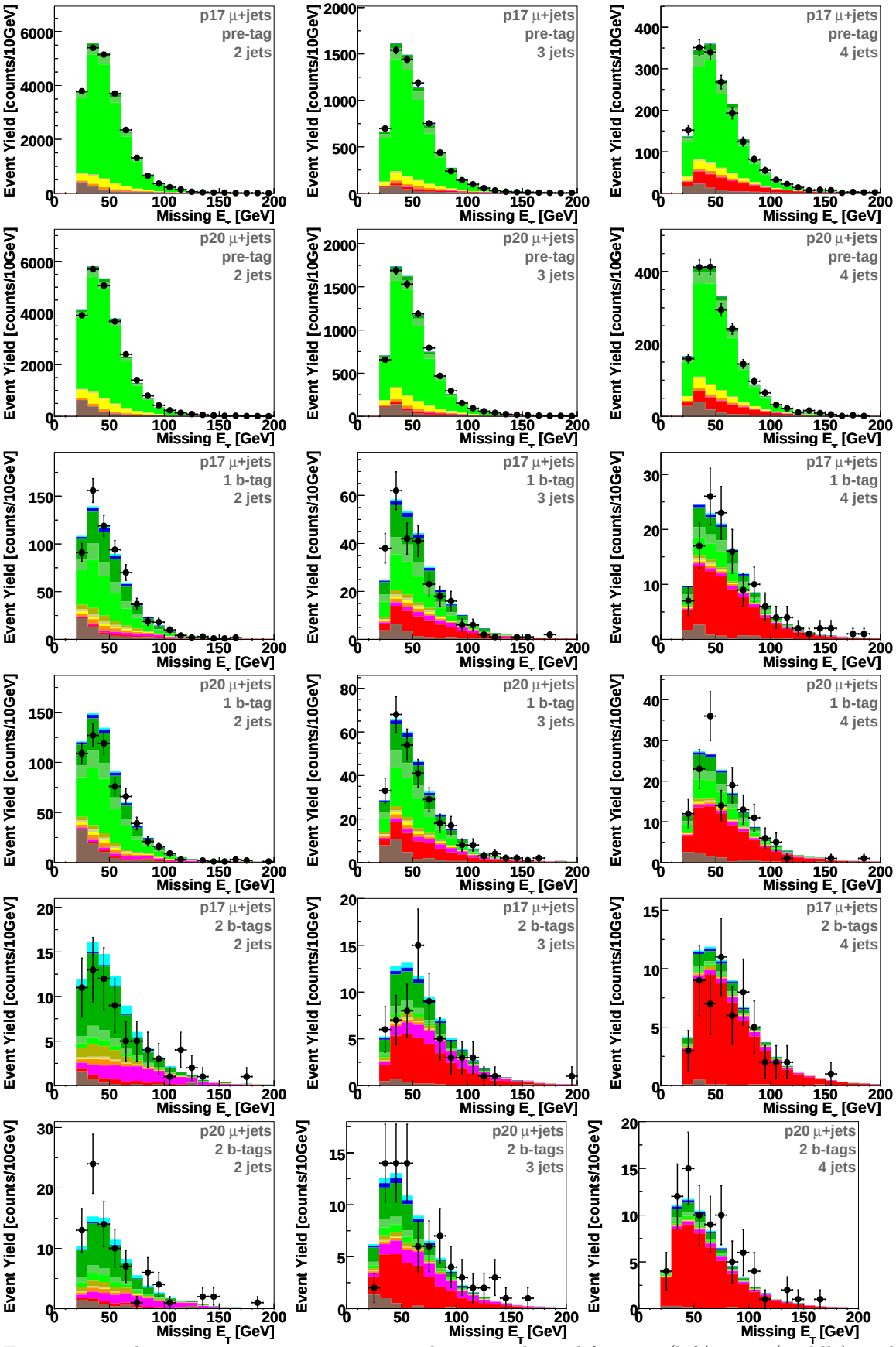

Figure 5.21: The missing transverse energy in the muon channel for 2-jet (left), 3-jet (middle), and 4-jet events (right), for p17 and p20, pretagged, single-tagged, and double-tagged events.

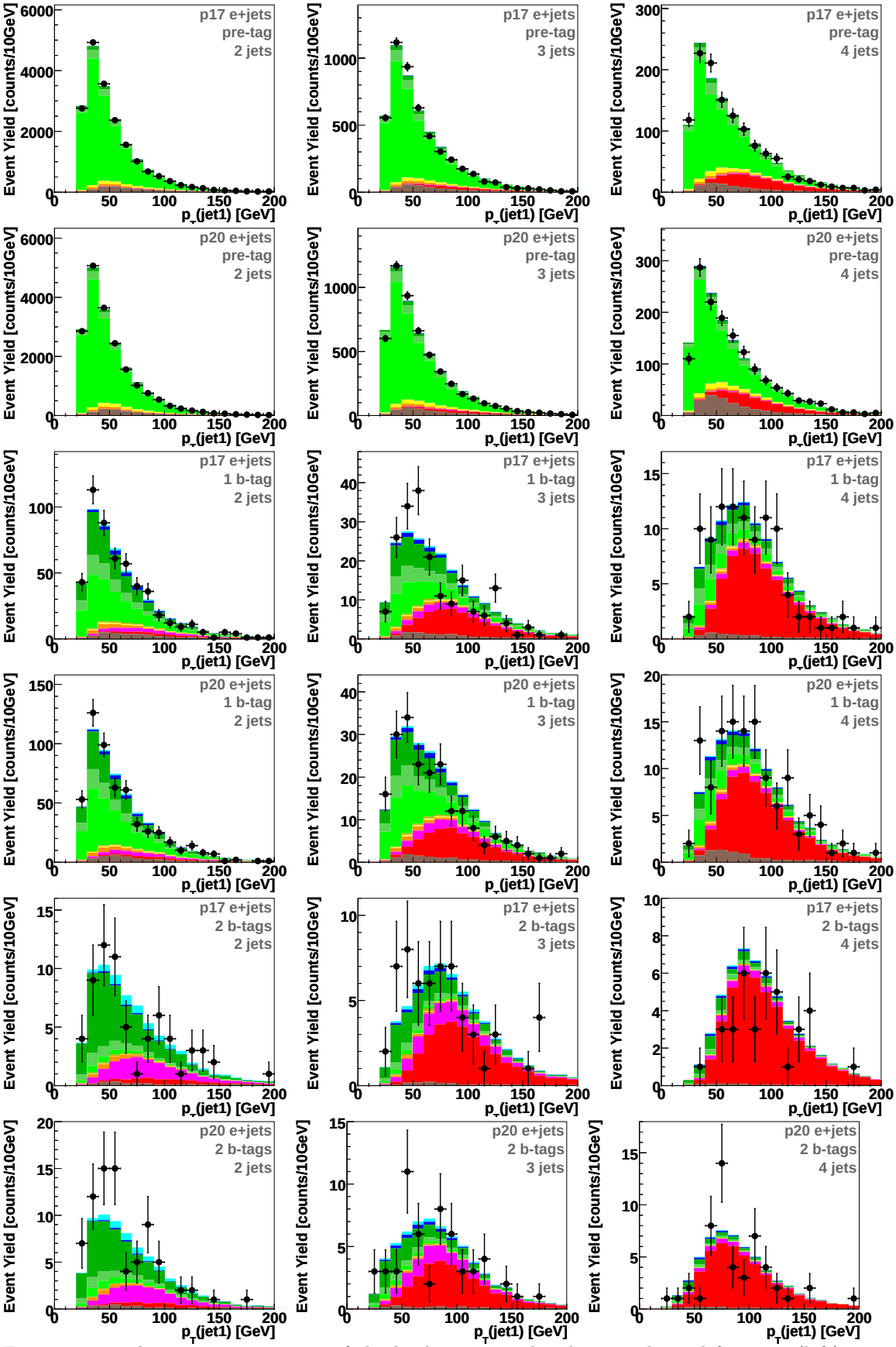

Figure 5.22: The transverse energy of the leading jet in the electron channel for 2-jet (left), 3-jet (middle), and 4-jet events (right), for p17 and p20, pretagged, single-tagged, and double-tagged events.

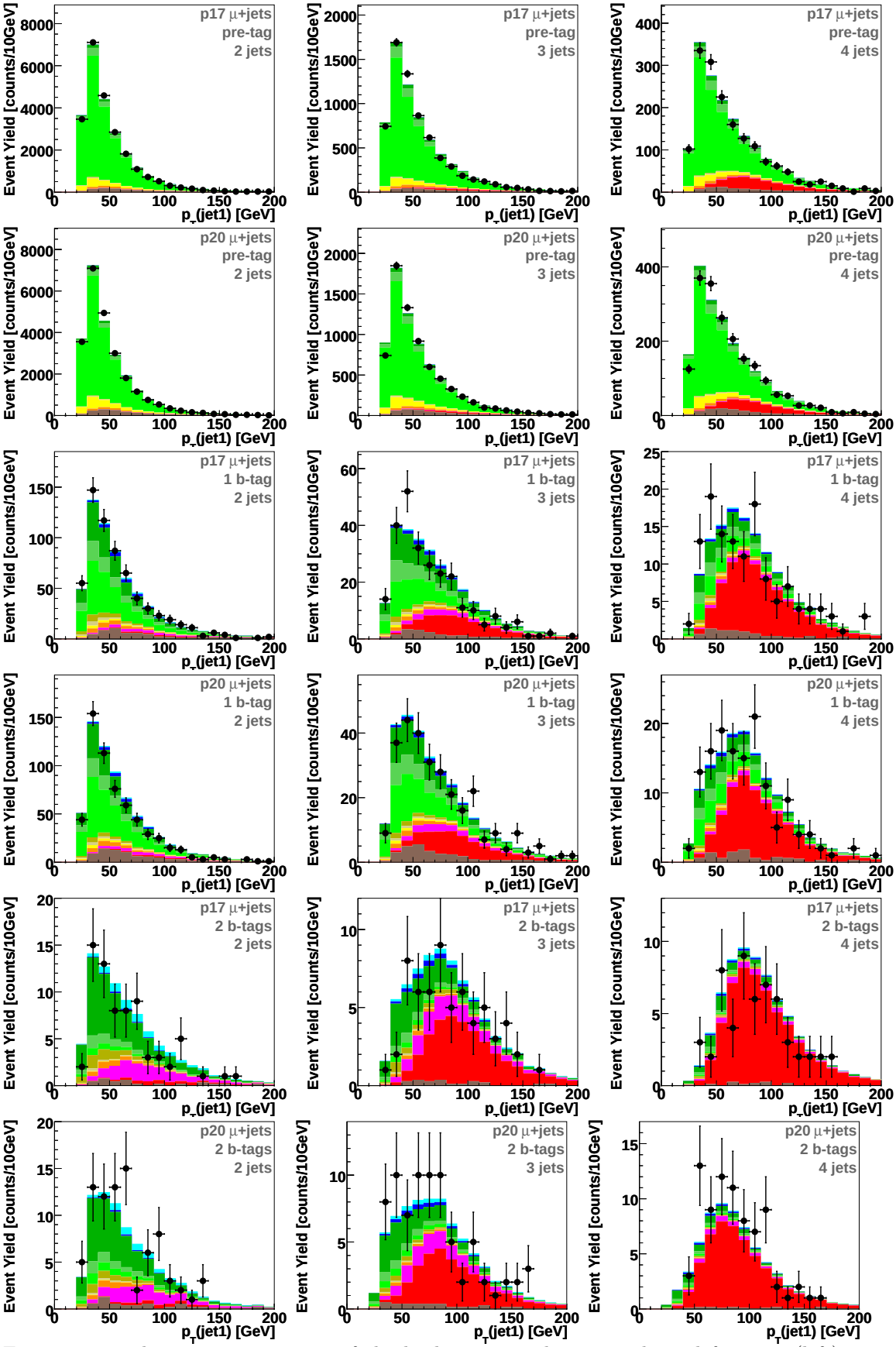

Figure 5.23: The transverse energy of the leading jet in the muon channel for 2-jet (left), 3-jet (middle), and 4-jet events (right), for p17 and p20, pretagged, single-tagged, and double-tagged events.

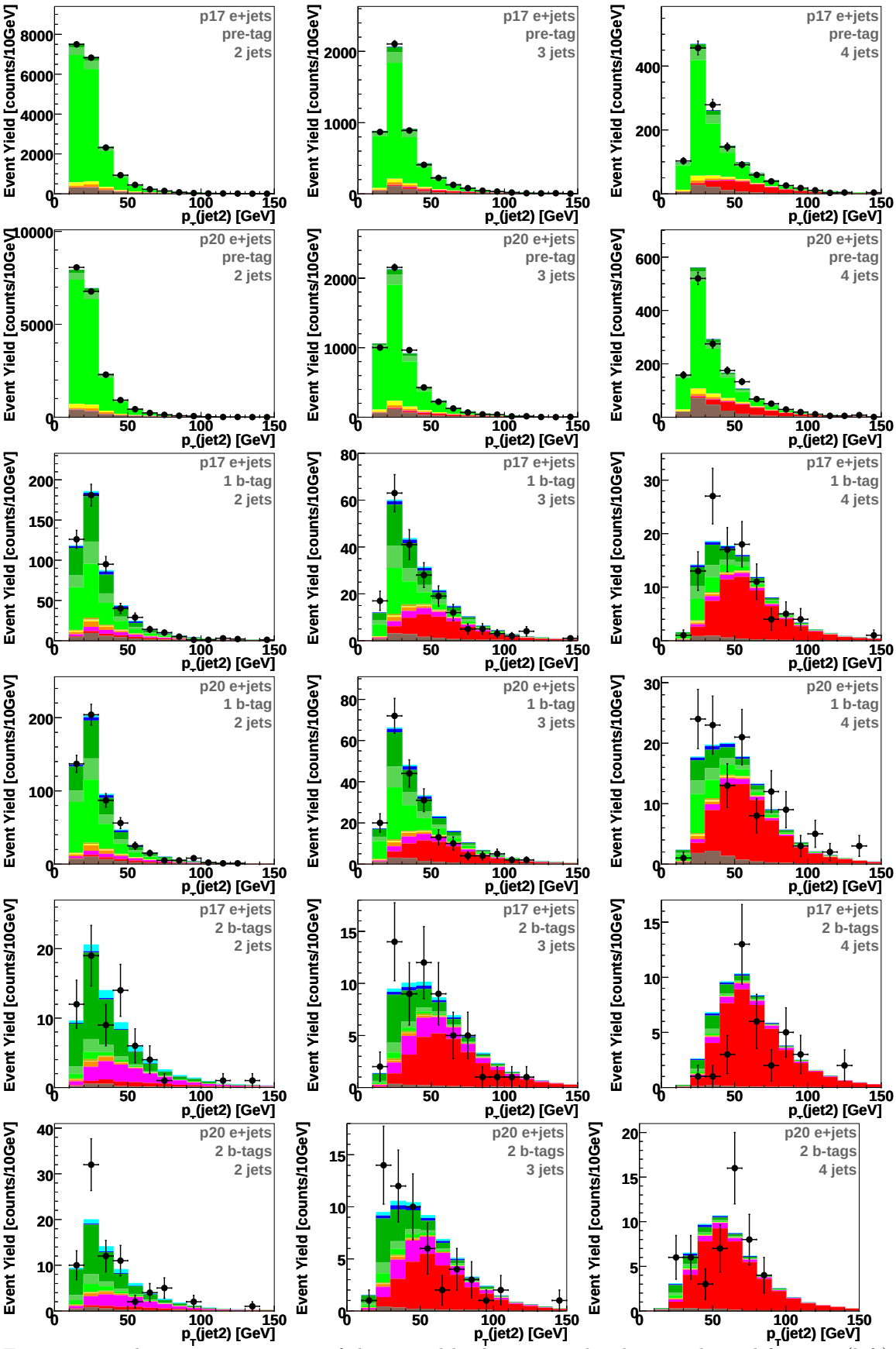

Figure 5.24: The transverse energy of the second leading jet in the electron channel for 2-jet (left), 3-jet (middle), and 4-jet events (right), for p17 and p20, pretagged, single-tagged, and double-tagged events.

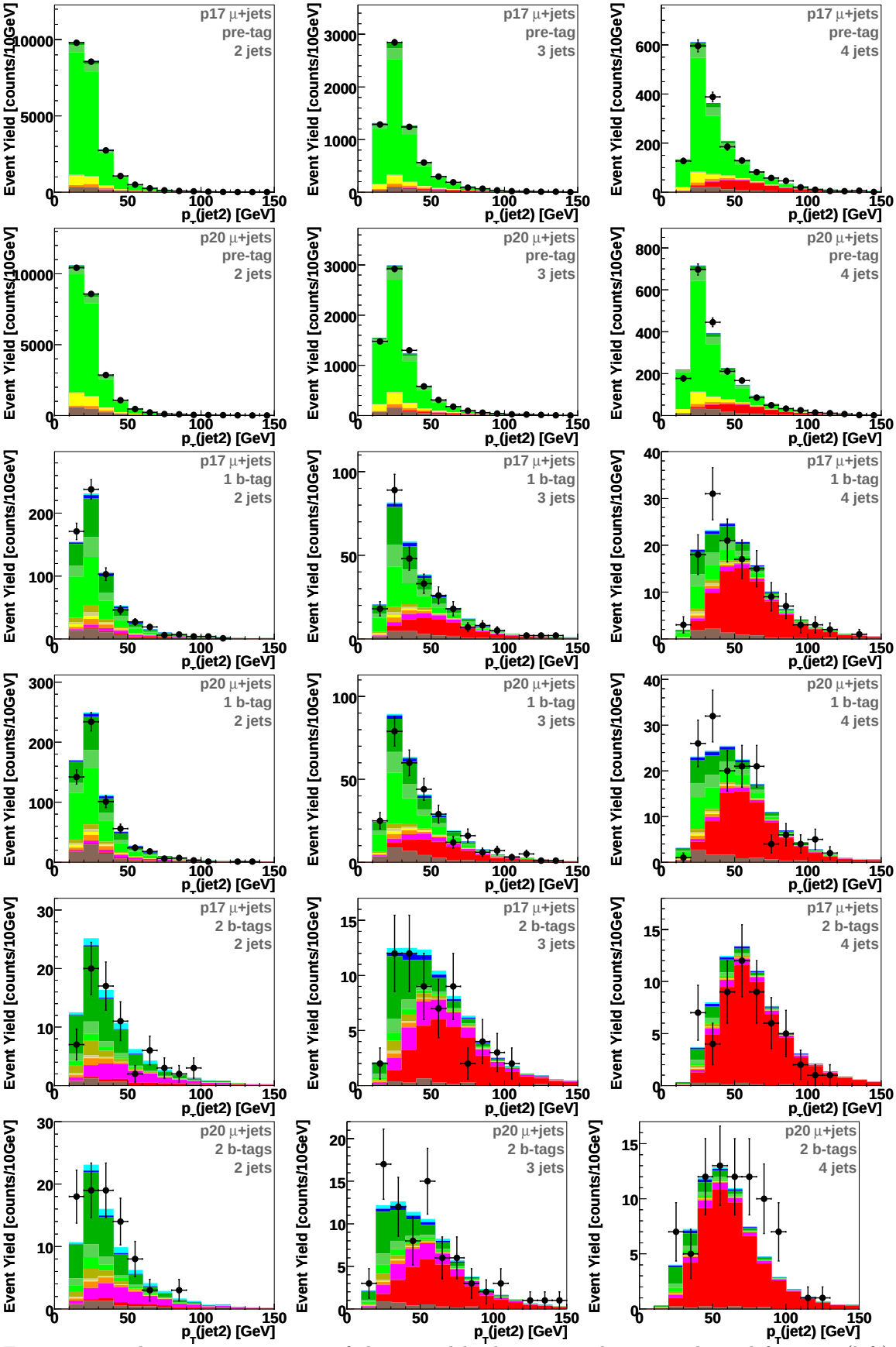

Figure 5.25: The transverse energy of the second leading jet in the muon channel for 2-jet (left), 3-jet (middle), and 4-jet events (right), for p17 and p20, pretagged, single-tagged, and double-tagged events.

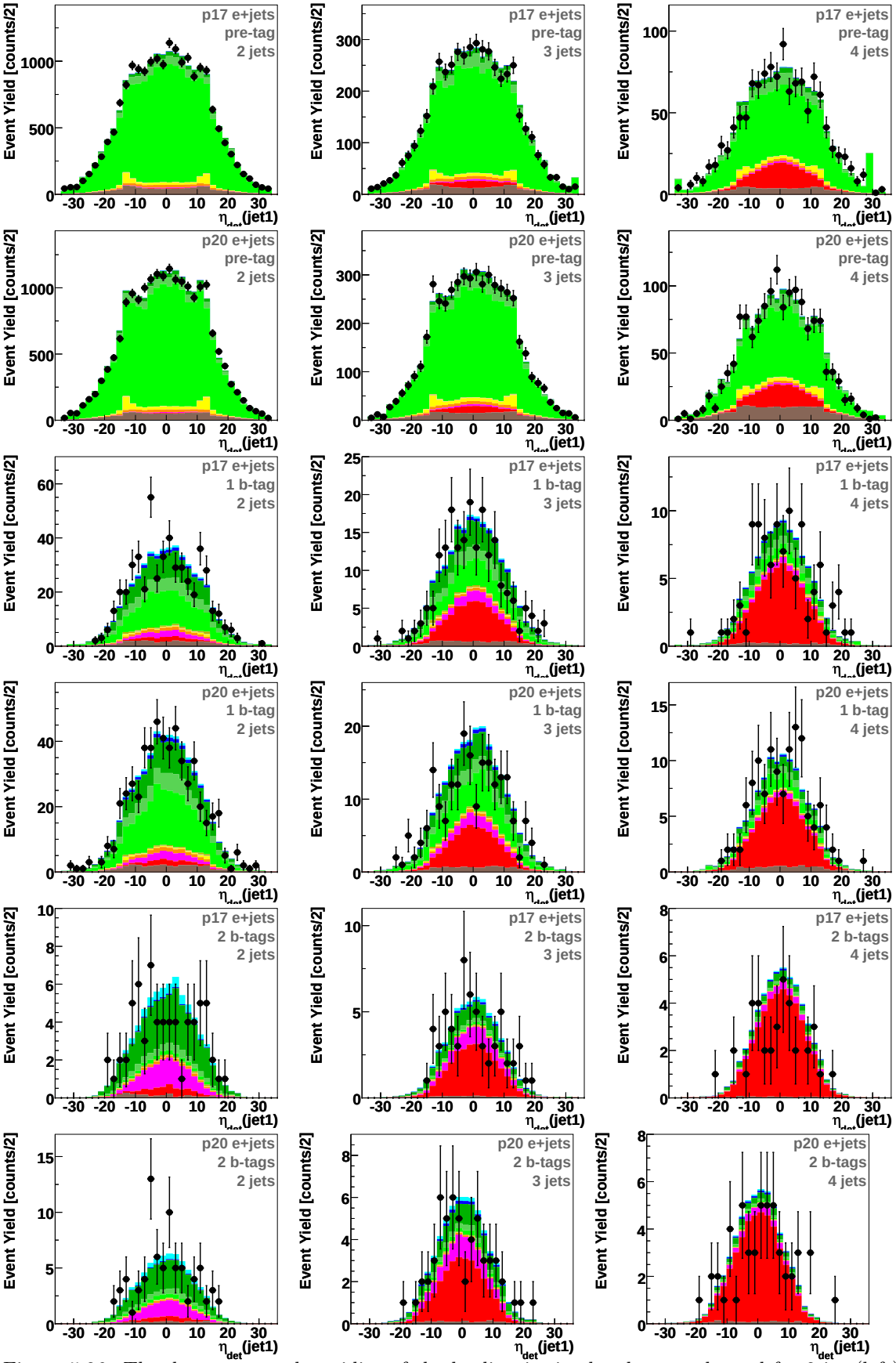

Figure 5.26: The detector pseudorapidity of the leading jet in the electron channel for 2-jet (left), 3-jet (middle), and 4-jet events (right), for p17 and p20, pretagged, single-tagged, and double-tagged events.

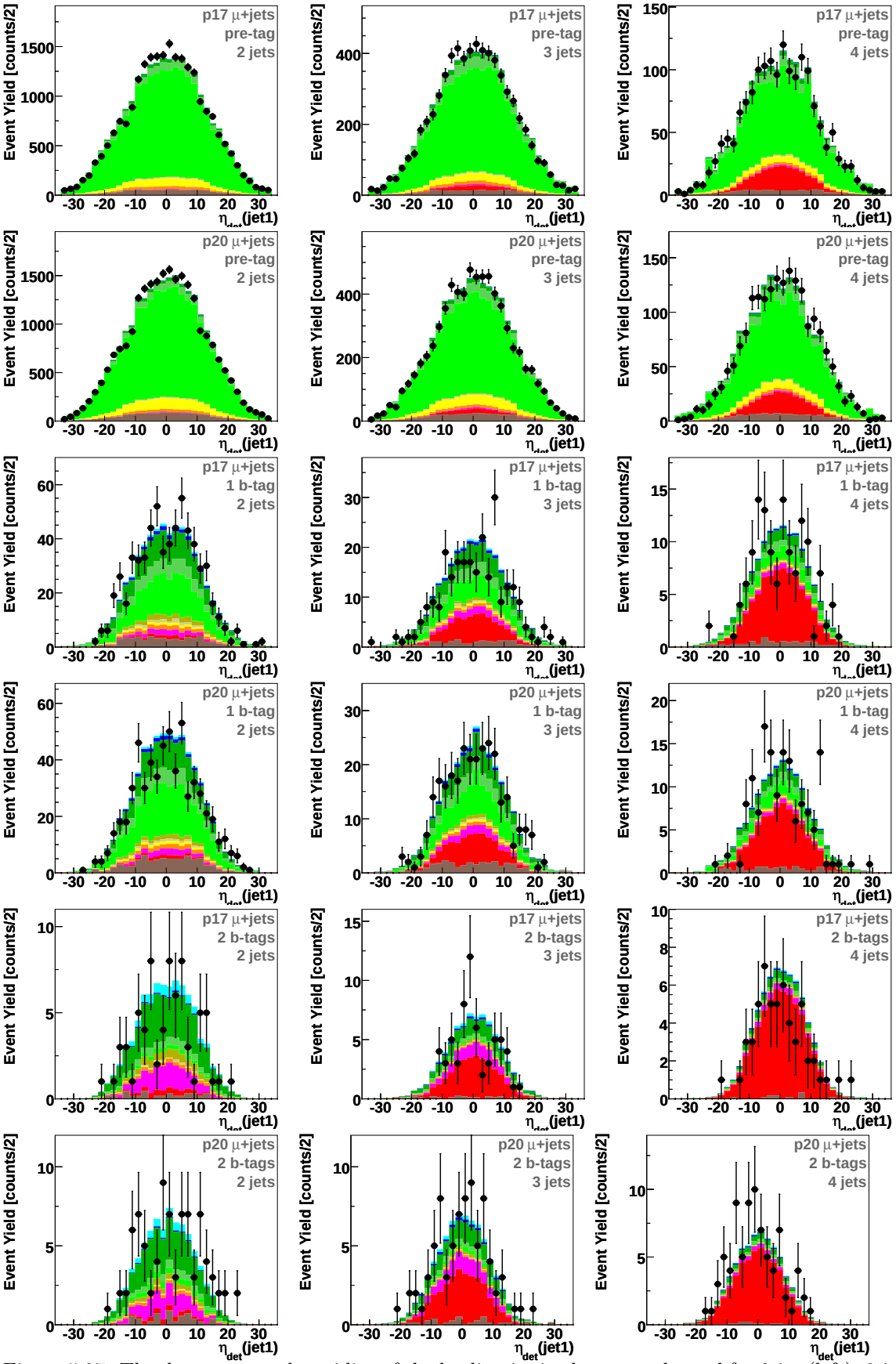

Figure 5.27: The detector pseudorapidity of the leading jet in the muon channel for 2-jet (left), 3-jet (middle), and 4-jet events (right), for p17 and p20, pretagged, single-tagged, and double-tagged events.

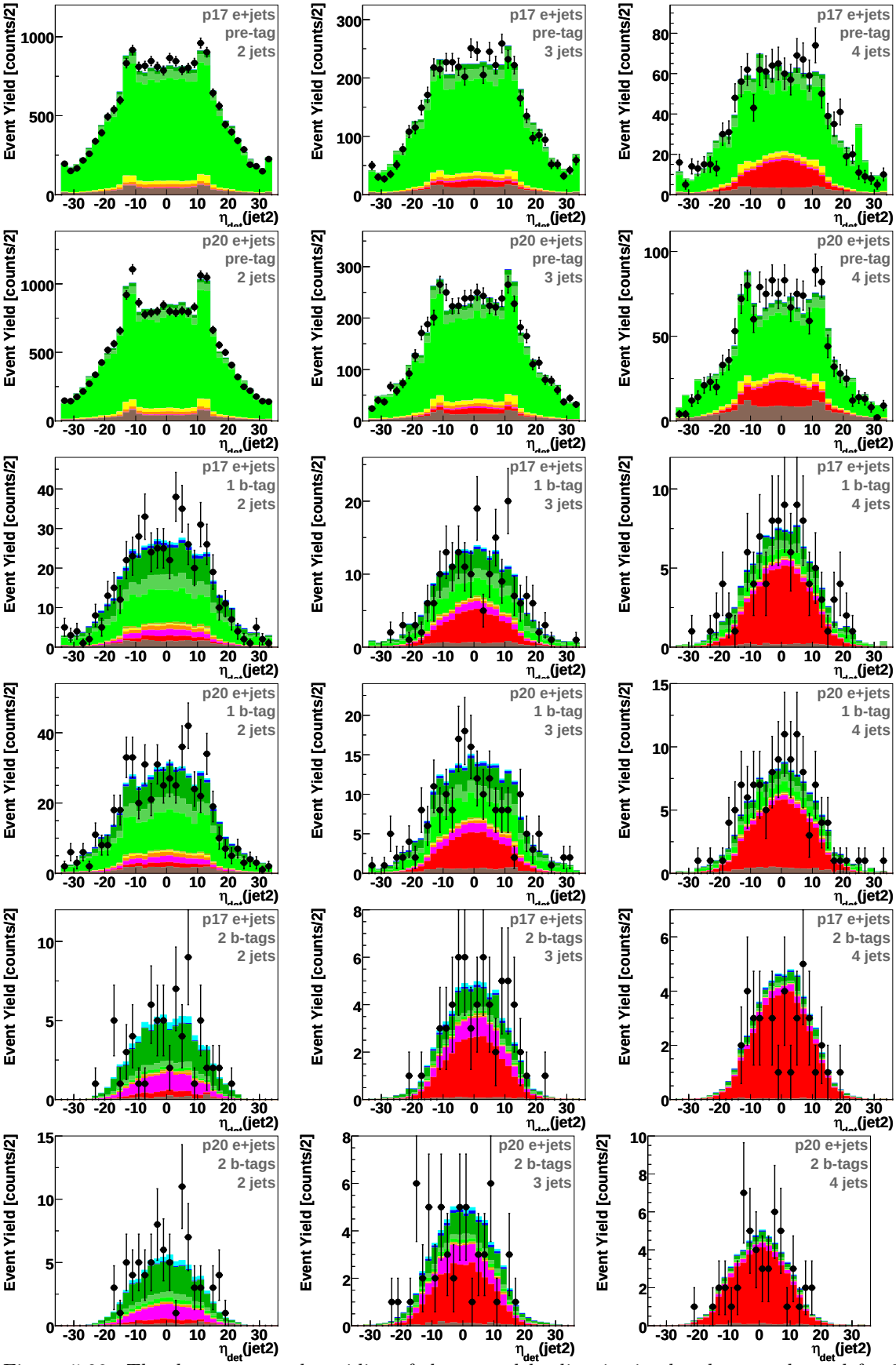

Figure 5.28: The detector pseudorapidity of the second leading jet in the electron channel for 2-jet (left), 3-jet (middle), and 4-jet events (right), for p17 and p20, pretagged, single-tagged, and double-tagged events.

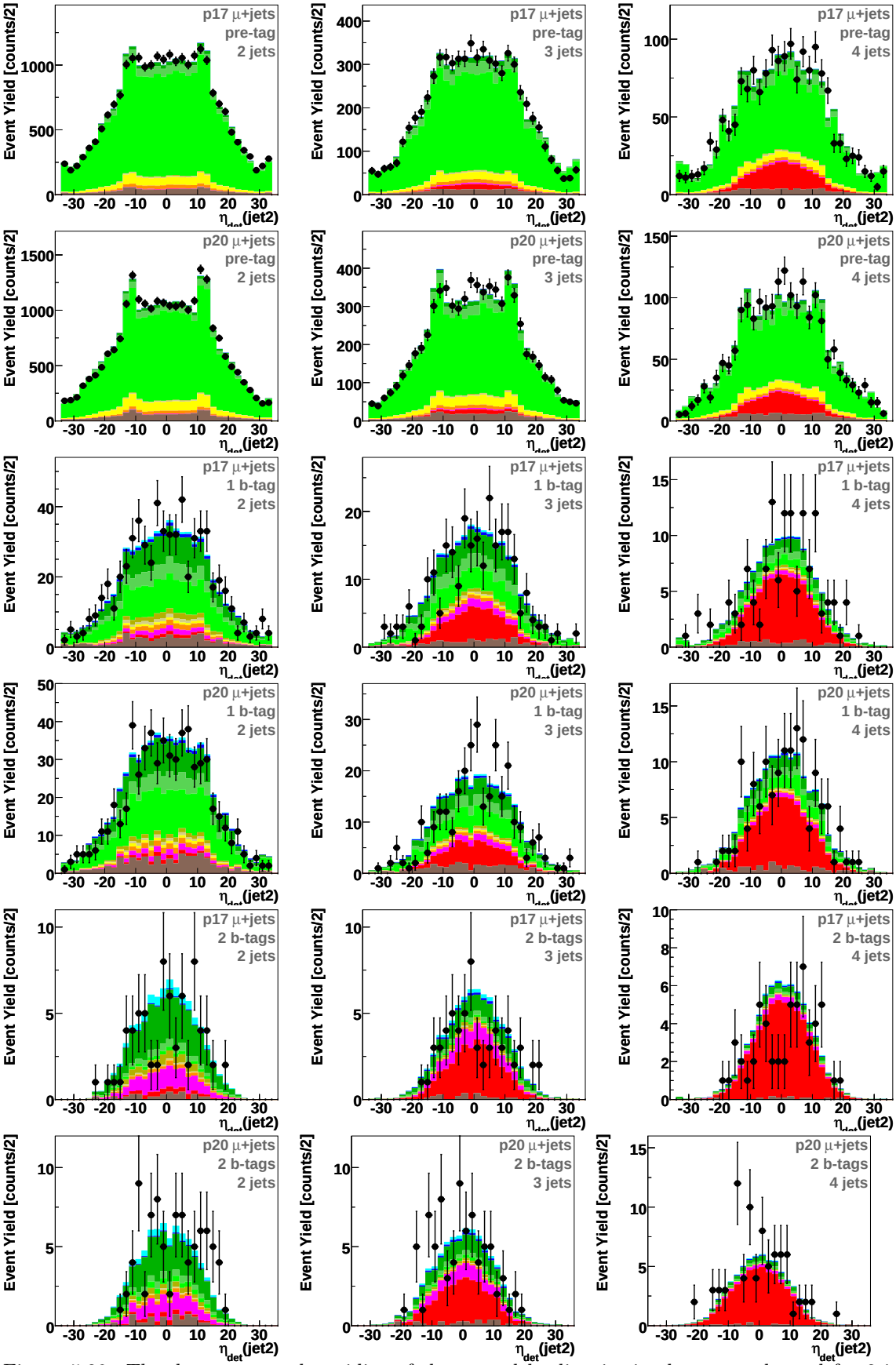

Figure 5.29: The detector pseudorapidity of the second leading jet in the muon channel for 2-jet (left), 3-jet (middle), and 4-jet events (right), for p17 and p20, pretagged, single-tagged, and double-tagged events.

Chapter 6

Matrix Element

Although the event selection cuts and btagging have reduced the S:B, a simple cuts based analysis is still not sensitive enough to measure the cross section of a top quark generated via the electroweak channel. The errors on the background modeling are of the same order as the signal yield. In order to unambiguously separate out the signal from the background, a multivariate technique must be used. A multivariate technique attempts to approximate the discriminant: $\frac{P(S)}{P(S)+P(B)}$. The discriminant optimally separates signal from background and relies on the signal probability density function P(S) and the background probability density function P(B). These probability density functions are approximated using normalized differential cross sections for the signal and background processes. The differential cross sections are found using the matrix element squared, and hence the name of this method is the Matrix Element (ME) Method.

6.1 Overview

For each event, the ME method calculates the probability density function for signal and background processes using the event four-momenta $\vec{x}$. The probability density function is defined as the following:

$$P(\vec{x}) = \frac{1}{\sigma} \times \frac{\partial\sigma}{\partial\vec{x}}. \tag{6.1}$$

where σ is the normalization constant to constrain the probability density functions to a maximum value of 1 and $\partial\sigma$ is the differential cross section which contains the matrix elements. Each part of this equation will be discussed in further detail.

The s- and t-channel discriminant is constructed from the signal and background calculated probability density functions and is defined as follows:

$$D_{tb(tqb)}(\vec{x}) = \frac{P_{tb(tqb)}(\vec{x})}{P_{tb(tqb)}(\vec{x}) + P_B(\vec{x})}. \tag{6.2}$$

where tb refers to the s-channel process, tqb refers to the t-channel process and B refers to a combination of background processes which are weighted based on the background yields. The processes used in the discriminant depend on whether the event is a two or three jet event.

The s-channel and t-channel discriminant is calculated for each reconstruction data set, lepton, b-tag, and jet channel and a cross section is measured using a signal/background reordered discriminant made from the s- and t-channel discriminants.

6.2 Differential Cross Section

The differential cross section, $d\sigma(\vec{x})$, is defined in Eq. 6.3. It is defined as the phase space integration of the differential cross section for hard scatter collisions at the parton level, convoluted with a transfer function that relates the reconstructed objects to the original partons.

$$d\sigma(\vec{x}) = \sum_{i,j} \int d\vec{y} \left[f_i(q_1, Q^2) dq_1 \times f_j(q_2, Q^2) dq_2 \times \frac{\partial\sigma_{hs,ij}(\vec{y})}{\partial\vec{y}} \times W(\vec{x}, \vec{y}) \times \Theta_{\text{Parton}}(\vec{y}) \right] \tag{6.3}$$

where

– $\sum_{i,j}$ is the sum of the initial parton flavors in the hard scatter collision. For example, an s-channel collision can occur via $u\bar{d}$, $c\bar{s}$, $d\bar{u}$, or $s\bar{c}$ annihilation. The third generation is not included as these initial collisions are highly unlikely from the parton distributions of a proton and antiproton.

– $f_i(q, Q^2)$ is the parton distribution function for parton i carrying momentum q, evaluated at the factorization scale Q^2. For W+jets processes, $Q^2 = M_W^2 + \sum_{jets}(M_i^2 + P_{i,T}^2)$ and for top quark processes, $Q^2 = m_t^2$. As for the leading-order parton distribution functions, CTEQ6 [42] is used with LHAPDF as an interface to the code used [60]

– $\partial\sigma_{hs,ij}(\vec{y})/\partial\vec{y}$ is the differential cross section for the hard scatter collision. Using the square of the leading order matrix element [1] , the differential cross section is the following:

$$d\sigma_{hs} = \frac{(2\pi)^4}{4\sqrt{(q_1 q_2)^2 - m_1^2 m_2^2}} |\mathcal{M}|^2 d\Phi_n(\vec{y}) \tag{6.4}$$

where the first term is the flux factor, the second term is the matrix element squared, and the third term is the n-body phase space factor, where $n = 4(5)$ for two-jet (three-jet) events. Madgraph [61] leading-order matrix-element generator provided the matrix elements used for the different signal and background processes.

– $W(\vec{x}, \vec{y})$ is the transfer function which represents the conditional probability of the observed state in the detector ($\vec{x}$) given the original partons ($\vec{y}$).

– $\Theta_{\text{Parton}}(\vec{y})$ represents the parton level cuts applied to avoid singularities in the matrix element evaluation. These cuts are looser than the corresponding cuts at the reconstructed level. All cross sections were calculated with the following parton level cuts:

  * Parton isolation: $\Delta\text{R}(q_i,q_j) > 0.5$
  * Minimum parton P_T: $P_T(q_i) > 6$ GeV
  * Maximum parton pseudorapidity: $|\eta(q_i)| < 3.5$
  * No cuts applied to the lepton or neutrino

– $\int d\vec{y} dq_1 dq_2$ is an integration over the matrix element phase space. The matrix element

phase space for two parton final state events is defined by the 14 independent spatial degrees of freedom for the lepton, neutrino, and two partons as shown in Eq. 6.5

$$d\vec{y}_2 = dq_1 dq_2 d|p|_\ell d\Omega_\ell d|p|_\nu d\Omega_\nu d|p|_{q1} d\Omega_{q1} d|p|_{q2} d\Omega_{q2} \tag{6.5}$$

Events with three partons in the final state have 17 independent degrees of freedom and has a phase space defined in Eq. 6.6.

$$d\vec{y}_3 = dq_1 dq_2 d|p|_\ell d\Omega_\ell d|p|_\nu d\Omega_\nu d|p|_{q1} d\Omega_{q1} d|p|_{q2} d\Omega_{q2} d|p|_{q3} d\Omega_{q3} \tag{6.6}$$

Matrix Element Processes

For events with exactly two jets, we consider a total of nine matrix elements for 2→4 processes (top quark and W bosons are treated off-shell): s-channel single top ($ud{\to}tb$), t-channel single top ($ub{\to}td$), Wbb production ($ud{\to}Wb\bar{b}$), Wcg production ($sg{\to}Wcg$), Wgg production ($ud{\to}Wgg$), ggg production, WW production, WZ production, and $t\bar{t}$ production ($t\bar{t}{\to}\ell\ell$ or $\ell + jets$), where one of the W bosons is lost in order to mimic a two jet event. "tqb" is used sometimes when referring to t-channel events because the main diagram that describes these events is the 2→5 diagram with "tqb" in the final state. This analysis uses a 2→4 diagram with "tq" as the final state, as seen in Fig 6.1, because events with two jets require at most two quarks or gluons in the final state. The three W+jets matrix elements were chosen by running the Madgraph Monte Carlo generator and selecting those processes that gave the largest cross section after an overall b-tagging efficiency was applied. The leading-order diagrams for these channels (displayed as 2→3 processes for simplicity) are shown in Fig. 6.1.

For events with three jets, we consider a total of five matrix elements: s-channel single top ($ud{\to}tbg$), t-channel single top ($ug{\to}tbd$), Wbb production ($ud{\to}Wb\bar{b}g$), $Wugg$ production, and $t\bar{t}$ production. The leading-order diagrams for these channels (displayed as $2{\to}3, 4$ processes for simplicity) are shown in Fig. 6.2.

The matrix elements used in this analysis are also listed in Table 6.1.

The Matrix Elements

Two Jets		Three Jets	
Name	Process	Name	Process
tb	$u\bar{d} \to t\bar{b}$	tbg	$u\bar{d} \to t\bar{b}g$
tq	$ub \to td$	tqg	$ub \to tdg$
	$\bar{d}b \to t\bar{u}$		$\bar{d}b \to t\bar{u}g$
		tqb	$ug \to td\bar{b}$
			$\bar{d}g \to t\bar{u}\bar{b}$
Wbb	$u\bar{d} \to Wb\bar{b}$	$Wbbg$	$u\bar{d} \to Wb\bar{b}g$
Wcg	$\bar{s}g \to W\bar{c}g$	$Wugg$	$\bar{u}g \to W\bar{u}gg$
Wgg	$u\bar{d} \to Wgg$		
WW	$q\bar{q} \to WW$		
WZ	$q\bar{q} \to WZ$		
ggg	$gg \to ggg$		
$t\bar{t}$	$q\bar{q} \to t\bar{t} \to \ell^+\nu b\bar{u}d\bar{b}, l^+\nu bl^-\nu\bar{b}$	$t\bar{t}$	$q\bar{q} \to t\bar{t} \to \ell^+\nu b\bar{u}d\bar{b}$

Table 6.1: The Matrix Elements used in the analysis are given. For simplicity, only the processes that contain a positively-charged lepton in the final state are shown. The charge conjugated processes are also used.

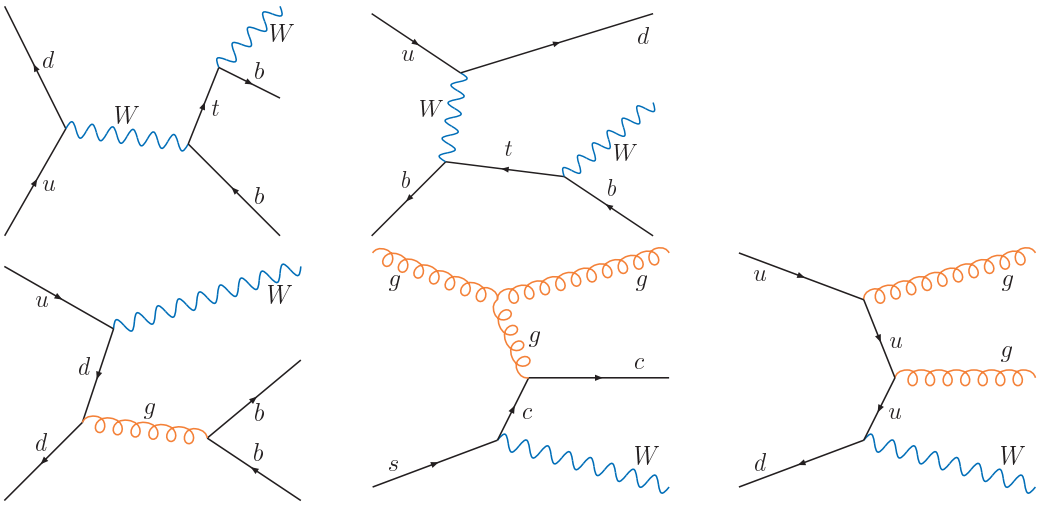

Figure 6.1: Representative Feynman diagrams corresponding to the leading-order matrix elements used for event probability calculation for events with exactly two jets. Upper row, signals: $ud \to tb$, $ub \to td$; lower row, backgrounds: $ud \to Wbb$, $sg \to Wcg$, $ud \to Wgg$.

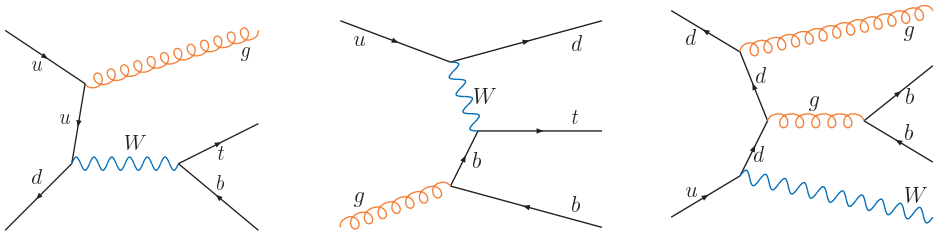

Figure 6.2: Representative Feynman diagrams corresponding to the leading-order matrix elements used for event probability calculation for events with exactly three jets. Left two plots: signals, $ud \to tbg$, $ug \to tbd$; right plot: background, $ud \to Wbbg$.

Transfer Functions

The transfer functions $W(x, y)$ yield the probability for a parton with kinematics $\vec{p_{evt}}$ to be reconstructed with $\vec{p_{fs}}$. It is assumed that $W(x, y)$ can be factorized into individual object transfer functions for electrons, muons, and jets. Thus, the electron, muon, and jets require transfer functions and are derived as described in the subsequent sections for the top mass analysis [62] and applied to the electroweak produced top quark cross section analysis.

Electron Transfer Functions

The electron transfer function [63] is assumed to be a function of the reconstructed energy of the electron, E_{reco}, the parton energy of the electron, E_{parton}, and the production angle with respect to the beam axis, θ:

$$W_e(E_x, E_y) = \frac{1}{\sqrt{2\pi}\sigma}\ \exp\left[-\frac{1}{2}\left(\frac{\mathrm{E_{reco}} - \mathrm{E_{center}}}{\sigma}\right)^2\right] \tag{6.7}$$

where

$$E_{center} = 1.0002E_{parton} + 0.324GeV/c^2 \tag{6.8}$$

$$\sigma = 0.028E_{center} \oplus Sampling(E_{center}, \eta)E_{center} \oplus 0.4 \tag{6.9}$$

$$Sampling(E, \theta) = \left[\frac{0.164}{\sqrt{E}} + \frac{0.122}{E}\right]\ \exp\left[\frac{\mathrm{p1(E)}}{\sin\theta} - \mathrm{p1(E)}\right] \tag{6.10}$$

$$p1(E) = 1.35193 - \frac{2.09564}{E} - \frac{6.98578}{E^2} \tag{6.11}$$

and $\oplus$ means the terms are added in quadrature.

The values were derived using Run IIa MC using $Z \rightarrow ee$ data. This comes from the following equation typically used to describe calorimeter energy resolutions at normal incidence [64]:

$$(\sigma/E)^2 = C^2 + \frac{S^2}{E} + \frac{N^2}{E^2} \tag{6.12}$$

where C is the constant term due to non-uniformities in the response, S is the sampling term due to sampling fluctuations, and N is the noise term that comes from the uranium in the calorimeter, readout electronics, and underlying events. However, this parameterization can be refined to take into account variations in the angle of incidence θ in the sampling term. This is not a complete description for the response of the EM calorimeter. Instead it can be described by

$$\frac{\sigma}{E} = p_0 \times\ \exp\left(-\mathrm{p_1} + \frac{\mathrm{p_1}}{\sin\theta}\right) \tag{6.13}$$

where p_0 is the resolution at normal incidence and is $\left[\frac{0.164}{\sqrt{E}} + \frac{0.122}{E}\right]$.

Muon Transfer Functions

Muon transfer functions [65] [66] are generated from $t\bar{t}$ and $Z \rightarrow \mu\mu$ MC events that are smeared in p_T. The events have the same selection cut as used in the top mass measurement, namely that $p_T \geq 20GeV$, $|\eta| \leq 2.0$, and the distance between the generated and reconstructed muon track is small in order to obtain matching tracks. This last requirement is defined as follows:

$$\Delta R = \sqrt{(\phi(\mu_{evt}) - \phi(\mu_{fs}))^2 + (\eta(\mu_{evt}) - \eta(\mu_{fs}))^2} \leq 0.005 \tag{6.14}$$

The muon resolution is parameterized in terms of the muon charge q and the transverse momentum p_T:

$$\Delta\left(\frac{q}{p_T}\right) = \left(\frac{q}{p_T}\right)_{evt} - \left(\frac{q}{p_T}\right)_{fs} \tag{6.15}$$

since the resolution of the tracking detector depends on the track curvature in the magnetic field which is proportional to q/p_T. A Gaussian fit is applied for different η_{evt} and $(1/p_T)_{evt}$ regions where the σ value of the fit is the muon resolution and is parameterized as follows:

$$W_\mu = \frac{1}{\sqrt{2\pi}\sigma_\mu} \exp\left(-\frac{1}{2}\left(\frac{(\mathrm{q/pt})_{\mathrm{evt}} - (\mathrm{q/pt})_{\mathrm{fs}}}{\sigma_\mu} \right)^2 \right) \tag{6.16}$$

The Gaussian widths are determined for 10×10 bins in η_{evt} and $(1/p_T)_{evt}$. There is a strong η dependence which can be described as follows:

$$\sigma_\mu = \sigma_0 \text{ for } |\eta_{\mathrm{det}}| \leq 1.4 \tag{6.17}$$

$$\sqrt{\sigma_0^2 + [c \cdot (|\eta_{det}| - \eta_0)]^2} \text{ for } |\eta_{\mathrm{det}}| > 1.4 \tag{6.18}$$

where σ_0 is a constant and c is the slope to fit the η dependence. σ_0 and c accounts for the slight dependence of $(1/p_T)_{evt}$ by fitting these terms to the form $a_i + b_i(1/p_T)_{evt}$. Furthermore, the

rise when $\eta_{evt} \geq 1.4$ comes from the fact that tracks can no longer produce hits in all detector layers.

These values are determined for Run IIa and Run IIb events and for muons with and without SMT hits where muons without SMT hits have the additional constraint that the muons must come from the primary vertex. Additionally, Run IIa is divided into pre- and post-shutdown since following the shutdown in 2004, the muon resolution was degraded by about 15% which is partly due to the magnetic field reduction.

Jet Transfer Functions

The jet transfer functions [67] [62] depend on the energy measurement E_x in the detector and the true quark energy E_y:

$$W_{jet} = \frac{1}{\sqrt{2\pi}(p_2 + p_3 p_5)} \left[\exp\left(- \frac{((\mathrm{E_x} - \mathrm{E_y}) - \mathrm{p_1})^2}{2\mathrm{p_2^2}} \right) + \mathrm{p_3} \exp\left(- \frac{((\mathrm{E_x} - \mathrm{E_y}) - \mathrm{p_4})^2}{2\mathrm{p_5^2}} \right) \right] \tag{6.19}$$

The p_i are functions of the quark energy and are parameterized as linear functions:

$$p_i = a_i + E_y \cdot b_i \tag{6.20}$$

The parameters a_i and b_i are determined from events with all jet energy corrections properly applied for nine different values of the top quark mass from 155 to 195 GeV/c^2 in 5 GeV/c^2 increments. For each of the three jet types (light quarks (u,d,s,c), b quarks with a soft muon tag in the associated jet, and all other b quarks) and the four detector regions ($|\eta| < 0.5$, $0.5 < |\eta| < 1.0$, $1.0 < |\eta| < 1.5$, and $1.5 < |\eta| < 2.5$), parameters a_i and b_i are determined by minimizing the logarithm of the likelihood function:

$$L = \prod_{i=1}^{N_{events}} W_{jet} \tag{6.21}$$

Integration Details

Four (six) degrees of freedom are removed from the integration for two (three) parton event by assuming equal angles for partons and jets. Two more degrees of freedom are removed by assuming well measured lepton angles. Four more degrees of freedom are removed from the integration by energy-momentum conservation, leaving four integration variables. The final integration phase space is then transformed to suit the matrix element being integrated. For two jet events, the phase space used for the different matrix elements are defined as follows: for W+jets matrix element, Eq. 6.22; for diboson matrix element integrations, Eq. 6.23; for $t\bar{t}$ matrix elements, Eq. 6.24, and for s-channel and t-channel processes, termed singletop, Eq. 6.25.

$$d\vec{y}_{\mathrm{W+jets-2jets}} = dr_W d|p_{q1}|d|p_{q2}|dp_z^{system} \tag{6.22}$$

$$\begin{aligned} d\vec{y}_{\mathrm{WW-2jets}} &= dr_W dr_W d|p_{q2}|dp_z^{system} \\ d\vec{y}_{\mathrm{WZ-2jets}} &= dr_W dr_Z d|p_{q2}|dp_z^{system} \end{aligned} \tag{6.23}$$

$$d\vec{y}_{\mathrm{ttbar-2jets}} = dr_{\mathrm{top}} dr_W dr_{\mathrm{top}} d|p_{q2}|dp_z^{system} \tag{6.24}$$

$$d\vec{y}_{\mathrm{singletop-2jets}} = dr_{\mathrm{top}} dr_W d|p_{q2}|dp_z^{system} \tag{6.25}$$

As for three jet events, the phase space is shown in Eq. 6.26 for W+jets matrix elements, in Eq. 6.27 for $t\bar{t}$ matrix elements, and in Eq. 6.28 for singletop matrix elements.

$$d\vec{y}_{\mathrm{W+jets-3jets}} = dr_W d|p_{q1}|d|p_{q2}|d|p_{q3}|dp_z^{system} \tag{6.26}$$

$$d\vec{y}_{\mathrm{ttbar-3jets}} = dr_{\mathrm{top}} dr_W dr_{\mathrm{top}}|d|p_{q3}|dp_z^{system} \tag{6.27}$$

$$d\vec{y}_{\mathrm{singletop-3jets}} = dr_{\mathrm{top}} dr_W d|p_{q2}|d|p_{q3}|dp_z^{system} \tag{6.28}$$

Here, dr_W, dr_Z and dr_{top} are used to uniformly sample a Breit-Wigner distribution from the square of the invariant mass distribution for W boson, Z boson, and top quark production, respectively. This choice of sampling minimizes integration time because the matrix elements for these processes are negligible in regions where the invariant mass of the lepton and neutrino is far from the W mass, for the Z events, the invariant mass of two jets is far from the Z mass, and similarly for top events where the mass of the lepton, neutrino, and b-quark is far from the top mass. Thus, by sampling near these resonances, the integration converges faster as points that contribute heavily to the integration are sampled more frequently. The multidimensional integrals are calculated using the GNU [68] Scientific Library's version of the VEGAS Monte Carlo integration technique [69]. where VEGAS outputs the four or six sampled numbers based on the remapping of the phase space outlined above. For each differential cross section, this integration through VEGAS is done twice and must be within the limits and error set by the settings of the integration. Otherwise VEGAS is rerun with more sampling points. From these numbers, the values are converted to get the final parton 4 vectors, taking into account the transfer functions which converts the reconstructed vectors to the parton vectors. The initial parton is then computed and all the components of the differential cross section can be solved.

Treatment of Combinatorial Background

Since the reconstructed jets cannot be accurately assigned to the parton from the matrix element, all possible assignments must be used. The event differential cross section is modified as shown in Eq. 6.29:

$$\begin{aligned} d\sigma(\ell, j_1, j_2) &= \alpha_{j_1 \to p_1} \alpha_{j_2 \to p_2} d\sigma(\ell, j_1 \to p_1, j_2 \to p_2) + \\ &+ \alpha_{j_2 \to p_1} \alpha_{j_1 \to p_2} d\sigma(\ell, j_2 \to p_1, j_1 \to p_2) \end{aligned} \tag{6.29}$$

where the α parameters relate to the probability of the jet-parton match. The neural network b tagger [58] [59] , described in the previous chapter, gives the probability for a jet-parton match. The α weights use the jet tag-rate functions for the different hypothesized jet flavors (b, c and light), as shown in Table 6.2, and are parametrized in terms of jet P_T and η: $\varepsilon_{\text{flavor}}(j) = \varepsilon_{\text{flavor}}(P_T(j), \eta(j))$.

Jet-Parton Matching Weight Factors

Parton flavor	b tagged	Not tagged
b	ε_b	$1 - \varepsilon_b$
c	ε_c	$1 - \varepsilon_c$
light	ε_l	$1 - \varepsilon_l$

Table 6.2: Weights for the event differential cross section depending on the b-tagging status of the jet and jet-parton assignment.

For example, a two-jet event with j_1 tagged and j_2 not tagged, the differential cross section for the Wcg process is given by the following:

$$\begin{aligned} d\sigma_{Wcg}(\ell, j_1, j_2) &= \varepsilon_c(j_1)(1 - \varepsilon_l(j_2))d\sigma_{Wcg}(\ell, j_1 \to c, j_2 \to g) + \\ &+ \varepsilon_l(j_2))(1 - \varepsilon_c(j_1))d\sigma_{Wcg}(\ell, j_2 \to c, j_1 \to g). \end{aligned} \tag{6.30}$$

This differential cross section must then be integrated for both cases where the j_1 and j_2 are assigned to either the c-quark or the gluon.

6.2.1 Cross Section

The normalization constant σ is the detector level phase space integration $\int d\vec{x}$ of the differential cross section defined in Eq. 6.3 and limits the maximum values of the probability density functions to 1.

$$\sigma = \sum_{i,j} \int d\vec{x} d\vec{y} \left[\frac{\partial \sigma_{i,j}(\vec{y})}{\partial \vec{y}} \times W(\vec{x}, \vec{y}) \times \Theta_{\text{cuts}}(\vec{x}) \right] \tag{6.31}$$

The integral has 13 dimensions for two-jet events, 17 dimensions for three-jet events other than $t\bar{t}$, and 20 dimensions for $t\bar{t}$ but only needs to be calculated once. The term $\Theta_{\text{cuts}}(\vec{x})$ is included in the calculation to simulate the selection cuts which are the following for all cross sections:

- Lepton $p_T > 15$ GeV
- Electron (muon) $|\eta| < 1.1(2.0)$
- $\not\!\!E_T > 15$ GeV
- Leading jet $p_T > 25$ GeV
- Leading jet $|\eta| < 2.5$
- Second jet $p_T > 20$ GeV
- Second jet $|\eta| < 3.5$
- Third jet $p_T > 20$ GeV (if three-jet event)
- Third jet $|\eta| < 3.5$ (if three-jet event)

Although these cuts slightly differ from the selection cuts in the previous chapter, the cuts included in the normalization calculation approximate the relative acceptance difference between signal and background events. In all instances, the statistical uncertainty from the Monte Carlo integration is below 1%.

6.2.2 Single Top Discriminant

Discriminant Definition

The channel-specific discriminants are defined as:

$$D_{tb(tqb)}(\vec{x}) = \frac{P_{tb(tqb)}(\vec{x})}{P_{tb(tqb)}(\vec{x}) + P_B(\vec{x})}. \tag{6.32}$$

where tqb here generically refers to the t-channel process, whether based on the tq matrix elements (two-jet events) or the tqb matrix elements (three-jet events).

For two-jet events, the background probability density function $P_B(\vec{x})$ is given by:

$$\begin{aligned} P_B(\vec{x}) &= C_{Wbb}P_{Wbb}(\vec{x}) + C_{Wcg}P_{Wcg}(\vec{x}) + C_{Wgg}P_{Wgg}(\vec{x}) \\ &+ C_{WW}P_{WW}(\vec{x}) + C_{WZ}P_{WZ}(\vec{x}) + C_{ggg}P_{ggg}(\vec{x}) + C_{t\bar{t}}P_{t\bar{t}}(\vec{x}), \end{aligned} \tag{6.33}$$

where C_{Wbb}, C_{Wcg}, C_{Wgg} , C_{WW}, C_{WZ}, C_{ggg}, and $C_{t\bar{t}}$ are the relative fractions of each background in the data. The relative fractions are determined based on the expected yields as follows for each reconstructed data, lepton, tag, and jet set:

$$C_{Wbb} = \frac{y_{wbb}}{\text{tot}} + \frac{y_{ttbar}}{2 \times 6\text{tot}} \tag{6.34}$$

$$C_{Wcg} = \frac{y_{wcc}}{\text{tot}} + \frac{y_{ttbar}}{2 \times 6\text{tot}} \tag{6.35}$$

$$C_{Wgg} = \frac{y_{wlp}}{\text{tot}} + \frac{y_{ttbar}}{2 \times 6\text{tot}} \tag{6.36}$$

$$C_{WW} = \frac{y_{diboson}}{2\text{tot}} + \frac{y_{ttbar}}{2 \times 6\text{tot}} \tag{6.37}$$

$$C_{WZ} = \frac{y_{diboson}}{2\text{tot}} + \frac{y_{ttbar}}{2 \times 6\text{tot}} \tag{6.38}$$

$$C_{ggg} = \frac{y_{qcd}}{\text{tot}} + \frac{y_{ttbar}}{2 \times 6\text{tot}} \tag{6.39}$$

$$C_{t\bar{t}} = \frac{y_{ttbar}}{2\text{tot}} \tag{6.40}$$

where y_{sample} is the yield for a specific background sample and tot is the total background yield for the specific reconstructed data, lepton, tag, and jet set. These coefficients are listed in Tables 6.3.

For the three-jet analysis, the background probability density function $P_B(\vec{x})$ is given by:

$$P_B(\vec{x}) = C_{Wbbg}P_{Wbbg}(\vec{x}) + C_{Wugg}P_{Wugg}(\vec{x}) + C_{t\bar{t}}P_{t\bar{t}}(\vec{x}), \tag{6.41}$$

and C_{Wbbg}, C_{Wugg}, $C_{tt\bar{b}}$, is calculated in the same manner using the expected yields as follows

Optimized Background Fractions

	Run IIa Events				Run IIb Events			
	1 tag		2 tags		1 tag		2 tags	
	Electron	Muon	Electron	Muon	Electron	Muon	Electron	Muon
C_{Wbb}	0.31	0.30	0.56	0.57	0.26	0.26	0.51	0.51
C_{Wcg}	0.15	0.16	0.10	0.11	0.14	0.14	0.11	0.11
C_{Wgg}	0.38	0.37	0.07	0.07	0.44	0.41	0.10	0.10
C_{WW}	0.025	0.02	0.04	0.04	0.025	0.02	0.04	0.04
C_{WZ}	0.025	0.02	0.04	0.04	0.025	0.02	0.04	0.04
C_{ggg}	0.07	0.10	0.05	0.06	0.07	0.12	0.06	0.09
$C_{t\bar{t}}$	0.04	0.03	0.14	0.11	0.04	0.03	0.14	0.11

Table 6.3: Background fractions chosen for each analysis channel in two-jet events.

for each reconstructed data, lepton, tag, and jet set:

$$C_{Wbbg} = \frac{y_{wbb}}{\text{tot}} \tag{6.42}$$

$$C_{tt\bar{b}} = \frac{y_{ttbar}}{\text{tot}} \tag{6.43}$$

$$C_{Wugg} = \frac{y_{wlp} + y_{qcd} + y_{diboson} + y_{wcc}}{\text{tot}} \tag{6.44}$$

where y_{sample} is the yield for a specific background sample and tot is the total background yield for the specific reconstructed data, lepton, tag, and jet set. These coefficients for the 3 jet events are listed in Tables 6.4.

Optimized Background Fractions

	Run IIa Events				Run IIb Events			
	1 tag		2 tags		1 tag		2 tags	
	Electron	Muon	Electron	Muon	Electron	Muon	Electron	Muon
C_{Wbbg}	0.23	0.25	0.23	0.26	0.20	0.21	0.22	0.24
$C_{t\bar{t}}$	0.33	0.27	0.66	0.61	0.33	0.25	0.64	0.58
C_{Wugg}	0.44	0.48	0.11	0.13	0.47	0.54	0.14	0.18

Table 6.4: Background fractions chosen for each analysis channel in three-jet events.

Discriminant Binning

For each event, two discriminant values are computed: (tb) and (tqb) discriminants. A two-dimensional histogram of these two discriminants is formed, and then converted to the final

one-dimensional (1D) discriminant which is used as input to measure the cross section which will be discussed in further detail in the next chapter. The *tb* and *tqb* discriminants can be found in Appendix B. The following procedure is applied to each one of the 16 channels, based on data reconstruction version, lepton flavor, jet multiplicity, and tag multiplicity independently. The *tb* and *tqb* discriminants are filled into a 2D histogram with 40 bins on the *tqb* axis and 20 bins on the *tb* axis. This is done for the signal and sum of all the backgrounds for the channel under consideration. For each of the 20 *tb* discriminant bins, the *tqb* discriminant is re-binned, starting from high discriminant values to lower ones, into variable size bins such that in each bin the (total background)^2/(error on background)^2 ≥ 4. This ensures that there are enough entries in each bin of the new rebinned 2D discriminant histogram. The N_{2D} bins of the rebinned 2D discriminant are then reordered according to signal:background ratio (s/b) into a 1D histogram with range [0, 1] and N_{1D}=800 bins. The bin in the 2D plane with highest value of s/b is assigned to bin N_{1D} which has the largest discriminant value in the 1D histogram. The ordering proceeds with the bin with the next lower s/b in the 2D plane being assigned to bin $N_{1D} - 1$ and so on, filling contiguous bins from right to the left of the histogram until all bins of the rebinned 2D histograms are mapped onto the 1D array. This 1D array is then re-binned to have 50 bins between [0,1].

Next, a cut on the value of H_T(alljets,lepton,$\not\!\!E_T$) is used to create two distinct sets of the 1D discriminants, one for events with H_T(alljets,lepton,$\not\!\!E_T$)$>$ 175 GeV and the other for events with H_T(alljets,lepton,$\not\!\!E_T$)$<$ 175 GeV. The value of the cut at 175 is based on optimization studies of expected sensitivity which can be found in the next section. The set with lower H_T values populates the region [0,1] of the 1D array with 50 bins, while the higher H_T value set populates the region [1,2] of the 1D array with another 50 bins. The yields for each H_T can be found in Tables 6.5 through 6.8. This final 1D discriminant histogram, mapped into two H_T regions, is provided as the input for the cross section measurement described in the next chapter. The normalized 1D histograms showing the final discriminant shapes for some background samples compared to the *tb*+*tqb* signal are shown in Figs 6.2.2 through 6.6. The

spikes in these histograms with all channels combined arise because the individual channels populate different numbers of bins. This is apparent from the final 1D discriminant histograms which can be found in Appendix C. It is important to note that we combine all channels for illustration purposes only and at no point is a discriminant spectrum used that was obtained by combining 1D discriminant spectra with different number of bins. The discriminant performance plots are shown in Figs. 6.2.2 and 6.2.2. Those for individual channels can be found in Appendix D. All these plots use the color code defined earlier.

Single-Tagged Event Yields with H_T(alljets,lepton,$\not\!\!E_T$)< 175 GeV

	Run IIa				Run IIb			
	Electron Channel		Muon Channel		Electron Channel		Muon Channel	
	2 jets	3 jets	2 jets	3 jets	2 jets	3 jets	2 jets	3 jets
Signals								
tb	2.5	0.3	3.0	0.4	2.7	0.3	2.7	0.4
tqb	6.0	0.8	7.1	1.1	5.9	0.8	6.6	1.1
tb+tqb	8.5	1.1	10.1	1.5	8.6	1.1	9.3	1.5
Backgrounds								
t→ll	2.6	0.4	2.7	0.5	2.9	0.4	2.8	0.6
t→l+jets	1.4	0.5	0.9	0.7	1.5	0.7	0.9	0.5
$Wb\bar{b}$	78.2	10.6	87.9	16.3	76.0	11.3	80.3	15.0
$Wc\bar{c}$	37.6	6.2	44.4	9.6	40.2	7.1	44.1	9.3
Wjj	106.9	13.6	125.7	20.5	133.6	20.8	148.6	25.0
$Zb\bar{b}$	2.5	0.4	15.2	1.9	2.3	0.3	11.5	1.8
$Zc\bar{c}$	1.4	0.1	7.6	1.0	0.9	0.2	6.0	1.1
Zjj	2.7	0.4	6.7	1.1	2.9	0.5	7.4	1.3
Dibosons	8.4	1.0	12.4	1.8	9.1	1.3	12.4	2.0
Multijets	15.8	3.0	31.1	6.8	18.3	3.3	48.1	12.0
Background Sum	257.3	36.3	334.5	60.2	287.7	45.9	362.0	68.6
Bkgds+Signals	265.8	37.4	344.6	61.7	296.3	47.0	371.3	70.1
Data	289	52	358	73	320	52	344	54

Table 6.5: Yields for events with exactly one b-tagged jet and H_T(alljets,lepton,$\not\!\!E_T$)< 175 GeV.

Single-Tagged Event Yields with H_T(alljets,lepton,$\not\!\!E_T$)> 175 GeV

	Run IIa				Run IIb			
	Electron Channel		Muon Channel		Electron Channel		Muon Channel	
	2 jets	3 jets	2 jets	3 jets	2 jets	3 jets	2 jets	3 jets
Signals								
tb	6.5	2.8	7.2	3.5	6.7	3.0	7.2	3.9
tqb	11.3	5.8	13.4	7.5	11.0	6.4	11.8	7.6
tb+tqb	17.9	8.7	20.6	11.0	17.8	9.5	19.1	11.5
Backgrounds								
t→ll	21.0	13.8	19.4	15.1	22.7	15.7	20.7	16.5
t→l+jets	15.0	51.5	11.6	53.6	14.9	53.0	11.3	53.1
$Wb\bar{b}$	57.2	33.6	58.5	16.3	53.5	33.0	55.7	38.4
$Wc\bar{c}$	28.3	18.6	29.5	40.8	28.4	19.2	28.3	23.3
Wjj	65.0	32.4	73.4	39.7	87.0	40.4	91.7	51.2
$Zb\bar{b}$	4.0	2.4	11.6	6.0	2.7	2.0	8.6	5.8
$Zc\bar{c}$	1.4	1.0	5.7	3.6	1.2	0.9	4.7	3.2
Zjj	2.8	1.3	6.0	3.1	3.0	1.6	6.6	3.7
Dibosons	7.8	4.2	10.0	6.0	8.3	4.5	10.3	6.4
Multijets	12.2	7.3	20.4	10.4	12.7	6.8	25.4	16.3
Background Sum	214.8	166.1	246.2	202.2	234.5	177.3	263.2	217.9
Bkgds+Signals	232.7	174.8	266.8	213.2	252.3	187.8	282.3	229.4
Data	219	150	269	186	227	155	251	236

Table 6.6: Yields for events with exactly one b-tagged jet and H_T(alljets,lepton,$\not\!\!E_T$)> 175 GeV.

Double-Tagged Event Yields with H_T(alljets,lepton,$\not\!\!E_T$)< 175 GeV

	Run IIa				Run IIb			
	Electron Channel		Muon Channel		Electron Channel		Muon Channel	
	2 jets	3 jets	2 jets	3 jets	2 jets	3 jets	2 jets	3 jets
Signals								
tb	1.1	0.1	1.4	0.2	1.1	0.1	1.1	0.1
tqb	0.3	0.1	0.3	0.2	0.3	0.1	0.3	0.2
tb+tqb	1.4	0.2	1.7	0.4	1.4	0.2	1.4	0.3
Backgrounds								
t→ll	1.1	0.2	1.2	0.3	1.1	0.1	1.0	0.2
t→l+jets	0.2	0.2	0.1	0.2	0.3	0.2	0.2	0.2
$Wb\bar{b}$	16.6	2.7	18.6	3.7	15.6	2.7	15.7	3.5
$Wc\bar{c}$	2.6	0.6	3.1	0.9	3.0	0.7	3.0	0.9
Wjj	1.6	0.4	1.8	0.6	2.5	0.6	2.8	0.8
$Zb\bar{b}$	0.3	0.1	3.1	0.5	0.2	0.1	2.0	0.4
$Zc\bar{c}$	0.1	0.01	0.5	0.1	0.1	0.02	0.5	0.1
Zjj	0.1	0.01	0.1	0.04	0.1	0.02	0.2	0.1
Dibosons	0.9	0.1	1.6	0.2	1.0	0.1	1.4	0.2
Multijets	0.8	0.3	2.1	0.3	1.3	0.4	2.6	1.1
Background Sum	24.3	4.6	32.3	6.8	25.0	5.0	29.3	7.5
Bkgds+Signals	25.7	4.8	34.0	7.2	26.4	5.2	30.7	7.8
Data	26	7	29	6	36	8	37	10

Table 6.7: Yields for events with exactly two b-tagged jets and H_T(alljets,lepton,$\not\!\!E_T$)< 175 GeV.

Double-Tagged Event Yields with H_T(alljets,lepton,$\not\!\!E_T$)> 175 GeV

	Run IIa				Run IIb			
	Electron Channel		Muon Channel		Electron Channel		Muon Channel	
	2 jets	3 jets	2 jets	3 jets	2 jets	3 jets	2 jets	3 jets
Signals								
tb	4.6	2.0	5.3	2.6	4.2	1.9	4.5	2.4
tqb	0.5	1.5	0.6	2.0	0.7	1.8	0.7	2.1
tb+tqb	5.1	3.5	5.9	4.5	4.8	3.7	5.2	4.5
Backgrounds								
t→ll	12.9	9.5	12.9	11.0	12.5	9.8	11.9	10.5
t→l+jets	4.1	28.4	3.4	32.0	3.8	27.5	3.0	28.8
$Wb\bar{b}$	17.3	9.6	17.0	12.0	14.9	9.5	15.1	10.9
$Wc\bar{c}$	2.5	2.2	2.6	2.6	2.6	2.5	2.6	2.8
Wjj	1.3	1.2	1.5	1.4	2.4	2.0	2.5	2.5
$Zb\bar{b}$	0.6	0.6	3.0	2.1	0.5	0.5	2.3	1.6
$Zc\bar{c}$	0.1	0.1	0.6	0.5	0.1	0.1	0.4	0.4
Zjj	0.1	0.1	0.2	0.2	0.1	0.1	0.2	0.2
Dibosons	1.1	0.7	1.5	1.1	0.9	0.8	1.6	1.1
Multijets	1.1	0.8	1.1	1.7	1.0	0.9	2.3	2.0
Background Sum	41.1	53.3	43.7	64.6	38.8	53.8	41.9	61.0
Bkgds+Signals	46.2	56.8	49.6	69.1	43.6	57.5	47.1	65.5
Data	41	54	42	56	43	48	48	69

Table 6.8: Yields for events with exactly two b-tagged jets and H_T(alljets,lepton,$\not\!\!E_T$)> 175 GeV.

Tagged Event Yields with Channels Combined and H_T < 175 GeV

	2 jets	3 jets	All Channels
Signal			
tb	15.6	1.9	17.5
tqb	26.8	4.4	31.2
tb+tqb	42.4	6.3	48.7
Backgrounds			
t→ll	15.4	2.7	18.1
t→l+jets	5.5	3.2	8.7
$Wb\bar{b}$	388.9	65.8	454.7
$Wc\bar{c}$	178.0	35.3	213.3
Wjj	523.5	82.1	605.6
$Zb\bar{b}$	37.1	5.5	42.6
$Zc\bar{c}$	17.1	2.6	19.7
Zjj	20.2	3.5	23.7
Dibosons	47.2	6.7	53.9
Multijets	120.1	27.2	147.3
Background Sum	1352.4	234.8	1587.2
Bkgds+Signals	1394.8	241.1	1635.9
Data	1439	262	1701

Table 6.9: Yields for each jet multiplicity and for all analysis channels combined for events with H_T(alljets,lepton,$\not\!\!E_T$)< 175 GeV.

Tagged Event Yields with Channels Combined and H_T> 175 GeV

	2 jets	3 jets	All Channels
Signal			
tb	46.2	22.1	68.3
tqb	50.0	34.7	84.7
tb+tqb	96.4	56.9	153.3
Backgrounds			
t→ll	134.0	101.9	235.9
t→l+jets	67.1	327.9	395.0
$Wb\bar{b}$	289.2	163.3	452.5
$Wc\bar{c}$	124.8	112.0	236.8
Wjj	324.8	170.8	495.6
$Zb\bar{b}$	33.3	21.0	54.3
$Zc\bar{c}$	14.2	9.8	24.0
Zjj	19.0	10.3	29.3
Dibosons	41.5	24.8	66.3
Multijets	76.2	46.2	122.4
Background Sum	1124.2	996.2	2120.4
Bkgds+Signals	1220.6	1053.1	2273.7
Data	1140	954	2094

Table 6.10: Yields for each jet multiplicity and for all analysis channels combined for events with H_T(alljets,lepton,$\not\!\!E_T$)> 175 GeV.

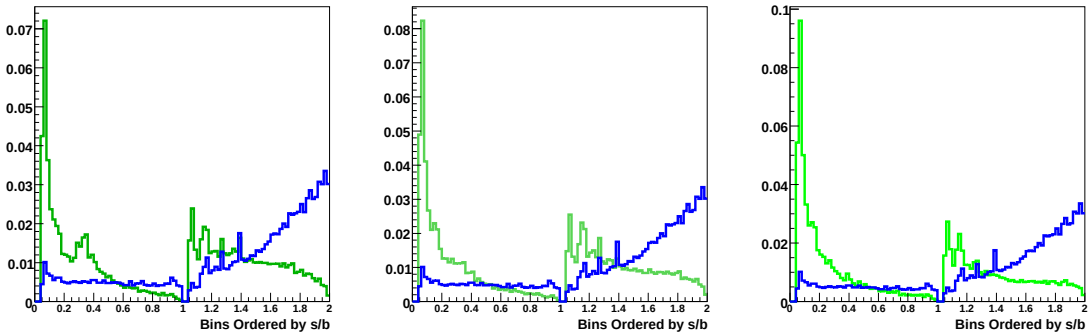

Figure 6.3: The final normalized 1D discriminant histograms for Run II a and Run II b data for all channels combined for tb+tqb and Wbb (left), tb+tqb and Wcc (center), tb+tqb and Wjj (right).

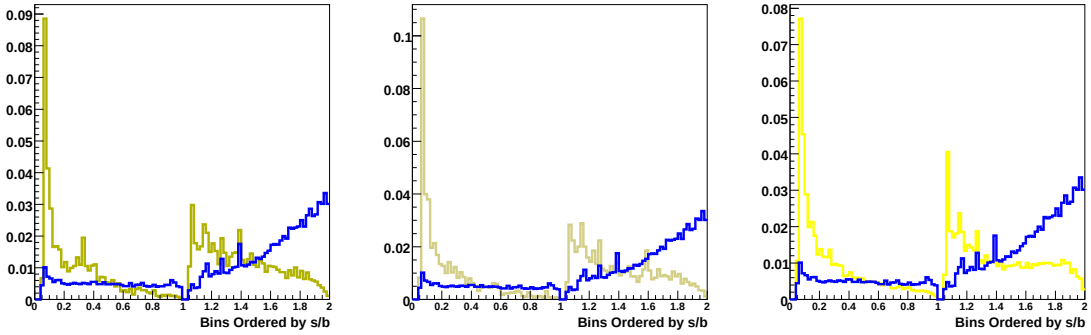

Figure 6.4: The final normalized 1D discriminant histograms for Run II a and Run II b data for all channels combined for tb+tqb and Zbb (left), tb+tqb and Zcc (center), tb+tqb and Zjj (right).

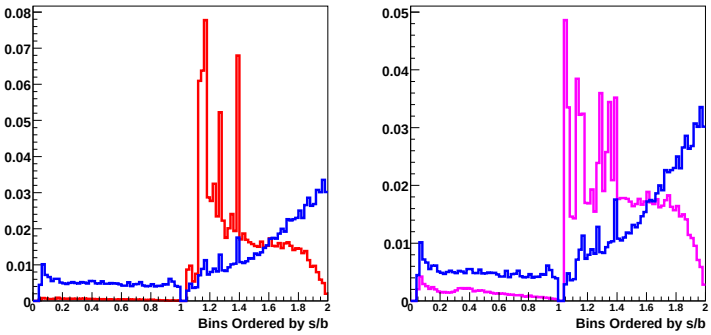

Figure 6.5: The final normalized 1D discriminant histograms for Run II a and Run II b data for all channels combined for tb+tqb andt$\rightarrow\ell$+jets (left) and tb+tqb and t$\rightarrow\ell\ell$ (right).

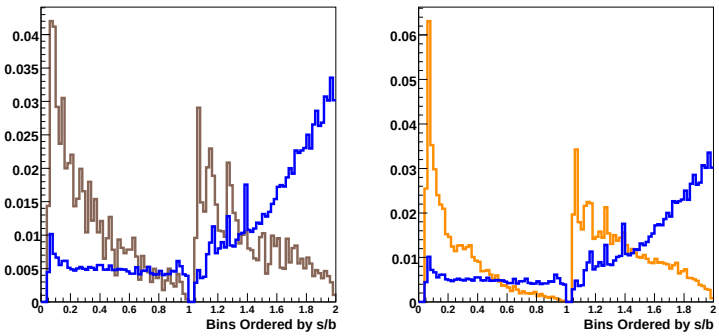

Figure 6.6: The final normalized 1D discriminant histograms for Run II a and Run II b data for all channels combined for tb+tqb and multijet events (left) and tb+tqb and $WW/WZ/ZZ$ (right).

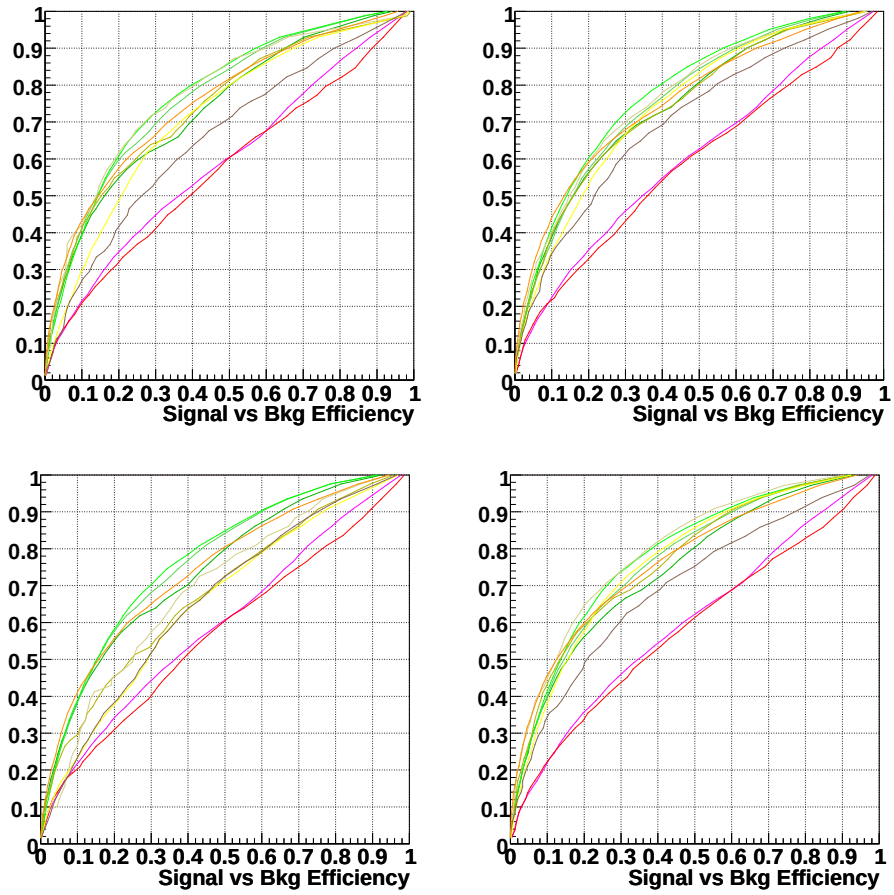

Figure 6.7: The discriminant performance plots for (top right) Run IIa data, (top left) Run IIb data, (bottom right) $e + jets$ events, and (bottom left) $\mu + jets$ events. The events are required to have H_T(alljets,lepton,$\not\!\!E_T$)$<$ 175 GeV.

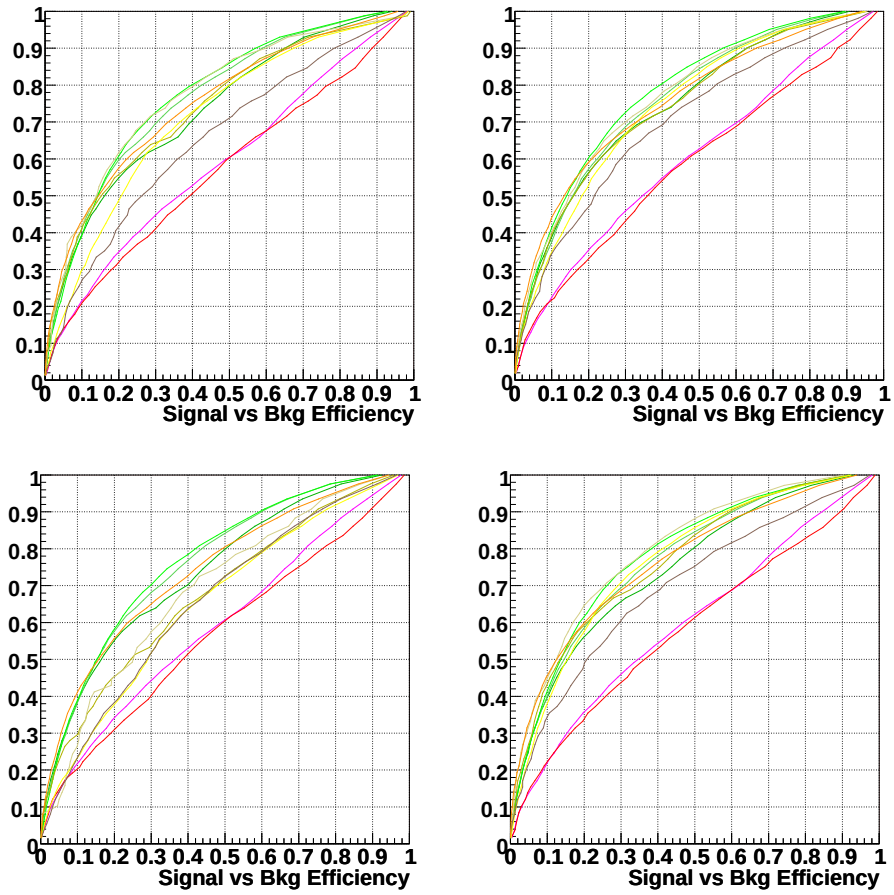

Figure 6.8: The discriminant performance plots for (top right) Run IIa data, (top left) Run IIb data, (bottom right) $e + jets$ events, and (bottom left) $\mu + jets$ events. The events are required to have H_T(alljets,lepton,$\not\!\!E_T$)$>$ 175 GeV.

6.2.3 Optimization

The prescription described above to make the final discriminant is based on optimization studies that measure an expected cross section which will be described in more detail in the next section and uses the peak over one-sigma to measure the sensitivity of the measurement. The peak over one-sigma comes from a posterior density function the expected cross section measurement generates.

H_T(alljets,lepton,$\not\!\!E_T$) Optimization Study

Different H_T(alljets,lepton,$\not\!\!E_T$) cuts were examined to determine which H_T(alljets,lepton,$\not\!\!E_T$) to use for measuring the electroweak produced top quark cross section. The highest expected sensitivity using the peak over one-sigma ($\sigma/\Delta\sigma$) for all channels of the analysis combined determined the H_T(alljets,lepton,$\not\!\!E_T$) cut at 175 GeV. Table 6.11 shows the results for these various cuts.

Expected Results Using Different H_T(alljets,lepton,$\not\!\!E_T$) Cuts

H_T(alljets,lepton,$\not\!\!E_T$) Cut	$\sigma \pm \Delta\sigma$	P/W
150 GeV	$3.53^{+1.15}_{-0.95}$	3.71
155 GeV	$3.70^{+1.00}_{-1.10}$	3.38
160 GeV	$3.61^{+1.12}_{-0.97}$	3.71
165 GeV	$3.63^{+1.10}_{-0.98}$	3.70
170 GeV	$3.66^{+1.07}_{-1.01}$	3.63
175 GeV	$\mathbf{3.60^{+1.12}_{-0.95}}$	**3.79**
180 GeV	$3.66^{+1.06}_{-1.01}$	3.61
185 GeV	$3.70^{+1.03}_{-1.05}$	3.53
190 GeV	$3.70^{+1.01}_{-1.07}$	3.48
195 GeV	$3.65^{+1.06}_{-1.02}$	3.58
200 GeV	$3.62^{+1.09}_{-0.98}$	3.68

Table 6.11: Comparison of expected cross section measurements and peak over one-sigma for different H_T(alljets,lepton,$\not\!\!E_T$) cuts using all channels of the analysis combined with full systematics. The highest sensitivity and its corresponding expected cross section is in bold type.

Binning Method

Different binning methods were examined to determine which method to use to generate the final cross section measurement. The expected sensitivity used is the peak over one-sigma ($\sigma/\Delta\sigma$) for all channels of the analysis combined accounting only for statistical uncertainties. The 2-D tb-tqb discriminant has the x-axis from the tb discriminant and the y-axis from the tqb discriminant. The 1-D reordered discriminant is formed from the 2-D tb-tqb discriminant where the bins are reordered based on its s/b yield. The H_T cut used, if it is applied, is at 175 GeV. Based on the results as seen in Table 6.12, the 1-D reordered discriminant is used with a H_T cut at 175 GeV.

Expected Results Using Different Binning Methods

Binning Method	$\sigma \pm \Delta\sigma$	P/W
2-D tb-tqb Disc. w/ no H_T cut	$3.46^{+0.75}_{-0.74}$	4.69
2-D tb-tqb Disc. w/H_T cut	$3.46^{+0.74}_{-0.72}$	4.80
1-D reorderd Disc. w/ no H_T cut	$3.46^{+0.72}_{-0.71}$	4.90
1-D reorderd Disc. w/ H_T cut	$\mathbf{3.46^{+0.70}_{-0.68}}$	**5.07**

Table 6.12: Comparison of expected cross section measurements and peak over one-sigma for different binning methods using all channels of the analysis combined with just statistical uncertainties accounted for. The highest sensitivity and its corresponding expected cross section is in bold type.

Chapter 7

Cross Section Measurement

Once the Matrix Element analysis separates out the signal from background, the resulting distribution of the discriminant is used to extract the limits and cross section measurements. The approach relies on Bayesian statistics, especially Bayes theorem. Furthermore, the uncertainties, both statistical and systematic, need to be evaluated prior to the final measurement. Once a cross section is extracted with the uncertainties properly accounted for, ensembles of experiments are used to estimate the sensitivity and bias of the measurement. These ensembles can also determine the significance of our measurement, incorporating a frequentist approach to the Bayesian statistics that form the foundation of our measurement. All of this will be discussed in detail in this chapter.

7.1 The Bayesian Approach

The Bayesian approach [70] [71] assigns a probability to how certain or uncertain an event will occur. For a random set of variables A and B, the joint probability that A = a and B = b can be denoted by P(a,b) which can be expressed as:

$$P(a,b) = P(b|a)P(a) \tag{7.1}$$

where $P(b|a)$ is the conditional probability that B = b given that A = a and $P(a)$ is the marginal probability or the probability that A = a regardless of what value B is. Using the sum rule,

$$\sum_b P(a,b) = P(a) \tag{7.2}$$

Bayes' theorem follows:

$$P(a|b) = \frac{P(b|a)P(a)}{P(b)} \tag{7.3}$$

where $P(b)$ can be replaced with $\sum_a P(b|a)P(a)$. $P(a)$ is defined as the prior probability of A = a prior to observing the value of B, and $P(a|b)$ is defined as the posterior probability after observing B. The same arguments can be made for continuous variables but the probabilities are replaced with probability densities and summations are replaced with integrations.

This approach can be applied to the belief in the SM defined by parameters ω versus all other theories given the data D that comes from the $D\emptyset$ experiment using Bayes' theorem:

$$p(\omega|D) = \frac{p(D|\omega)\pi(\omega)}{\int_\Omega p(D|\omega)\pi(\omega)d\omega} \tag{7.4}$$

Here, $p(D|\omega)$ is the probability of the observed data D given some unknown value of the parameters ω; $\pi(\omega)$ is the prior probability density over the parameter space Σ of the probability model; and $p(\omega|D)$ is the posterior density which is the distribution we want to compute in order to measure the cross section.

Using the binned distributions of signal, backgrounds and data, the likelihood to observe a count D corresponds to $p(D|\omega)$ where the parameters are the cross section, the effective luminosity and the background yields. For a given bin, the likelihood to observe a count D, with a mean $< D >= d$, is given by the Poisson distribution:

$$L(D|d) = \frac{e^{-d}d^D}{\Gamma(D+1)} \tag{7.5}$$

where Γ is the Gamma function. This Gamma function becomes D! if D is an integer as is the case when data is used for the cross section measurement rather than the expected yields from MC. The mean count d is the sum of the predicted contributions from the signal and the N different backgrounds:

$$d = \alpha L\sigma + \sum_{i=1}^{N} b_i \equiv a\sigma + \sum_{i=1}^{N} b_i \tag{7.6}$$

where α is the signal acceptance, L the integrated luminosity, σ the signal cross section, b_i the yield for the background source i, and a $\equiv$ α L which is the effective luminosity. For a distribution of observed counts, the likelihood is the product of all these single-bin likelihoods:

$$L(D|d) \equiv L(D|\sigma, a, b) = \prod_{j=1}^{M} L(D_j|d_j) \tag{7.7}$$

where D and d represent a vector of the observed counts and mean counts in M bins, a is a vector of the effective luminosity, and b is a vector of the background yields. To add up separate channels together, the combined likelihood is a product of the single-channel likelihoods since these channels are statistically independent.

To get the posterior probability density for the signal cross section, Bayes theorem is invoked to compute the posterior probability density of the parameters, $p(\sigma, a, b|D)$ which then needs to be integrated with respect to the parameters a and b:

$$p(\sigma|D) = \frac{1}{N} \int\int L(D|\sigma, a, b)\pi(\sigma, a, b)dadb \tag{7.8}$$

N is an overall normalization that ensures that posterior of the cross section over all possible cross sections adds to 1. The prior probability $\pi(\sigma, a, b)$ encodes our knowledge of the parameters σ,a, and b. Since any prior knowledge of a and b is independent of the signal cross section, the prior can be separated out into two components:

$$\pi(\sigma, a, b) = \pi(a, b)\pi(\sigma) \tag{7.9}$$

For $\pi(\sigma)$, we assume that it is flat in σ:

$$\pi(\sigma) = \frac{1}{\sigma_{max}}, \quad 0 < \sigma < \sigma_{max} \tag{7.10}$$

$$= 0, \text{ otherwise.} \tag{7.11}$$

so the posterior probability density becomes

$$p(\sigma|D) = \frac{1}{N\sigma_{max}} \int\int L(D|\sigma, a, b)\pi(a, b)dadb. \tag{7.12}$$

This integral is done numerically using Monte Carlo importance sampling:

$$p(\sigma|D) \propto \int\int L(D|\sigma, a, b)\pi(a, b)dadb \tag{7.13}$$

$$\approx \frac{1}{K}\sum_{k=1}^{K} L(D|\sigma, a_k, b_k) \tag{7.14}$$

Here K is a large number of points (a_k,b_k) which are randomly sampled from the prior density $\pi(a, b)$. The prior density encodes our knowledge of the effective signal luminosities and background yields and these things are affected by the systematic uncertainties. A large number of these samples of systematic shifts are made and a separate likelihood distribution is made for each sample where the final posterior is the sum over all these individual likelihoods. The uncertainty for each systematic is directly sampled from a Gaussian distribution of mean 0 and width 1 and this shift is applied to each bin of each source in each channel and is denoted by $g(0, 1)_{isys}$ for systematic $isys$. The only exception to this is the statistical error which instead uses a Gamma prior since a Gaussian prior would require over 100,000 systematic samples to be generated, resulting in an impractical amount of CPU time to derive limits. A yield shift δy_{isys} for each bin then becomes the following:

$$\delta y_{isys} = s^{+}_{tot} \times g(0, 1)_{isys} \times (y^{+}_{isys} - y) \text{ if g}(0, 1)_{\text{isys}} \text{ is a positive number} \tag{7.15}$$

$$= s^{-}_{tot} \times g(0, 1)_{isys} \times (y - y^{-}_{isys}), \text{ otherwise} \tag{7.16}$$

where $y_{isys}^{+/-}$ is the plus or minus systematic yield for systematic $isys$ and y is the yield for the bin. The scale factor s_{tot} is 1 for both shape and normalization changes but for shape uncertainties only, $s_{tot}^{+(-)} = \frac{\sum y}{\sum y_{isys}^{+(-)}}$ where the sum goes through all the bins of the histogram for a particular source. In each bin, the yield y' is then the sum over these shifted yields (y_{isys}) plus the nominal yield y:

$$y' = y + \sum_{isys} \delta y_{isys} \tag{7.17}$$

The specific systematics used in this analysis will be discussed in detail later.

A 1D posterior density distribution can now be made as seen in Figure 7.1.

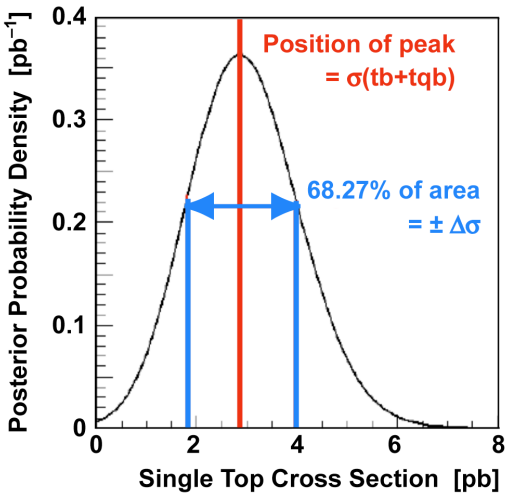

Figure 7.1: Posterior density distribution used to measure the cross section. The peak corresponds to the cross section and the 68% interval about the mode gives the uncertainty of the cross section measurement.

The mode (peak) of the posterior density distribution is the measured cross section and the 68% interval about the mode gives the uncertainty of the cross section measurement.

A posterior density distribution is built for each channel where two channels are statistically independent from each other. In this case, there are 16 channels, separated by data set (Run IIa (p17), or Run IIb (p20)), lepton (electron (CC) or muon (MU)), tag (one b-tag or two b-tags), and jet (two jets or three jets or four jets for the W' analysis).

7.2 Systematics

There are two types of uncertainties: shape-changing uncertainties and normalization uncertainties.

7.2.1 Shape-changing Systematics

Shape-changing uncertainties, as the name suggests, arise from parameters which when varied change the entire shape of the discriminant over its full range. The shape-changing uncertainties in this analysis are from the Jet Energy Scale (JES), tag rate functions for b-tagging (TRF), and the reweighting applied to the W+jets sample.

Taggability and tag-rate functions for MC events

The TRFs depend on the taggability of the jet and the efficiency of the jet to be b-tagged or the tagging rate function. The uncertainties associated with b-tagging, the taggability and the tag rate function, are added together in quadrature.

Taggability Errors

The taggability errors have two main contributions: statistical errors as a result of the fits to the taggability functions and flavor dependence of the taggability [32]. For this last component, the data used to measure taggability is dominated by light jets. As a result, the ratios of b quark to light quark and c to light quark taggabilities are measured as a function of jet p_T and η in multijet MC samples for a $t\bar{t}$ tagged cross section measurement. The fits to the ratios are used as flavor-dependent correction factors to the taggability with $\approx 5\%$ as the largest difference found in the low jet p_T ratio for b quark to light quark.

Tagging Efficiency Errors

As noted earlier, the tagging rate function depends on different components used to derive the b-tagging efficiency. The different errors accounted for in the correlation coefficients are statistical errors where the correlations are properly accounted between the samples, sample dependency which is added in quadrature to the statistical error, and systematic errors which were determined by varying the value of the coefficient within their errors [58] [59].

The total statistical error is determined at $\pm$ 1σ using the following equation:

$$\sigma_{stat} = \frac{f^{\pm 1\sigma}(p_T) \times f^{\pm 1\sigma}(\eta)}{f^{\pm 1\sigma}_{All}} - \frac{f(p_T) \times f(\eta)}{f_{All}} \tag{7.18}$$

chap:evtsel As for the b-tagging efficiency, the System8 Method (S8) [56] equations as described in Chapter 5 are solved and a systematic uncertainty due to the correlation coefficients is determined by varying the coefficients by their errors and resolving the S8 equations in different p_T and η bins. The difference in efficiencies is used as the error which is added in quadrature with the Minuit fit error [57].

The total tagging rate function systematic uncertainty is determined by checking in different p_T and η bins the number of actual tags with the predicted value. This is done on each of the MC samples used to make the tagging rate function and the percentage differences from each sample is weighted by the number of actual tags in the p_T, η bin. The RMS of the resulting distributions is used as the total error on each of the TRFs and is added to the mean offset of the closure distribution for each sample. The error taken is the largest one amongst the samples.

As for the fake rate, the systematic uncertainties are derived in the same way as mentioned above but an additional uncertainty due to the scale factor must be taken account. This uncertainty is calculated by varying the b and c contents by one σ and seeing how much the scale factor changes.

Total TRF systematics

The TRF values are raised and lowered by one standard deviation for all MC samples and the analysis is repeated. This is because the taggability and tag-rate functions will affect the number of b-jets in an event, resulting in events migrating from b-jet bins or being removed entirely. In particular for the ME analysis, for a 1-b-tag 2 jet event, if the event, when applying this systematic shift, changes the event to a 2-b-tag 2 jet event, the differential cross section for Wbb and tb will increase while the differential cross section for Wcg and tq will decrease. The TRF uncertainties arise from the statistical errors of the MC events; the assumed fraction of heavy flavor in the multijets MC events used to determine the mistag rate; and the parameterizations used. The normalization component varies from 2.3% (9.9%) to 4.7% (10.8%) for single-tagged (double-tagged) signal acceptances, and from 2.1% (9.0%) to 7.0% (11.4%) for single-tagged (double-tagged) combined backgrounds.

Jet energy scale

The JES depends on the different corrections derived to account for the calorimeter response for jets. For the offset correction, the main sources of systematic uncertainty come from the residual instantaneous luminosity dependence within a given primary vertex multiplicity bin and come from the difference between the offset energy outside the jet and inside the jet due to the impact difference of zero-suppression of the cell energies. The relative response correction is remeasured after the full JES correction is applied. If the correction differs from 1, this correspond to small residuals of at most 2% that come from imperfections on the energy-dependent parameterization and η-interpolation. The residuals are symmetrized and assigned as the systematic uncertainty for this correction. For the absolute response correction, the systematic uncertainties arise from limited statistics and from biases related to photon energy scale and purity, the limited understanding of non-Gaussian tails in the response distribution, and the sensitivity of the selection. As for the showering correction, the dominant uncertainty comes from the subtraction procedure and the choice of the "jet limit" radius [30] [31].

The JES correction uses jets found at one standard deviation above and below the JES scale used based on all these uncertainties added together. The entire analysis is rerun from the event selection cuts to the multivariate analyses. This is because the JES correction can change the number of jets in an event as a result of the jet p_T changing and thus an event can shift jet bins or even be removed by the event selection. Additionally, even if the event does not shift jet bins, the differential cross section is calculated using the jet p_T and the α weights from the tag-rate functions depend on the jet p_T and η. The normalization ranges from 1.1% to 13.1% on the signal acceptance and from 0.1% to 2.1% for the combined backgrounds.

ALPGEN reweighting (RWT)

This systematic only affects the W+jets background and so these backgrounds are reweighted by one standard deviation. The uncertainty of the combination is calculated by adding in quadrature the statistical uncertainty of the combination:

$$\left[\sum_{channels} 1/\sigma^2_{i,\text{channel}}\right]^{-1/2} \tag{7.19}$$

where $\sigma_{i,channel}$ is the uncertainty of the reweighting histogram for bin i and a particular channel. The systematic uncertainty is taken as half the difference between the weight and 1. These error bars constitute the one σ band for the reweighting function which is applied to each event in the W+jets sample, thus modifying the shape of the discriminant since the shape of the W+jets sample changes.

Examples of these shape changing systematics can be seen in Fig 7.2

7.2.2 Normalization Systematics

Normalization uncertainties arise from parameters that shift the entire discriminant up or down by a constant factor. The normalization systematics included in the cross section measurement are discussed below.

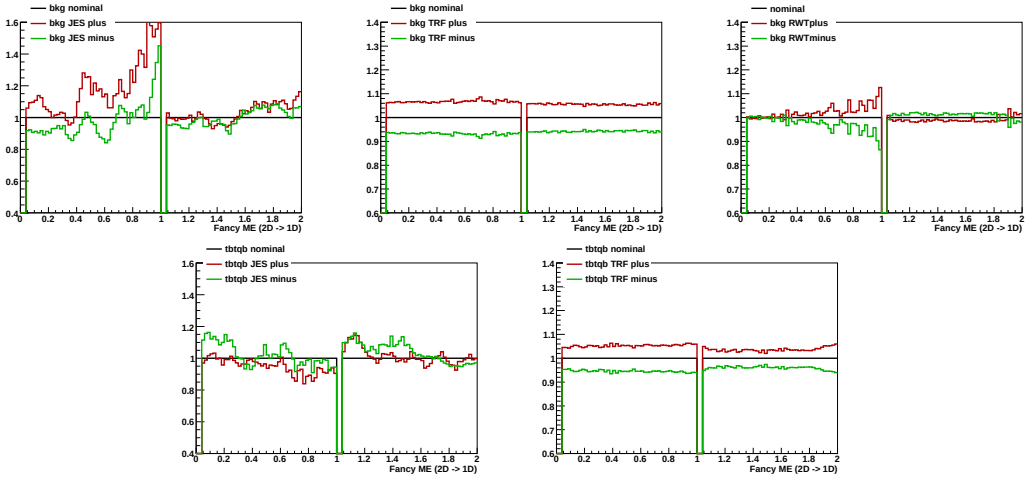

Figure 7.2: Systematic shift when varying the JES, TRF, and RWT by $\pm 1\sigma$ for the background files (top row) and the signal files (bottom row) for the matrix element discriminant in the e+jets, Run IIa, 1-tag 2-jet channel. The RWT systematics is only applied to the W+jets backgrounds.

Integrated luminosity

The 6.1% uncertainty on the luminosity estimate affects the signal, $t\bar{t}$, Z+jets, and diboson yields since these samples are normalized to the cross sections expected for the total integrated luminosity used in this analysis. This uncertainty is derived for period A which is data from April 20, 2002 to August 23, 2004 triggered by the experiment's highest E_T jet trigger which is present in every data-taking run used for physics analysis and is affected by all normalization corrections [35].

The dominant contribution is 5.4% which comes from the final value of $\sigma_{eff} = 48mb$ which has equal contributions from the uncertainties in determining $\sigma_{inelastic}$ and in determining the acceptance and efficiency of the LM detectors for registering inelastic collisions. The σ_{eff} uncertainty is added in quadrature with the correction procedure applied for different effects that come from electronics changes, dead time where inelastic collisions cannot be measured, and current changes in the magnet. The correction procedure has fit uncertainties in the analytic correction functions derived and also an estimated uncertainty associated with the effect of scintillator radiation damage.

Theory cross section

The uncertainties on the cross section for top quark produced through the electroweak process and top produced through the strong force come from [8] and [9]. These theoretical uncertainties are due to the scale and the PDF variations for the electroweak produced top quark cross section and for the NLO cross section for the top pair cross section. For the NNLO cross section for top pair, the scale, the PDF variations, and the kinematics are the theoretical uncertainties. The calculations for the top quark pair cross section are at a scale set to the top quark mass and so these calculations are repeated at a factor two above and below the top mass to derive the scale uncertainty which is also a rough estimate of uncertainties from higher-order terms. The PDF uncertainty is derived by repeating the calculation with the 44 different CTEQ6.6M eigensets. This uncertainty is relatively large due to the uncertainty in the large x region of the PDFs. The kinematics uncertainty for the NNLO cross section comes from the treatment of the $q\bar{q}$ channel which uses the average of two different calculation methods whereas the gg channel uses just one of these methods. The kinematics uncertainty is found by looking at the two extremes, meaning the calculation results for each method separately. These uncertainties are added in quadrature.

The mass uncertainty is the difference between the cross section at a top mass of 170 GeV which our samples were generated at and the current world average top mass of 172.4 GeV [72] plus one standard deviation at 1.2 GeV. The uncertainties are +4.3%, -11.2% for s-channel, +5.5%, -7.4% for t-channel, and +7.7%, -12.7% for $t\bar{t}$. For s and t-channels combined, the uncertainty is +5.2%, -8.4%. The signal cross section uncertainties are only used for the measurement of $|V_{tb}|$.

The diboson uncertainties for the scale and PDF were calculated at NLO using the MCFM generator [46]. The uncertainties for WW, WZ and ZZ are respectively 5.6%, 6.8%, 5.5%. For the sum of the three, the uncertainty is 5.8% which is also used as a rough estimate for the Z+jets background cross section uncertainty as we do not have direct measurements for these values.

Branching Fractions

The branching fractions for a W boson to decay to any lepton has an average uncertainty of 1.5%. This is included in the MC normalization uncertainties and comes from the Particle Data Book [1] error on the W boson decay branching fraction uncertainty divided by the branching fraction.

Parton distribution functions

A systematic uncertainty of 3% is assigned to the signal acceptances due to the PDFs. This was determined by re-weighting signal events according to the 40 CTEQ error PDFs [42] and remeasuring the signal acceptance. The error PDFs are made by varying the 20 parameters most sensitive to the input data set used to make the PDFs. Each of these parameters is varied up and also down while the other 19 are held fixed, yielding 40 error PDFs used to find the maximal difference in the signal acceptance.

Trigger efficiency

The uncertainty was determined by the 90% bands in the ratio of ratios as a function of variables sensitive to the trigger selection. Since almost all the points are in between 0.95 and 1.05, a 5% uncertainty was assigned to the trigger efficiency to all channels except for Run IIb muons which has a systematic uncertainty of 10% derived in the same way. These uncertainties are treated as uncorrelated between data sets and between leptons.

Instantaneous luminosity reweighting

The instantaneous luminosity distributions for the MC samples are reweighted to match the Run IIa or Run IIb data distributions. The initial distributions are from the zero-bias data overlaid on the MC events to simulate the underlying events but these are generally at too low values for the higher luminosity data-taking conditions. The uncertainty for this is 1.0%.

Primary vertex modeling and selection

The distribution of the primary vertices along the beamline are reweighted in the MC to match the data [73]. This method fits zero bias events in dijets and $\gamma - jets$ samples to a z vertex distribution described by the convolution of two Gaussian beams representing the proton and antiproton beam and the beta function. Then using this shape description on MC, the produced event shape is compared with the detected primary vertex shape. This comparison gives the effects of efficiency of data to MC and also of finding the wrong vertex. The uncertainty from this reweighting is 0.05% whereas the uncertainty on the difference in the selection efficiency for the primary vertex between data and MC is 1.4 %.

Electron reconstruction and identification efficiency

These uncertainties come from the correction factors calculated for both data and MC efficiencies [22] [23]. These uncertainties are added in quadrature with also the uncertainties from the background subtraction procedure which is assigned as 1% for MC and 1.5% for data. The total uncertainties are $3 - 4\%$ at electron p_T ranges of 18 -20 GeV, and then stabilizes to $2.5 - 3\%$ for electron $p_T > 28\ GeV$. Additionally, efficiency changes in data and MC as a function of the distance of the electron to a closest jet $dR(jet, e)$ were examined but the efficiency does not change for the electron definitions used in this analysis. Furthermore, the total number of jets in the event is examined but is very well reproduced in MC that this uncertainty does not need to be taken into account. Lastly, different amounts of radiation lengths in the solenoid region in the CC was examined but the identification efficiencies with respect to the default MC changes by about 0.3 - 1.2% which is consistent within statistical uncertainties. The total uncertainty assigned to the electron reconstruction and identification efficiency is 2.5%.

Muon reconstruction and identification efficiency

The muon reconstruction and identification efficiency is composed of a scale factor associated with the muon id, the tracking, and the isolation [33] [34]. For the muon id, the systematic uncertainties come from the tag/probe method in that correlations between the tag and probe muon or correlations between the preselection of the probe and the criteria to be tested are not taken into account; from a bias coming from different requirements on the data versus MC, specifically the trigger requirement on data; from background contamination from the multijets, $W \rightarrow \mu\nu$, $Z \rightarrow \tau^{+}\tau^{-}$, or cosmic muons; from the parameterization used; and from limited statistics. These uncertainties contribute 0.7% to the Data/MC scale factor.

As for the tracking efficiency, the systematic uncertainties are the same as the muon id but there are additional uncertainties that must be taken into account. The time and luminosity effects yield large variations in the tracking efficiency. This may yield a correlation between the tag and probe muon which has selection criteria on the tracking requirements that change the luminosity profile of the sample. This was tested by using the different tag and probe samples and seeing the variations between the samples and a set tracking criteria. The efficiencies are also averaged over the full data set used although different time periods have different trigger efficiencies. Also, since the tracking efficiency is highly dependent on the z of the primary vertex, the assumption used in the MC that the Gaussian beam width is fixed at 25 cm is tested. This width depends on the run period and the instantaneous luminosity. The variation in tracking acceptance is found between the MC and the MC reweighted with the corrected beam shape. The last additional systematic comes from the use of averaging out the ϕ variations although there are clearly ϕ variations that arise from the bottom muon hole, different optical fiber lengths for the CTT detector, and dead channels in the SMT. These uncertainties with the beam shape uncertainty is 0.8% for a medium track.

For the isolation, the systematic uncertainty comes from the luminosity dependence though this is very small since we used the scaled variables, and from the sample dependency of the efficiencies since the efficiency is jet dependent although the variation between the jet samples

used is small for the isolation point we use. The combined uncertainty used is 2.5%.

Jet fragmentation

This uncertainty arises from the MC generators used. $t\bar{t}$ events generated with ALPGEN are processed via PYTHIA [39] and HERWIG [74] to estimate the uncertainty. The acceptances of the two sets of $t\bar{t}$ events generated with the same parameters are analyzed and the difference used as the uncertainty. The variation in acceptance ranges from 1% to 8% and is applied as the jet fragmentation uncertainty to all the MC samples.

Initial-state and final-state radiation

Samples of $t\bar{t}$ were generated with initial and final-state radiation and the acceptance of these events are compared to the nominal sample to find the uncertainty. The values found range from 0.6% to 12.6%

B-jet fragmentation

For the tuning of the b fragmentation in PYTHIA, different tune settings were compared to the default used in this analysis. Using $t\bar{t}$ samples, the tagging efficiencies are compared for the different tune settings and found to differ by 2% [75].

Jet reconstruction and identification

The errors for the jet reconstruction and identification come from the fits used to derive the efficiency, from a PV z dependence, and from a luminosity dependence [26] [27]. For the fits, the jet identification efficiencies for data and MC take the statistical fit error into account when determining the parameters of the efficiency fits. The largest systematic error for the fits come from the maximum EMF cut and is taken as the difference between the efficiency plateau value and the fit itself. As for the data/MC scale factor, it is taken as a constant that is fit with the statistical and systematic errors.

As for the PV z dependence, it is evaluated looking at the $JetID(PVz \cdot sign(\eta_{jet}^{det}))$ after an 80 GeV cut on the tag jet p_T which is used to focus on the plateau region. In each η bin, two spread estimators are used: error of the constant fit inflated by χ^2/number of degrees of freedom, and $[max_2 - min_2]/2$ where max_2 (min_2) is the second maximum (minimum) of the efficiency points on the y-axis. The maximum of the two spread estimators is taken as the PV z systematic error for the data and MC jet identification efficiencies and for the data/MC scale factor.

As for the luminosity dependence, the efficiency for data and MC is examined at three instantaneous luminosity bins. Half of the maximal difference between the three luminosity bins is taken as the luminosity systematic error. This systematic is extremely small: it is about 0.001 for individual jet ids and up to 0.005 for the data/MC scale factor in the forward η region. These errors, both statistical and systematic, are added in quadrature and was determined to be 1% for this analysis.

Jet energy resolution

The jet resolution uncertainties primarily come from statistical errors in the fits used [80]. Additionally the resolution determined from using RMS or the σ from a Gaussian fit is taken as a systematic error. The luminosity dependence, although small and mostly affects jets with low p_T, is incorporated in the variation of the noise term. From these uncertainties, jets with one standard deviation above and below the jet energy resolution used was rerun through the event selection and the Boosted Decision Tree analysis [81] to estimate its effects on the Matrix Element analysis. This uncertainty was found to be flat and is set to 4%.

W+jets and multijets normalization

The uncertainties for this systematic vary from channel to channel and range from 30% to 54% for multijets and from 1.8% to 5.0% for the W+jets background. The uncertainties δS_{W+jets} and $\delta S_{multijets}$ are estimated by examining each of the kinematic variables used in this method

separately and then finding the maximum variation seen in the scale factor for each variable compared to the final scale factors. δS_{W+jets} and $\delta S_{multijets}$ are defined as follows:

$$\delta S_{W+jets} = max|S^i_{W+jets} - S_{W+jets}| \tag{7.20}$$

$$\delta S_{multijets} = max|S^i_{multijets} - S_{multijets}| \tag{7.21}$$

where i are the kinematic variables used to derive the scale factors or the lepton p_T, $\not\!\!E_T$, and transverse mass of the W.

W+jets heavy-flavor scale factor correction

This uncertainty comes from a number of multiple sources: the statistical error, the uncertainty in the signal cross section, the uncertainty in the Wcj heavy-flavor scale factor correction, and the assumption that the $Wc\bar{c}$ and $Wb\bar{b}$ have the same heavy-flavor scale factor correction [50]. The cross section is varied by 40%, which is chosen to cover the values published by DØ [76] and CDF [77] of the measured cross sections of the electroweak top quark, and the scale factor is calculated to see the differences from the nominal value. As for the Wcj factor, it is varied by 10%, which is the difference in the Wcj factor of 1.8 chosen based on Fig. 1 in Ref. [78] and the NLO calculation which yields a Wcj factor of 1.648 [79]. The scale factor is re-derived to see how much it differs from the nominal value. As for the assumption that the $Wc\bar{c}$ and $Wb\bar{b}$ have the same heavy-flavor scale factor correction, a systematic of 5% is assigned which leads to a 10% shift in the K'_{HF} value of $Wc\bar{c}$ in comparison with $Wb\bar{b}$. The total uncertainty is 13.7%.

Z+jets heavy-flavor scale factor correction

The heavy-flavor scale factor K'_{HF} for $Zb\bar{b}$ and $Zc\bar{c}$ is determined from NLO calculations. We set the correction to this to be 1.0 with an uncertainty similar to the S_{HF} of the W+jets events, 13.7%.

Sample statistic

This comes from the limited size of our samples used in this analysis and is of order $(1/\sqrt{N})$ where N is the number of events in the sample.

Table 7.1 shows the uncertainty assigned for the systematics mentioned above.

Relative Systematic Uncertainties

Components for Normalization	
Integrated luminosity	6.1%
$t\bar{t}$ cross section	12.7%
Z+jets cross section	5.8%
Diboson cross sections	5.8%
Branching fractions	1.5%
Parton distribution functions (signal acceptances only)	3.0%
Triggers	5.0%
Instantaneous luminosity reweighting	1.0%
Primary vertex selection	1.4%
Lepton identification	2.5%
Jet fragmentation	(0.7–4.0)%
Initial-and final-state radiation	(0.6–12.6)%
b-jet fragmentation	2.0%
Jet reconstruction and identification	1.0%
Jet energy resolution	4.0%
W+jets heavy-flavor correction	13.7%
Z+jets heavy-flavor correction	13.7%
W+jets normalization to data	(1.8–5.0)%
Multijets normalization to data	(30–54)%
MC and multijets statistics	(0.5–16)%
Components for Normalization and Shape	
Jet energy scale for signal	(1.1–13.1)%
Jet energy scale for total background (not shape for Z+jets or dibosons)	(0.1–2.1)%
b tagging, single-tagged	(2.1–7.0)%
b tagging, double-tagged	(9.0–11.4)%
Component for Shape Only	
ALPGEN reweighting	—

Table 7.1: A summary of the relative systematic uncertainties for each of the correction factors or normalizations. The uncertainty shown is the error on the correction or the efficiency, before it has been applied to the MC or data samples.

7.3 Cross Checks

Once the cross section is measured, a couple of cross checks need to be done to make sure the analysis is behaving as one expects. One cross check looks at background modeling while the other looks at the ability to measure the cross section.

7.3.1 W+jets and $t\bar{t}$ Enriched samples

First, a sample heavily populated by W+jets is made. This corresponds to the 2-jet bin with a H_T(alljets,lepton,$\not\!\!E_T$) cut of 175 GeV. If the distributions look reasonable, this means that the W+jets was correctly treated in terms of the normalization applied using the IKS method and also the reweighting applied to the W+jets samples as is the case in Fig 7.3.

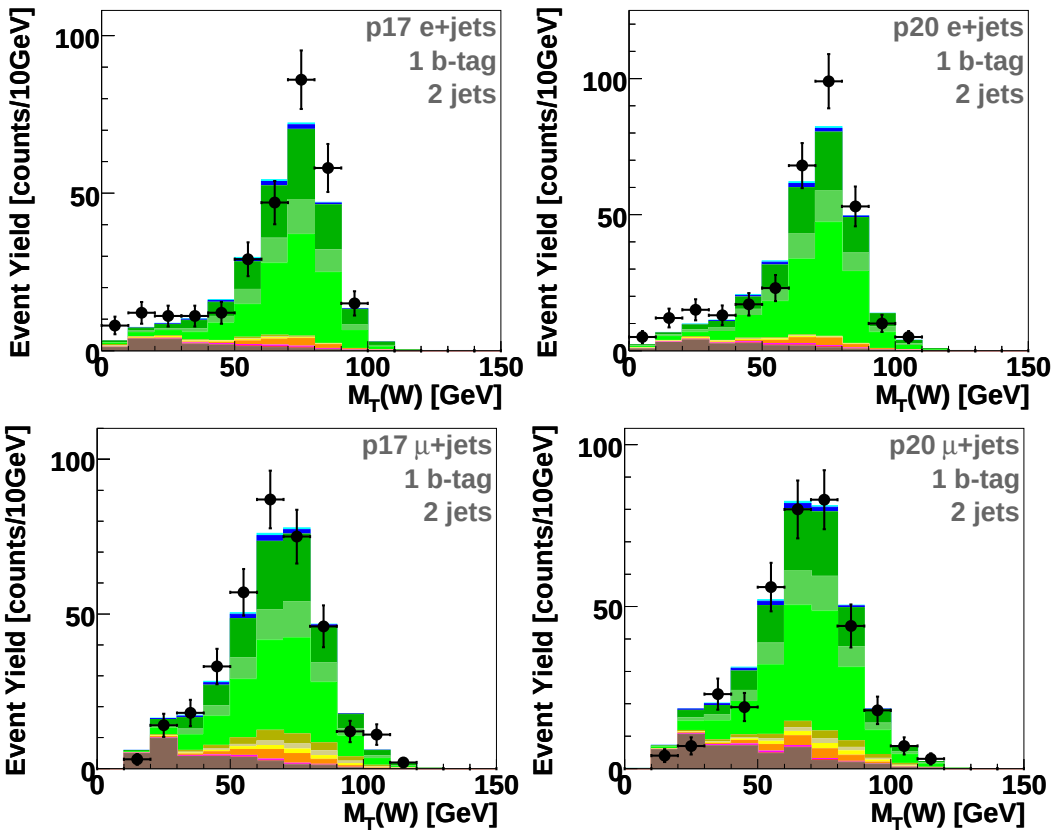

Figure 7.3: Cross-check plots for the W transverse mass in the W+jets cross-check sample.

The other sample is that dominated by $t\bar{t}$. This corresponds to the 3 jet bin with a 300 GeV

H_T(alljets,lepton,$\not\!\!E_T$) cut with both b-tagging cases used for increased statistics. If the agreement is good, this means the $t\bar{t}$ is modeled correctly. Additionally, the multivariate analysis is working correctly when after applying it to both cross check samples, the data/background

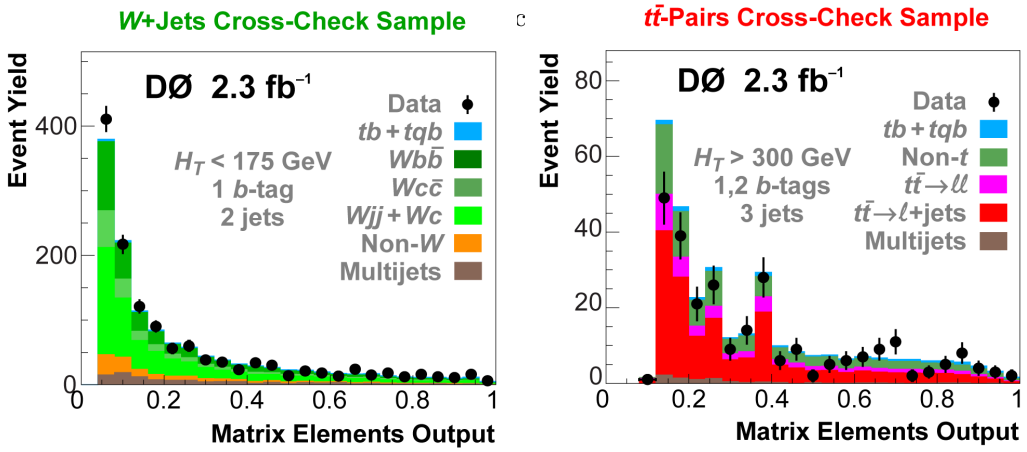

Figure 7.4: Cross-check plots for the matrix element discriminant in the W+jets cross-check sample (left) and the $t\bar{t}$ cross-check sample (right).

7.3.2 Linearity

A linearity test cross checks our ability to measure the electroweak produced top quark cross section. Several ensembles of data sets from pseudo DØ experiments are generated where each ensemble has a electroweak produced top quark cross section at particular value. The same sampling approach used for systematics is also used to generate these ensembles [71]. First, a systematics sample is at random and then the count in each bin is sampled from a Poisson distribution with the mean set to the yield of the background sum plus the signal which depends on the cross section value for the ensemble. For the case of zero signal cross section, meaning no top quarks are produced via the electroweak process, the mean is set to the yield of the backgrounds sum. For each ensemble, the multivariate technique measures a cross section for all events generated. A Gaussian fit is made to this distribution where the mode is the average cross section the multivariate technique measures. Fig 7.5 shows the Gaussian fits for different ensembles.

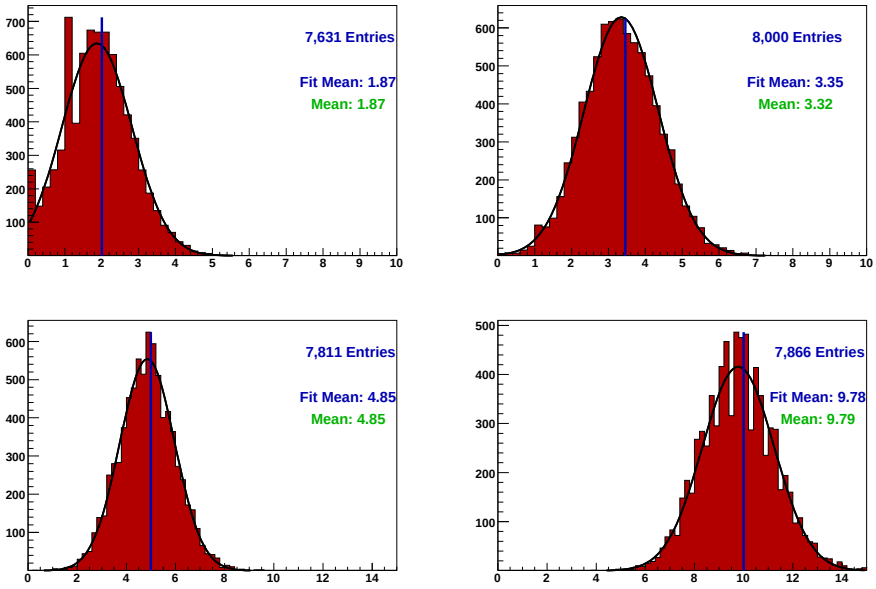

Figure 7.5: Measured electroweak produced top quark cross sections for different ensembles with different cross section values. The upper row shows the results from the 2 pb and the SM (3.46 pb) ensembles. We see that measuring at least a 4.30 pb cross section with standard model expected single top occurs 17.5% of the time. The lower row shows the 5 pb and 10 pb ensembles.

A plot is made of the input cross section as a function of the cross section measured by the multivariate technique. A linear response shows that the multivariate technique is behaving properly as well as the machinery to measure the cross section which can be seen in Fig 7.6.

7.4 Significance

Over 60 million pseudo-data sets are generated with zero single top cross section. The multivariate technique measures a cross section for each zero single top pseudo-data set. For the expected significance, the p-value is the number of pseudo-data sets that measure a cross section above 3.46 pb, the theoretical value we expect for the signal samples we use, over the total number of pseudo-data sets. For the measured significance, the p-value is the number of pseudo-data sets that have a cross section measurement above the cross section measurement we get from the real data collected from DØ over the total number of pseudo-data sets generated. These p-values tell us how often can the case where no top quarks are produced

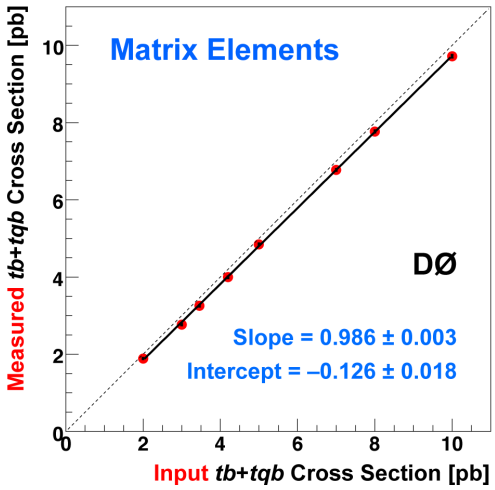

Figure 7.6: Linearity plot for the matrix element analysis. The response is very linear within errors, showing that the matrix element analysis as well as the machinery to measure the cross section is working properly.

by the electroweak process fluctuate to measure the theoretical cross section expected by the Standard Model or the cross section we measure from the DØ data. These p-values can then be converted to significances.

7.5 Matrix Element Results

The matrix element analysis yields a measurement of 4.30 + 0.98 - 1.20 pb for the cross section for the top quark produced via the electroweak process. From the zero signal ensembles, the expected p-value is 2.0 $\times 10^{-7}$, yielding a significance of 4.1σ. From our measured value, the p-value is 4.0 $\times 10^{-7}$ with a significance of 4.9σ. The zero signal ensemble results can be found in Fig. 7.7.

7.6 Combination Results

The matrix element analysis is then combined with the Bayesian Neural Network (BNN) analysis [84] and the Boosted Decision Tree (BDT) analysis [81] in another BNN trained

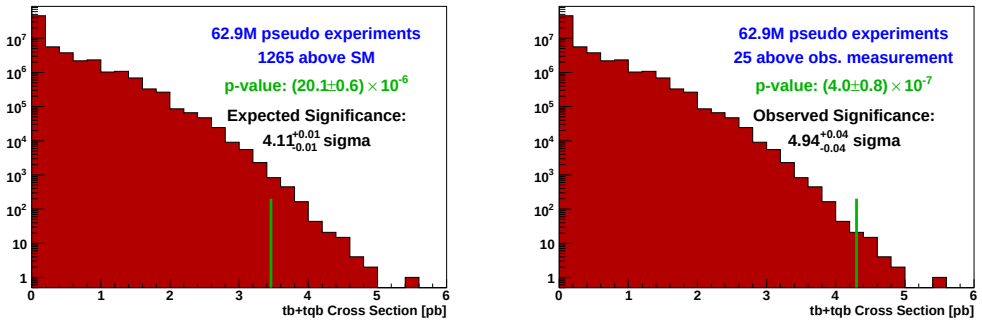

Figure 7.7: The zero signal ensembles are used to calculate the expected significance (left) and the measured significance (right) based on the fluctuations of the zero signal pseudo-data sets to measure a cross section higher than the theoretical cross section of 3.46 pb or the measured cross section from the matrix element analysis of 4.30 pb.

on these three discriminants [86]. More information about the BDT analysis and the BNN analysis can be found in [82] [83]and [85] respectively. The combined results yield a cross section measurement of 3.94 ± 0.88 pb with a significance of 5.0σ, resulting in the discovery of top quarks produced singly via the electroweak process.

The posterior and the significance for the BNN combination can be found in Fig. 7.8

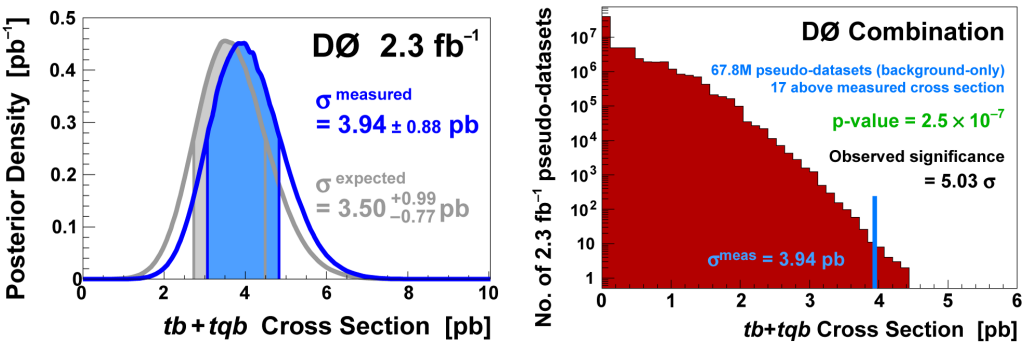

Figure 7.8: The Bayesian posterior density (left) and the observed significance (right) for the BNN combination yields a cross section measurement of 3.94 ± 0.88 pb with a significance of 5.0σ. With a 5.0σ significance, the top quark produced through the electroweak channel has finally been discovered.

7.7 V_{tb} Measurement

Top quark interactions with a W boson and a down-type quark $q(q = d, s, b)$ is described as follows:

$$\gamma^{\mu}_{tqW} = -\frac{g}{\sqrt{2}} V_{tq} \overline{u}(p_b) \gamma^{\mu} P_L u(p_t) \tag{7.22}$$

where $|V_{tq}|$ is the CKM matrix elements and $P_{L,R} = (1 \mp \gamma_5)/2$ is the left-handed/right-handed projection operator.

Using the cross section measurement from the combination results, V_{tb} can be directly measured with no unitarity constraints [87]. The assumptions made for this measurement are that the only existing production mechanism of electroweak produced top quarks are by a W boson; that $|V_{td}|^2 + |V_{ts}|^2 << |V_{tb}|^2$, implying that the branching fraction of $W \rightarrow tb \simeq 100\%$ and that the electroweak produced top quark is dominated by this interaction; and that the Wtb interaction is CP-conserving and of the $V - A$ type. The Wtb interaction can be anomalous since $|V_{tb} f_1^L|$ can be greater than 1 where f_1^L is the left-handed Wtb coupling. The cross section for an electroweak produced top quark is thus directly proportional to the square of the effective tbW coupling or in other words V_{tb}.

A Bayesian posterior using the BNN cross section analysis is made where a flat prior in $|V_{tb} f_1^L|^2$ is chosen. In order to extract $|V_{tb}|$ from the measured cross section, additional theoretical uncertainties need to be considered and applied to the s-channel and t-channel samples separately. These additional uncertainties are listed in Table 7.2.

Additional Systematic Uncertainties for $|V_{tb}|$

	s-channel	t-channel
Top quark mass	5.56%	3.48%
Factorization scale	3.7%	1.74%
PDF	3.0%	3.0%
α_s	1.4%	0.01%

Table 7.2: Additional systematic uncertainties used in the $|V_{tb}|$ measurement. They are applied for the s-channel and t-channel samples separately.

The Bayesian posterior density for $|V_{tb}f_1^L|^2$ is shown in Fig. 7.9 for both cases where the Bayesian posterior density is unrestricted and where the Bayesian posterior density is constrained to [0,1], corresponding to a SM V_{tb} coupling where $f_1^L = 1$.

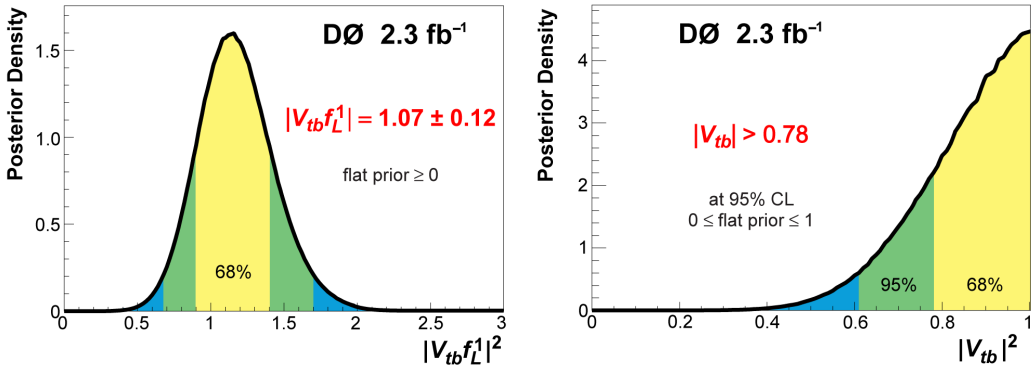

Figure 7.9: The Bayesian posterior density for $|V_{tb}f_1^L|^2$ is shown for the case when the V_{tb} coupling is SM-like but anomalous since $f_1^L > 1$ and when the V_{tb} coupling is that theorized by the SM since $f_1^L = 1$.

For $|V_{tb}f_1^L|^2$, the most probable value is $1.15^{+0.25}_{-0.26}$, corresponding to $|V_{tb}f_1^L| = 1.07^{+0.11}_{-0.12}$. This is above the SM expectation by about 0.6 standard deviations. However, constraining the prior to [0,1], $|V_{tb}|^2 = 1.0^{+0.0}_{-0.22}$ which gives $|V_{tb}| = 1.0^{+0.0}_{-0.12}$. A 95% confidence lower limit yields $|V_{tb}| > 0.78$.

Chapter 8

W' Analysis

As seen in the previous chapters, the electroweak produced top quark was finally discovered using multivariate techniques that can extract a small signal from an extremely large background. The cross section measurement seems consistent with the SM; however, a more precise measurement is necessary before one can rule out if physics beyond the SM does not exist in this production channel. As mentioned earlier, the top quark has many interesting properties that make it an ideal sector to discover physics extensions to the SM and in particular, the electroweak production channel. One such particle, heavy gauge bosons called W$'$, is predicted by various extensions of the SM and the s-channel processes in the electroweak produced top quark is an ideal channel to rule out or discover this particle. Using the same techniques to discover the electroweak produced top quark, parameters on the W$'$ boson can be set to further constrain existing theories that predict this particle. This chapter focuses on W$'$, from theories that predict it to how the limits are set on parameters that define W$'$.

8.1 Theory

New charged massive bosons usually called W$'$ are predicted by various extensions to the Standard Model (SM) such as Non-Commuting Extended Technicolor [88], Composite [89] [90]

and Little Higgs models [91] [92] [93] , models of composite gauge bosons [94], Supersymmetric top-flavor models [95], Grand Unification [96], and Superstring theories [97] [98] [99]. The physical properties and interaction parameters of W′ bosons differ from model to model. For example, in models of Universal extra dimensions [100] [101], W′ is the lowest Kaluza-Klein mode and has the same (V - A) chiral structure of interactions to fermions much like the SM W boson. As for top-flavor models, the gauge couplings to the first two generations (g_l) and to the third generation of fermions (g_h) can differ in magnitude where models with $g_l > g_h$ or $g_h > g_l$ exist [102] [103].

The simplest extension to the SM that predicts W′ bosons is the Left-Right symmetry [104] [105] [106] [107] [108] [109] [110] which is based on the U(1) $\times$ $SU(2)_L$ $\times$ $SU(2)_R$ gauge group. The left-handed fermions transform as doublets under $SU(2)_L$ and are invariant under $SU(2)_R$ contrary to the right-handed ones which transform as doublets under $SU(2)_L$. The linear combinations of charged gauge fields produce massive eigenstates where W_1 = cos ψ W_L + sin ψ W_R and W_2= -sin ψ W_L + cos ψ W_R. W_1 is the SM W boson and W_2 is the new W′ boson where ψ as the mixing parameter between bosons of the right and left gauge groups. This mixing parameter must be very small to suppress (V+A) charged currents for light SM fermions in accordance with experimental data [111] [112]. As a result, the W′ boson interactions becomes almost purely right-handed.

Experimental limits exist for the mass of the W′ boson since it has not been discovered yet. Indirect searches using semileptonic decays and also from cosmological and astrophysical data give a wide range for the upper limits on the W′ boson mass: 549 GeV to 23 TeV [1]. Direct searches have also set limits on the mass based on purely right or left-handed interacting W′ boson with SM-like coupling constants. The W′ boson can be divided into left and right handed couplings where the left handed couplings can interfere with the SM W boson interactions and the right handed couplings can be divided into two cases based on the mass of the right-handed neutrino ν_R. If $M(\nu_R) > M(W')$, then W′ can only decay hadronically but if $M(\nu_R) < M(W')$, then the W′ boson can decay both hadronically and leptonically. Using the leptonic decay

modes of W′ boson, for the case of $M(\nu_R) > M(W')$, $M(W') > 800$ GeV [113] and for $M(\nu_R) < M(W')$, $M(W') > 768$ GeV [114].

Using the same decay mode as that of the s-channel process for the electroweak production of top quarks, this channel has a small multijets background in comparison to the light jet channel used by the direct searches and is also less model dependent [115]. Additionally, if left-handed W′ bosons exist, then it should interfere with the SM W boson and would be more dominant in this channel since $|V_{tb}| \approx 1$ [116]. This interference term is not small and is negative in the region $M_W^2 < \hat{s} < M_{W'}^2$ and positive for $\hat{s} > M_{W'}^2$ when the left-handed coupling is positive. Here, $\hat{s}$ is the Mandelstam variable and is E_{cm} for the center of mass frame. At the Tevatron, the destructive interference can approach as large as 30% for $M(W')$ at 800 GeV and leads to a local minimum in the invariant mass distribution, referred to in the subsequent sections as $\hat{s}$, at $\sqrt{\frac{M_{W'}^2 + M_W^2}{2}}$ [116]. Furthermore, right-handed coupling limits can be made which would provide more constraints on which W′ boson theories are still possible.

8.2 Signal and Background Modeling

The most general, model independent lowest order effective interaction Lagrangian of the W′ boson to SM fermions can be written as

$$\mathcal{L} = \frac{V_{f_i f_j}}{2\sqrt{2}} g_w \overline{f}_i \gamma_\mu \big(a^R_{f_i f_j}(1+\gamma^5) + a^L_{f_i f_j}(1-\gamma^5)\big) W' f_j + \text{H.c.}\,, \tag{8.1}$$

where $a^L_{f_i f_j}$ and $a^R_{f_i f_j}$ are the left and right-handed couplings of the W′ boson to fermions, $g_w = e/(s_w)$ is the SM weak coupling constant and $V_{f_i f_j}$ is the SM CKM matrix element if the fermion (f) is a quark, and $V_{f_i f_j} == \delta_{ij}$ if it is a lepton, where δ_{ij} is the Kronecker delta and i, j is the generation number.

This Lagrangian has been incorporated into the CompHEP package as a new theoretical model and has been included into the SINGLETOP [38] generator for event generation [116]. Three

sets of samples are generated: the left handed, right handed, and mixed W′ boson. For the left-handed case, SINGLETOP simulates the SM s-channel W′ boson signal with interference with the SM W boson. Here, $a^L_{ud} = a^L_{cs} = a^L_{tb} = 1, a^R_{ud} = a^R_{cs} = a^R_{tb} = 0$. For the right-handed case, SINGLETOP generates a W′ boson signal with no interference with $a^L_{ud} = a^L_{cs} = a^L_{tb} = 0, a^R_{ud} = a^R_{cs} = a^R_{tb} = 1$ since the W'_R boson couples with different final state particles than the SM W boson. For the mixed case, SINGLETOP generates a W′ boson signal with interference with the SM W boson and $a^L_{ud} = a^L_{cs} = a^L_{tb} = a^R_{ud} = a^R_{cs} = a^R_{tb} = 1$. The complete chain of W′ boson, top quark, and SM W boson decays taking into account finite widths and spin correlations between resonance state production and subsequent decay are simulated using CTEQ611 [42] parton distribution functions with M_t at 172 GeV and the QCD scale set to M'_W. Next-to-Leading-Order (NLO) corrections are included in the SINGLETOP generator and normalization and matching between various partonic sub-processes are performed such that not only NLO rates but also the NLO shapes of distributions are reproduced.

For the W'_R boson, the two possible decay modes have the same parton level invariant mass distributions as seen in Figure 8.1. Furthermore, the W'_R boson decay mode where all decays are possible is the same as W'_L boson with no interference. Since the shape distributions are the same, one can just run the analysis once through Boosted Decisions Trees (BDT) where an overview of this technique is described in a later section. The W'_R boson BDT distribution is then scaled to the theoretical cross sections [117] for each of the two decay modes to determine two mass limits. The right-handed samples are generated where all decays are allowed.

The samples are generated for masses from 600 to 1000 GeV in 50 GeV steps. These L0 cross-sections are then scaled to NLO using the k-factors from Ref. [117]. Table 8.1 shows the signal samples total NLO cross sections and its uncertainty which includes scale, PDFs, and top quark mass uncertainties. The parton-level samples are then processed with PYTHIA [39] and a GEANT-based [36] simulation of the $D\emptyset$ detector [37]. The samples go through the same smearing and corrections mentioned in Chapter 5.

Additionally, the left-handed and mixed sample events have a cut on $\sqrt{\hat{s}}$, defined as the

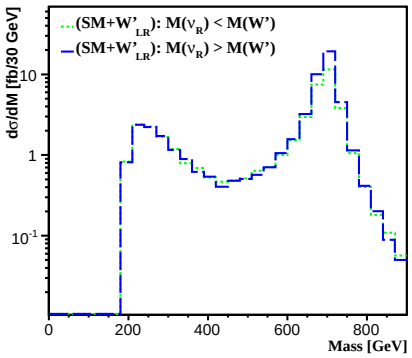

Figure 8.1: Parton level invariant mass distribution for right handed W′ boson production at a mass of 700 GeV.

$M_{W'}$ (GeV)	$\sigma(W'_L) \times BR(W'_L \to t\bar{b})$ (pb)	$\sigma(W'_R) \times BR(W' \to t\bar{b})$ $(M_{\nu_R} < M_{W'})$ (pb)	$(M_{\nu_R} > M_{W'})$ (pb)	$\sigma(W'_{mixed}) \times BR(W'_L \to t\bar{b})$ (pb)
600	2.23 (±11%)	2.10 (±11%)	2.79 (±11%)	4.13 (±11%)
650	1.04 (±13%)	1.25 (±13%)	1.65 (±12%)	2.62 (±13%)
700	0.81 (±13%)	0.74 (±13%)	0.97 (±13%)	1.74 (±13%)
750	0.68 (±14%)	0.44 (±14%)	0.57 (±14%)	1.23 (±14%)
800	0.61 (±15%)	0.26 (±15%)	0.34 (±15%)	0.94 (±15%)
850	0.61 (±16%)	0.16 (±16%)	0.20 (±16%)	0.78 (±16%)
900	0.61 (±17%)	0.09 (±17%)	0.12 (±18%)	0.69 (±17%)
950	0.57 (±15%)	0.06 (±15%)	0.05 (±15%)	0.64 (±15%)
1000	0.57 (±16%)	0.03 (±16%)	0.03 (±16%)	0.62 (±16%)
1050	0.57 (±17%)	0.02 (±17%)	0.02 (±18%)	0.61 (±17%)
1100	0.58 (±17%)	0.01 (±17%)	0.01 (±18%)	0.60 (±17%)

Table 8.1: List of signal samples and total NLO cross sections for the process $p\bar{p} \to \sigma(W') \times BR(W' \to t\bar{b})$. The uncertainty includes contributions from scale, PDFs, and the top quark mass.

invariant mass constructed from the jets, lepton and neutrino. The events must have an $\sqrt{\hat{s}}$ greater than 400 GeV since this tends to cut away most of the SM W boson. The yield values for all data and MC for left-handed samples, mixed samples, and right handed samples can be found in Table 8.2 - 8.13 where the left-handed and mixed data and MC background events are the same as the right-handed events except they must have a $\sqrt{\hat{s}}$ greater than 400 GeV. Furthermore, the right-handed MC background and data form the basis of the electroweak produced top quark analysis already mentioned.

Yields with One b-Tagged Jet

	Electron Channel			Muon Channel		
	2 jets	3 jets	4 jets	2 jets	3 jets	4 jets
Right-handed signals (alldecays)						
W' (600) GeV	15.20	8.01	2.50	16.50	9.70	3.13
W' (650) GeV	8.78	4.72	1.45	9.28	5.62	1.87
W' (700) GeV	5.04	2.70	0.84	5.18	3.23	1.08
W' (750) GeV	2.90	1.54	0.47	3.01	1.90	0.61
W' (800) GeV	1.65	0.91	0.26	1.67	1.06	0.37
W' (850) GeV	0.97	0.52	0.16	0.99	0.62	0.22
W' (900) GeV	0.54	0.28	0.08	0.55	0.34	0.12
W' (950) GeV	0.32	0.17	0.05	0.33	0.21	0.07
W' (1000) GeV	0.20	0.10	0.03	0.21	0.13	0.04
W' (1050) GeV	0.13	0.06	0.02	0.15	0.09	0.03
W' (1100) GeV	0.09	0.04	0.01	0.08	0.04	0.01
Right-handed signals (qqdecays)						
W' (600) GeV	20.2	10.6	3.37	21.9	12.9	4.29
W' (650) GeV	11.6	6.22	1.96	12.2	7.4	2.53
W' (700) GeV	6.59	3.53	1.13	6.78	4.23	1.43
W' (750) GeV	3.76	2	0.616	3.91	2.47	0.818
W' (800) GeV	2.16	1.19	0.357	2.19	1.38	0.499
W' (850) GeV	1.21	0.649	0.215	1.24	0.776	0.279
W' (900) GeV	0.721	0.37	0.118	0.727	0.457	0.161
W' (950) GeV	0.263	0.142	0.0456	0.272	0.167	0.0588
W' (1000) GeV	0.161	0.0827	0.0247	0.169	0.102	0.0338
W' (1050) GeV	0.104	0.0516	0.0167	0.121	0.0724	0.0248
W' (1100) GeV	0.0694	0.0345	0.0107	0.0619	0.036	0.0119
Backgrounds						
tb	9.06	3.11	0.821	10.2	3.93	1.02
tqb	17.4	6.61	2.14	20.5	8.58	2.61
ttbar-dilepton	23.6	14.2	4.35	22.1	15.6	4.81
ttbar-lepjets	16.3	52	57	12.5	54.3	69.8
wbb	135	44.2	12	146	57.1	16
wcc	66	24.8	8.06	73.9	33.4	9.89
wlp	172	46	11.1	199	60.2	14.4
zbb	6.52	2.76	0.891	26.8	7.95	2.51
zcc	2.75	1.18	0.549	13.3	4.57	1.46
zlp	5.45	1.77	0.633	12.7	4.26	1.07
QCD	28	10.3	3.03	51.4	17.2	7.32
diboson	16.2	5.27	1.38	22.3	7.77	2.12
Background Sum (for W'_R)	498.5	212.3	102.0	611.3	274.9	132.0
DATA	508	202	103	627	259	131

Table 8.2: Yields for W'_R signal and background, after selection for p17 events with exactly one b-tagged jet.

Yields with Two b-Tagged Jet

	Electron Channel			Muon Channel		
	2 jets	3 jets	4 jets	2 jets	3 jets	4 jets
Right-handed signals (alldecays)						
W' (600) GeV	10.10	5.93	1.95	12.40	7.61	2.56
W' (650) GeV	5.87	3.51	1.15	7.14	4.47	1.48
W' (700) GeV	3.28	2.00	0.65	3.93	2.58	0.89
W' (750) GeV	1.93	1.14	0.38	2.35	1.52	0.50
W' (800) GeV	1.06	0.67	0.21	1.31	0.85	0.31
W' (850) GeV	0.62	0.37	0.13	0.75	0.49	0.18
W' (900) GeV	0.34	0.20	0.07	0.42	0.27	0.09
W' (950) GeV	0.20	0.13	0.04	0.25	0.16	0.06
W' (1000) GeV	0.13	0.07	0.02	0.16	0.10	0.03
W' (1050) GeV	0.08	0.05	0.01	0.11	0.07	0.02
W' (1100) GeV	0.06	0.03	0.01	0.06	0.03	0.01
Right-handed signals (qqdecays)						
W' (600) GeV	13.4	7.88	2.61	16.5	10.1	3.48
W' (650) GeV	7.73	4.63	1.54	9.41	5.88	1.99
W' (700) GeV	4.29	2.62	0.866	5.14	3.38	1.17
W' (750) GeV	2.5	1.47	0.484	3.05	1.97	0.668
W' (800) GeV	1.39	0.871	0.28	1.71	1.12	0.409
W' (850) GeV	0.771	0.466	0.167	0.941	0.614	0.225
W' (900) GeV	0.452	0.266	0.0913	0.557	0.364	0.132
W' (950) GeV	0.165	0.104	0.0344	0.204	0.133	0.0479
W' (1000) GeV	0.102	0.0593	0.0193	0.126	0.0804	0.0271
W' (1050) GeV	0.0667	0.0379	0.0128	0.0897	0.0564	0.0197
W' (1100) GeV	0.0451	0.0252	0.00802	0.0456	0.0281	0.00935
Backgrounds						
tb	5.69	2.12	0.583	6.66	2.75	0.747
tqb	0.808	1.61	0.903	0.923	2.15	1.07
ttbar-dilepton	13.9	9.7	3.12	14.1	11.2	3.58
ttbar-lepjets	4.32	28.6	43.2	3.51	32.2	55.4
wbb	34	12.3	3.69	35.6	15.7	4.77
wcc	5.12	2.75	1.28	5.62	3.56	1.5
wlp	2.89	1.54	0.533	3.32	2.03	0.727
zbb	0.881	0.739	0.307	6.14	2.6	0.905
zcc	0.147	0.133	0.104	1.04	0.537	0.248
zlp	0.144	0.089	0.0448	0.31	0.203	0.073
QCD	1.9	1.1	0.484	3.28	1.98	0.927
diboson	2.05	0.853	0.281	3.06	1.37	0.459
Background Sum (for W'_R)	71.8	61.5	54.5	83.6	76.3	70.4
DATA	67	61	37	71	62	56

Table 8.3: Yields for W'_R signal and background, after selection for p17 events with exactly two b-tagged jet.

Yields with One b-Tagged Jet

	Electron Channel			Muon Channel		
	2 jets	3 jets	4 jets	2 jets	3 jets	4 jets
Right-handed signals (alldecays)						
W' (600) GeV	14.10	8.18	2.91	15.30	9.99	3.54
W' (650) GeV	8.14	4.80	1.78	8.42	5.68	2.09
W' (700) GeV	4.52	2.74	0.96	5.01	3.29	1.20
W' (750) GeV	2.57	1.59	0.53	3.01	2.07	0.84
W' (800) GeV	1.44	0.89	0.31	1.54	1.05	0.40
W' (850) GeV	0.86	0.52	0.18	0.89	0.63	0.24
W' (900) GeV	0.47	0.28	0.10	0.49	0.33	0.13
W' (950) GeV	0.28	0.17	0.06	0.31	0.20	0.07
W' (1000) GeV	0.18	0.10	0.03	0.19	0.12	0.04
W' (1050) GeV	0.12	0.06	0.02	0.13	0.08	0.03
W' (1100) GeV	0.08	0.04	0.01	0.09	0.05	0.02
Right-handed signals (qqdecays)						
W' (600) GeV	18.7	10.9	3.97	20.4	13.3	4.85
W' (650) GeV	10.7	6.33	2.39	11.1	7.48	2.83
W' (700) GeV	5.91	3.58	1.29	6.55	4.31	1.63
W' (750) GeV	3.33	2.07	0.711	3.9	2.69	1.12
W' (800) GeV	1.88	1.17	0.416	2.02	1.37	0.536
W' (850) GeV	1.08	0.655	0.23	1.11	0.781	0.315
W' (900) GeV	0.618	0.375	0.133	0.654	0.444	0.175
W' (950) GeV	0.228	0.138	0.052	0.248	0.165	0.0618
W' (1000) GeV	0.142	0.082	0.0292	0.153	0.0985	0.0395
W' (1050) GeV	0.0932	0.0523	0.0188	0.103	0.0644	0.0237
W' (1100) GeV	0.0628	0.0349	0.0125	0.0698	0.0423	0.0155
Backgrounds						
tb	9.46	3.29	0.909	9.94	4.27	1.23
tqb	16.9	7.21	2.47	18.5	8.75	2.96
ttbar-dilepton	25.6	16.1	4.89	23.5	17	5.04
ttbar-lepjets	16.4	53.8	61.5	12.2	53.6	70.6
wbb	130	44.3	11.6	136	53.4	16.8
wcc	68.6	26.2	7.56	72.4	32.6	10.9
wlp	221	61.2	15	240	76.2	21
zbb	4.95	2.37	1.01	20.1	7.66	2.17
zcc	2.09	1.1	0.565	10.7	4.3	1.18
zlp	5.99	2.08	0.791	13.9	5.02	1.34
QCD	31	10.1	7.15	73.5	28.2	9.02
diboson	17.4	5.83	1.66	22.7	8.36	2.41
Background Sum (for W'_R)	548.5	233.6	114.2	653.7	299.5	144.7
DATA	547	207	124	595	290	142

Table 8.4: Yields for W'_R signal and background, after selection for p20 events with exactly one b-tagged jet.

Yields with Two b-Tagged Jet

	Electron Channel			Muon Channel		
	2 jets	3 jets	4 jets	2 jets	3 jets	4 jets
Right-handed signals (alldecays)						
W' (600) GeV	7.17	4.79	1.85	8.29	5.94	2.22
W' (650) GeV	3.97	2.70	1.10	4.45	3.35	1.29
W' (700) GeV	2.12	1.51	0.58	2.56	1.90	0.74
W' (750) GeV	1.18	0.87	0.31	1.50	1.18	0.50
W' (800) GeV	0.65	0.48	0.18	0.76	0.58	0.24
W' (850) GeV	0.38	0.27	0.10	0.44	0.34	0.14
W' (900) GeV	0.21	0.15	0.05	0.24	0.18	0.07
W' (950) GeV	0.13	0.09	0.03	0.15	0.11	0.04
W' (1000) GeV	0.08	0.05	0.02	0.09	0.07	0.03
W' (1050) GeV	0.05	0.04	0.01	0.07	0.04	0.01
Right-handed signals (qqdecays)						
W' (600) GeV	9.52	6.36	2.52	11	7.89	3.04
W' (650) GeV	5.22	3.55	1.48	5.86	4.41	1.73
W' (700) GeV	2.77	1.97	0.781	3.35	2.48	0.988
W' (750) GeV	1.53	1.12	0.419	1.94	1.53	0.685
W' (800) GeV	0.848	0.622	0.243	0.993	0.755	0.318
W' (850) GeV	0.477	0.337	0.133	0.55	0.426	0.182
W' (900) GeV	0.273	0.195	0.0779	0.321	0.241	0.101
W' (950) GeV	0.102	0.072	0.0301	0.121	0.0892	0.0361
W' (1000) GeV	0.0653	0.0432	0.0168	0.077	0.0544	0.0232
W' (1050) GeV	0.0446	0.0288	0.011	0.0538	0.036	0.0143
W' (1100) GeV	0.0312	0.0195	0.00744	0.0373	0.0243	0.00931
Backgrounds						
tb	5.26	2	0.575	5.61	2.59	0.782
tqb	0.941	1.89	1.01	0.994	2.22	1.21
ttbar-dilepton	13.6	9.99	3.17	13	10.8	3.33
ttbar-lepjets	4.07	27.7	43.4	3.11	29	51.1
wbb	30.5	12.2	3.43	30.8	14.4	5.07
wcc	5.55	3.15	1.17	5.6	3.72	1.67
wlp	4.85	2.63	0.918	5.27	3.24	1.31
zbb	0.688	0.601	0.341	4.34	2.07	0.696
zcc	0.137	0.141	0.104	0.86	0.533	0.186
zlp	0.158	0.105	0.056	0.341	0.239	0.0912
QCD	2.25	1.37	1.13	4.92	3.12	0.966
diboson	1.96	0.911	0.298	2.98	1.38	0.46
Background Sum (for W'_R)	69.99	62.68	55.03	77.81	73.31	66.87
DATA	79	56	51	85	79	80

Table 8.5: Yields for W'_R signal and background, after selection for p20 events with exactly two b-tagged jet.

Yields with One b-Tagged Jet

	Electron Channel			Muon Channel		
	2 jets	3 jets	4 jets	2 jets	3 jets	4 jets
Left-handed signals (SM+W'_L)						
W' (600) GeV	12.3	7.32	1.98	12.6	8.75	2.46
W' (650) GeV	7.04	4.25	1.19	7.03	5.03	1.49
W' (700) GeV	3.9	2.39	0.707	3.85	2.82	0.89
W' (750) GeV	2.18	1.43	0.466	2.15	1.67	0.544
W' (800) GeV	1.21	0.803	0.267	1.21	0.976	0.362
W' (850) GeV	0.709	0.584	0.193	0.721	0.65	0.226
W' (900) GeV	0.477	0.392	0.141	0.502	0.462	0.199
W' (950) GeV	0.362	0.317	0.13	0.318	0.406	0.162
W' (1000) GeV	0.284	0.266	0.119	0.306	0.376	0.149
W' (1050) GeV	0.24	0.278	0.113	0.301	0.343	0.157
W' (1100) GeV	0.24	0.262	0.106	0.241	0.306	0.144
Backgrounds						
tqb	1.7	1.89	1.17	1.95	2.45	1.41
ttbar-dilepton	2.71	3.85	2.33	2.46	4.18	2.49
ttbar-lepjets	3.01	17.2	30.2	2.4	18.2	36.6
wbb	7.05	8.46	4.84	7.12	10.4	6.67
wcc	3.1	4.49	3.23	3.47	6.01	4.08
wlp	9.05	8.35	4.23	12.7	12.3	6.73
zbb	0.586	0.805	0.425	1.31	1.38	0.884
zcc	0.294	0.339	0.351	0.506	0.781	0.401
zlp	0.6	0.505	0.328	0.872	0.914	0.436
QCD	3.86	3.23	1.5	7.64	6.2	3.58
diboson	0.844	0.804	0.513	1.08	1.2	0.815
Background Sum (for W'_L)	32.80	49.92	49.12	41.51	64.02	64.10
DATA	36	49	56	40	59	71

Table 8.6: Yields for W'_L signal and background, after selection for p17 events with exactly one b-tagged jet with $\sqrt{\hat{s}}$ cut > 400 GeV.

Yields with Two b-Tagged Jet

	Electron Channel			Muon Channel		
	2 jets	3 jets	4 jets	2 jets	3 jets	4 jets
Left-handed signals (SM+W'_L)						
W' (600) GeV	9.37	5.64	1.55	10.2	7.07	1.98
W' (650) GeV	5.44	3.28	0.954	5.71	4.1	1.22
W' (700) GeV	2.94	1.85	0.564	3.16	2.33	0.725
W' (750) GeV	1.63	1.13	0.374	1.71	1.37	0.433
W' (800) GeV	0.862	0.604	0.214	0.985	0.804	0.281
W' (850) GeV	0.536	0.423	0.149	0.591	0.506	0.168
W' (900) GeV	0.339	0.288	0.113	0.398	0.36	0.156
W' (950) GeV	0.25	0.244	0.0854	0.271	0.285	0.129
W' (1000) GeV	0.212	0.198	0.0927	0.233	0.288	0.117
W' (1050) GeV	0.165	0.193	0.0778	0.224	0.228	0.123
W' (1100) GeV	0.165	0.181	0.0787	0.177	0.229	0.107
Backgrounds						
tqb	0.0584	0.507	0.535	0.0535	0.66	0.586
ttbar-dilepton	1.75	2.78	1.69	1.74	3.14	1.9
ttbar-lepjets	0.849	10.2	23.3	0.757	12	29.8
wbb	1.89	1.75	1.26	1.87	2.28	2.01
wcc	0.247	0.446	0.444	0.26	0.62	0.613
wlp	0.158	0.289	0.212	0.223	0.414	0.321
zbb	0.119	0.141	0.146	0.365	0.361	0.282
zcc	0.0173	0.0322	0.0698	0.05	0.0953	0.0629
zlp	0.0201	0.0289	0.0251	0.0246	0.046	0.0314
QCD	0.456	0.312	0.269	0.571	0.688	0.464
diboson	0.115	0.134	0.103	0.164	0.197	0.219
Background Sum (for W'_L)	5.68	16.6	28.1	6.08	20.5	36.3
DATA	4	14	24	3	18	30

Table 8.7: Yields for W'_L signal and background, after selection for p17 events with exactly two b-tagged jet with $\sqrt{\hat{s}}$ cut > 400 GeV.

Yields with One b-Tagged Jet

	Electron Channel			Muon Channel		
	2 jets	3 jets	4 jets	2 jets	3 jets	4 jets
Left-handed signals (SM+W'_L)						
W' (600) GeV	12	7.9	2.36	12	8.89	2.92
W' (650) GeV	6.45	4.36	1.36	6.66	4.89	1.59
W' (700) GeV	3.59	2.47	0.844	3.61	2.91	0.989
W' (750) GeV	1.89	1.41	0.493	1.91	1.59	0.623
W' (800) GeV	1.06	0.811	0.322	1.08	0.986	0.372
W' (850) GeV	0.666	0.505	0.214	0.61	0.613	0.276
W' (900) GeV	0.412	0.399	0.189	0.404	0.466	0.206
W' (950) GeV	0.286	0.292	0.149	0.321	0.384	0.172
W' (1000) GeV	0.252	0.299	0.153	0.28	0.35	0.185
W' (1050) GeV	0.232	0.26	0.164	0.234	0.276	0.19
W' (1100) GeV	0.202	0.272	0.156	0.231	0.33	0.175
Backgrounds						
tqb	1.6	2.07	1.4	1.59	2.39	1.68
ttbar-dilepton	2.75	4.21	2.51	2.6	4.55	2.45
ttbar-lepjets	2.66	17.2	32.2	2.27	17.4	36.3
wbb	5.49	6.88	4.14	5.53	8.73	6.9
wcc	2.71	3.88	3.01	2.87	5.36	4.39
wlp	12.5	10.6	5.47	16.5	14	8.46
zbb	0.381	0.476	0.453	0.893	1.23	0.842
zcc	0.168	0.261	0.26	0.395	0.663	0.414
zlp	0.659	0.594	0.41	0.958	1.08	0.545
QCD	3.41	2.59	3.07	6.84	7.89	5.12
diboson	0.899	0.867	0.606	1.15	1.39	0.905
Background Sum (for W'_L)	33.23	49.63	53.53	41.60	64.68	68.01
DATA	27	47	60	33	73	68

Table 8.8: Yields for W'_L signal and background, after selection for p20 events with exactly one b-tagged jet with $\sqrt{\hat{s}}$ cut > 400 GeV.

Yields with Two b-Tagged Jet

	Electron Channel			Muon Channel		
	2 jets	3 jets	4 jets	2 jets	3 jets	4 jets
Left-handed signals (SM+W'_L)						
W' (600) GeV	6.38	4.59	1.48	6.57	5.27	1.81
W' (650) GeV	3.31	2.41	0.836	3.51	2.78	0.956
W' (700) GeV	1.76	1.35	0.503	1.84	1.64	0.596
W' (750) GeV	0.878	0.735	0.291	0.968	0.879	0.357
W' (800) GeV	0.483	0.432	0.194	0.514	0.532	0.219
W' (850) GeV	0.314	0.277	0.125	0.297	0.33	0.171
W' (900) GeV	0.174	0.226	0.112	0.193	0.259	0.124
W' (950) GeV	0.143	0.172	0.0942	0.164	0.219	0.11
W' (1000) GeV	0.125	0.171	0.0955	0.146	0.216	0.118
W' (1050) GeV	0.126	0.156	0.106	0.118	0.16	0.119
W' (1100) GeV	0.111	0.162	0.105	0.126	0.199	0.106
Backgrounds						
tqb	0.0668	0.61	0.58	0.0609	0.687	0.716
ttbar-dilepton	1.47	2.65	1.64	1.43	2.92	1.68
ttbar-lepjets	0.625	9.45	23.2	0.569	10	26.4
wbb	1.13	1.64	1.23	1.13	1.84	2.06
wcc	0.188	0.454	0.449	0.251	0.564	0.681
wlp	0.339	0.507	0.365	0.38	0.661	0.565
zbb	0.0781	0.139	0.156	0.196	0.355	0.307
zcc	0.0103	0.0325	0.0436	0.0298	0.0848	0.0705
zlp	0.0221	0.0339	0.0314	0.0271	0.0541	0.0392
QCD	0.183	0.413	0.537	0.351	0.719	0.644
diboson	0.137	0.152	0.117	0.174	0.24	0.174
Background Sum (for W'_L)	4.25	16.08	28.35	4.60	18.13	33.34
DATA	2	10	33	7	19	48

Table 8.9: Yields for W'_L signal and background, after selection for p20 events with exactly two b-tagged jet with $\sqrt{\hat{s}}$ cut > 400 GeV.

Yields with One b-Tagged Jet

	Electron Channel			Muon Channel		
	2 jets	3 jets	4 jets	2 jets	3 jets	4 jets
Mixed Signals (SM+W'_L+W'_R)						
W' (600) GeV	24.8	14.7	4.87	25.4	16.6	5.96
W' (650) GeV	9.67	5.82	1.88	10.4	6.9	2.52
W' (700) GeV	8.34	4.8	1.79	8.18	5.75	2.14
W' (750) GeV	4.89	2.91	1.04	4.92	3.27	1.31
W' (800) GeV	2.79	1.75	0.668	2.68	2.08	0.809
W' (850) GeV	1.71	1.04	0.456	1.67	1.28	0.51
W' (900) GeV	1.06	0.682	0.286	2.07	1.73	0.753
W' (950) GeV	0.643	0.52	0.254	0.681	0.581	0.302
W' (1000) GeV	0.508	0.384	0.193	0.497	0.477	0.245
Backgrounds						
tqb	1.7	1.89	1.17	1.95	2.45	1.41
ttbar-dilepton	2.71	3.85	2.33	2.46	4.18	2.49
ttbar-lepjets	3.01	17.2	30.2	2.4	18.2	36.6
wbb	7.05	8.46	4.84	7.12	10.4	6.67
wcc	3.1	4.49	3.23	3.47	6.01	4.08
wlp	9.05	8.35	4.23	12.7	12.3	6.73
zbb	0.586	0.805	0.425	1.31	1.38	0.884
zcc	0.294	0.339	0.351	0.506	0.781	0.401
zlp	0.6	0.505	0.328	0.872	0.914	0.436
QCD	3.86	3.23	1.5	7.64	6.2	3.58
diboson	0.844	0.804	0.513	1.08	1.2	0.815
Background Sum (for W'_L)	32.80	49.92	49.12	41.51	64.02	64.10
DATA	36	49	56	40	59	71

Table 8.10: Yields for mixed W'_L and W'_R signal and background, after selection for p17 events with exactly one b-tagged jet and $\sqrt{\hat{s}}$ cut > 400 GeV.

Yields with Two b-Tagged Jet

	Electron Channel			Muon Channel		
	2 jets	3 jets	4 jets	2 jets	3 jets	4 jets
Mixed Signals (SM+W'_L+W'_R)						
W' (600) GeV	18.1	11.3	3.8	20	13.2	4.83
W' (650) GeV	6.95	4.36	1.44	8.34	5.5	2.02
W' (700) GeV	5.86	3.63	1.39	6.48	4.63	1.74
W' (750) GeV	3.41	2.15	0.819	3.9	2.58	1.05
W' (800) GeV	1.94	1.33	0.524	2.18	1.67	0.658
W' (850) GeV	1.14	0.775	0.342	1.29	1.02	0.413
W' (900) GeV	0.731	0.505	0.226	1.66	1.41	0.621
W' (950) GeV	0.437	0.374	0.187	0.531	0.458	0.239
W' (1000) GeV	0.366	0.288	0.144	0.394	0.375	0.188
Backgrounds						
tqb	0.0584	0.507	0.535	0.0535	0.66	0.586
ttbar-dilepton	1.75	2.78	1.69	1.74	3.14	1.9
ttbar-lepjets	0.849	10.2	23.3	0.757	12	29.8
wbb	1.89	1.75	1.26	1.87	2.28	2.01
wcc	0.247	0.446	0.444	0.26	0.62	0.613
wlp	0.158	0.289	0.212	0.223	0.414	0.321
zbb	0.119	0.141	0.146	0.365	0.361	0.282
zcc	0.0173	0.0322	0.0698	0.05	0.0953	0.0629
zlp	0.0201	0.0289	0.0251	0.0246	0.046	0.0314
QCD	0.456	0.312	0.269	0.571	0.688	0.464
diboson	0.115	0.134	0.103	0.164	0.197	0.219
Background Sum (for W'_L)	5.68	16.6	28.1	6.08	20.5	36.3
DATA	4	14	24	3	18	30

Table 8.11: Yields for mixed W'_L and W'_R signal and background, after selection for p17 events with exactly two b-tagged jets and $\sqrt{\hat{s}}$ cut > 400 GeV.

Yields with One b-Tagged Jet

	Electron Channel			Muon Channel		
	2 jets	3 jets	4 jets	2 jets	3 jets	4 jets
Mixed Signals (SM+W'_L+W'_R)						
W' (600) GeV	23.1	14.7	5.87	23.4	17	6.48
W' (650) GeV	13.8	8.61	3.57	13.6	9.94	3.9
W' (700) GeV	7.63	5.06	1.96	7.62	5.53	2.39
W' (750) GeV	4.23	2.87	1.14	4.49	3.22	1.47
W' (800) GeV	2.42	1.73	0.755	2.44	1.98	0.908
W' (850) GeV	1.48	1.05	0.494	1.53	1.25	0.604
W' (900) GeV	0.901	0.711	0.376	0.95	0.834	0.42
W' (950) GeV	0.635	0.512	0.274	0.649	0.607	0.357
W' (1000) GeV	0.466	0.382	0.235	0.481	0.516	0.296
Backgrounds						
tqb	1.6	2.07	1.4	1.59	2.39	1.68
ttbar-dilepton	2.75	4.21	2.51	2.6	4.55	2.45
ttbar-lepjets	2.66	17.2	32.2	2.27	17.4	36.3
wbb	5.49	6.88	4.14	5.53	8.73	6.9
wcc	2.71	3.88	3.01	2.87	5.36	4.39
wlp	12.5	10.6	5.47	16.5	14	8.46
zbb	0.381	0.476	0.453	0.893	1.23	0.842
zcc	0.168	0.261	0.26	0.395	0.663	0.414
zlp	0.659	0.594	0.41	0.958	1.08	0.545
QCD	3.41	2.59	3.07	6.84	7.89	5.12
diboson	0.899	0.867	0.606	1.15	1.39	0.905
Background Sum (for W'_L)	33.23	49.63	53.53	41.60	64.68	68.01
DATA	27	47	60	33	73	68

Table 8.12: Yields for mixed W'_L and W'_R signal and background, after selection for p20 events with exactly one b-tagged jet and $\sqrt{\hat{s}}$ cut > 400 GeV.

Yields with Two b-Tagged Jet

	Electron Channel			Muon Channel		
	2 jets	3 jets	4 jets	2 jets	3 jets	4 jets
Mixed Signals (SM+W'_L+W'_R)						
W' (600) GeV	11.9	8.59	3.68	12.7	10	4.09
W' (650) GeV	6.87	4.84	2.11	7.2	5.71	2.37
W' (700) GeV	3.69	2.82	1.17	3.92	3.13	1.44
W' (750) GeV	2.01	1.56	0.685	2.25	1.76	0.868
W' (800) GeV	1.12	0.926	0.451	1.19	1.09	0.528
W' (850) GeV	0.712	0.56	0.279	0.785	0.717	0.366
W' (900) GeV	0.408	0.377	0.222	0.463	0.466	0.255
W' (950) GeV	0.302	0.285	0.177	0.322	0.334	0.214
W' (1000) GeV	0.237	0.219	0.147	0.254	0.311	0.189
Backgrounds						
tqb	0.0668	0.61	0.58	0.0609	0.687	0.716
ttbar-dilepton	1.47	2.65	1.64	1.43	2.92	1.68
ttbar-lepjets	0.625	9.45	23.2	0.569	10	26.4
wbb	1.13	1.64	1.23	1.13	1.84	2.06
wcc	0.188	0.454	0.449	0.251	0.564	0.681
wlp	0.339	0.507	0.365	0.38	0.661	0.565
zbb	0.0781	0.139	0.156	0.196	0.355	0.307
zcc	0.0103	0.0325	0.0436	0.0298	0.0848	0.0705
zlp	0.0221	0.0339	0.0314	0.0271	0.0541	0.0392
QCD	0.183	0.413	0.537	0.351	0.719	0.644
diboson	0.137	0.152	0.117	0.174	0.24	0.174
Background Sum (for W'_L)	4.25	16.08	28.35	4.60	18.13	33.34
DATA	2	10	33	7	19	48

Table 8.13: Yields for mixed W'_L and W'_R signal and background, after selection for p20 events with exactly two b-tagged jets and $\sqrt{\hat{s}}$ cut > 400 GeV.

8.3 Analysis

This analysis builds upon the singly produced top quark analysis mentioned in previous chapters. The limits set are based on W′ boson that decays in the following manner: $W' \rightarrow tb \rightarrow Wbb \rightarrow l\nu bb$ using the $l\nu$+jet events. Since the signal sample is much smaller than the background, a multivariate technique is used to separate the signal and background where the background samples are the same as the electroweak produced top quark analysis except the s-channel and t-channel electroweak produced top quark is now a background process (though in the case of W'_L and W'_{mixed} boson, only the t-channel electroweak produced top quark is

added to the background since the s-channel production is incorporated in the W'_L and W'_{mixed} boson signal samples). The multivariate technique used is the Boosted Decision Tree (BDT) and a general outline of the technique will be discussed. A more in-depth discussion can be found in [83] and [82].

8.3.1 Boosted Decision Trees

The BDTs also try to approximate the discriminant: $D(x) = \frac{P(S)}{P(S)+P(B)}$. The way that a decision tree operates is, using a list of topological variables that have different shapes for signal and background, a cut is imposed on the sample that gives the optimal separation between signal and background. In a simple cuts based analysis, the events that do not pass the cut are thrown away. However, in a decision tree analysis, both the events that do and do not pass the cut are used, branching off into two daughter nodes. For each daughter node, another cut is applied on a topological variable at a cut value which gives the most optimal separation between signal and background, leading to two new daughter nodes for each node. This process continues for each node until there are less than 100 events or until there is no overall improvement over the entire decision tree. The basis of optimal separation and improvement is measured using the Gini Factor which will be discussed more in detail in a subsequent section. In this implementation of the decision tree, each node is run over where cuts at set steps are applied for all the topological variables selected by the user and the Gini Factor is calculated for each cut until the highest Gini factor is found. This cut is applied unless there is not enough events in the node or there is no overall improvement for the sample. Once this process is over, the discriminant value for the event is just the purity in the node that the event ends up where the purity is the signal yield over the total yield in the node. A pictorial representation of a decision tree can be found in Fig. 8.2.

However, events can be misclassified and this process done once may lead to discrete discriminant distributions. The decision tree also might not be robust enough on a sample that is not exactly that used for training. These problems can be solved using boosting which will be

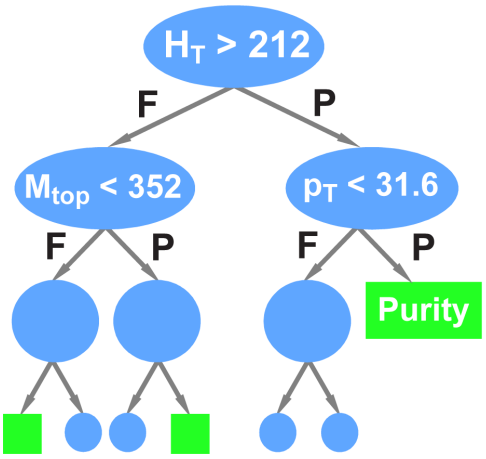

Figure 8.2: A pictorial depiction of a decision tree where a cut on a variable is used to separate events that pass and fail the cut. Events that fail the cut are kept and another cut on a variable is used for events that pass and fail the first cut. This process is repeated until there is not enough events to continue or there is no improvement in the separation by adding more cuts.

discussed further in a subsequent section.

8.3.2 Variables

Variables that highlight the shape difference between the W′ boson signal samples and the background play a key role in this analysis since this analysis relies on multiple cuts applied to these variables on different event subsets which include subsets that would normally be excluded from a cuts based analysis. As a result, MC must be well modeled to data in order to understand what cuts work best and to have confidence in the discriminant built by the DT and the cross section measurement that comes from this discriminant. For a variable to be well modeled it must have at least a Kolmogorov-Smirnov (KS) [48] probability value of 0.1 as described earlier.

In total, from 600 variables, only 49 are used by the BDTs where each jet, lepton, b-tag, data, and W′ boson handedness are trained for each mass point. The variables can be divided into five types: object kinematics,s event kinematics, jet reconstruction, top quark reconstruction, and angular correlations.

Object Kinematics

These are individual object (i.e. jets, lepton, $\not\!\!E_T$) transverse energy (E_T) or momentum (p_T).

- p_T(BestJet): The transverse momentum of the best jet. The best jet is defined as the jet that produces an invariant mass $M(W, \text{jet})$ closest to $m_{\text{top}} = 170$ GeV.
- p_T(Jet1): transverse momentum of the leading jet
- p_T(NotBest1): transverse momentum of the leading jet that is not the best jet.
- p_T(Jet2): transverse momentum of the second leading jet
- p_T(NotBest2): transverse momentum of the second leading jet that is not the best jet.
- p_T(Jet3): transverse momentum of the third leading jet.
- p_T(Jet4): transverse momentum of the fourth leading jet.
- p_T(LeadingBTaggedJet): transverse momentum of the leading b-tagged jet.
- p_T(LeadingLightQuarkJet): transverse momentum of the leading jet associated with the light quark.
- $\not\!\!E_T$: the $\not\!\!E_T$ of the event.
- Q(lepton)$\times$ η(jet1): pseudorapidity of the leading jet multiplied with the charge of the lepton.
- p_T(SecondLightQuarkJet): transverse momentum of the second leading jet associated with the light quark.

Event kinematics

These are total transverse energy or invariant mass variables.

- Aplanarity(W,AllJets): This describes the momentum flow of jets in the event. It is based on the smallest of the three eigenvalues of the momentum tensor M_{ab} of the jets in the event. Planar events have $Q_1 = Q_2 = 0$ and $Q_3 = 1$. The aplanarity is $\frac{3Q_1}{2}$.

- H_T(AllJets): scalar sum of the transverse momenta of all jets in the event.
- H_T(AllJets,Lepton,$\not\!\!E_T$): scalar sum of the transverse momenta of all the jets, the lepton, and the $\not\!\!E_T$
- H_T(AllJets - BestJet): scalar sum of the transverse momenta of all jets except the best jet.
- H_T(AllJets - BTaggedJet): scalar sum of the transverse momenta of all jets except the leading b-tagged jet.
- H_T(Jet1,Jet2): scalar sum of the transverse momenta of the two leading jets.
- H_T(Jet1,Jet2,Lepton,$\not\!\!E_T$): scalar sum of the transverse momenta of the two leading jets, the lepton, and the $\not\!\!E_T$.
- M_T(AllJets): invariant mass of all the jets in the event.
- M_T(AllJets - BestJet): invariant mass of all the jets except for the best jet.
- M_T(AllJets - BTaggedJet): invariant mass of all the jets except for the leading b-tagged jet.
- M_T(Jet1,Jet2): invariant mass of the leading two jets.
- M_T(Jet1,Jet2,W): invariant mass of the leading two jets and the W boson.
- p_T(AllJets - BestJet): transverse momentum of all the jets in the event except for the best jet.
- p_T(AllJets - BTaggedJet): transverse momentum of all the jets in the event except for the leading b-tagged jet.
- p_T(Jet1,Jet2): transverse momentum of the two leading jets.
- $\sqrt{\hat{s}}$: invariant mass of all the objects in the event.
- Sphericity(AllJets,W): a variable used to describe the momentum flow of jets in the event. It is based on the smaller two eigenvalues of the momentum tensor M_{ab} of the jets in the event. Spherical events have $Q_1 = Q_2 = Q_3 = \frac{1}{3}$. The sphericity is defined as $S = \frac{3}{2}(Q_1 + Q_2)$.

- M_T(Jet1,Jet2): transverse mass of the leading two jets.
- $M_T(W)$: transverse mass of the W boson.

Angular correlations

These are either ΔR, $\Delta\phi$ angles between jets and leptons or top quark spin correlation variables.

- cos(BestJet,Lepton)$_{BestTop}$: cosine of the angle between the best jet and the lepton in the rest frame of the top quark reconstructed with the best jet.
- cos(BestJet,NotBestJet)$_{BestTop}$: cosine of the angle between the best jet and to the leading jet that is not the best jet in the rest frame of the top quark reconstructed with the best jet.
- cos(BTaggedJet,AllJets)$_{AllJets}$: cosine of the angle between the best jet and the alljets system in the alljets rest frame.
- cos(BTaggedJet,Lepton)$_{BTaggedTop}$: cosine of the angle between the leading b-tagged jet and the lepton in the rest frame of the top quark reconstructed with the leading tagged jet.
- cos(Jet1,AllJets)$_{AllJets}$: cosine of the angle between the leading jet and the alljets system in the alljets rest frame.
- cos(Jet1,Lepton)$_{BTaggedTop}$: cosine of the angle between the leading jet and the lepton in the rest frame of the top quark reconstructed with the leading tagged jet.
- cos(Jet2,AllJets)$_{AllJets}$: cosine of the angle between the second leading jet and the alljets system in the alljets rest frame.
- cos(Jet2,Lepton)$_{BTaggedTop}$: cosine of the angle between the second leading jet and the lepton in the rest frame of the top quark reconstructed with the leading tagged jet.
- cos(Lepton,Q(lepton) $\times$ z)$_{BestTop}$: cosine of the angle between the lepton and the z-axis in the rest frame of the top quark reconstructed with the best jet.

- cos(Lepton,BestTopFrame)$_{CMofBestTop}$: cosine of the angle between the lepton and the top quark mass frame where the top quark is reconstructed with the best jet in the center of mass frame of the top quark reconstructed with the best jet.
- cos(Lepton,BTaggedTopFrame)$_{CMofBTaggedTop}$: cosine of the angle between the lepton and the top quark mass frame reconstructed with the leading b-tagged jet in the center of mass frame of the top quark reconstructed with the leading b-tagged jet.
- cos(NotBestJet,AllJets)$_{AllJets}$: cosine of the angle between the leading jet that is not the best jet and the alljets system in the alljets rest frame.
- cos(NotBestJet,Lepton)$_{BestTop}$: cosine of the angle between the leading jet that is not the best jet and the lepton in the rest frame of the top quark reconstructed with the best jet.
- cos(LightQuarkJet,AllJets)$_{AllJets}$: cosine of the angle between the jet associated with the light quark in the alljets system in the alljets rest frame.
- cos(LightQuarkJet,Lepton)$_{BTaggedTop}$: cosine of the angle between the jet associated with the light quark and the lepton in the rest frame of the top quark reconstructed with the leading b-tagged jet.
- ΔR(Jet1,Jet2): angular separation in η and ϕ between the leading two jets.

Top quark reconstruction

These are variables used to reconstruct the top quark, identifying which jet to use.

- M_{top}(BestJet): The top quark mass using the best jet to reconstruct the top quark mass.
- M_{top}(LeadingBTaggedJet): The top quark mass using the leading b-tagged jet to reconstruct the top quark mass

8.3.3 Gini Index

The determination of what variable to use in splitting a node and what value to cut at is determined by the degradation D. This is formed from the weight of the events in the node where the change in degradation can be expressed as ΔD:

$$\Delta D = D - D_L - D_R = D(s,b) - D(s_L,b_L) - D(s_R,b_R) \tag{8.2}$$

where L and R correspond to the right and left daughter nodes, $s = s_L + s_R$, and $b = b_L + b_R$ where s and b refer to the signal and background yields respectively. ΔD is sometimes referred to as the "goodness of the split" and the variable and cut value is determined by maximizing ΔD. Here the degradation is measured using the Gini Index which is a function of the node purity p:

$$D = 2p(1-p) \tag{8.3}$$

The Gini Index is maximal when there are equal amounts of signal and background and can also be defined in terms of the signal and background yield s and b:

$$D = \frac{sb}{s+b} \tag{8.4}$$

This second definition is what is used in calculating the Gini Index.

8.3.4 Boosting

Boosting tries to generate a new decision tree with a smaller error function by looking at misclassified events from the previous decision tree and giving these events an additional weight. An event is misclassified if

$$|D_n(\vec{x_j}) - y_i| > 0.5 \tag{8.5}$$

where $D_n(\vec{x_j})$ is the discriminant associated with the n^{th} tree, y is 1 for signal and 0 for background. However, before any boosting occurs, the signal and background yields are scaled so that the total sum of the signal and the sum of the background event weights are both 0.5.

The boosting algorithm used is known as AdaBoost. This algorithm scales the event weight of misclassified events by a factor of e^{α_n} where α_n is described as follows:

$$\alpha_n = \beta \times ln\frac{1-\epsilon_n}{\epsilon_n} \tag{8.6}$$

Here, β is the Boosting parameter which is set to 0.2 and ϵ_n is the error associated with tree n. The error comes from the weighted sum of misclassified events and is either the misclassified signal or misclassified background yield, whichever is smallest.

Once all these misclassified events have been weighted, the signal and background yields are again scaled to 0.5 and a new DT is created. This process is done 20 times and with each new boosted tree, the next DT will work harder to correctly classify events that are misclassified.

8.3.5 Final BDT Discriminant

The final boosted decision tree result $D(\vec{x_j})$ for event j is

$$D(\vec{x_j}) = \frac{1}{\sum_{n=1}^{N}\alpha_n}\sum_{n=1}^{N}\alpha_n D_n(\vec{x_j}) \tag{8.7}$$

where $D_n(\vec{x_j})$ is the decision tree output for event j from tree T_n and N is the total number of decision trees generated which is 21 in this case for each orthogonal sample.

Additionally, the final discriminant goes through a binning transformation to ensure that there are signal and background events in every bin. This is because boosting causes both signal and background to move closer to 0.5 and as a result, the low and high discriminant regions are scarcely populated, yielding bins that can have all signal or all background. Bins need to have both signal and background events otherwise the results suffer from a large MC statistical

uncertainty. A monotonic transformation is applied to the BDT output to solve this problem:

$$f_1(x) = k/x \text{ , when x} < 0.8 \tag{8.8}$$

$$f_2(x) = M - Kx \text{ , when } 0.8 < \text{x} < 0.95 \tag{8.9}$$

where k = 0.346, K = 2.88 and M = 2.74, such that $f_1(0.8) = f_2(0.8)$. These values are derived by applying the method described below. From (0.95, 1), there are no shape constraints aside from there must be at least 40 background events in bins of width 0.02. This is done by splitting the BDT output of the total background sample into 10,000 uniform bins. The histogram is then normalized to 1 and then starting from the right in the original histogram, the content of each bin is moved to the rightmost bin in the new histogram of 50 uniform bins until there are enough background statistics and enough background events to make the weighted sum equal or greater than the value expected from the function. The next rightmost bin in the new histogram is then filled from the remaining 10,000 uniform bins in the original histogram starting from the remaining rightmost bin until the two conditions mentioned above are met. This is repeated until all 10,000 bins have been run through. The rebinning algorithm is done for each analysis channel and the new histogram can be thought of as the original histogram with variable bin widths that satisfy the conditions described above. Fig 8.3 shows this transformation applied to the BDT output.

Fig. 8.4 shows the BDT output distributions for the W'_L boson signals as well as data and background for all the mass points. Fig. 8.5 and 8.6 show similar plots for W'_R bosons, except the right-handed samples do not have the $\sqrt{\hat{s}}$ cut applied. Fig 8.7 is for the mixed case. The final discriminant plots for each analysis channel that are used to generate the limits for each mass point for the left-handed, mixed, and right-handed W′ bosons can be found in Appendix E.

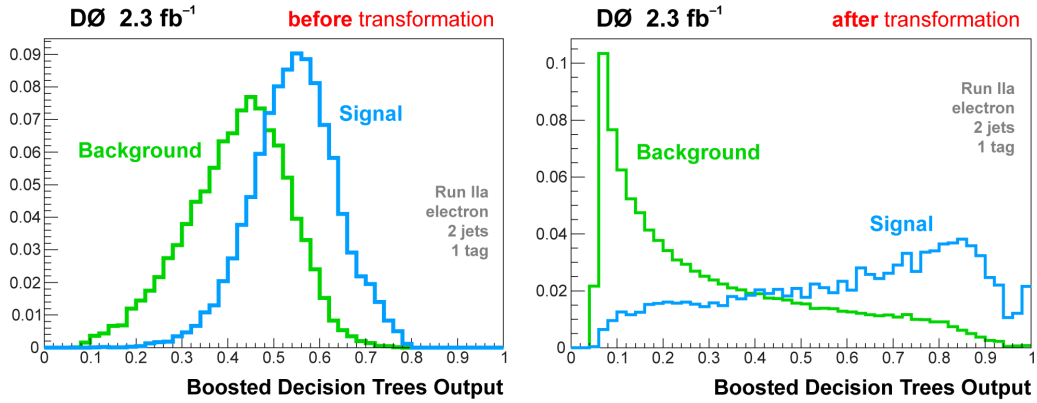

Figure 8.3: The decision tree output (left) is transformed (right) to ensure that there is enough signal and background in each bin in order to get stable limits on W′ boson.

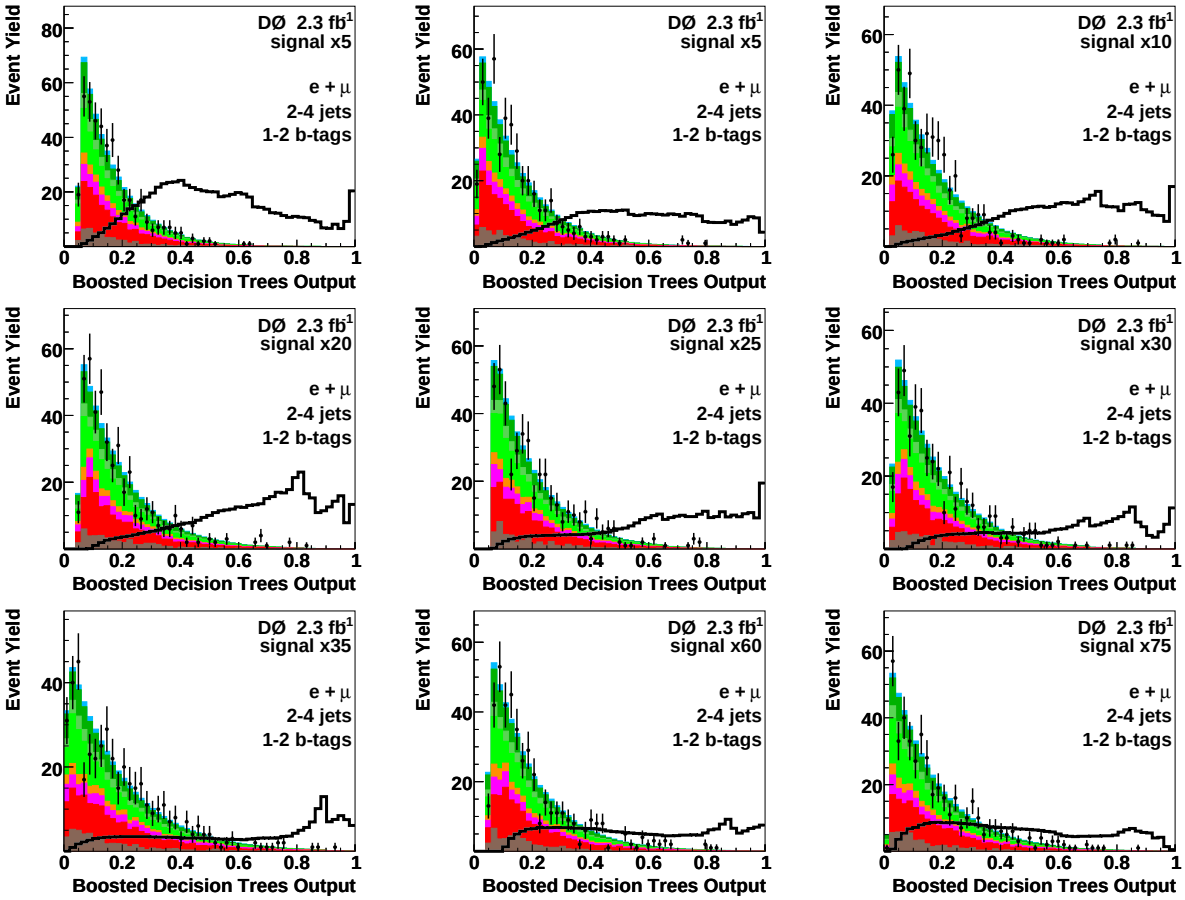

Figure 8.4: Distributions of Decision Tree output with $\sqrt{\hat{s}}$ cut > 400 GeV for combined p17 p20, one tag, two tag, and two jet, three jet and four jet of data, background, and W'_L signal. Plots, starting from top row to bottom and left to right, are from W'_L signal with mass 600 GeV to 1000 GeV in intervals of 50 GeV.

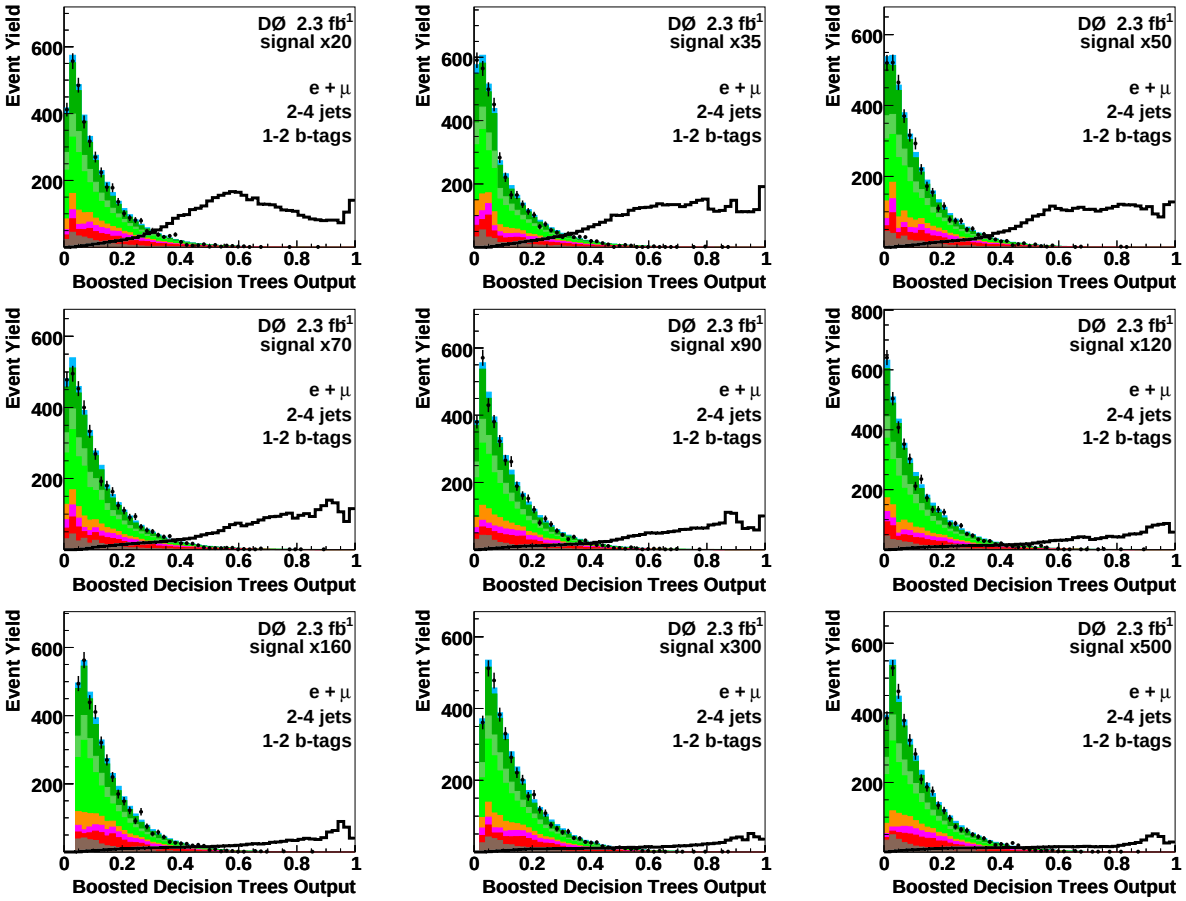

Figure 8.5: Distributions of Decision Tree output for combined p17 p20, one tag, two tag, and two jet, three jet and four jet of data, background, and W'_R with $q\overline{q'}$decays signal. Plots, starting from top row to bottom and left to right, are W'_L with $q\overline{q'}$decays signal with mass 600 GeV to 1000 GeV in intervals of 50 GeV.

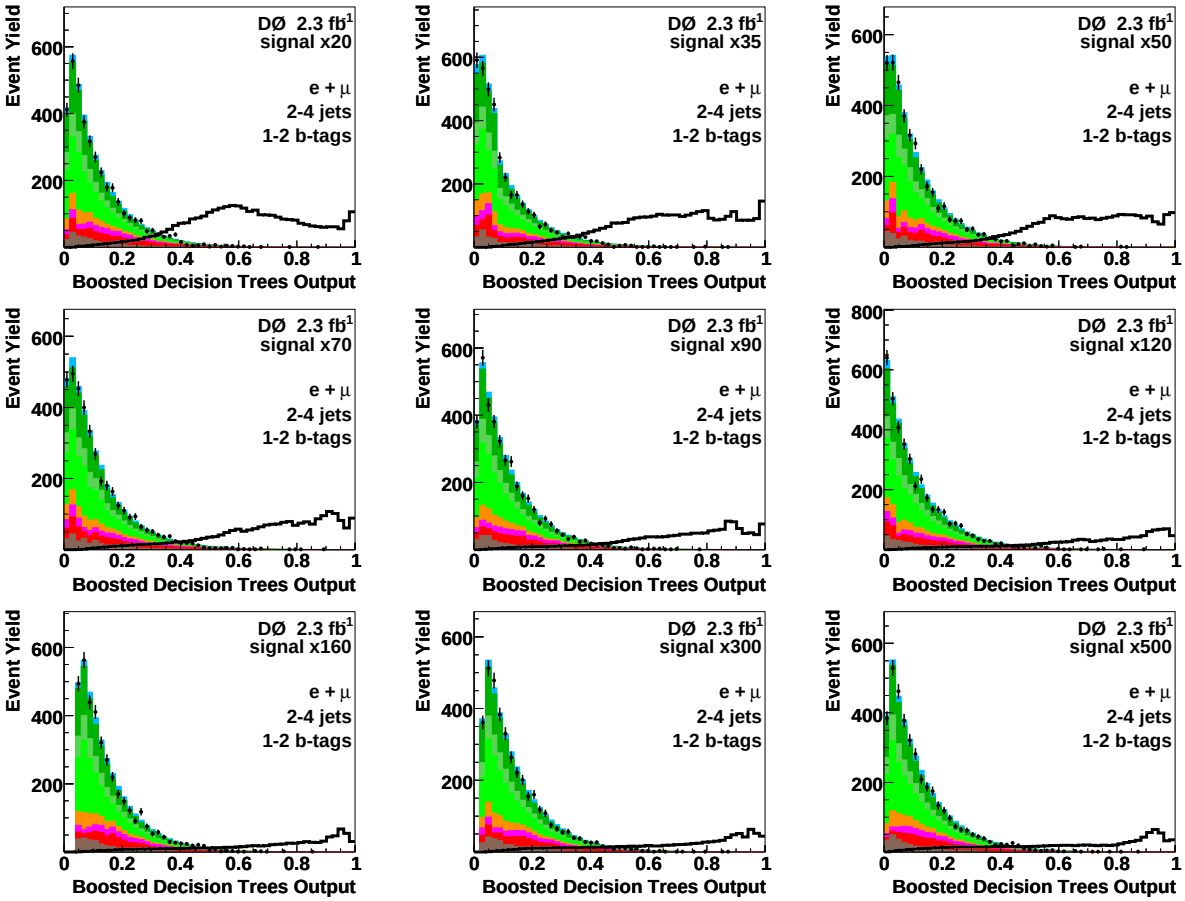

Figure 8.6: Distributions of Decision Tree output for combined p17 p20, one tag, two tag, and two jet, three jet and four jet of data, background, and W'_R with alldecays signal. Plots, starting from top row to bottom and left to right, are W'_R with alldecays signal with mass 600 GeV to 1000 GeV in intervals of 50 GeV.

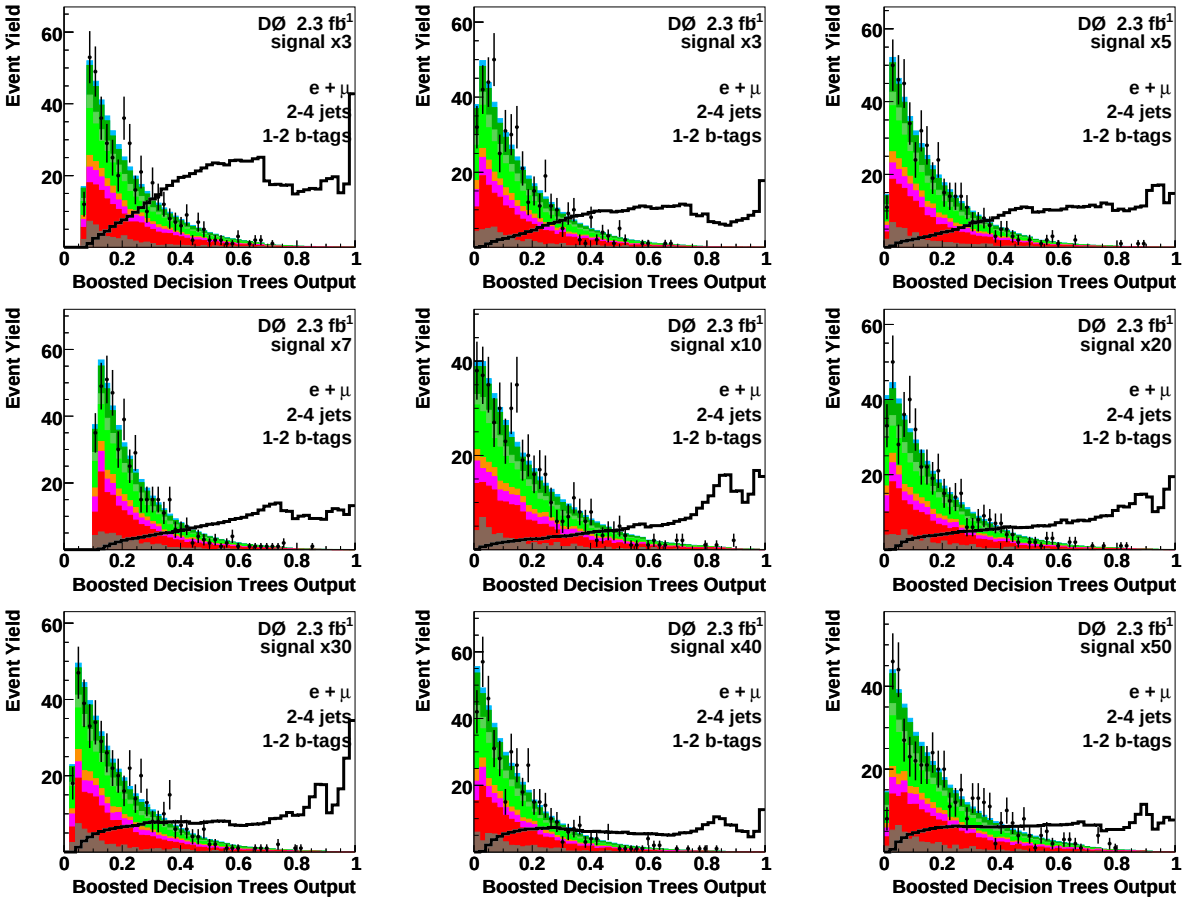

Figure 8.7: Distributions of Decision Tree output for combined p17 p20, one tag, two tag, and two jet, three jet and four jet of data, background, and mixed W' signal with $\sqrt{\hat{s}}$ cut > 400 GeV. Plots, starting from top row to bottom and left to right, are mixed W' signal with mass 600 GeV to 1000 GeV with 50 GeV interval

8.4 Limits

The limits are found in the same manner as described in Chapter 7. Since there is no excess of W′ bosons for all cases, 95% confidence level limits are found. These limits correspond to the cross section where 95% of the posterior probability density function's area is found.

The systematic uncertainties are the same as those mentioned in the previous chapter. However, an additional normalization systematic must be added due to the top mass difference used in the factorization scale of the generation of the W′ samples as compared to the top

quark processes (top pair, s-channel and t-channel electroweak produced top quark processes). The W′ samples are generated with a top quark mass at 172.5 GeV while the other top quark processes are generated with a top quark mass at 170 GeV. This systematic uncertainty was determined by computing the average change in expected limits from backgrounds with top quark mass set at 170 GeV or 172.5 GeV and is set to 1.6%.

Table 8.14 and 8.15 are the expected and measured limits for the left-handed and mixed W′ bosons respectively. As for the right-handed W′ bosons, the limits for the case when $M(\nu_R) < M(W')$ are found in Table 8.16 and the limits for the case when $M(\nu_R) > M(W')$ are found in Table 8.17.

	Statistical Uncertainty Only			All Uncertainties		
	Two jets	Three jets	Four jets	Two jets	Three jets	Four jets
W' (700 GeV)						
Exp.	0.24	0.19	0.18	0.28	0.21	0.20
Obs.	0.17	0.13	0.12	0.23	0.18	0.14
W' (750 GeV)						
Exp.	0.36	0.27	0.26	0.41	0.31	0.30
Obs.	0.36	0.23	0.22	0.45	0.32	0.25
W' (800 GeV)						
Exp.	0.58	0.43	0.42	0.67	0.49	0.47
Obs.	0.62	0.42	0.42	0.74	0.52	0.45
W' (850 GeV)						
Exp.	1.04	0.75	0.72	1.21	0.85	0.80
Obs.	0.88	0.62	0.61	1.16	0.80	0.67
W' (900 GeV)						
Exp.	1.70	1.23	1.17	2.03	1.47	1.34
Obs.	1.37	1.01	0.99	1.84	1.31	1.08
W' (950 GeV)						
Exp.	2.73	2.01	1.94	3.22	2.35	2.22
Obs.	1.58	1.30	1.38	2.02	1.66	1.47
W' (1000 GeV)						
Exp.	3.73	2.73	2.60	4.54	3.46	3.19
Obs.	4.18	2.73	2.83	5.65	4.25	3.42

Table 8.14: Expected and measured 95% C.L. upper limits on the production cross section of left handed W' bosons. Each sample includes electron and muon, one and two tag samples. The units are in pico barns.

The observed and expected limits, along with the theoretical cross section predictions, are shown in Figs. 8.8, 8.9, and 8.10 for W'_L and W'_R (all decays), and W'_R ($q\overline{q'}$ decays) respectively. The solid line denotes the observed limit and the shaded areas above the line are excluded at 95% CL. The lower mass limit is defined by the intersection of the solid line denoting the observed limit with the dashed line for the nominal value of the theoretical cross section. For a $M(W'_L)$ boson the mass limit is 840 GeV, when interference with SM $W \to t\bar{b}$ is included. The limit is 880 GeV for a $M(W'_R)$ when $M(\nu_R) < M(W')$ and applies also to a left-handed W' boson if no interference with the SM is taken into account. For the case $M(\nu_R) > M(W')$, we find $M(W'_R) > 890$ GeV for a W'_R boson. For the mixed scenario, the observed and expected 95% C.L. experimental limits are presented in Fig. 8.11, along with the theoretical prediction. From these curves we infer that for the case of mixed couplings $M(W') > 915$ GeV.

	Statistical Uncertainty Only			All Uncertainties		
	Two jets	Three jets	Four jets	Two jets	Three jets	Four jets
W' (600 GeV)						
Exp.	0.23	0.20	0.19	0.28	0.23	0.22
Obs.	0.10	0.08	0.09	0.13	0.09	0.09
W' (650 GeV)						
Exp.	0.30	0.24	0.24	0.35	0.29	0.27
Obs.	0.13	0.09	0.09	0.19	0.12	0.11
W' (700 GeV)						
Exp.	0.27	0.22	0.21	0.31	0.25	0.23
Obs.	0.20	0.13	0.13	0.24	0.18	0.15
W' (750 GeV)						
Exp.	0.31	0.25	0.24	0.39	0.30	0.28
Obs.	0.29	0.22	0.23	0.39	0.30	0.28
W' (800 GeV)						
Exp.	0.42	0.32	0.31	0.50	0.37	0.35
Obs.	0.33	0.23	0.22	0.38	0.29	0.25
W' (850 GeV)						
Exp.	0.58	0.45	0.43	0.68	0.51	0.48
Obs.	0.45	0.28	0.27	0.51	0.33	0.29
W' (900 GeV)						
Exp.	0.68	0.50	0.47	0.96	0.67	0.60
Obs.	0.47	0.32	0.32	0.84	0.56	0.59
W' (950 GeV)						
Exp.	1.45	1.10	1.04	1.78	1.31	1.21
Obs.	1.10	0.86	0.84	1.43	1.17	0.94
W' (1000 GeV)						
Exp.	2.09	1.63	1.55	2.69	2.07	1.90
Obs.	1.40	1.15	1.14	1.88	1.69	1.32

Table 8.15: Expected and measured 95% C.L. upper limits on the production cross section of mix W' bosons. Each sample includes electron and muon, one and two tag samples. The units are in pico barns.

	Statistical Uncertainty Only			All Uncertainties		
	Two jets	Three jets	Four jets	Two jets	Three jets	Four jets
W' (700 GeV)						
Exp.	0.17	0.13	0.13	0.19	0.15	0.14
Obs.	0.10	0.08	0.08	0.13	0.10	0.09
W' (750 GeV)						
Exp.	0.17	0.13	0.12	0.19	0.14	0.14
Obs.	0.09	0.08	0.09	0.11	0.10	0.11
W' (800 GeV)						
Exp.	0.17	0.13	0.12	0.19	0.14	0.13
Obs.	0.10	0.09	0.09	0.12	0.11	0.09
W' (850 GeV)						
Exp.	0.19	0.14	0.13	0.21	0.15	0.14
Obs.	0.10	0.09	0.10	0.11	0.11	0.12
W' (900 GeV)						
Exp.	0.20	0.14	0.13	0.22	0.16	0.15
Obs.	0.10	0.10	0.11	0.12	0.14	0.14
W' (950 GeV)						
Exp.	0.24	0.17	0.16	0.27	0.19	0.18
Obs.	0.12	0.09	0.10	0.16	0.10	0.13
W' (1000 GeV)						
Exp.	0.21	0.15	0.14	0.23	0.16	0.15
Obs.	0.12	0.08	0.09	0.14	0.09	0.10

Table 8.16: Expected and measured 95% C.L. upper limits on the production cross section of right handed W' bosons (all decays). Each sample includes electron and muon, one and two tag samples. The units are in pico barns.

	Statistical Uncertainty Only			All Uncertainties		
	Two jets	Three jets	Four jets	Two jets	Three jets	Four jets
W' (700 GeV)						
Exp.	0.17	0.14	0.13	0.19	0.15	0.14
Obs.	0.10	0.08	0.08	0.13	0.10	0.09
W' (750 GeV)						
Exp.	0.17	0.13	0.12	0.19	0.14	0.14
Obs.	0.09	0.08	0.09	0.11	0.10	0.11
W' (800 GeV)						
Exp.	0.17	0.13	0.12	0.19	0.14	0.13
Obs.	0.10	0.09	0.09	0.12	0.11	0.09
W' (850 GeV)						
Exp.	0.19	0.14	0.13	0.21	0.15	0.14
Obs.	0.10	0.09	0.10	0.11	0.11	0.12
W' (900 GeV)						
Exp.	0.20	0.14	0.13	0.22	0.16	0.15
Obs.	0.10	0.10	0.11	0.12	0.14	0.14
W' (950 GeV)						
Exp.	0.24	0.17	0.16	0.28	0.20	0.18
Obs.	0.13	0.09	0.10	0.17	0.11	0.13
W' (1000 GeV)						
Exp.	0.26	0.19	0.18	0.29	0.21	0.19
Obs.	0.15	0.09	0.10	0.21	0.10	0.12

Table 8.17: Expected and measured 95% C.L. upper limits on the production cross section of right handed W' bosons ($q\overline{q}$ decays). Each sample includes electron and muon, one and two tag samples. The units are in pico barns.

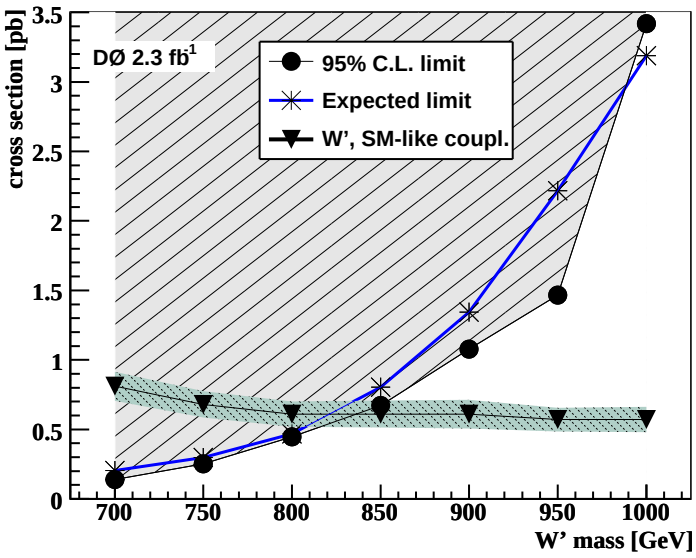

Figure 8.8: 95% C.L. expected and observed limits for left handed W' as a function of its mass. NLO theoretical cross sections are also shown for a left-handed W', including interference effects with the SM. The shaded region is excluded by this analysis.

	σ_{nom}	σ_{min}	σ_{max}
with SM interference			
$M(W'_L) >$	840 GeV	820 GeV	850 GeV
$M(W'_{mixed}) >$	970 GeV	960 GeV	980 GeV
without SM interference			
$M_\nu < M_{W'}$: $M(W') >$	880 GeV	860 GeV	890 GeV
$M_\nu > M_{W'}$: $M(W') >$	890 GeV	880 GeV	900 GeV

Table 8.18: 95% C.L. lower limits on the mass of the W' for the nominal (σ_{nom}), nominal-1σ (σ_{min}) and nominal$+1\sigma$ (σ_{max}) values of the theoretical cross section.

.

The limits determined by intersecting the experimental limit curve with the nominal theory cross section prediction and with the theory cross section varied up and down by their uncertainties are listed in Table 8.18.

Constraints on the W' gauge couplings are depicted in Fig. 8.12 and listed in Table 8.19.

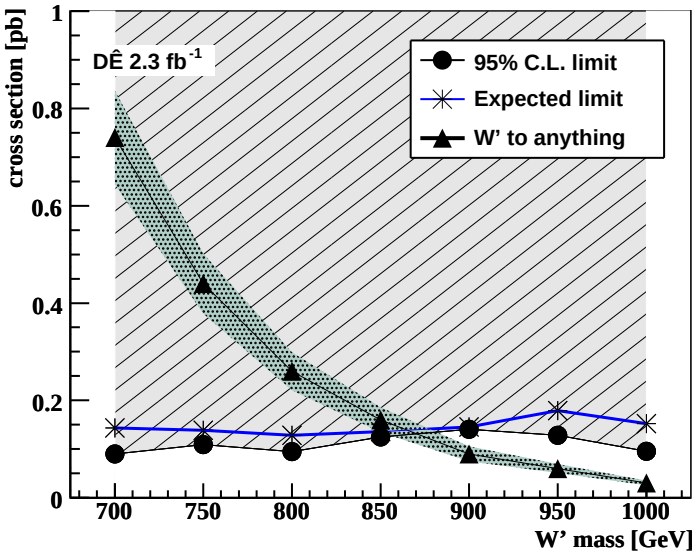

Figure 8.9: 95% C.L. upper limits for right handed W' as a function of its mass. NLO theoretical cross sections for the case $M(\nu_R) < M(W')$ is also shown. No interference with the SM is included. The shaded region is excluded by this analysis.

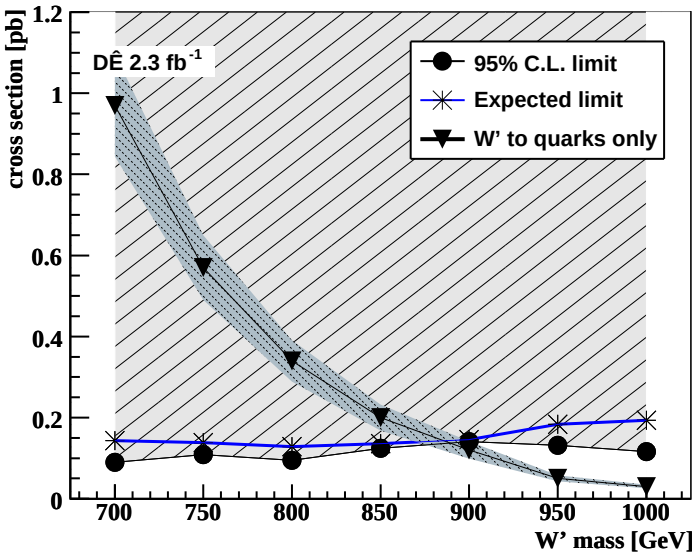

Figure 8.10: 95% C.L. upper limits for right handed W' as a function of its mass. NLO theoretical cross sections for the case $M(\nu_R) > M(W')$ is also shown. No interference with the SM is included. The shaded region is excluded by this analysis.

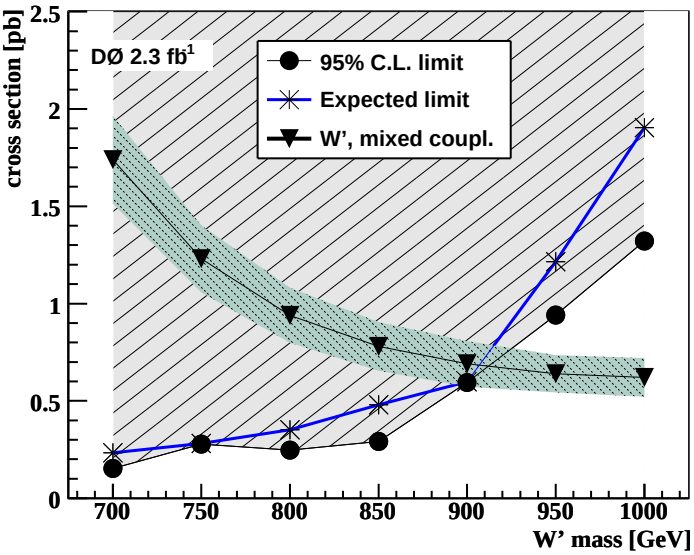

Figure 8.11: 95% C.L. upper limits for mixed W' as a function of its mass. NLO theoretical cross sections including interference with the SM is shown. The shaded region is excluded by this analysis.

$M_{W'}[GeV]$	coupling constant (g′/g)	
	$M_\nu < M_{W'}$	$M_\nu > M_{W'}$
600	0.46	0.43
650	0.54	0.51
700	0.62	0.58
750	0.69	0.65
800	0.76	0.71
850	1.06	1.00
900	1.01	0.94
950	1.30	1.37
1000	1.32	1.36
1050	1.47	1.54
1100	1.94	2.07

Table 8.19: 95% C.L. upper limits for the couplings of the right handed W' as a function of its mass for the cases $M(\nu_R) < M(W')$ and $M(\nu_R) > M(W')$

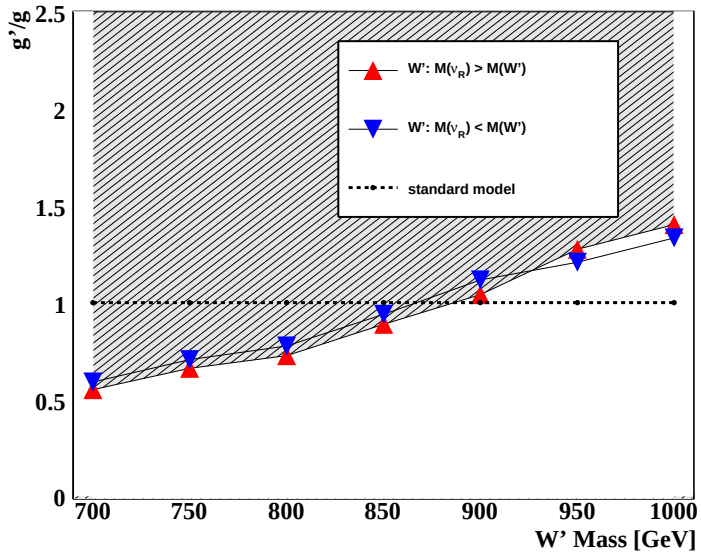

Figure 8.12: 95% C.L. upper limits for the couplings of the right handed W' as a function of its mass for the cases $M(\nu_R) < M(W')$ and $M(\nu_R) > M(W')$

Chapter 9

Conclusion

This thesis presents a measurement of the top quark produced through the electroweak channel using 2.3 fb^{-1} of data collected for the DØ detector. The events selected must have one isolated lepton, large $\not\!\!E_T$, at least one b-tagged jet, and at least one more jet. A multivariate analysis, the ME, is performed to separate out the small signal from a large background where the uncertainties in the background modeling are of the same order as the signal yield. This is done for 16 orthogonal samples divided by reconstruction data sets (Run IIa, Run IIb), lepton (e or μ), b-tag jets (1 or 2 b-tagged jets), and number of jets (2, 3 jets). Using Bayesian statistics, this analysis using the ME method measures a cross section of 4.30 + 0.98 - 1.20 pb for the top quark produced via the electroweak process. The p-value for this measurement is 4.0 $\times 10^{-7}$, yielding a significance of 4.9σ.

By combining this analysis with the BNN analysis and BDT analysis using another BNN [86] , the measured electroweak produced top quark cross section is 3.94 $\pm$ 0.88 pb with a significance of 5.0σ, resulting in the discovery of top quarks produced through the electroweak channel [5].

Furthermore, $|V_{tb}f_1^L|$ can be measured using the combined cross section measurement and is found to be $1.07^{+0.11}_{-0.12}$. This is above the SM expectation by about 0.6 standard deviations. However, constraining $|V_{tb}| < 1$, a 95% confidence lower limit yields $|V_{tb}| > 0.78$ [87] [5].

Figs. 9.1 - 9.3 show the event displays of possible top quarks produced through the electroweak channel. These data events were selected based on their high combined BNN discriminant values. This measurement will become more precise as there is more than 5 fb^{-1} of data available to be analyzed.

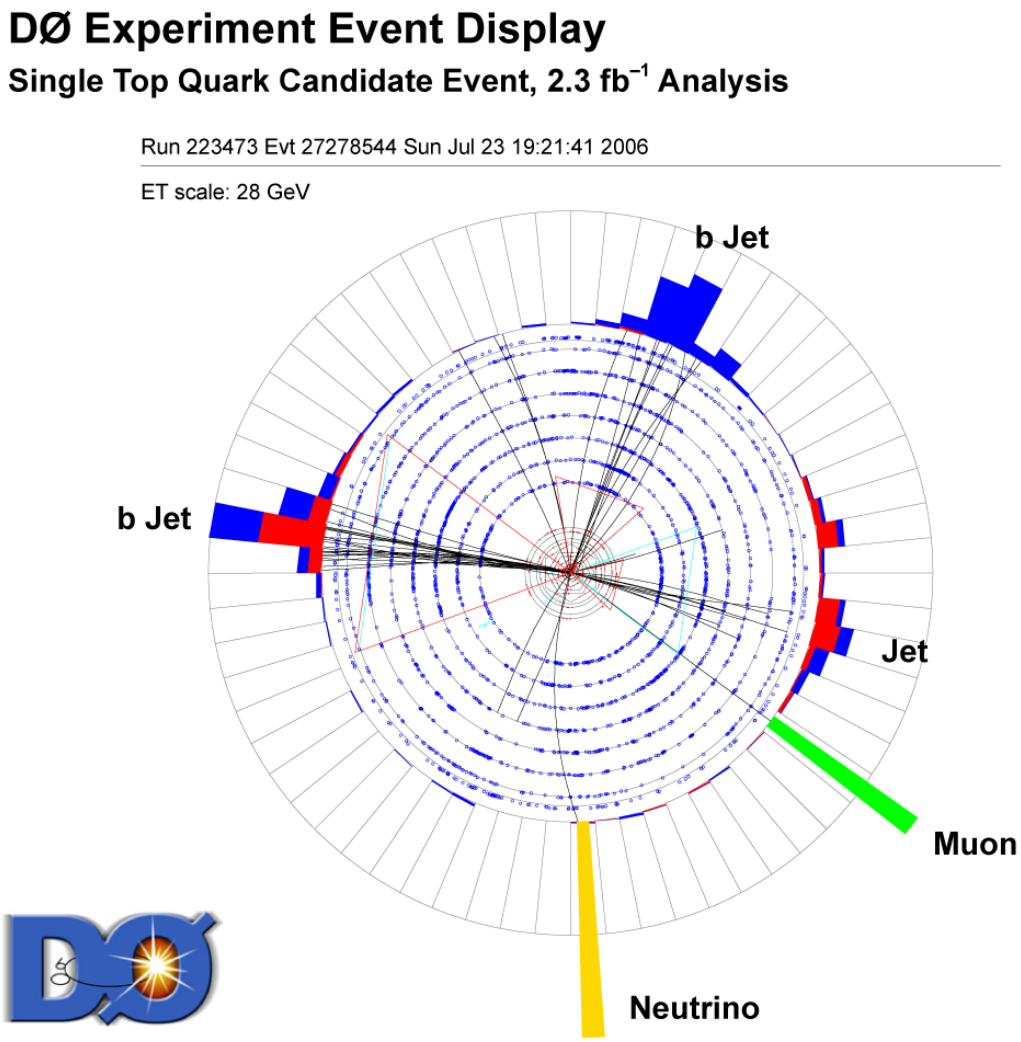

Figure 9.1: Event display for an electroweak produced top quark with 2 b-tagged jets and 3 jets in a Run IIb muon event.

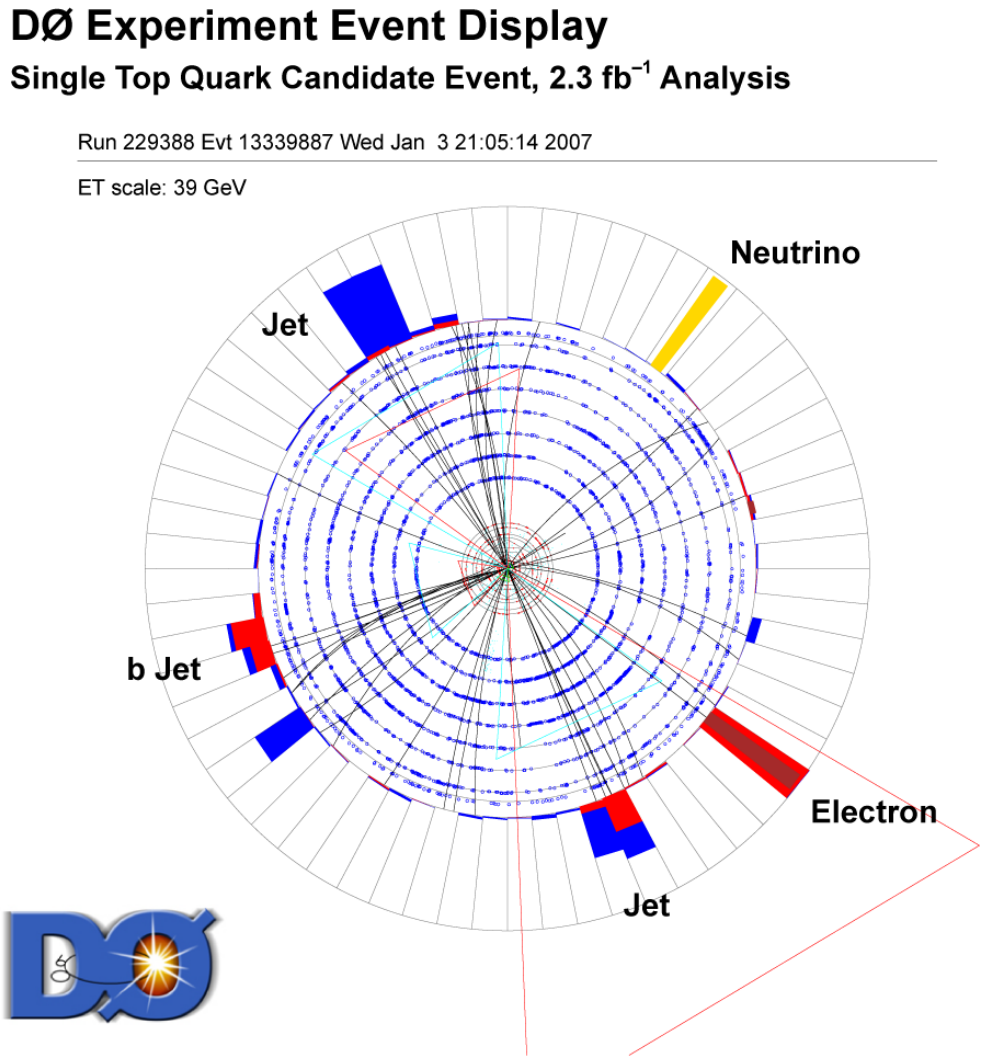

Figure 9.2: Event display for an electroweak produced top quark with 1 b-tagged jet and 3 jets in a Run IIb electron event.

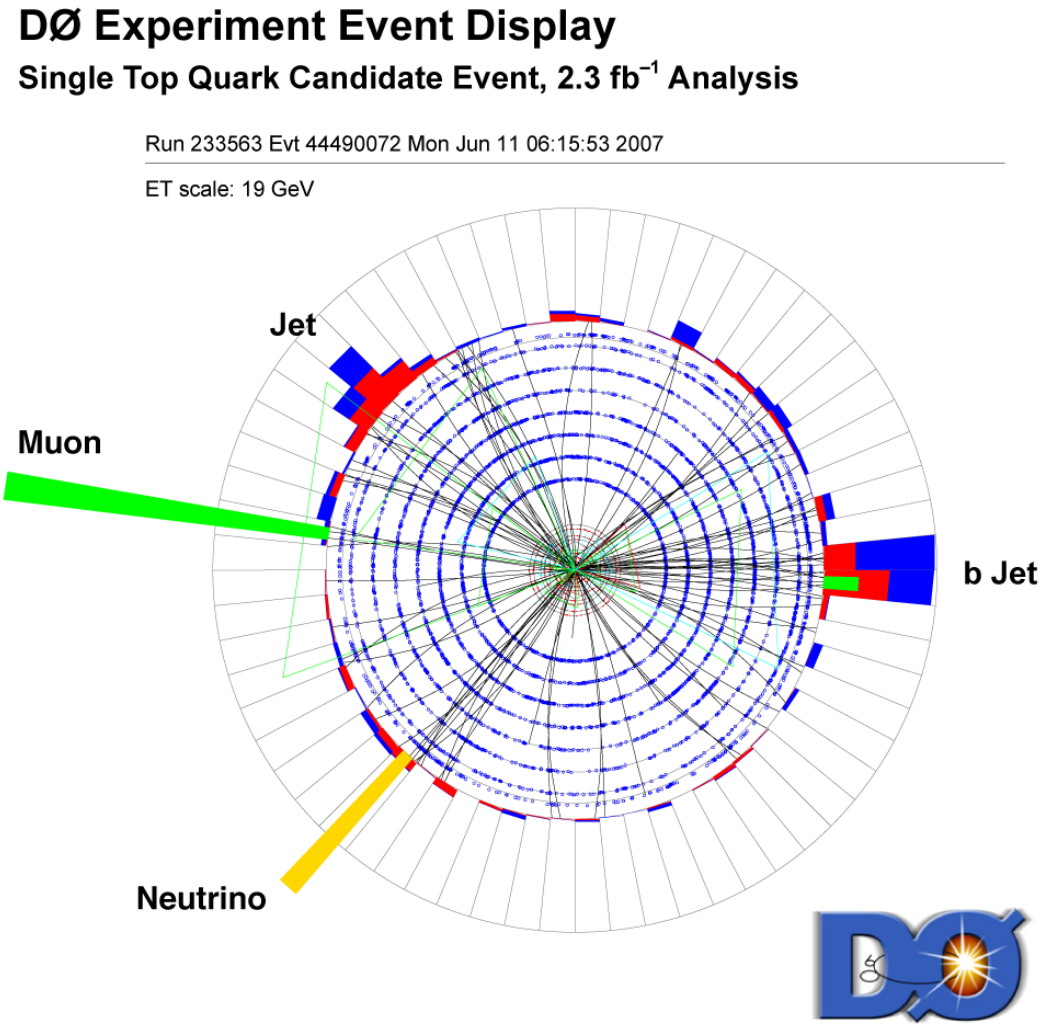

Figure 9.3: Event display for an electroweak produced top quark with 1 b-tagged jet and 2 jets in a Run IIb muon event.

	$D\emptyset$ (2.3 fb^{-1})	previous $D\emptyset$ (0.9 fb^{-1})	CDF (1.9 fb^{-1})
with SM interference			
$M(W'_L) >$	840 GeV	731 GeV	-
$M(W'_{mixed}) >$	915 GeV	-	-
without SM interference			
$M_\nu < M_{W'}$: $M(W') >$	880 GeV	739 GeV	800 GeV
$M_\nu > M_{W'}$: $M(W') >$	890 GeV	768 GeV	825 GeV

Table 9.1: Limits from this analysis as compared to the results from the previous D0 analysis [119] and limits from the latest CDF results [118].

Additionally, limits on theories beyond the SM can be set using this electroweak production channel for top quarks. Heavier charged gauge bosons, termed W$'$ boson, that behave much like the SM W boson can be generated where now the top quarks produced in the electroweak channel become backgrounds to the W$'$ boson. Four different cases of W$'$ bosons can be tested: the left-handed case where the W$'$ boson couples to left-handed fermions and thus interferes with the SM W boson, the right-handed case where the W$'$ boson couples to right-handed fermions and two cases exist where $M(\nu_R) > M(W')$ or $M(\nu_R) < M(W')$, and the mixed-case where there are equal amounts of left-handed and right-handed W$'$ boson interactions. For the left-handed and mixed case, the event selection additionally has an $\sqrt{\hat{s}} > 400$ GeV to remove most of the SM W boson. The events go through another multivariate analysis, the BDT, using 49 variables to separate the W$'$ boson signal from the background. Since there is no excess in signal, 95% confidence level limits are set and are summarized in Table 9.1 which also compares recent results to CDF's analysis [118] and another DØ analysis that uses only 0.9 fb^{-1} [119]. Furthermore, limits can be set on the couplings for the right-handed W$'$ and are depicted as a function of the W$'$ mass for both cases where $M(\nu_R) > M(W')$ and $M(\nu_R) < M(W')$ in Fig. 9.4

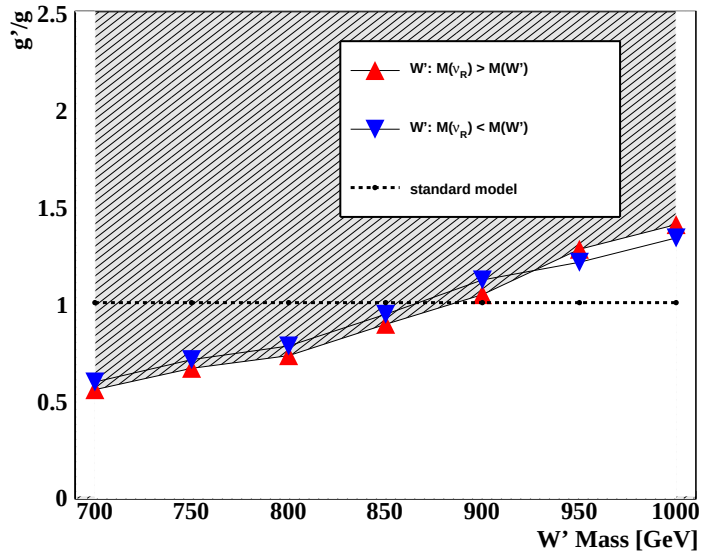

Figure 9.4: 95% C.L. upper limits for the couplings of the right handed W' boson as a function of its mass for the cases $M(\nu_R) < M(W')$ and $M(\nu_R) > M(W')$

Appendix A

Central Track Trigger

The Central Track Trigger (CTT) [120] is part of the three tiered trigger system that $D\emptyset$ uses to reduce data acquired at a frequency of 1.7 MHz to 100 Hz which is the maximum amount that can be recorded. The CTT is used at L1 and reconstructs the hits from the Central Fiber Tracker (CFT) and the Central Preshower (CPS) into tracks with a given momentum and location. An example of a track can be seen in Fig. A.1. This is accomplished by the Digital Front End Analog (DFEA) boards [121], where each board accounts for two sectors of the CFT. The full ϕ range has 80 sectors. For each sector, the CTT, through the DFEA boards, looks at the fiber hits along with that of its two neighboring sectors and compares them to predefined hit patterns to make a list of the six highest momentum tracks found for momentum ranges 1.5 - 3.0 GeV (LOW), 3 - 5 GeV (MED), 5 - 10 GeV (HIGH), and $>$ 10 GeV (MAX). This information is then sent to the Trigger Framework which uses the tracking information as an effective criteria to cut down the event rate.

A.1 CTT Overview

The CTT receives hit information from the Mixer, a system of 20 boards that reorganizes digital data from the AFE boards into trigger sectors. The Mixer processes data at 311 gigabits per

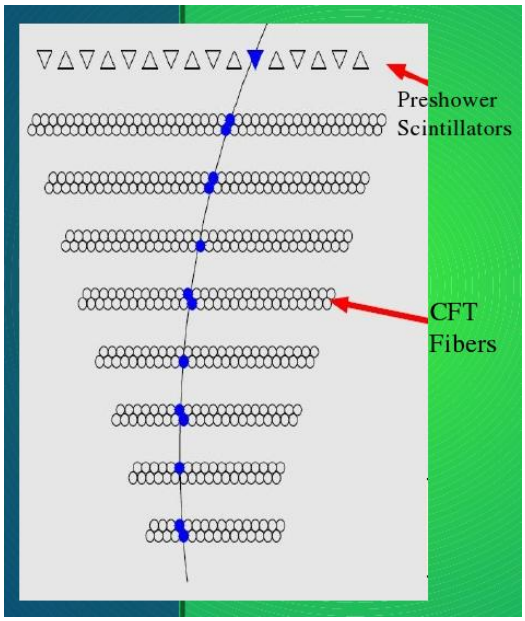

Figure A.1: For a sector in the CFT, the CFT fiber and the CPS scintillator hits are used to reconstruct tracks where the momentum of the track comes from the curvature of the track.

second with an input to output delay of 200 ns. The DFEA boards receive 496 bits that contain all the CPS and fiber hits for all CFT sectors as well as some control information from the Mixer. The DFEA boards, upgraded to the DFEA2 boards [122]in 2006, are perhaps the most important part of the CTT system as it reconstructs these hits into tracks with momentum and location information which is sent to the CTOC and CTTT boards. The CTOC boards process the DFEA2 records and send to the CTTT at L1, the number of total track counts and total occupancy from all sectors combined and to L2, tracks sorted by p_T and clusters sorted by increasing ϕ. The CTTT is what forms the trigger terms sent to the trigger framework where the trigger terms use the number of tracks found, whether the tracks are isolated or not, and the total number of fiber hits. The overview of the system can be found in Fig. A.2.

A.2 Digital Front End Analog (DFEA) boards

The DFEA boards had a major upgrade in 2006 and are the heart of the CTT system. The DFEA boards are responsible for finding tracks and sending out this information in time for

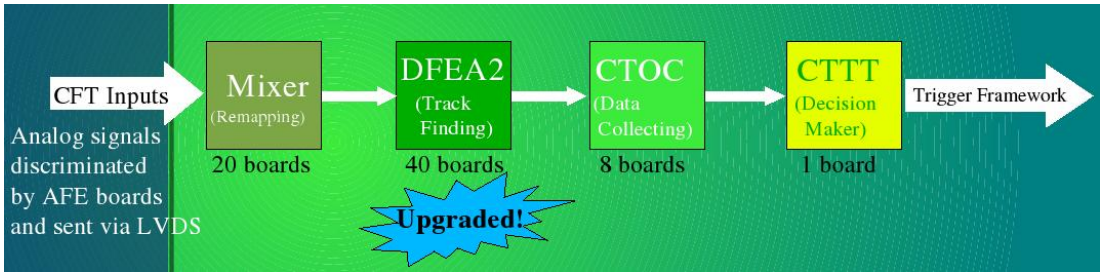

Figure A.2: The CFT information is sent to the CTT via the Mixer boards which reorganize the hit information into trigger sectors for the DFEA2. The DFEA2 boards then determine the momentum, location, and even isolation of the tracks for each trigger sector. This information is sent to the CTOC boards which organizes this information and sends it to the CTTT which forms trigger terms that is then sent to the Trigger Framework.

L1 and L2 trigger decisions. For the entire system, there are 40 boards where each board is responsible for two sectors. Each board has five Field Programmable Gate Arrays (FPGAs) where four of them are used for finding tracks in a specific momentum ranges and the other one organizes the information from the track finding FPGAs. The major time constraint on the system is from the L1 muon system which needs the six highest momentum tracks in 263 ns.

A.2.1 Track Finding Functionality

The track finding FPGA uses CFT hits to define tracks. The CFT has eight doublet layers where each doublet layer has two sublayers of fibers. A CFT track must have a hit in each of these doublet layers where a hit can be defined as either a doublet hit or a singlet hit as seen in Fig. A.3. For tracks defined by doublet hits, the two sublayers will have a hit in each sublayer defined although there may be only one sublayer that has a fiber firing. As a result, a track equation is defined by many combinations of track hits. For tracks defined by singlet hits, track equations use information from both sublayers including sublayers that have no fibers firing. These hits are used to define a ϕ and p_T value for each track.

For each p_T bin, there are four sub-bins except for the LOW p_T bin which has eight. This is because there a higher number of low p_T tracks and so the LOW p_T bin requires the highest amount of resources. In two 53 MHz clocks, the hits are formed and then matched to a track

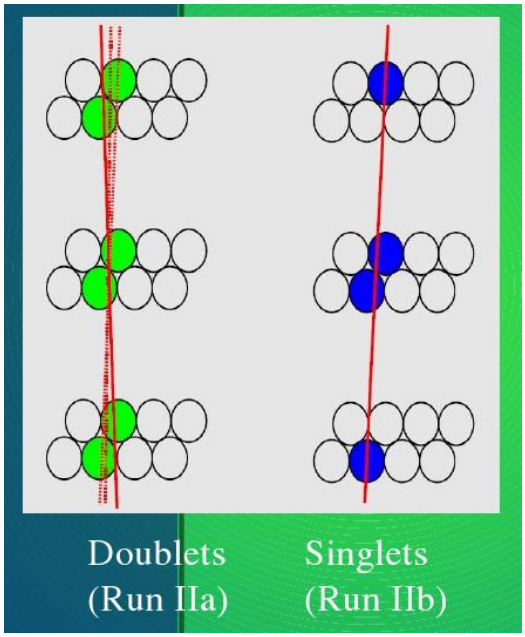

Figure A.3: CFT hits can be defined as either doublet (right) or singlet (left) hits. The doublet hits were used for Run IIa events and the singlet hits are now used for Run IIb events. Doublet hits will use both sublayers although only one sublayer has a fiber firing. As a result, other tracks (dashed red lines) besides the correct track (solid red line) can trigger the same equation. As for the singlet equation, the track equations use information from both sublayers which includes sublayers with no fiber hits. As a result, only the correct track fires the trigger.

equation.

A CFT track's curvature, p_T, and ϕ are determined by matching the CFT hits found in each doublet layer to a list of possible eight CFT axial layer hit combinations for the doublet scheme and to at most 16 axial layer hit combinations for the singlet scheme. These hits correspond to a specific curvature, p_T, and ϕ. The six highest p_T tracks for each momentum range has to be found quickly. This is done by making a 8 (16) $\times$ 44 matrix which is composed of the 352 (704) track possibilities for the MED, HIGH, and MAX (LOW) momentum bin. The amount of possibilities comes from whether the track has a positive or negative curvature (2), from the number of p_T sub-bins (4 or 8), and from the ϕ in the sector where each sector is divided into 44 segments (44).

Each row corresponds to a specific curvature and sub-bin where the 44 columns correspond to the ϕ in the sector. The rows are further divided into two blocks from 0 to 21 and 22 to 43 where 0 to 21 is processed first. Starting from the top row and the block from 0 to 21, corresponding to a positive curvature and the highest p_T sub-bin with the sector ϕ ranging from 0 to 21, the block is scanned both from left to right and from right to left and the first track from both scans is kept. This produces at most two tracks although there maybe more than two tracks in each block. However, deciding which tracks to send to L1 Muon takes time so the first six tracks found using only the leftmost track in each block is sent to L1Muon. Otherwise, the first six tracks found using both the leftmost and rightmost track in each block are kept. An example of what a hit in this matrix corresponds to can be found in Fig. A.4.

A.2.2 Track Equation Generation

The track equations consist of all probable patterns of hits consistent with tracks originating from close to the beam-spot. This is defined on average by 13 singlet hits per track though the current pattern-sets require $\geq$ 8 singlet hits per track. The probable patterns of hits are found using a toy Monte Carlo model that includes the geometrical acceptance of all 16 CFT axial singlet layers [123]. Each ϕ bin generates about 7 million track trajectories which is

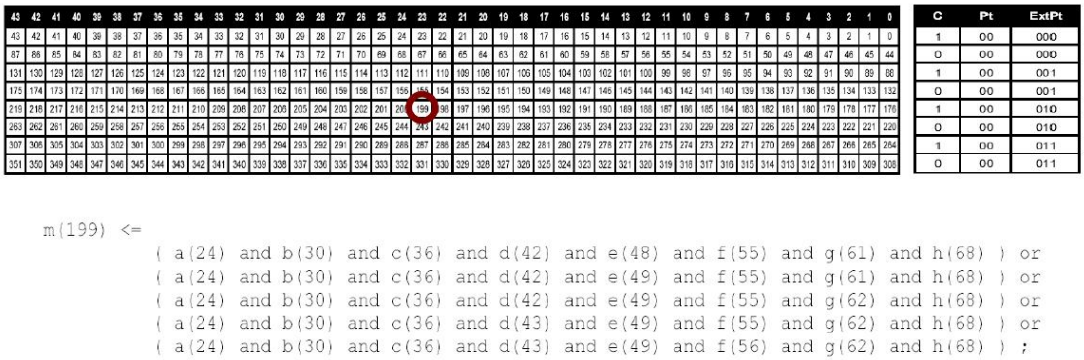

C	Pt	ExtPt
1	00	000
0	00	000
1	00	001
0	00	001
1	00	010
0	00	010
1	00	011
0	00	011

```
m(199) <=
          ( a(24) and b(30) and c(36) and d(42) and e(48) and f(55) and g(61) and h(68) ) or
          ( a(24) and b(30) and c(36) and d(42) and e(49) and f(55) and g(61) and h(68) ) or
          ( a(24) and b(30) and c(36) and d(42) and e(49) and f(55) and g(62) and h(68) ) or
          ( a(24) and b(30) and c(36) and d(43) and e(49) and f(55) and g(62) and h(68) ) or
          ( a(24) and b(30) and c(36) and d(43) and e(49) and f(56) and g(62) and h(68) ) ;
```

Figure A.4: For a hit of the LOW p_T bin track finding matrix at 199, this corresponds to track equations with specific fiber hits in layers a - h labeled by a specific number. These tracks correspond to a positive curvature (C = 1) found in the second highest p_T sub-bin (ExtPt = 001).

sampled uniformly in q/p_T, ϕ, and η. The maximum and minimum q/p_T values are recorded for each pattern found. The expected longitudinal beam spread (σ_z = 30 cm) and allowance for beam-spot instability by sampling uniformly from a circular pseudo beam-spot with radius of 300 μm are taken into account. The tracks are extrapolated by simulating the effects of a 1.92 T axial B-field. Hits in individual axial singlet fibers take into account the track-length in the active scintillator of the fiber, the estimated light yield of each fiber which is $\approx$ 10.3 photo-electrons/mm, and the discriminator threshold which is set to 1.5 photo-electrons. Each found pattern is then assigned an acceptance value proportional to the number of generated tracks satisfying this particular pattern. Here, the total acceptance of all generated track patterns for the LOW p_T bin is 2π rad $\times$ 2 $\times$ 1/1.5 GeV^{-1} = $8\pi/3$ rad/GeV in (ϕ, q/p_T) space. A particular pattern is kept if its acceptance exceeds 6 nrad/GeV and if the pattern has at least eight singlet hits. For each ϕ bin, tracks are assigned to unique q/p_T bins based on the tracks averaged recorded $(q/p_T)_{min}$ and $(q/p_T)_{max}$. For each p_T-bin, redundant and duplicated logic equations are removed prior to incorporation in the FPGAs. The algorithm described above has estimated efficiencies exceeding 99.5% for $n_{hits} \geq 13$ and an average efficiency of 99%.

A.2.3 Cluster Finding Functionality

In the HIGH FPGA, the Central PreShower (CPS) clusters are found for each sector. Looking at the 16 axial fibers per sector and eight axial fibers from neighboring sectors, the algorithm starts from the midpoint axial fiber location of the 32 fibers and scans right and scans left from this location. The first four clusters found from both scans are kept with each cluster's location and size. This process can be seen in Fig. A.5

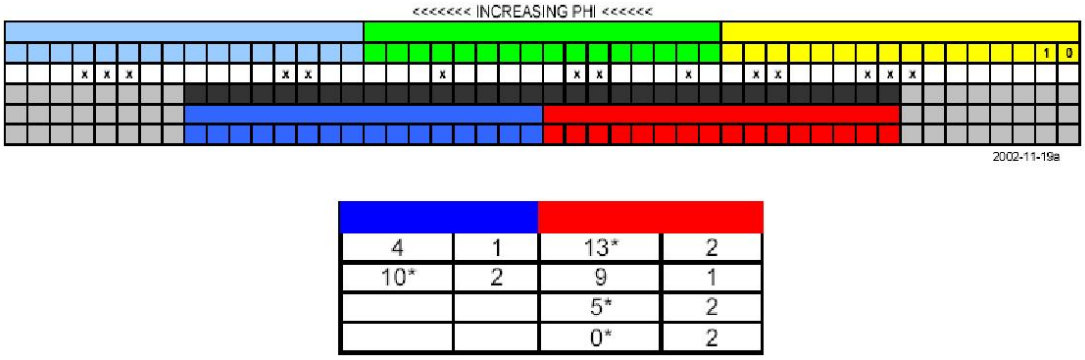

Figure A.5: The cluster finding algorithm uses the 16 CPS fibers (green) from the sector and 8 axial fibers from neighboring sectors (light blue and yellow). Starting from the center of all 32 fibers (where the dark blue and red sections meet), the first four clusters found in the scans from increasing ϕ in the dark blue section and from decreasing ϕ in the red section are recorded. The location and cluster size are recorded for each cluster. The location uses numbers 0 - 15 where for the blue scan, 0 marks the center and 15 marks the fiber furthest from the center, and for the red scan 0 marks the fiber furthest from the center and 15 marks the fiber at the center.

A.2.4 Track Cluster Matching Functionality

The matching between track and cluster is done using another lookup table. An infinite projection is made where a straight line drawn from the center of the sector to the specific hit of the last axial layer is extended out to the CPS scintillator layer. Based on the track's curvature and the momentum range it belongs to, a correction factor is given that shifts the location of the CPS scintillator picked by the infinite projection. These first steps are pictured in Fig. A.6. In three iterations, the smallest difference is found between the corrected CPS scintillator location and the centroid of clusters found. The corresponding cluster's centroid

with the smallest difference is matched with the CFT track.

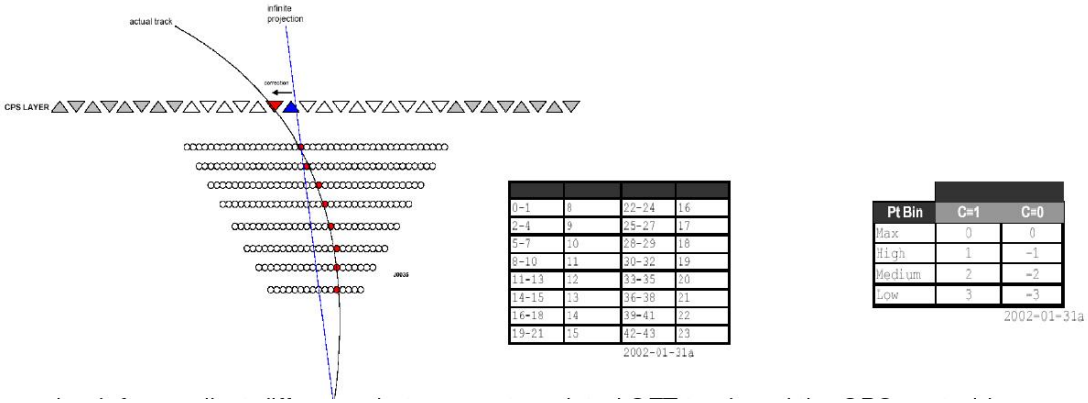

Figure A.6: On the left, an infinite projection (blue line) is made from the center of the sector to the hit in the last axial layer. The corresponding CPS scintillator is found from the central table that gives the CPS scintillator position , numbered 0 - 23 from the right to left, based on the position of the hit in the last layer numbered 0 - 43 starting from right to left. Based on the curvature and p_T bin of the track, the position of the CPS scintillator position from the infinite projection is corrected for using the table on the right.

All this information is organized by the backend FPGA which produces L1Muon tracks, L1CTOC and L2CTOC records. For L1Muon, the six highest p_T tracks are sent. For L1CTOC records, CFT tracks and CPS clusters are matched and the number of tracks in each p_T bin are counted. The record also includes the sum of the p_T of all tracks found as well as the occupancy or the amount of hits in each sector. Isolated tracks are also defined by making sure there are no tracks in neighboring sectors. The two types of L2CTOC records store a list of tracks with matching cluster information (L2CFT) and a list of clusters with matching track information (L2CPS) using the algorithm mentioned above.

A.2.5 DFEA Upgrade

In 2006, the DFEA boards were upgraded [124]to accommodate the higher luminosity expected at DØ. Prior to this upgrade, each doublet layer was mapped as one point in space, resulting in at most eight space points. At higher luminosity, high p_T tracks will be dominated by fakes and at the time the DFEA boards were made, memory constraints required the use of the doublet scheme. With the reduction in cost for memory allocation, the DFEA2 boards now

have larger FPGAs in the form of Xilinx Virtex II [125] with 6 million gates to handle singlet equations where the eight doublet layers can now incorporate the hits in the two scintillator layers. By doing this, more track equations are required due to the larger combinatorics from eight possible hits to now at most 16 hits. Thus, 50,000 equations are required instead of 16,000.

The boards also use one integrated board instead of a motherboard and daughterboard and the wiring that connects the boards to the Mixer other components of the CTT is done in the backplane, allowing for easier access to the boards in case of board failure. These improvements can be seen in Fig. A.7. There are also improved diagnostics such as front panel LEDs that have eight display modes that can provide information on the status of the boards, test vectors that can be sent downstream, the ability to load arbitrary fake events or test patterns into the datastream at a rate of 396 ns, a capture buffer that can take a snapshot of the DFEA2's inputs and outputs for an event, and the ability to produce a known, fixed output record. Additionally, the DFEA2s have a gigabit ethernet connection for faster firmware downloading in case the boards lose their programming.

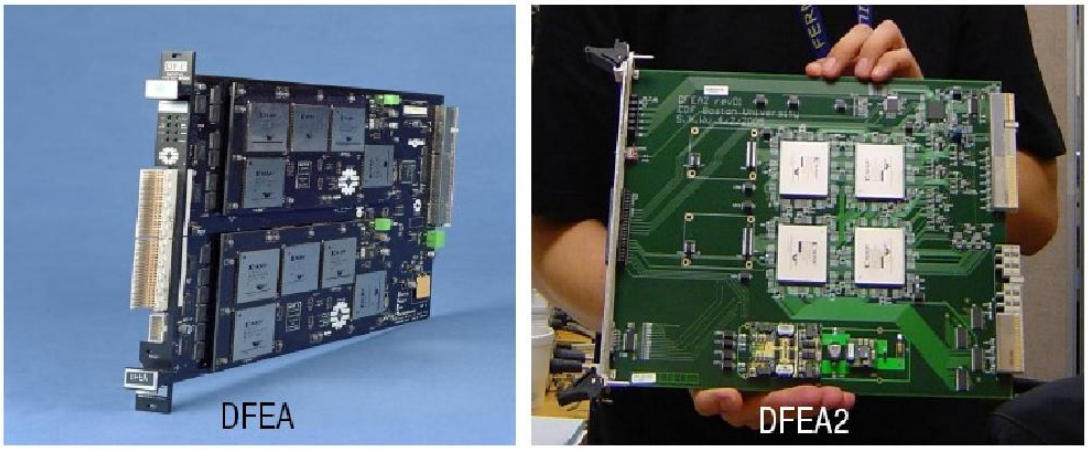

Figure A.7: The DFEA (left) was upgraded to the DFEA2 (right). The DFEA2 now has an integrated board instead of a mother and daughter board. Additionally, the four FPGAs in the center of the board has more gates to handle the singlet equations.

Since this is replacing an already working system, two DFEA2 boards were installed in a

parallel chain prior to the full system upgrade to check that the boards can handle real time data. The boards were checked at a test stand, pictured in Fig. A.8. The test stand looked at the bit error rate from LVDS cables that are similar to those used in the platform and at the tracks found from a known fake hit pattern sent at a rate similar to data taking conditions.

Figure A.8: The test stand pictured here was used to find the bit error rates from LVDS cables similar to those used in the platform and to check the track finding abilities using fake hit patterns sent at a rate similar to data taking conditions. After the upgrade, the test stand can also be used to test problematic boards.

Once installed on the platform as seen in Fig. A.9, the DFEA2 boards were properly integrated into the *DØ* detector by checking the cabling was correct, the timing matched that of the detector, and the data structure sent downstream to other subsystems and the CTT is correct. There have been no failures since installation.

A.2.6 DFEA2 Performance

The CTT performance is now better with the upgrade, reducing the rate of tracks found [126] especially in the higher momentum range as seen in Fig. A.10. This is important because current run taking conditions have higher luminosity rates, resulting in too many tracks being found using the doublet scheme. The singlet scheme lowers the rates at a level that the trigger system can still handle. Additionally, the trigger turn on curves are sharper and have equal or better efficiencies using the singlet scheme as pictured in Fig. A.11.

Figure A.9: The 40 DFEA2 boards are pictured here from the front (left) and back (right) view after being installed in the platform. The boards can be tested in the front end and easily removed since the wiring is all in the back of the crate.

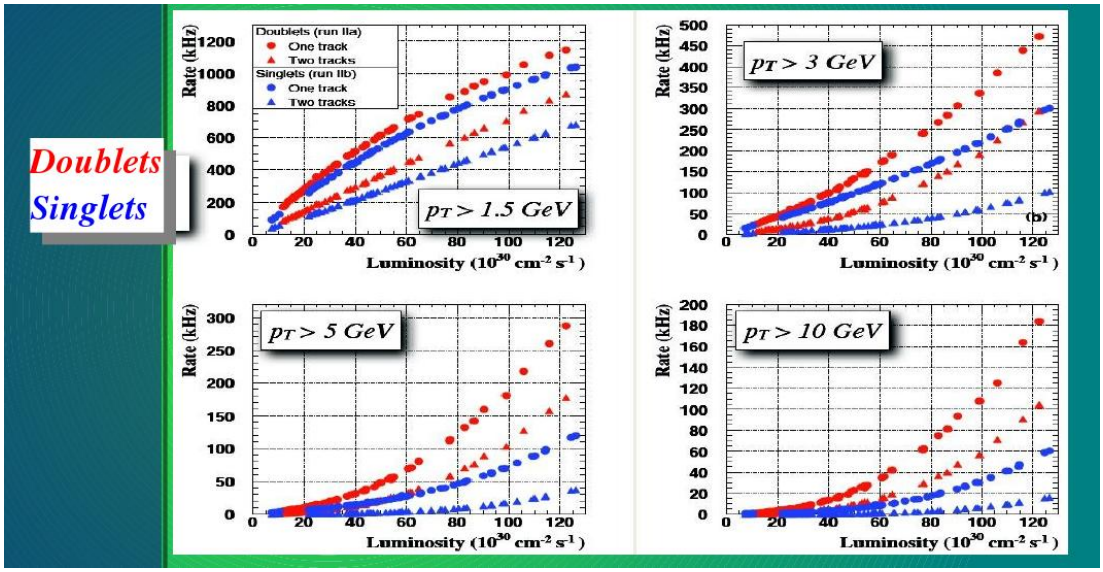

Figure A.10: The trigger rates for the doublet (red) and singlet (blue) scheme are determined for the four p_T bins used by the CTT. The singlet scheme has lower rates which is particularly important for current run taking conditions that reach luminosities well above $10^{32} cm^{-2} s^{-1}$

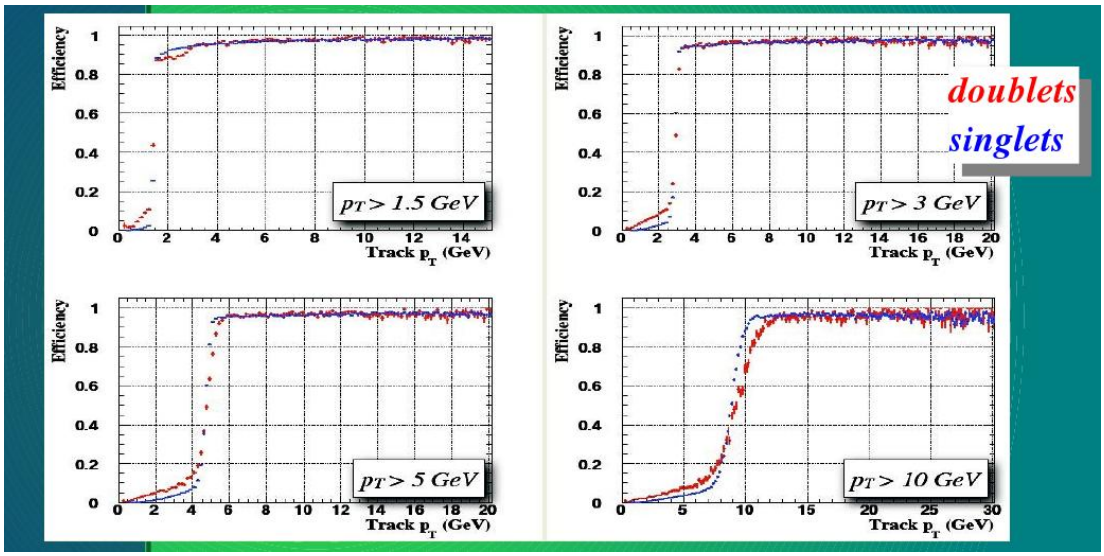

Figure A.11: The trigger turn on curves for the doublet (red) and singlet (blue) scheme are determined for the four p_T bins used by the CTT. The trigger turn on curves are sharper and have equal or better efficiencies using the singlet scheme.

Appendix B

tb and tqb Discriminant Plots Used for Reordering

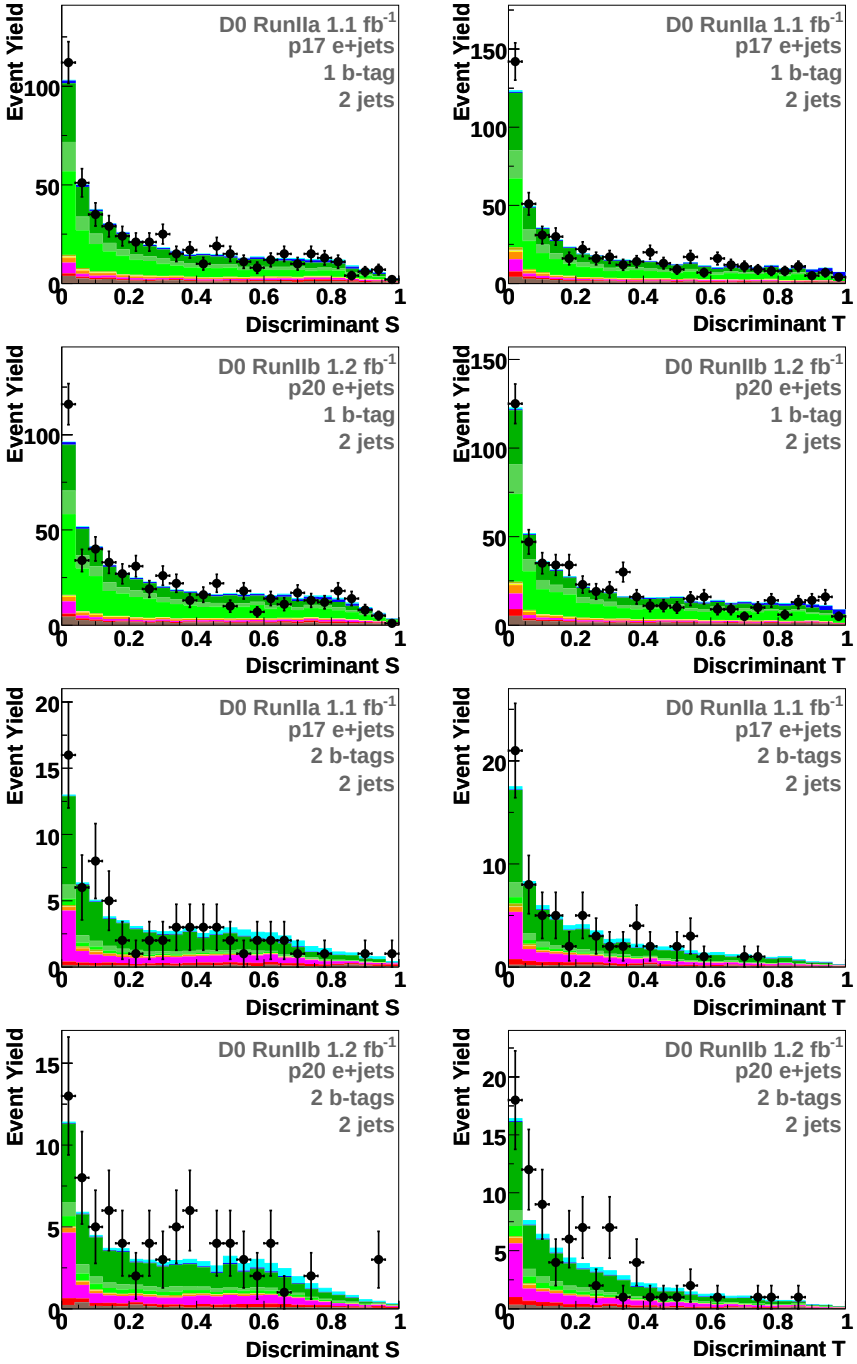

Figure B.1: Input discriminant plots for two jet events in the electron channel (first row) with one b tag for Run IIa data for Discriminant tb and Discriminant tqb, (second row) with one b tag for Run IIb data for Discriminant tb and Discriminant tqb, (third row) two b tag for Run IIa data for Discriminant tb and Discriminant tqb, (fourth row) with two b tag for Run IIb data for Discriminant tb and Discriminant tqb.

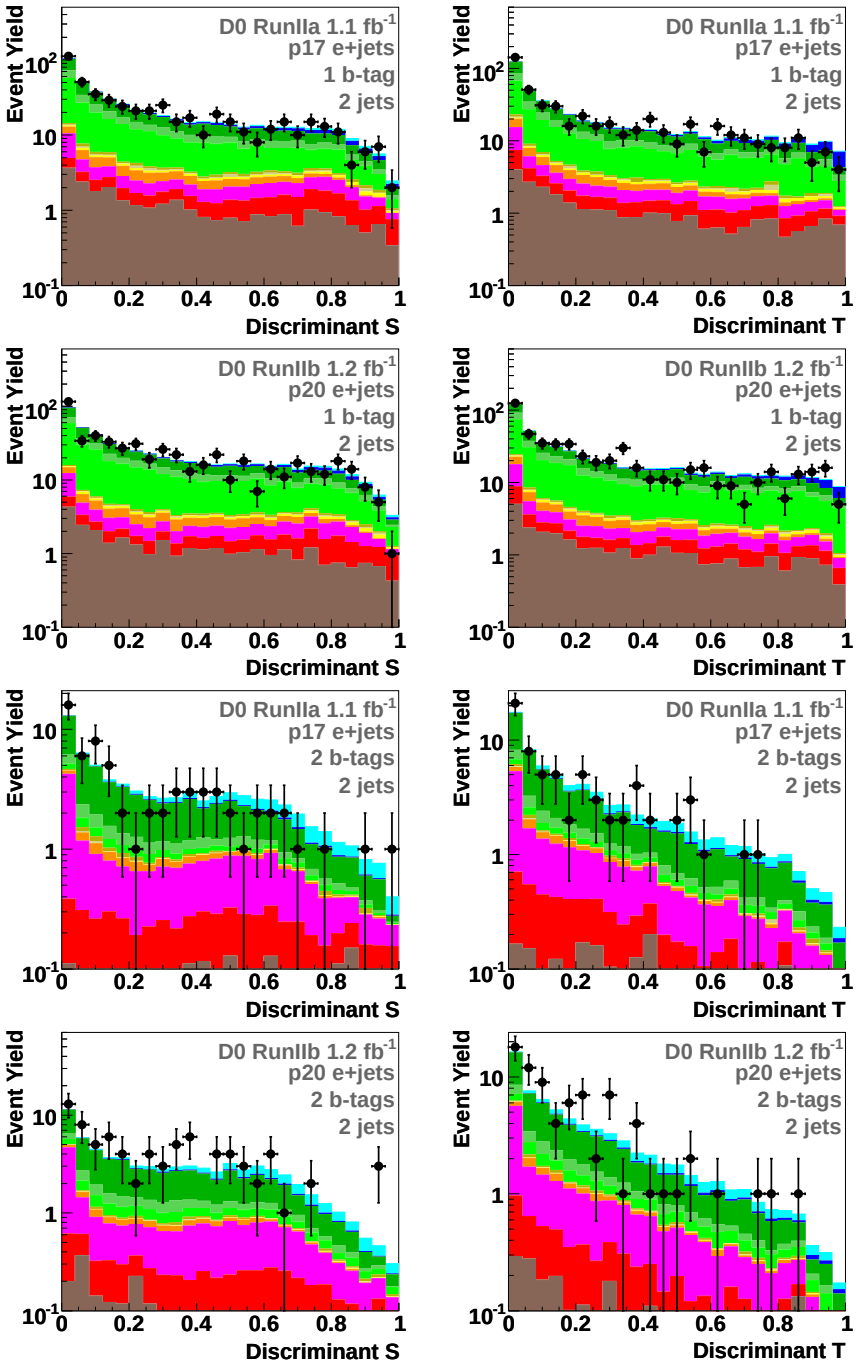

Figure B.2: Input discriminant plots for two jet events in log scale in the electron channel (first row) with one b tag for Run IIa data for Discriminant tb and Discriminant tqb, (second row) with one b tag for Run IIb data for Discriminant tb and Discriminant tqb, (third row) two b tag for Run IIa data for Discriminant tb and Discriminant tqb, (fourth row) with two b tag for Run IIb data for Discriminant tb and Discriminant tqb.

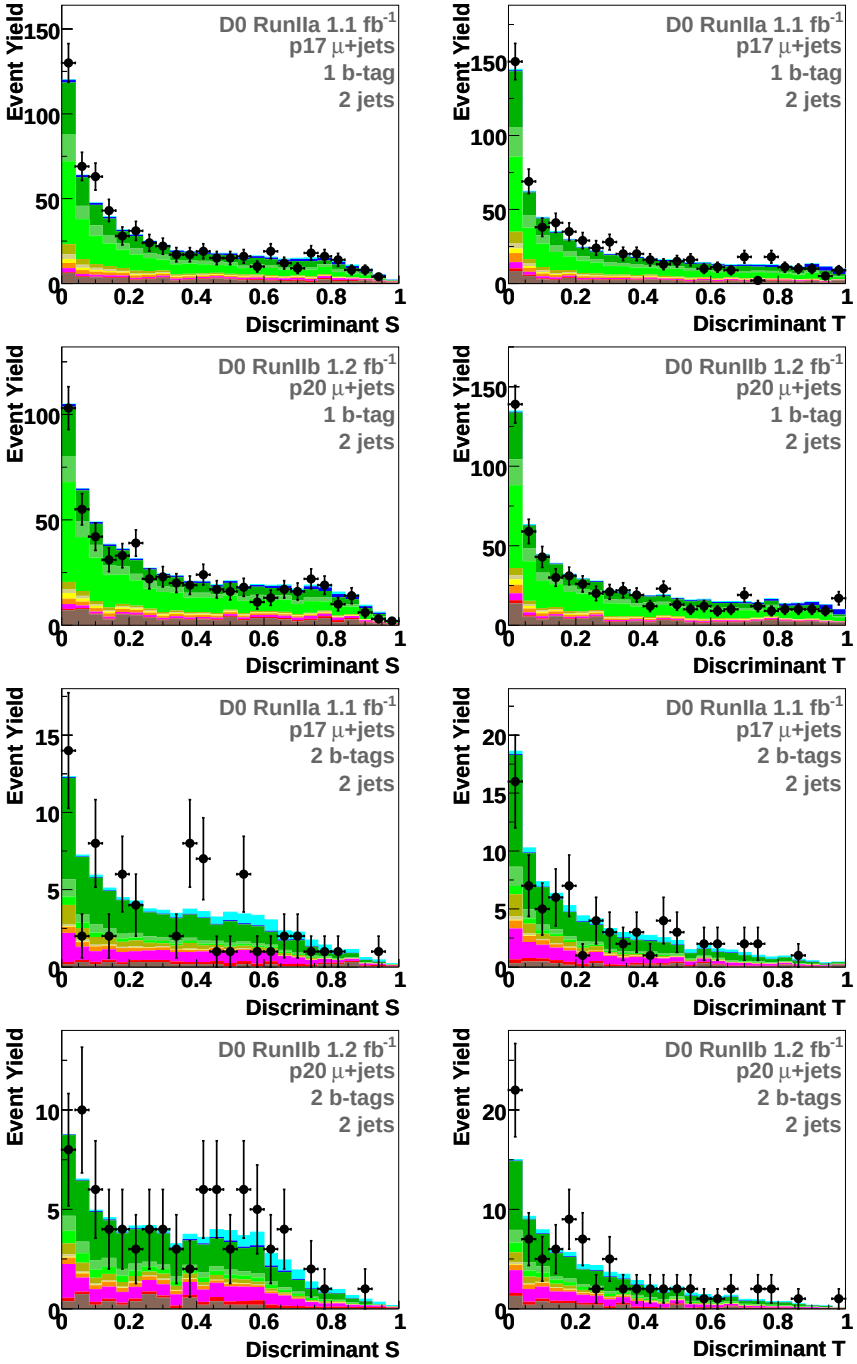

Figure B.3: Input discriminant plots for two jet events in the muon channel (first row) with one b tag for Run IIa data for Discriminant tb and Discriminant tqb, (second row) with one b tag for Run IIb data for Discriminant tb and Discriminant tqb, (third row) two b tag for Run IIa data for Discriminant tb and Discriminant tqb, (fourth row) with two b tag for Run IIb data for Discriminant tb and Discriminant tqb.

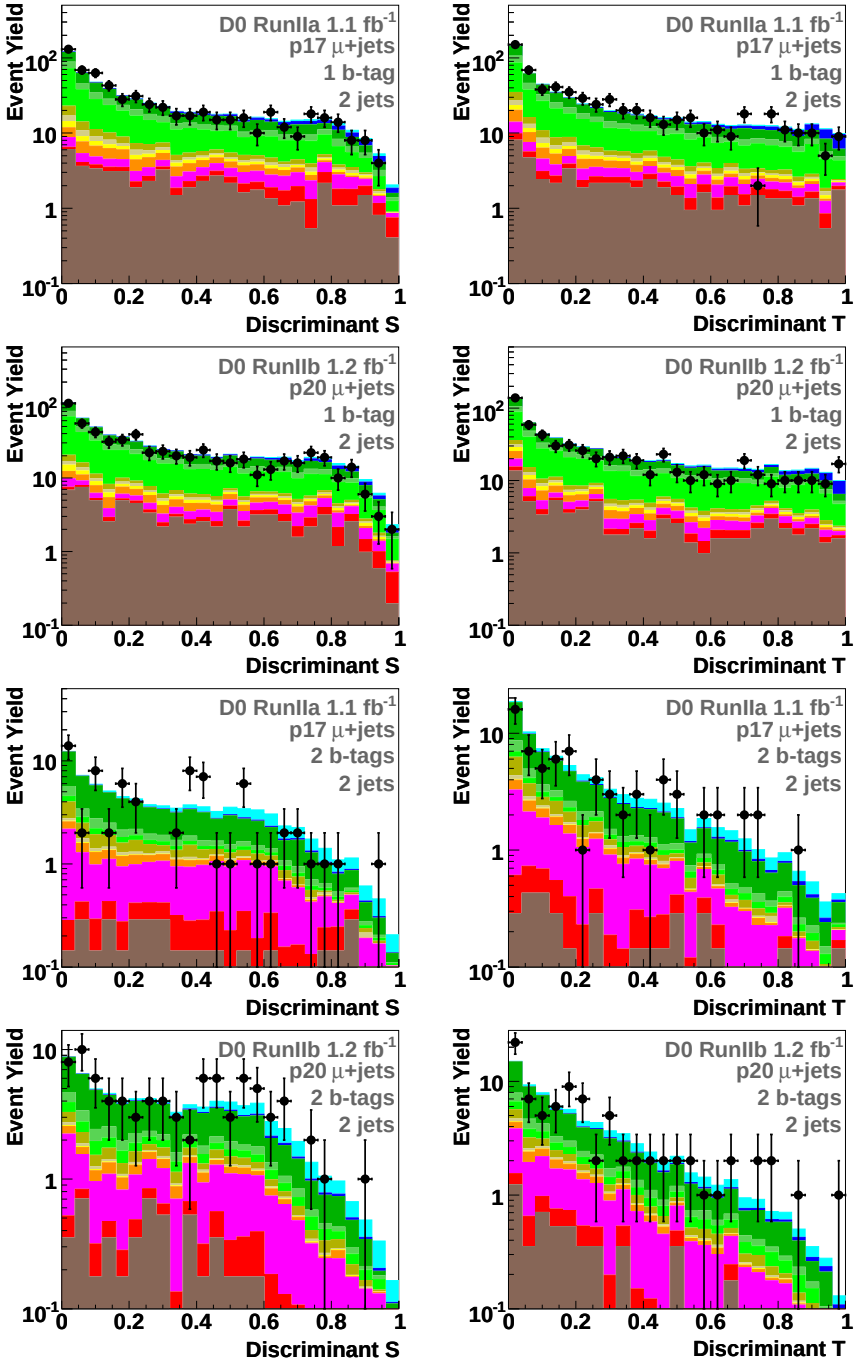

Figure B.4: Input discriminant plots for two jet events in the muon channel in log scale (first row) with one b tag for Run IIa data for Discriminant tb and Discriminant tqb, (second row) with one b tag for Run IIb data for Discriminant tb and Discriminant tqb, (third row) two b tag for Run IIa data for Discriminant tb and Discriminant tqb, (fourth row) with two b tag for Run IIb data for Discriminant tb and Discriminant tqb.

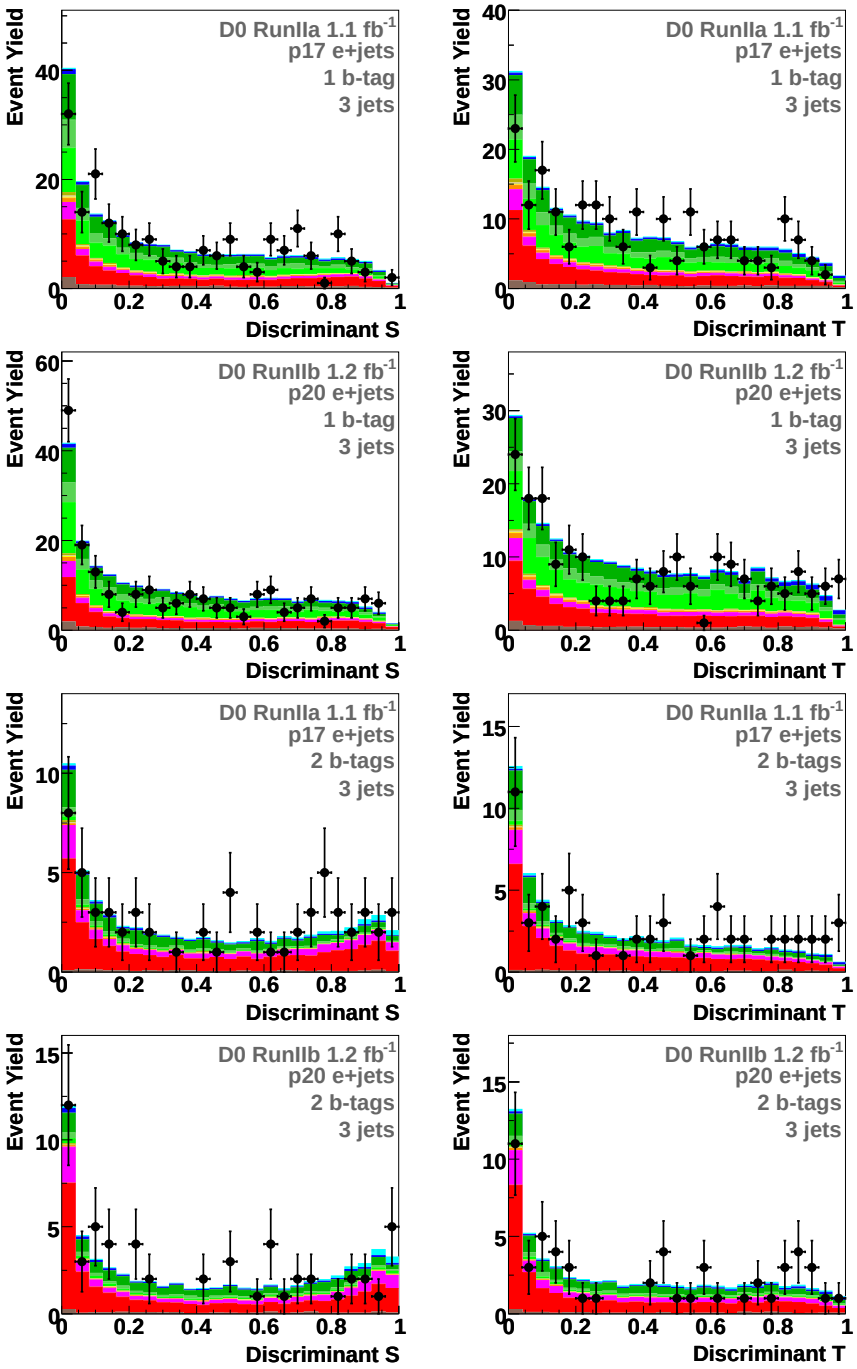

Figure B.5: Input discriminant plots for three jet events in the electron channel (first row) with one b tag for Run IIa data for Discriminant tb and Discriminant tqb, (second row) with one b tag for Run IIb data for Discriminant tb and Discriminant tqb, (third row) two b tag for Run IIa data for Discriminant tb and Discriminant tqb, (fourth row) with two b tag for Run IIb data for Discriminant tb and Discriminant tqb.

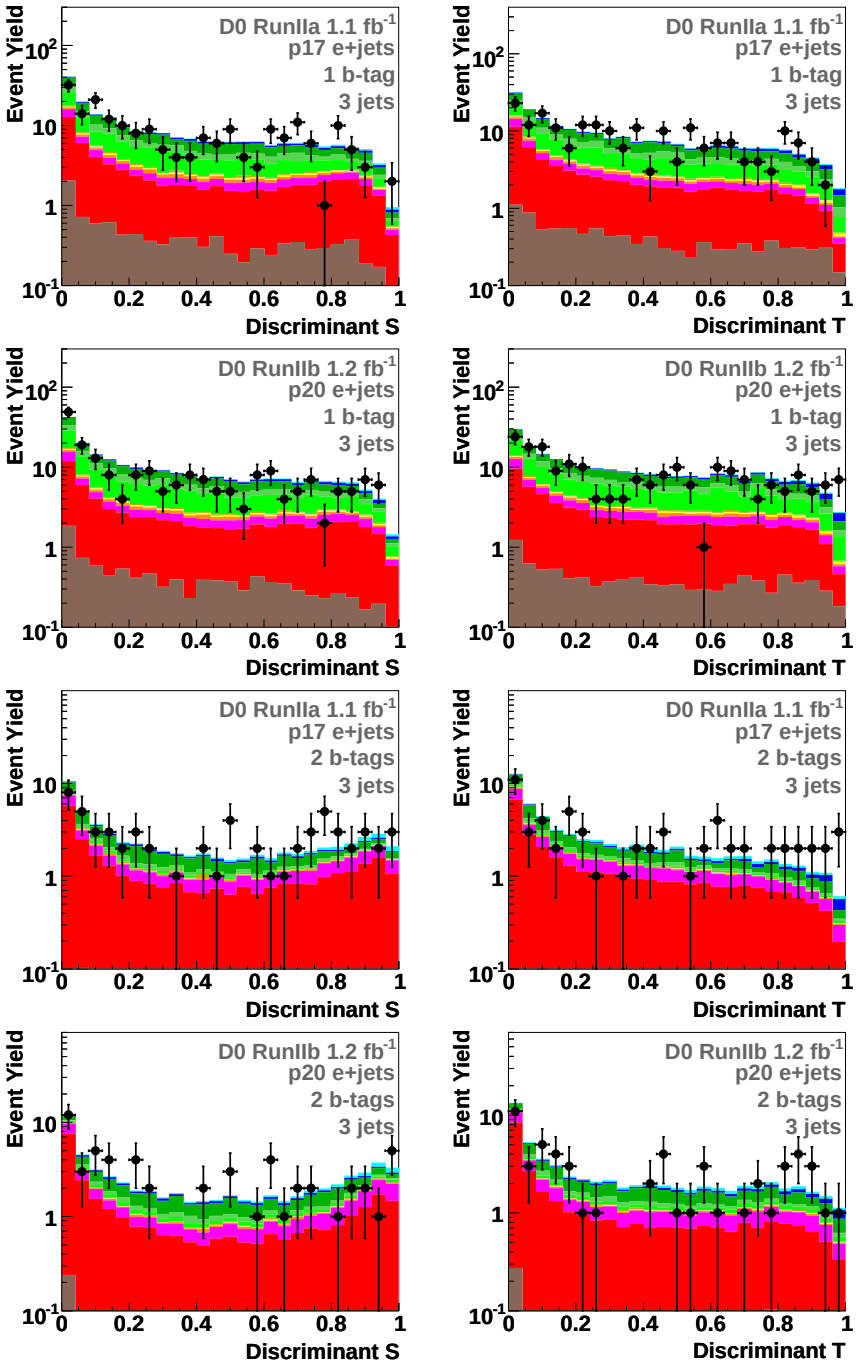

Figure B.6: Input discriminant plots for three jet events in log scale in the electron channel (first row) with one b tag for Run IIa data for Discriminant tb and Discriminant tqb, (second row) with one b tag for Run IIb data for Discriminant tb and Discriminant tqb, (third row) two b tag for Run IIa data for Discriminant tb and Discriminant tqb, (fourth row) with two b tag for Run IIb data for Discriminant tb and Discriminant tqb.

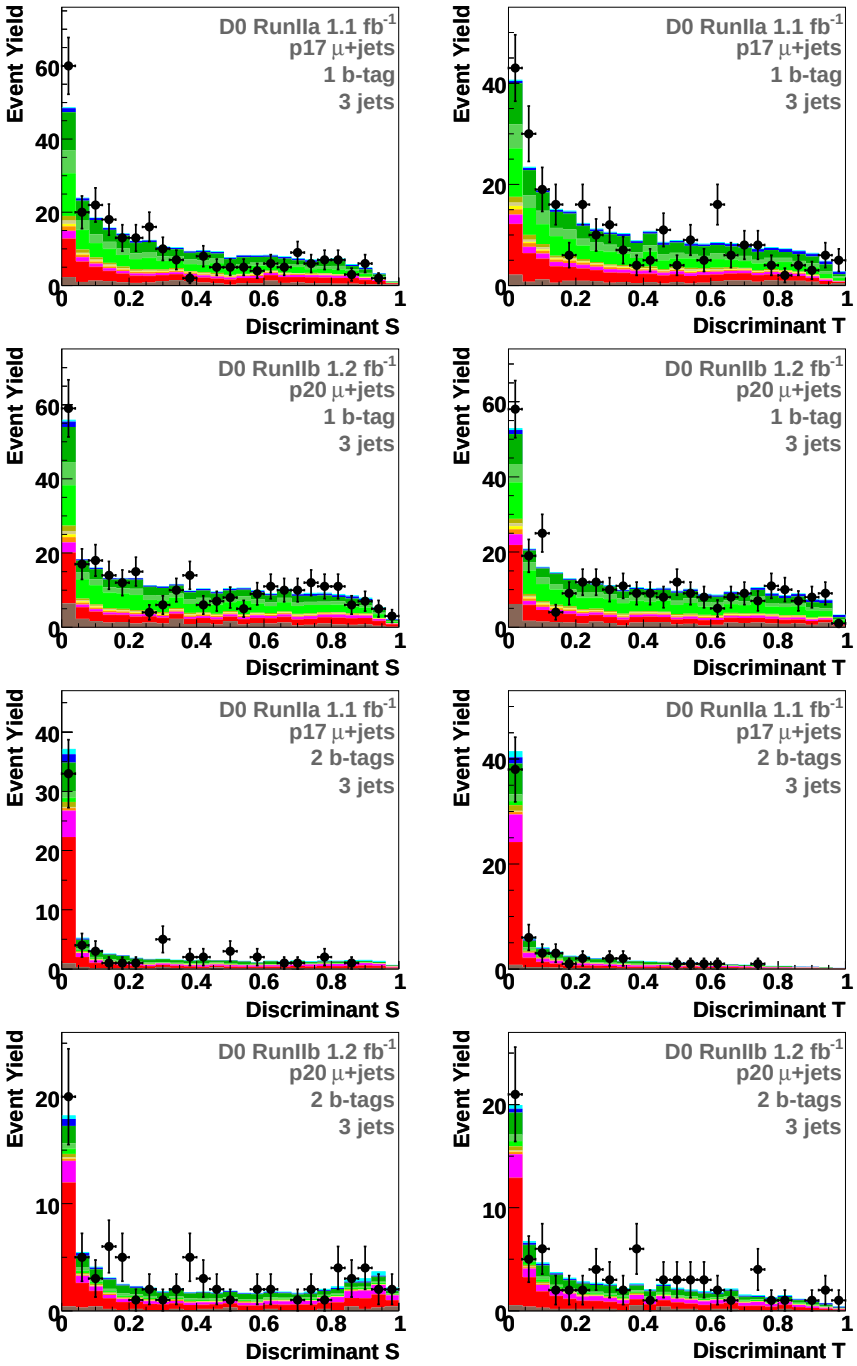

Figure B.7: Input discriminant plots for three jet events in the muon channel (first row) with one b tag for Run IIa data for Discriminant tb and Discriminant tqb, (second row) with one b tag for Run IIb data for Discriminant tb and Discriminant tqb, (third row) two b tag for Run IIa data for Discriminant tb and Discriminant tqb, (fourth row) with two b tag for Run IIb data for Discriminant tb and Discriminant tqb.

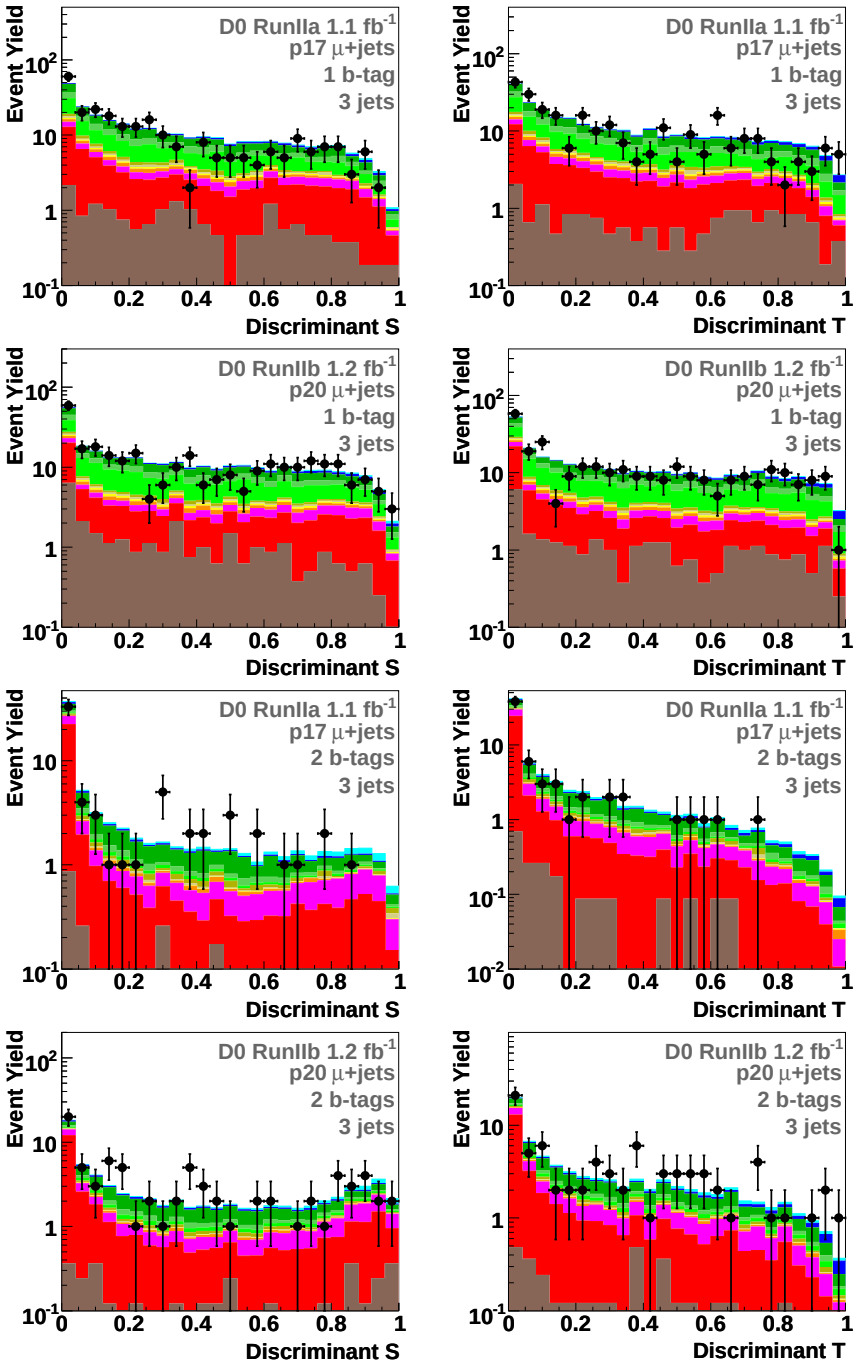

Figure B.8: Input discriminant plots for three jet events in the muon channel in log scale (first row) with one b tag for Run IIa data for Discriminant tb and Discriminant tqb, (second row) with one b tag for Run IIb data for Discriminant tb and Discriminant tqb, (third row) two b tag for Run IIa data for Discriminant tb and Discriminant tqb, (fourth row) with two b tag for Run IIb data for Discriminant tb and Discriminant tqb.

Appendix C

Signal over Background Ordered Matrix Element Discriminant

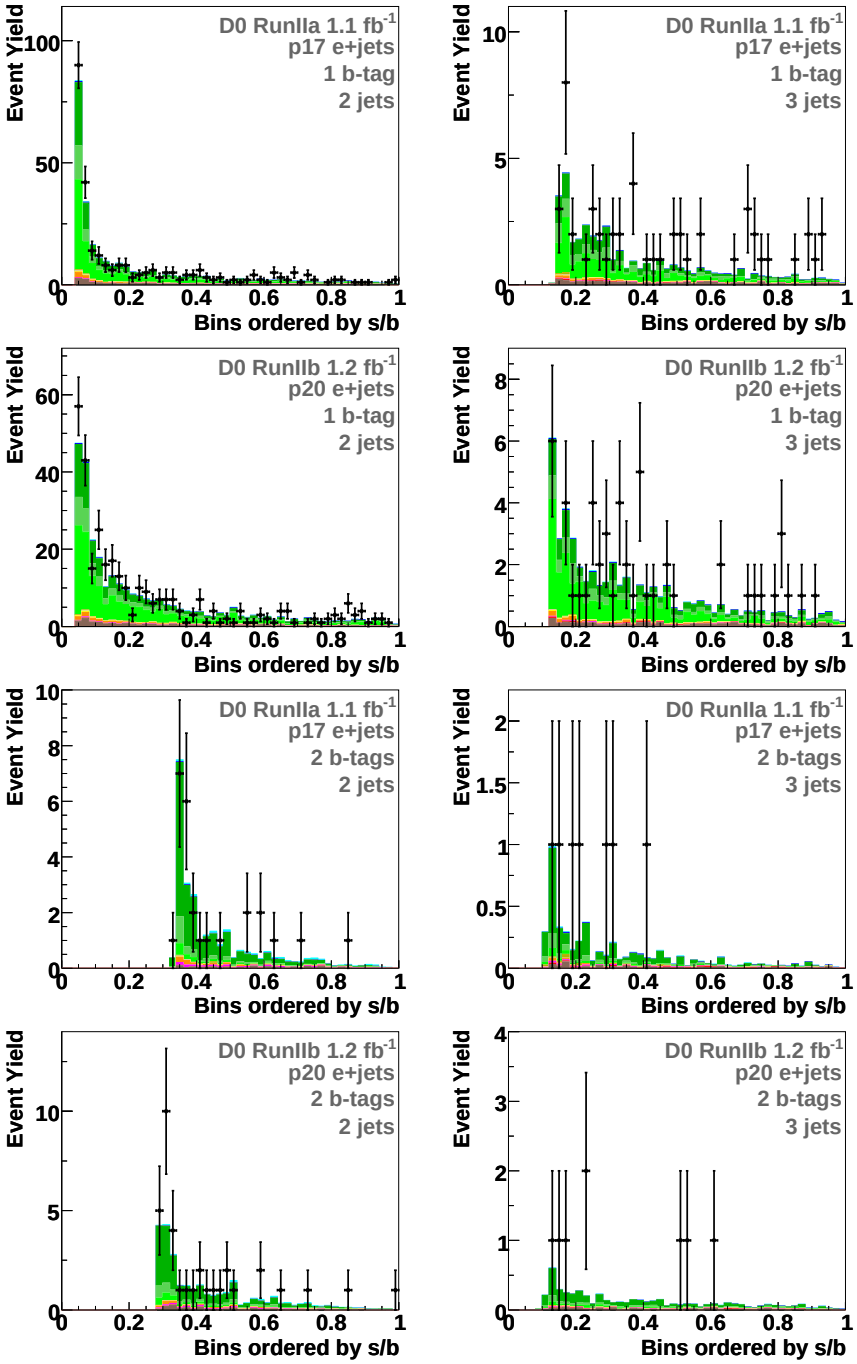

Figure C.1: Discriminant plots for events in the electron channel (first row) with one b tag for Run IIa data with two jets and three jets, (second row) with one b tag for Run IIb data with two jets and three jets , (third row) with two b tag for Run IIa data with two jets and three jets, (fourth row) with two b tag for Run IIb data with two jets and three jets. These plots are from 0 to 1 and are events with H_T(alljets,lepton,$\not\!\!E_T$)$<$ 175 GeV

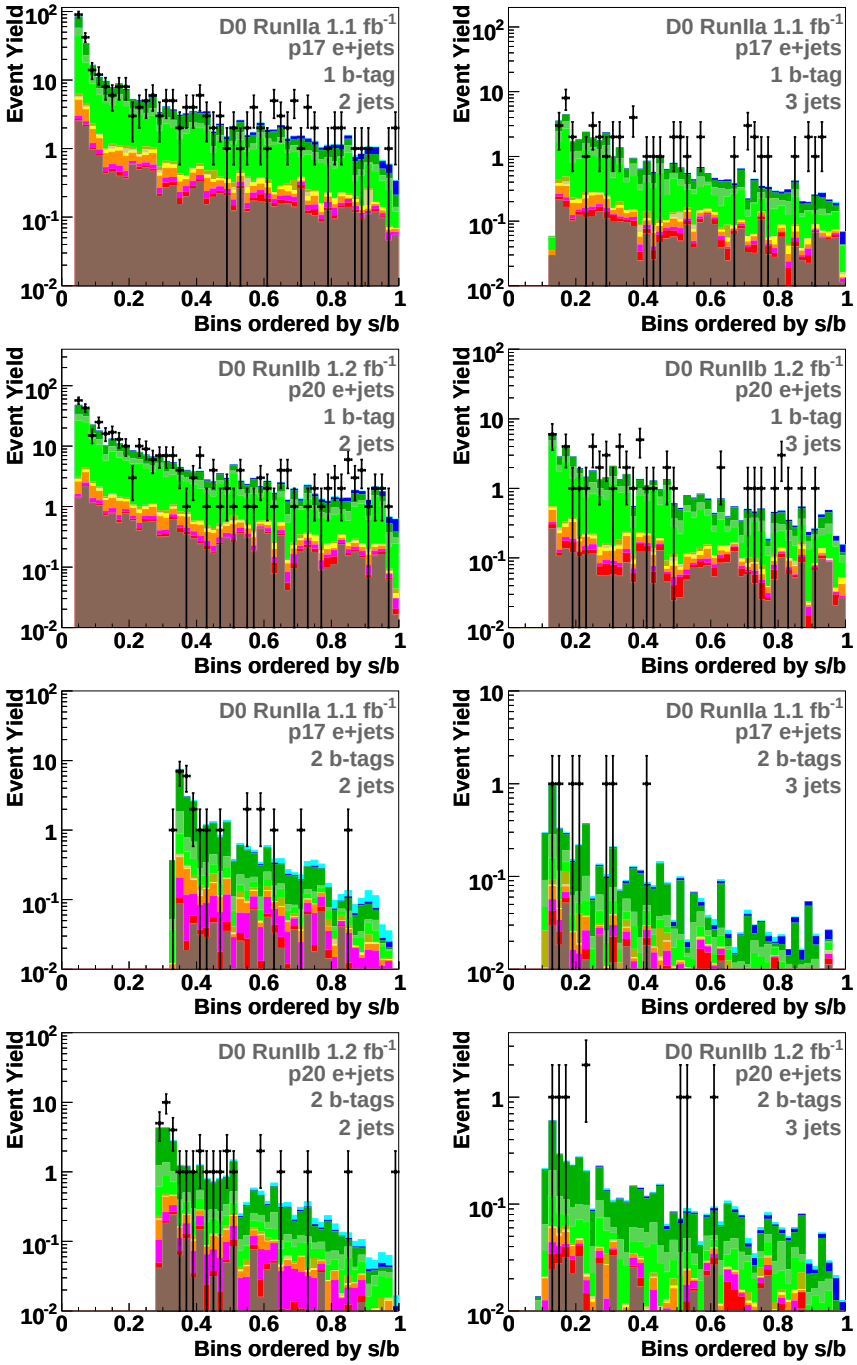

Figure C.2: Discriminant plots for events in the electron channel in log scale (first row) with one b tag for Run IIa data with two jets and three jets, (second row) with one b tag for Run IIb data with two jets and three jets , (third row) with two b tag for Run IIa data with two jets and three jets, (fourth row) with two b tag for Run IIb data with two jets and three jets. These plots are from 0 to 1 and are events with H_T(alljets,lepton,$\not\!\!E_T$)$<$ 175 GeV

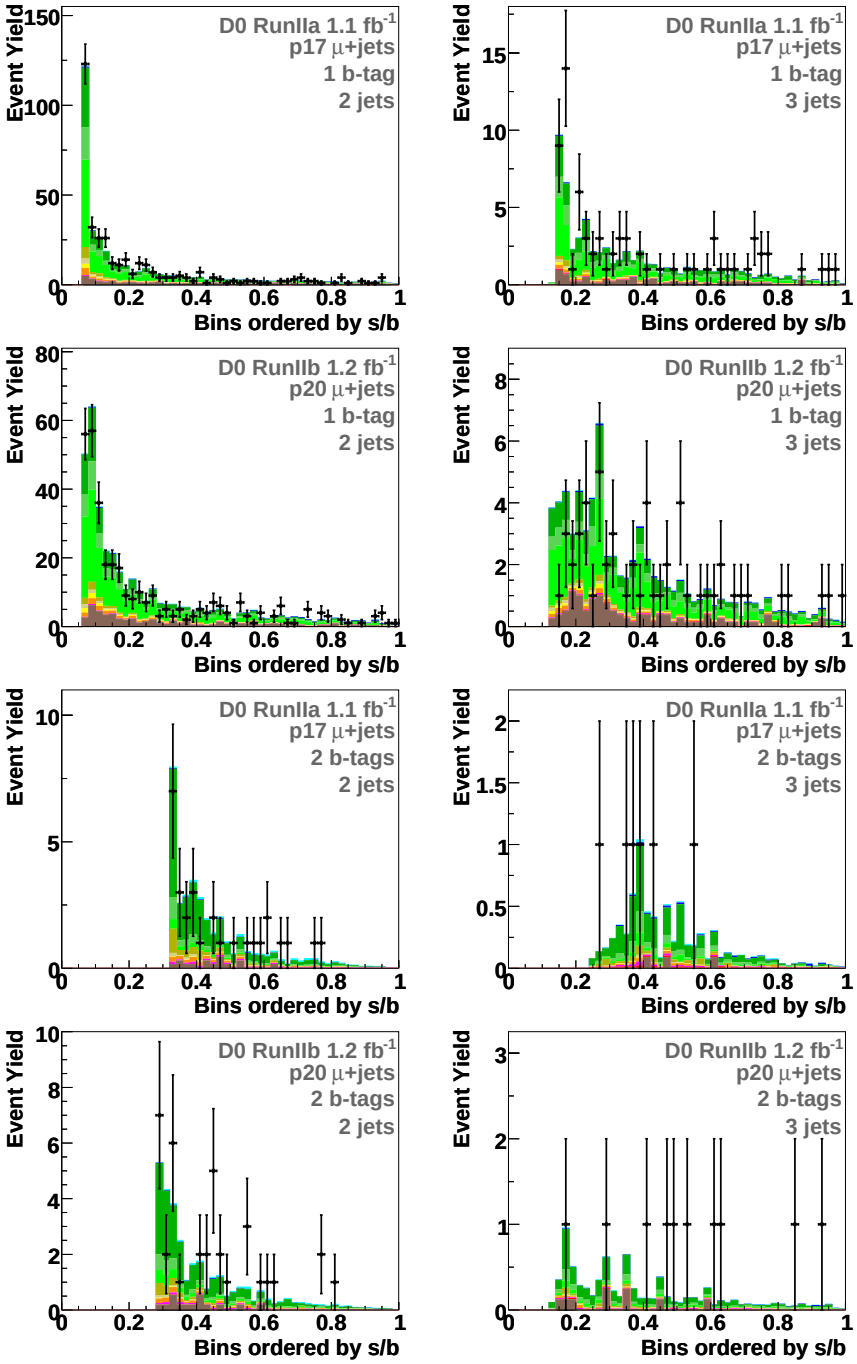

Figure C.3: Discriminant plots for events in the muon channel (first row) with one b tag for Run IIa data with two jets and three jets, (second row) with one b tag for Run IIb data with two jets and three jets , (third row) with two b tag for Run IIa data with two jets and three jets, (fourth row) with two b tag for Run IIb data with two jets and three jets. These plots are from 0 to 1 and are events with H_T(alljets,lepton,$\not\!\!E_T$)$<$ 175 GeV

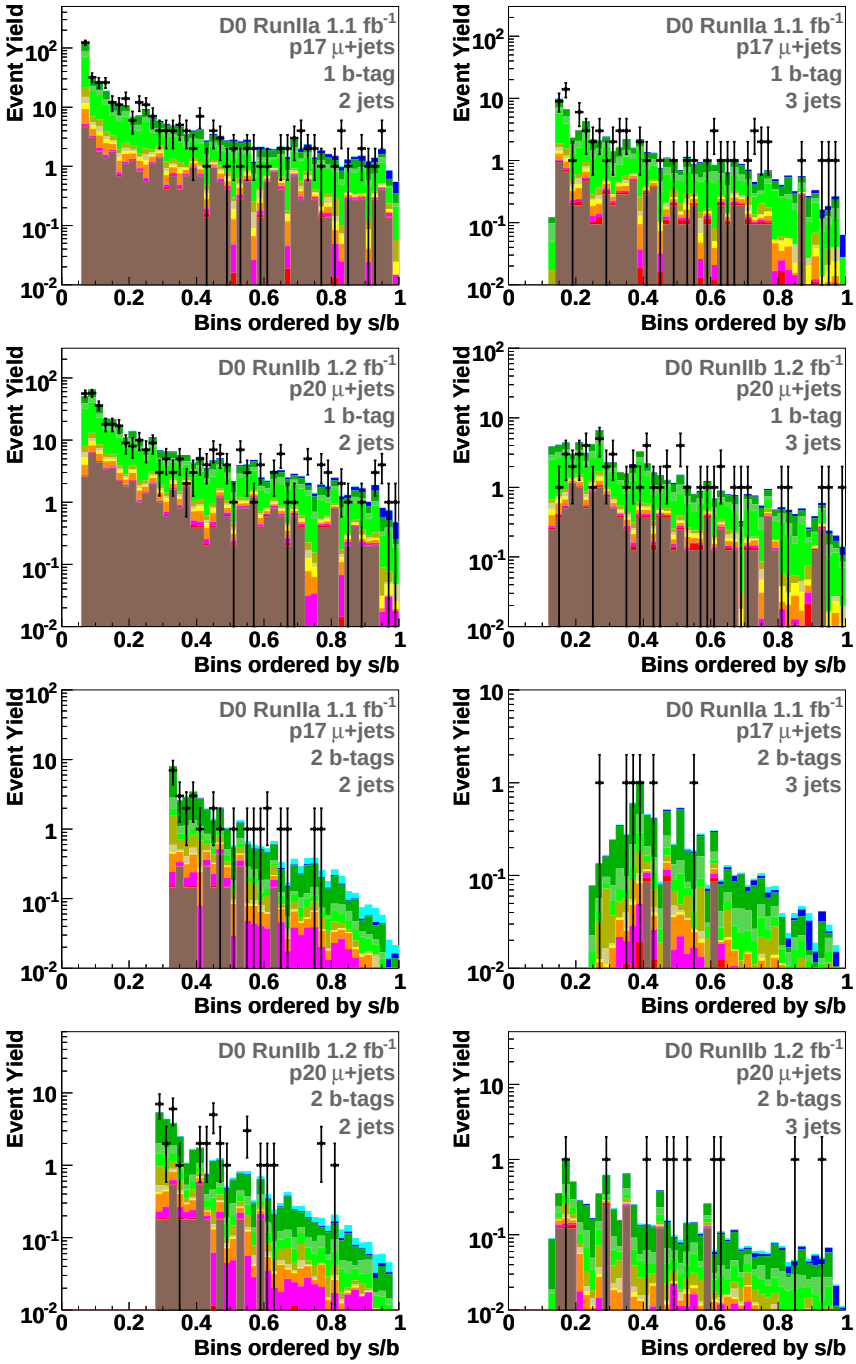

Figure C.4: Discriminant plots for events in the muon channel in log scale (first row) with one b tag for Run IIa data with two jets and three jets, (second row) with one b tag for Run IIb data with two jets and three jets , (third row) with two b tag for Run IIa data with two jets and three jets, (fourth row) with two b tag for Run IIb data with two jets and three jets. These plots are from 0 to 1 and are events with H_T(alljets,lepton,$\not\!\!E_T$)$<$ 175 GeV

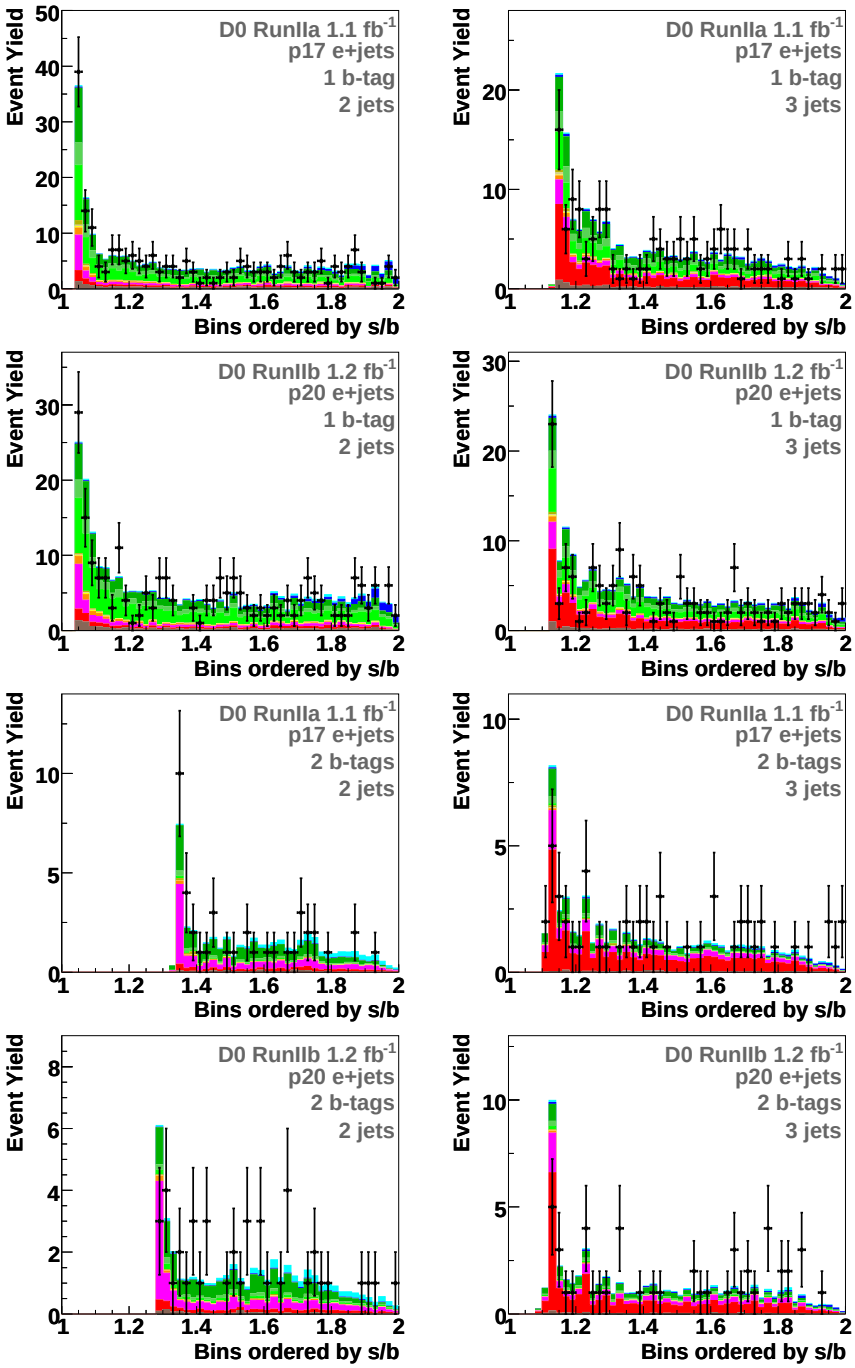

Figure C.5: Discriminant plots for events in the electron channel (first row) with one b tag for Run IIa data with two jets and three jets, (second row) with one b tag for Run IIb data with two jets and three jets , (third row) with two b tag for Run IIa data with two jets and three jets, (fourth row) with two b tag for Run IIb data with two jets and three jets. These plots are from 0 to 1 and are events with H_T(alljets,lepton,$\not\!\!E_T$)$>$ 175 GeV

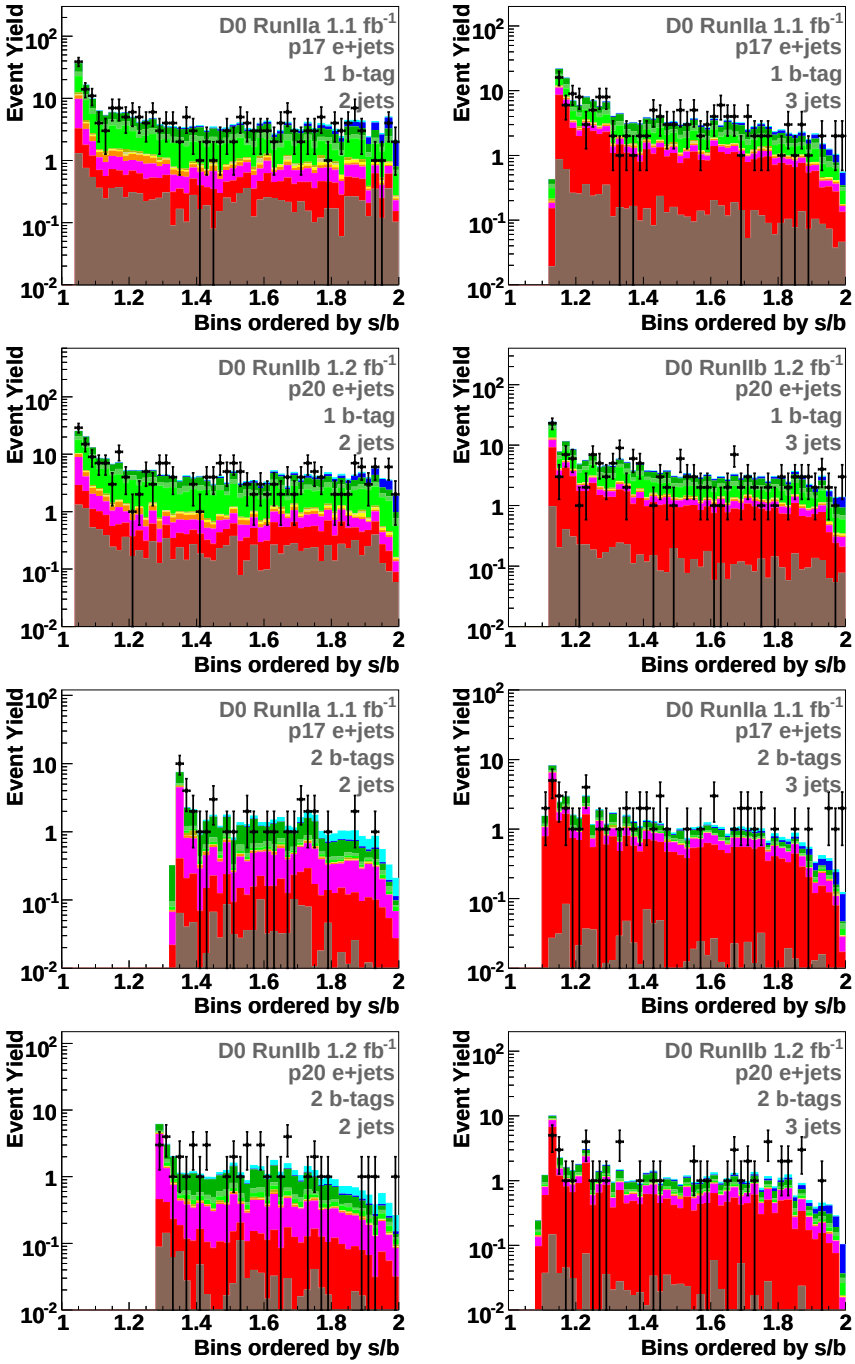

Figure C.6: Discriminant plots for events in the electron channel in log scale (first row) with one b tag for Run IIa data with two jets and three jets, (second row) with one b tag for Run IIb data with two jets and three jets , (third row) with two b tag for Run IIa data with two jets and three jets, (fourth row) with two b tag for Run IIb data with two jets and three jets. These plots are from 0 to 1 and are events with H_T(alljets,lepton,$\not\!\!E_T$)$>$ 175 GeV

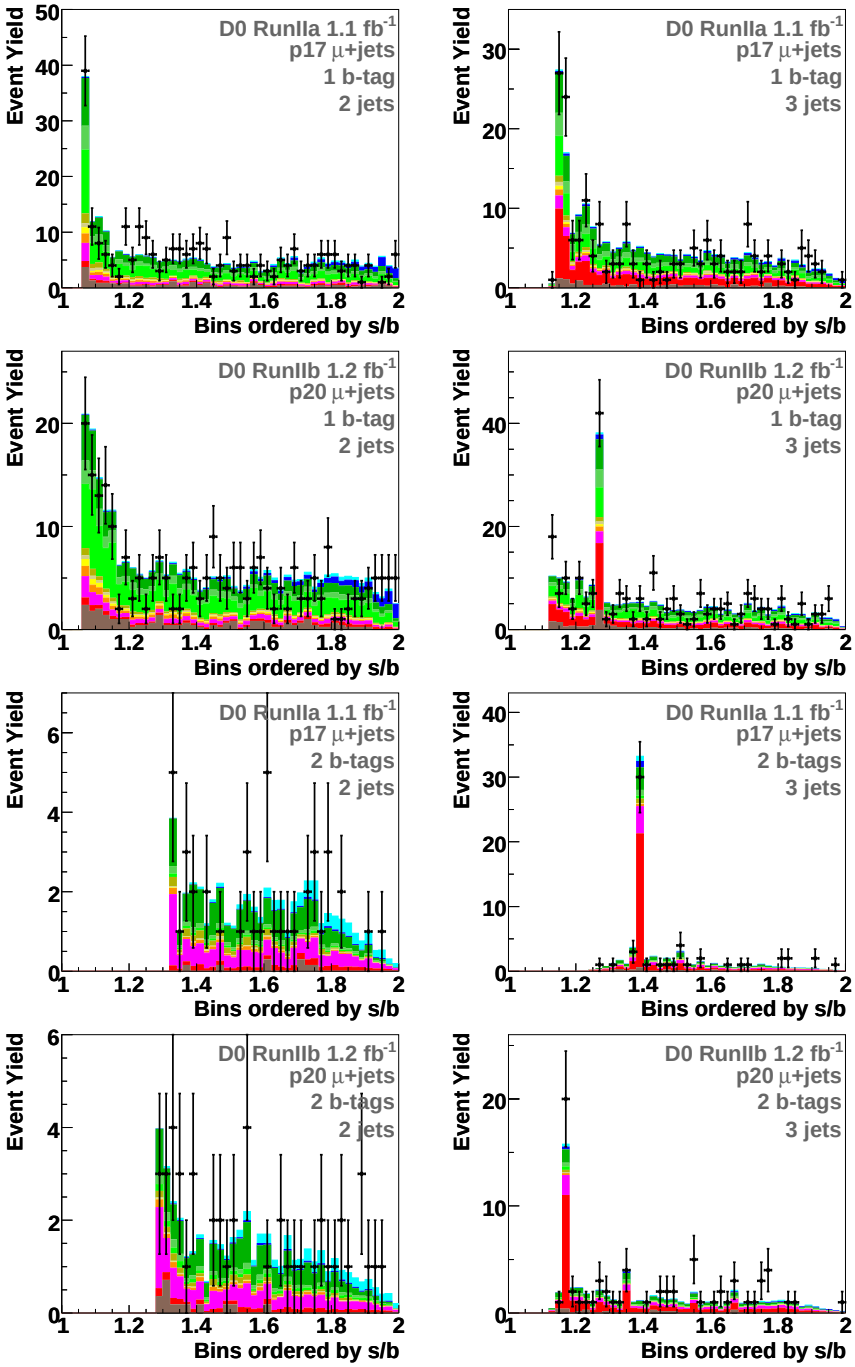

Figure C.7: Discriminant plots for events in the muon channel (first row) with one b tag for Run IIa data with two jets and three jets, (second row) with one b tag for Run IIb data with two jets and three jets , (third row) with two b tag for Run IIa data with two jets and three jets, (fourth row) with two b tag for Run IIb data with two jets and three jets. These plots are from 0 to 1 and are events with H_T(alljets,lepton,$\not\!\!E_T$)$>$ 175 GeV

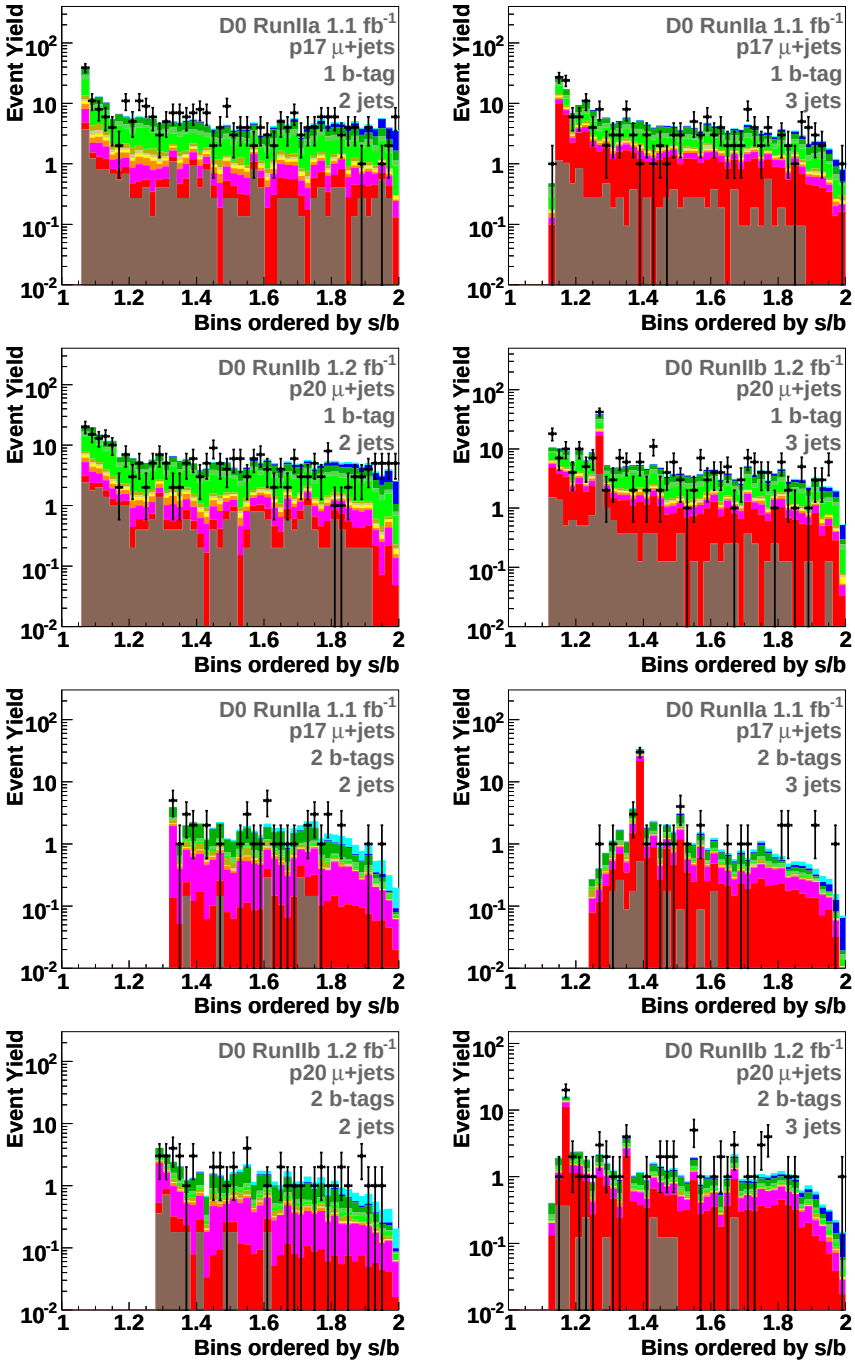

Figure C.8: Discriminant plots for events in the muon channel in log scale (first row) with one b tag for Run IIa data with two jets and three jets, (second row) with one b tag for Run IIb data with two jets and three jets , (third row) with two b tag for Run IIa data with two jets and three jets, (fourth row) with two b tag for Run IIb data with two jets and three jets. These plots are from 0 to 1 and are events with H_T(alljets,lepton,$\not\!\!E_T$)$>$ 175 GeV

Appendix D

Efficiency of Signal over Background Ordered Matrix Element Discriminant

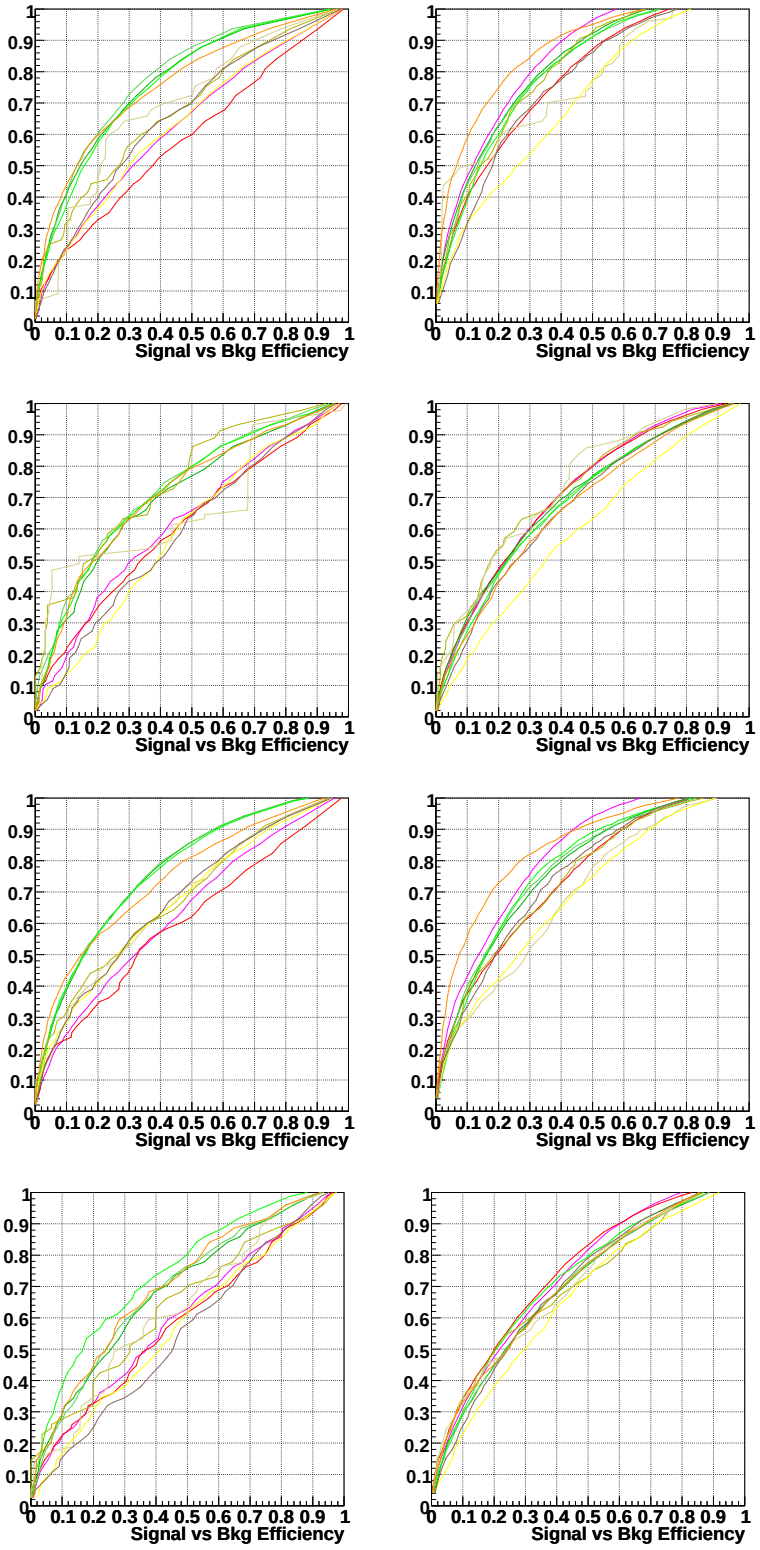

Figure D.1: The discriminant performance for $e + jets$ events with one b tag. The top two rows are Run IIa data and the bottom two rows are Run IIb data. The first and third row are two-jet events, while the second and fourth row are three-jet events. On the left is the performance for H_T(alljets,lepton,$\not\!\!E_T$) < 175 GeV events while on the right for H_T(alljets,lepton,$\not\!\!E_T$) > 175 GeV events.

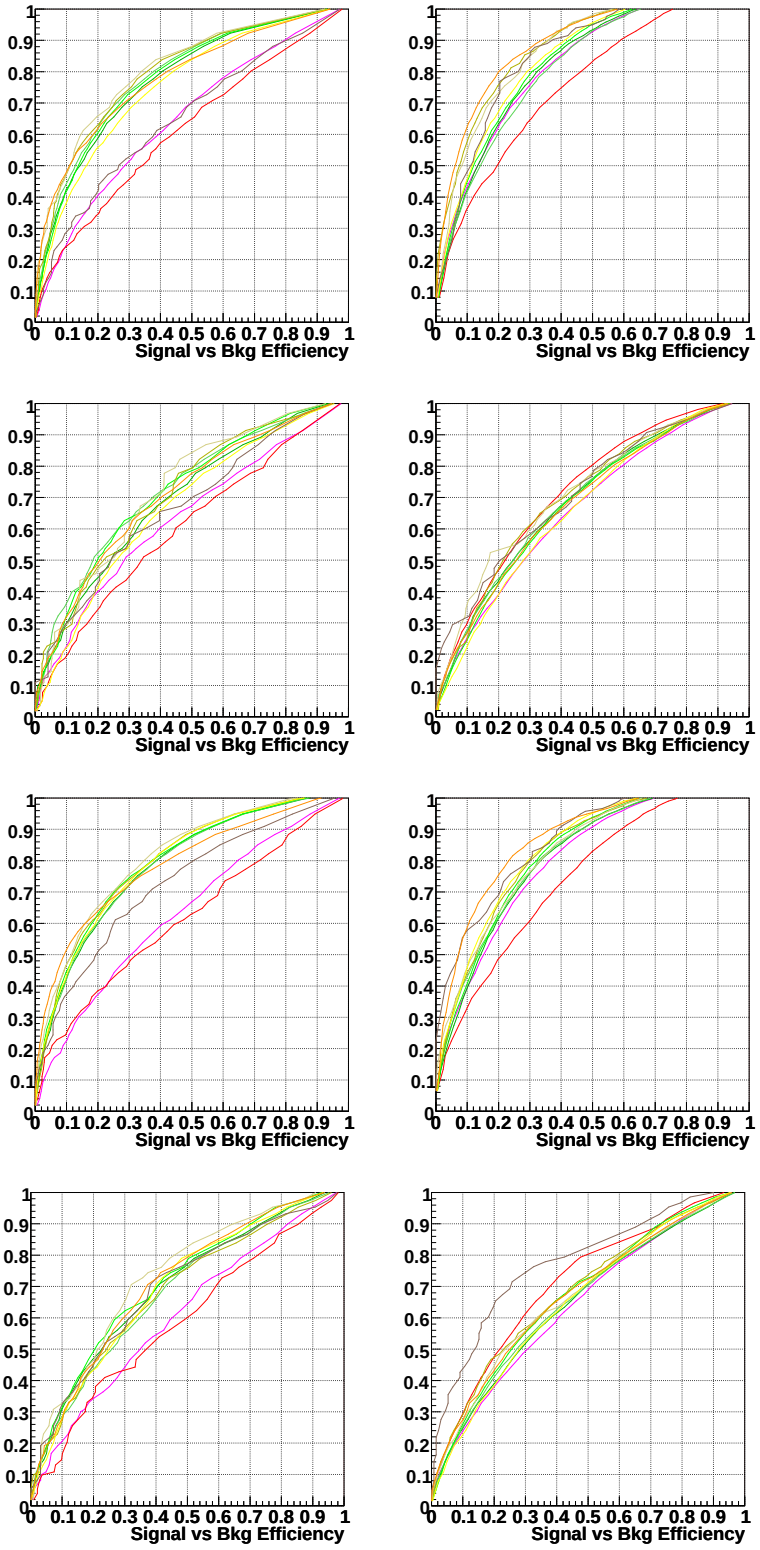

Figure D.2: The discriminant performance for $\mu + jets$ events with one b tag. The top two rows are Run IIa data and the bottom two rows are Run IIb data. The first and third row are two-jet events, while the second and fourth row are three-jet events. On the left is the performance for H_T(alljets,lepton,$\not\!\!E_T$) < 175 GeV events while on the right for H_T(alljets,lepton,$\not\!\!E_T$) > 175 GeV events.

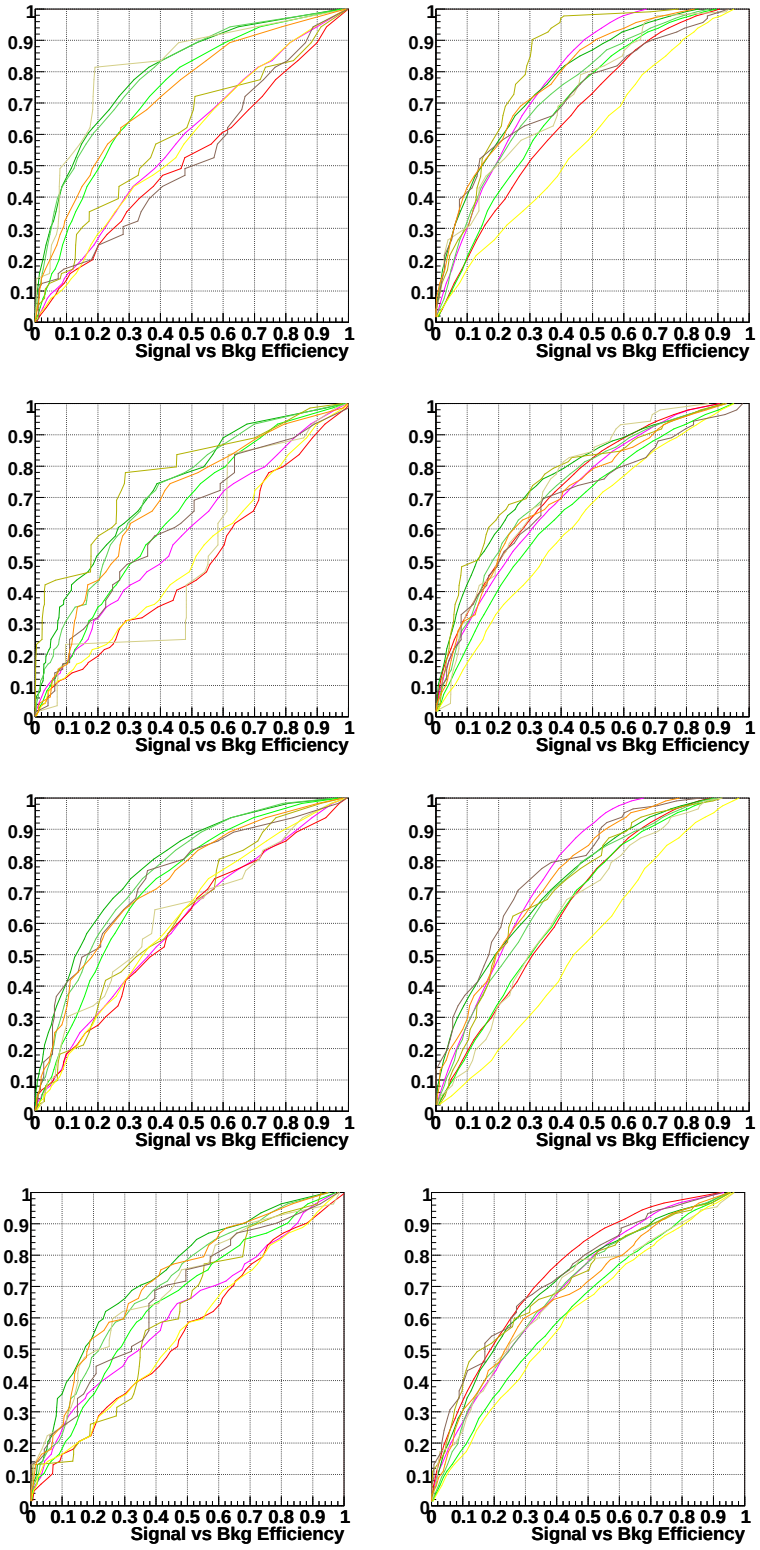

Figure D.3: The discriminant performance for $e + jets$ events with two b tags. The top two rows are Run IIa data and the bottom two rows are Run IIb data. The first and third row are two-jet events, while the second and fourth row are three-jet events. On the left is the performance for H_T(alljets,lepton,$\not\!\!E_T$) < 175 GeV events while on the right for H_T(alljets,lepton,$\not\!\!E_T$) > 175 GeV events.

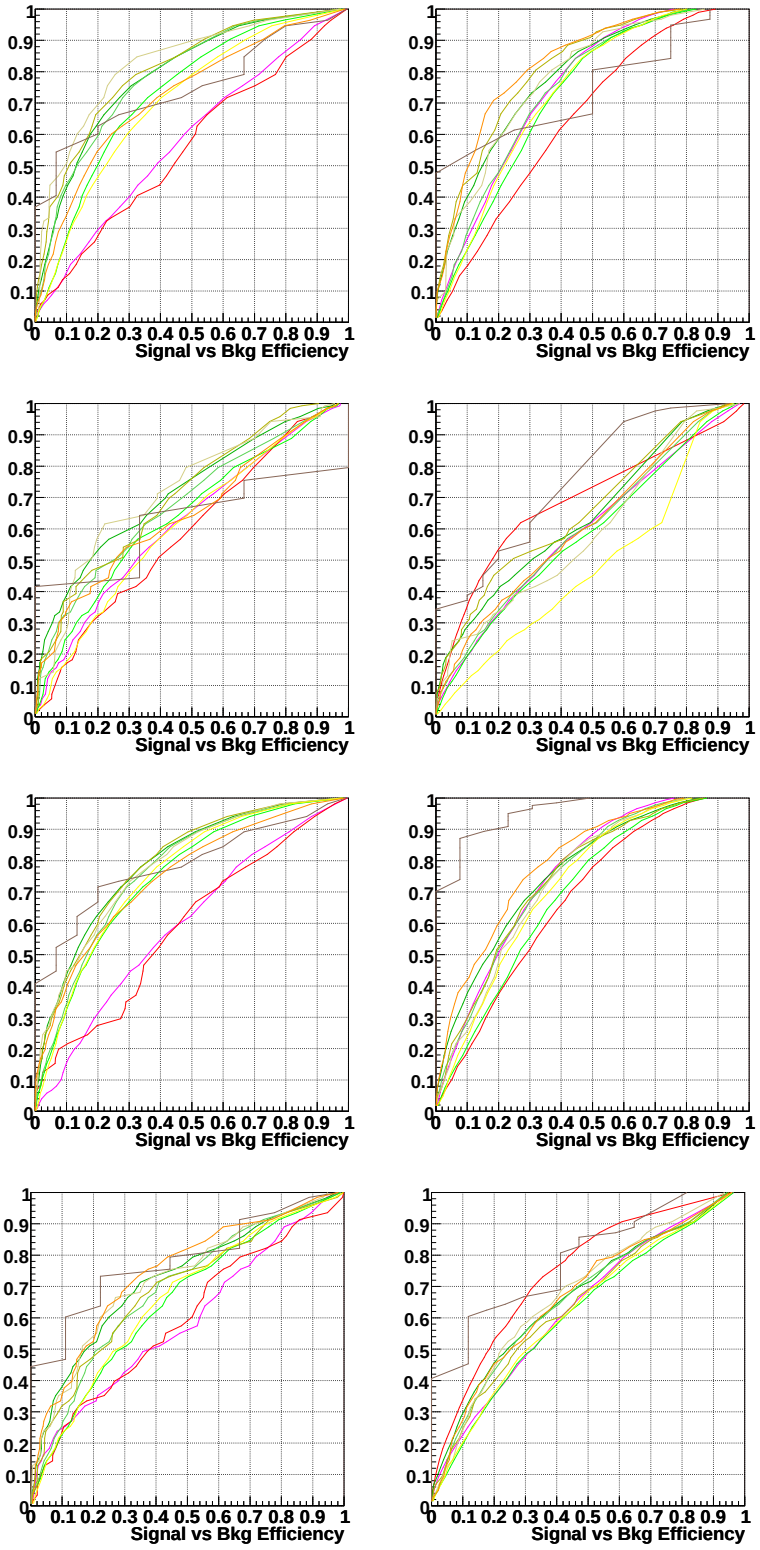

Figure D.4: The discriminant performance for $\mu + jets$ events with two b tags. The top two rows are Run IIa data and the bottom two rows are Run IIb data. The first and third row are two-jet events, while the second and fourth row are three-jet events. On the left is the performance for H_T(alljets,lepton,$\not\!\!E_T$) < 175 GeV events while on the right for H_T(alljets,lepton,$\not\!\!E_T$) > 175 GeV events.

Appendix E

W/ Boosted Decision Trees

Discriminant

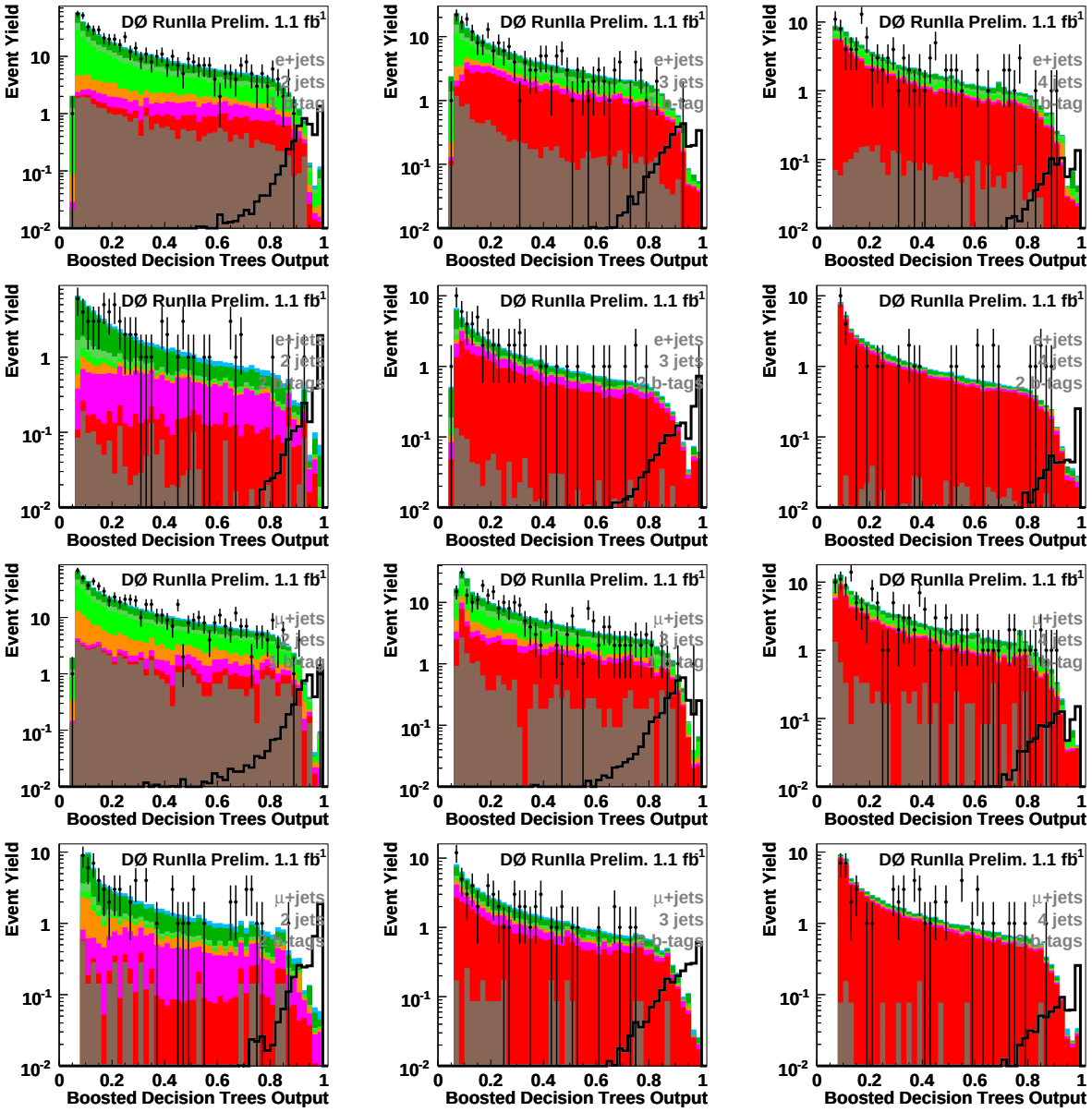

Figure E.1: Distributions of Decision Tree output for p17 data, background, and W'_R signal with mass 700 GeV. Plots in the four rows, starting from the top row, are from events with electrons with one b-tagged, electrons with both b-tagged, muons with one b-tagged, and muons with both b-tagged respectively. In the three columns, starting from left to right, are events with two jets, three jets, and four jets, respectively.

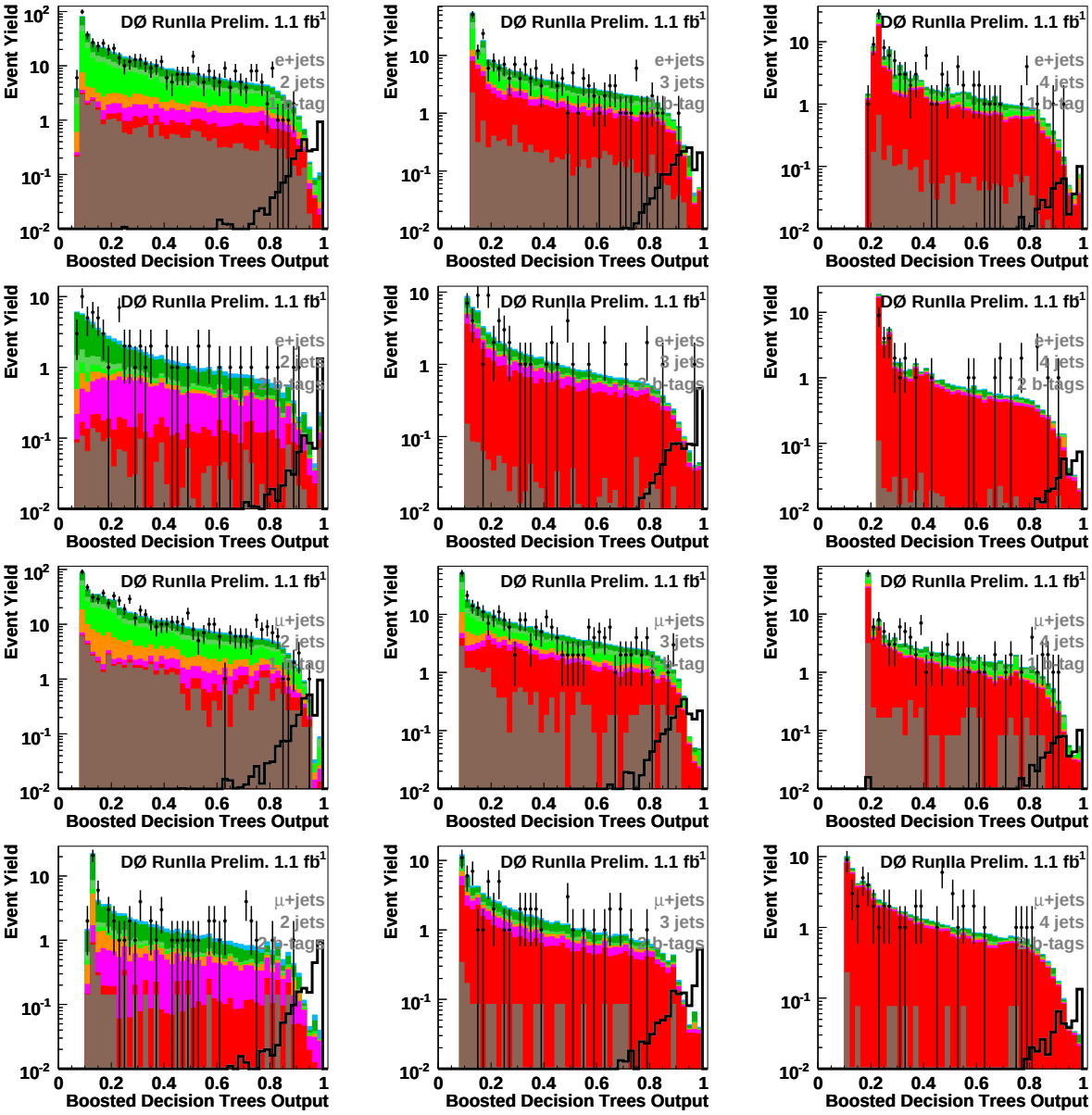

Figure E.2: Distributions of Decision Tree output for p17 data, background, and W'_R signal with mass 750 GeV. Plots in the four rows, starting from the top row, are from events with electrons with one b-tagged, electrons with both b-tagged, muons with one b-tagged, and muons with both b-tagged respectively. In the three columns, starting from left to right, are events with two jets, three jets, and four jets, respectively.

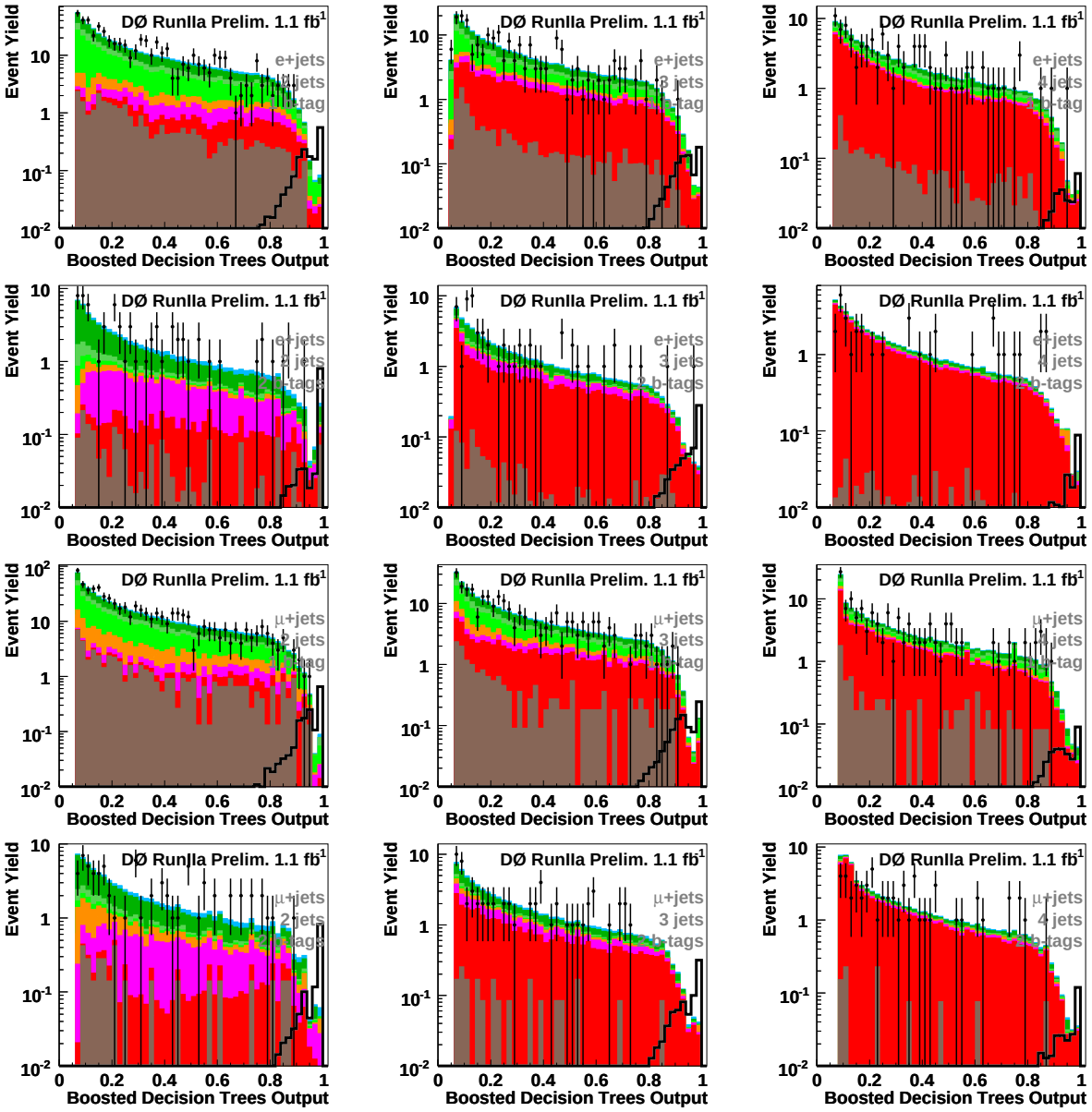

Figure E.3: Distributions of Decision Tree output for p17 data, background, and W'_R signal with mass 800 GeV. Plots in the four rows, starting from the top row, are from events with electrons with one b-tagged, electrons with both b-tagged, muons with one b-tagged, and muons with both b-tagged respectively. In the three columns, starting from left to right, are events with two jets, three jets, and four jets, respectively.

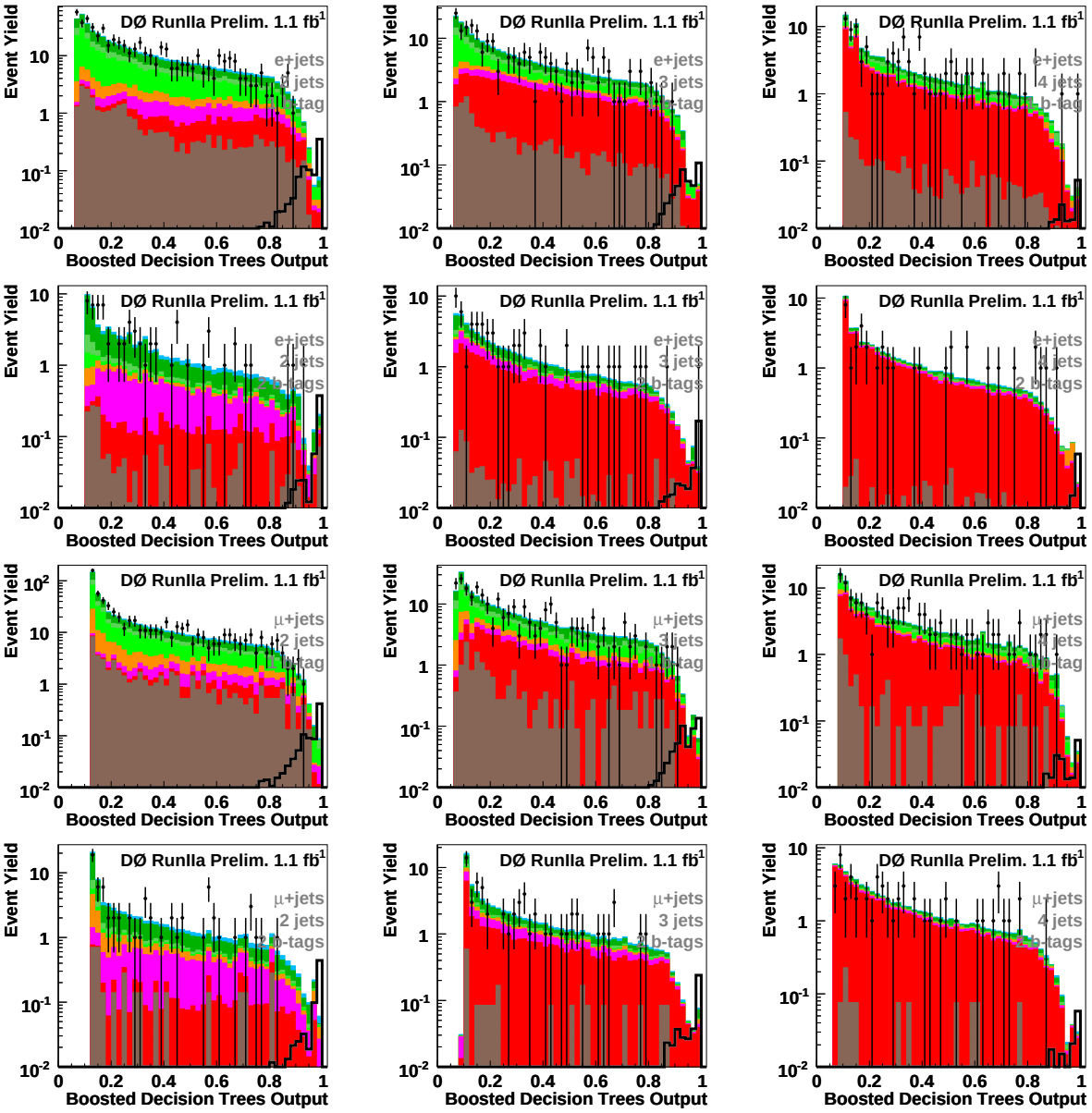

Figure E.4: Distributions of Decision Tree output for p17 data, background, and W'_R signal with mass 850 GeV. Plots in the four rows, starting from the top row, are from events with electrons with one b-tagged, electrons with both b-tagged, muons with one b-tagged, and muons with both b-tagged respectively. In the three columns, starting from left to right, are events with two jets, three jets, and four jets, respectively.

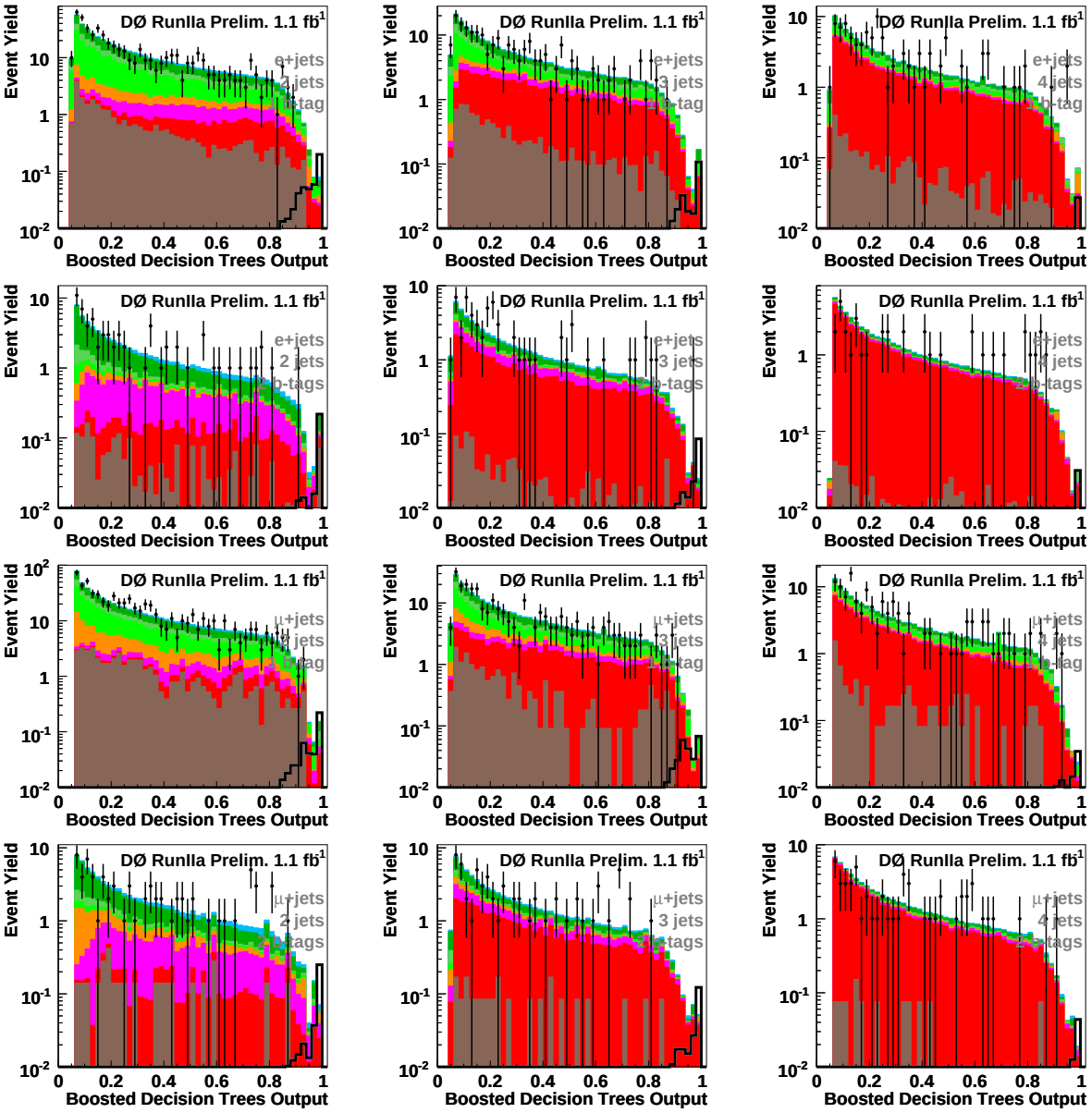

Figure E.5: Distributions of Decision Tree output for p17 data, background, and W'_R signal with mass 900 GeV. Plots in the four rows, starting from the top row, are from events with electrons with one b-tagged, electrons with both b-tagged, muons with one b-tagged, and muons with both b-tagged respectively. In the three columns, starting from left to right, are events with two jets, three jets, and four jets, respectively.

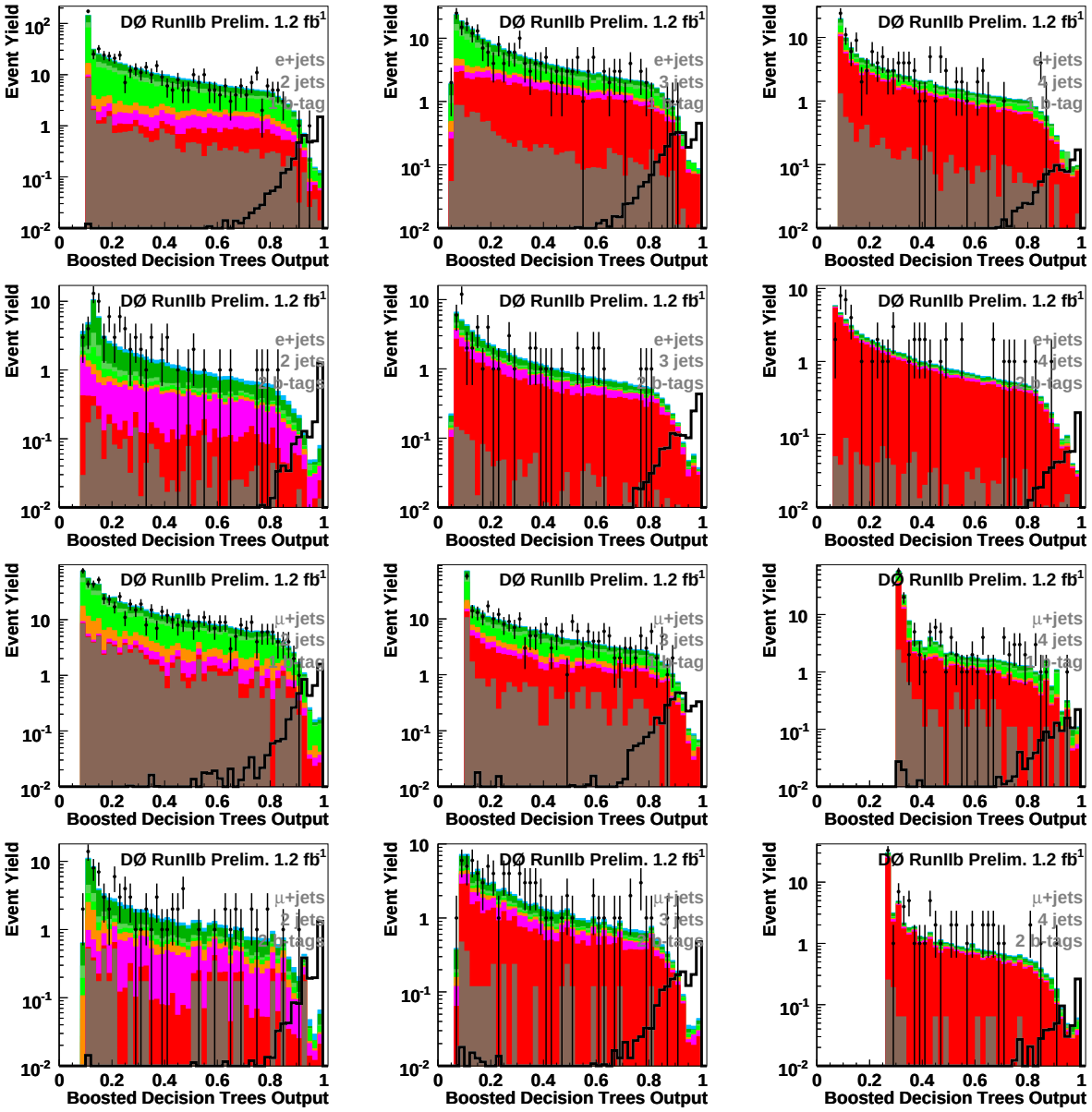

Figure E.6: Distributions of Decision Tree output for p20 data, background, and W'_R signal with mass 700 GeV. Plots in the four rows, starting from the top row, are from events with electrons with one b-tagged, electrons with both b-tagged, muons with one b-tagged, and muons with both b-tagged respectively. In the three columns, starting from left to right, are events with two jets, three jets, and four jets, respectively.

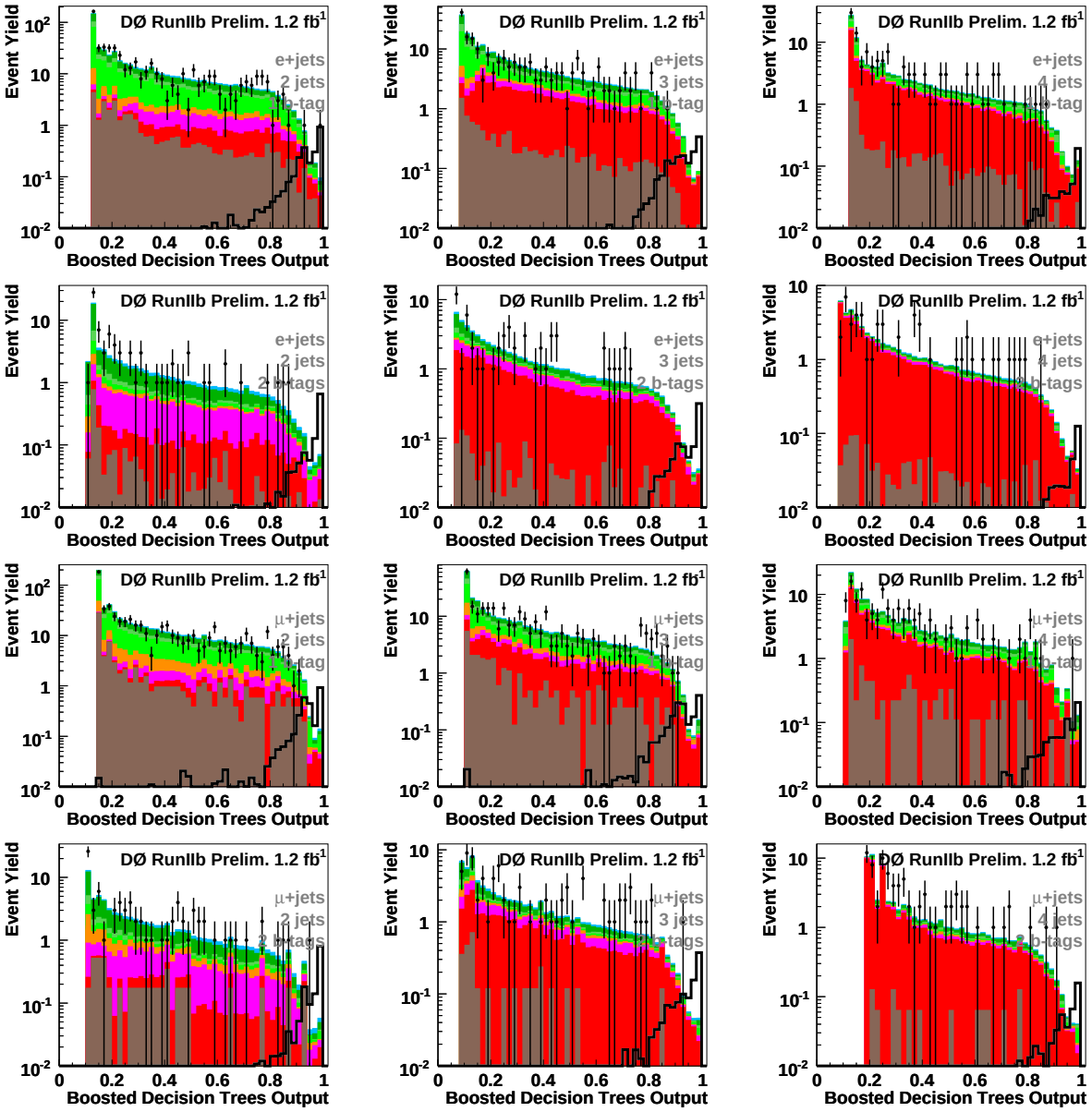

Figure E.7: Distributions of Decision Tree output for p20 data, background, and W'_R signal with mass 750 GeV. Plots in the four rows, starting from the top row, are from events with electrons with one b-tagged, electrons with both b-tagged, muons with one b-tagged, and muons with both b-tagged respectively. In the three columns, starting from left to right, are events with two jets, three jets, and four jets, respectively.

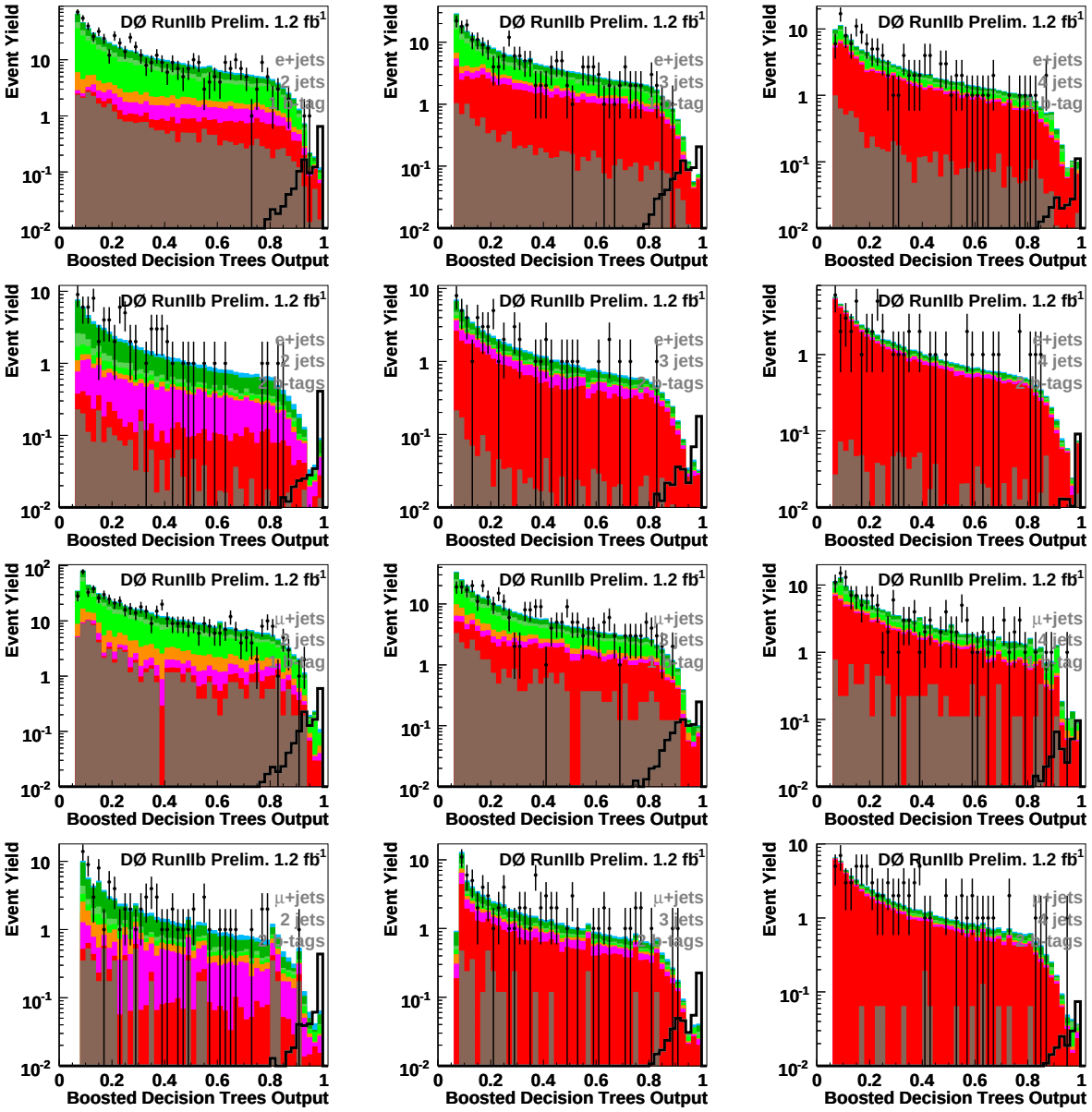

Figure E.8: Distributions of Decision Tree output for p20 data, background, and W'_R signal with mass 800 GeV. Plots in the four rows, starting from the top row, are from events with electrons with one b-tagged, electrons with both b-tagged, muons with one b-tagged, and muons with both b-tagged respectively. In the three columns, starting from left to right, are events with two jets, three jets, and four jets, respectively.

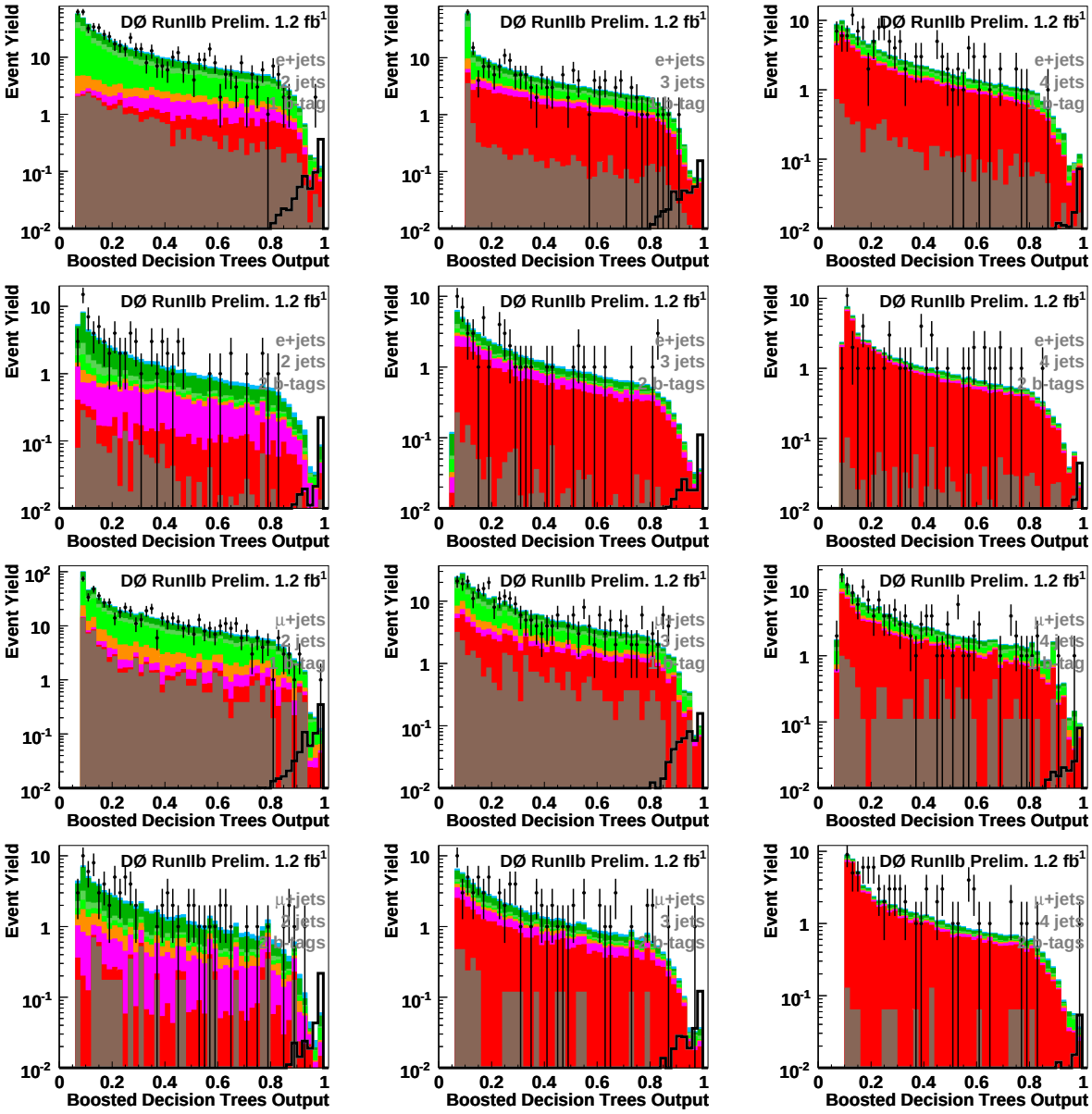

Figure E.9: Distributions of Decision Tree output for p20 data, background, and W'_R signal with mass 850 GeV. Plots in the four rows, starting from the top row, are from events with electrons with one b-tagged, electrons with both b-tagged, muons with one b-tagged, and muons with both b-tagged respectively. In the three columns, starting from left to right, are events with two jets, three jets, and four jets, respectively.

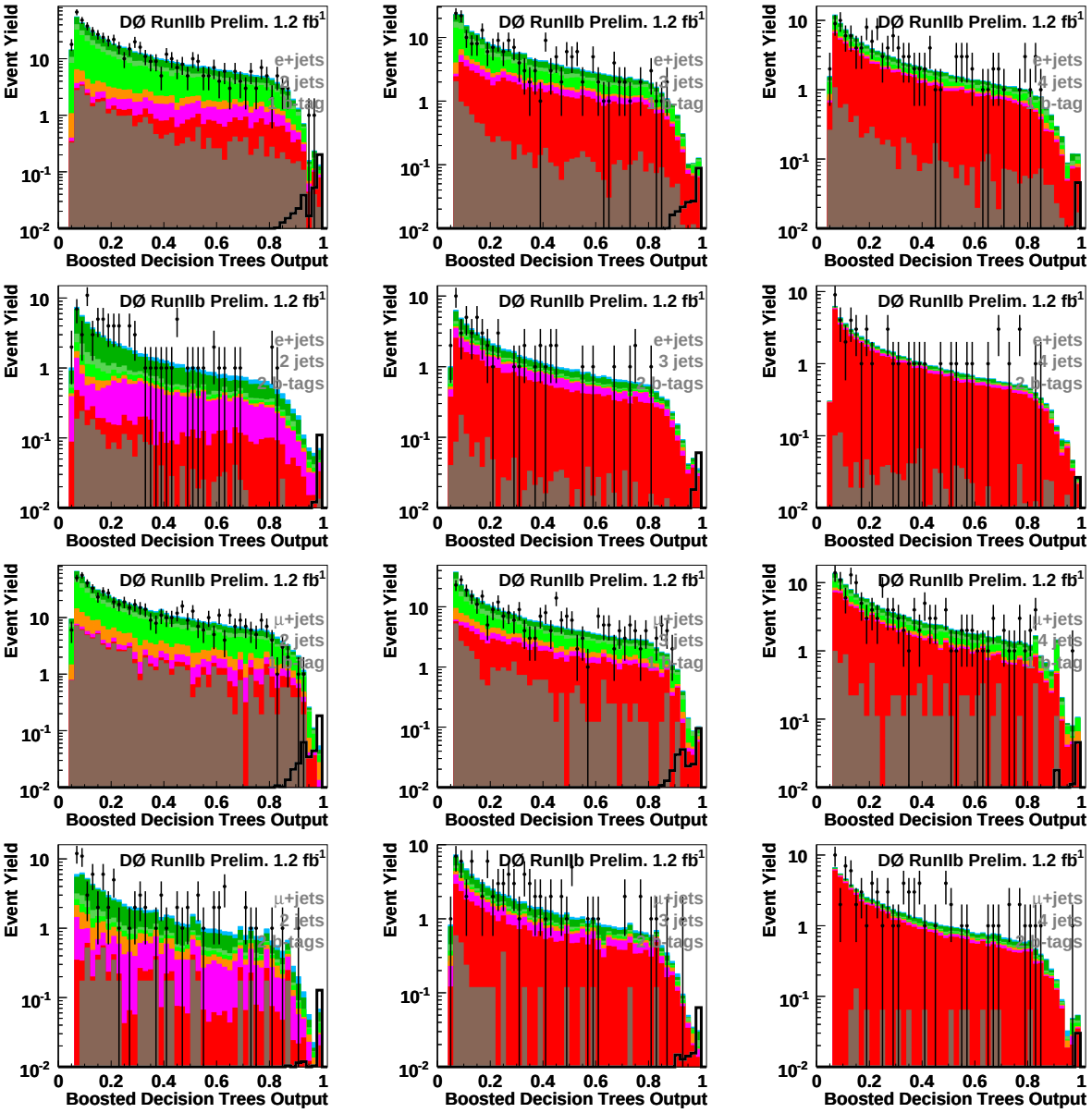

Figure E.10: Distributions of Decision Tree output for p20 data, background, and W'_R signal with mass 900 GeV. Plots in the four rows, starting from the top row, are from events with electrons with one b-tagged, electrons with both b-tagged, muons with one b-tagged, and muons with both b-tagged respectively. In the three columns, starting from left to right, are events with two jets, three jets, and four jets, respectively.

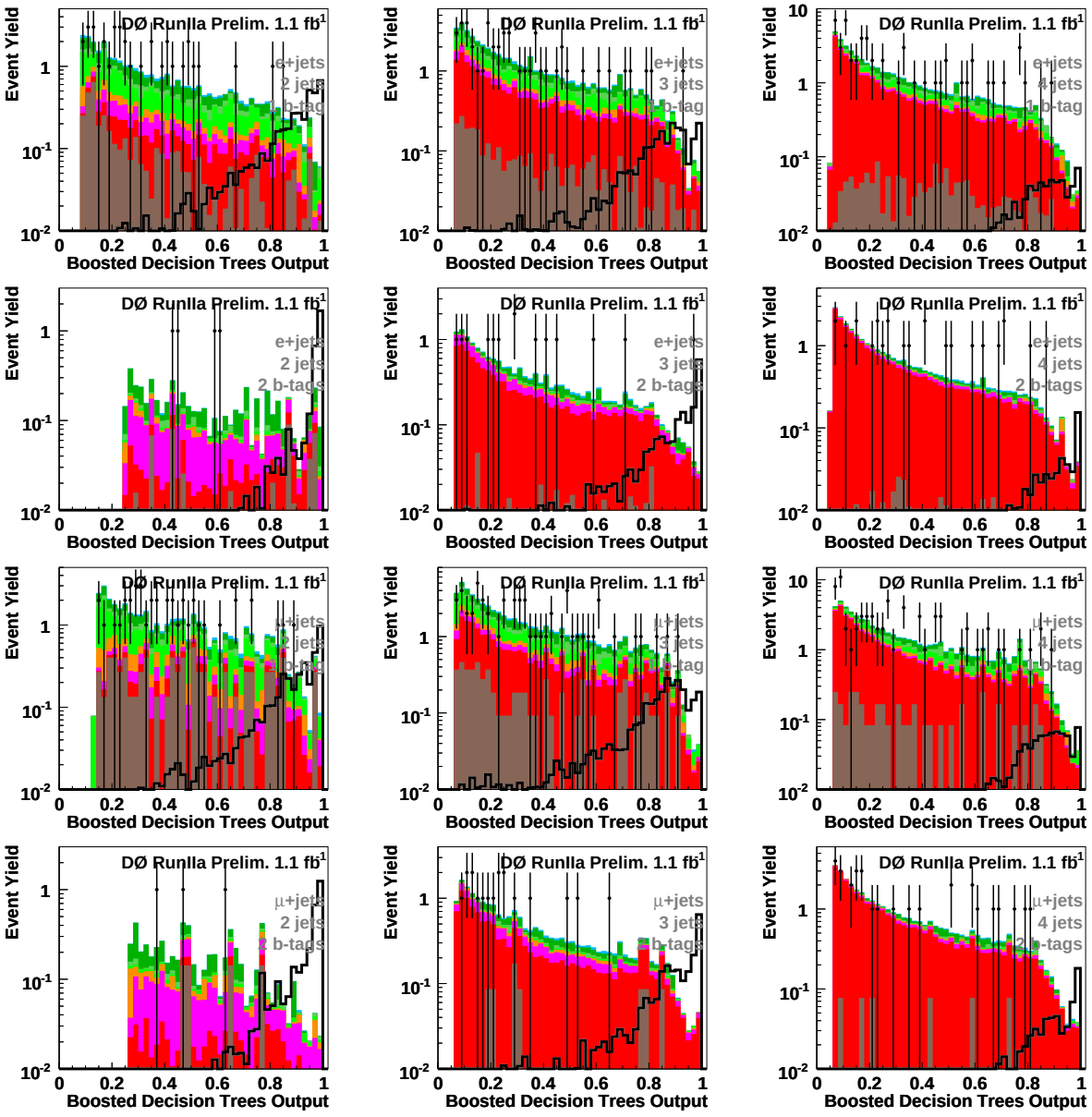

Figure E.11: Distributions of Decision Tree output with $\hat{s}$ cut > 400 GeV for p17 data, background, and W'_L signal with mass 700 GeV. Plots in the four rows, starting from the top row, are from events with electrons with one b-tagged, electrons with both b-tagged, muons with one b-tagged, and muons with both b-tagged respectively. In the three columns, starting from left to right, are events with two jets, three jets, and four jets, respectively.

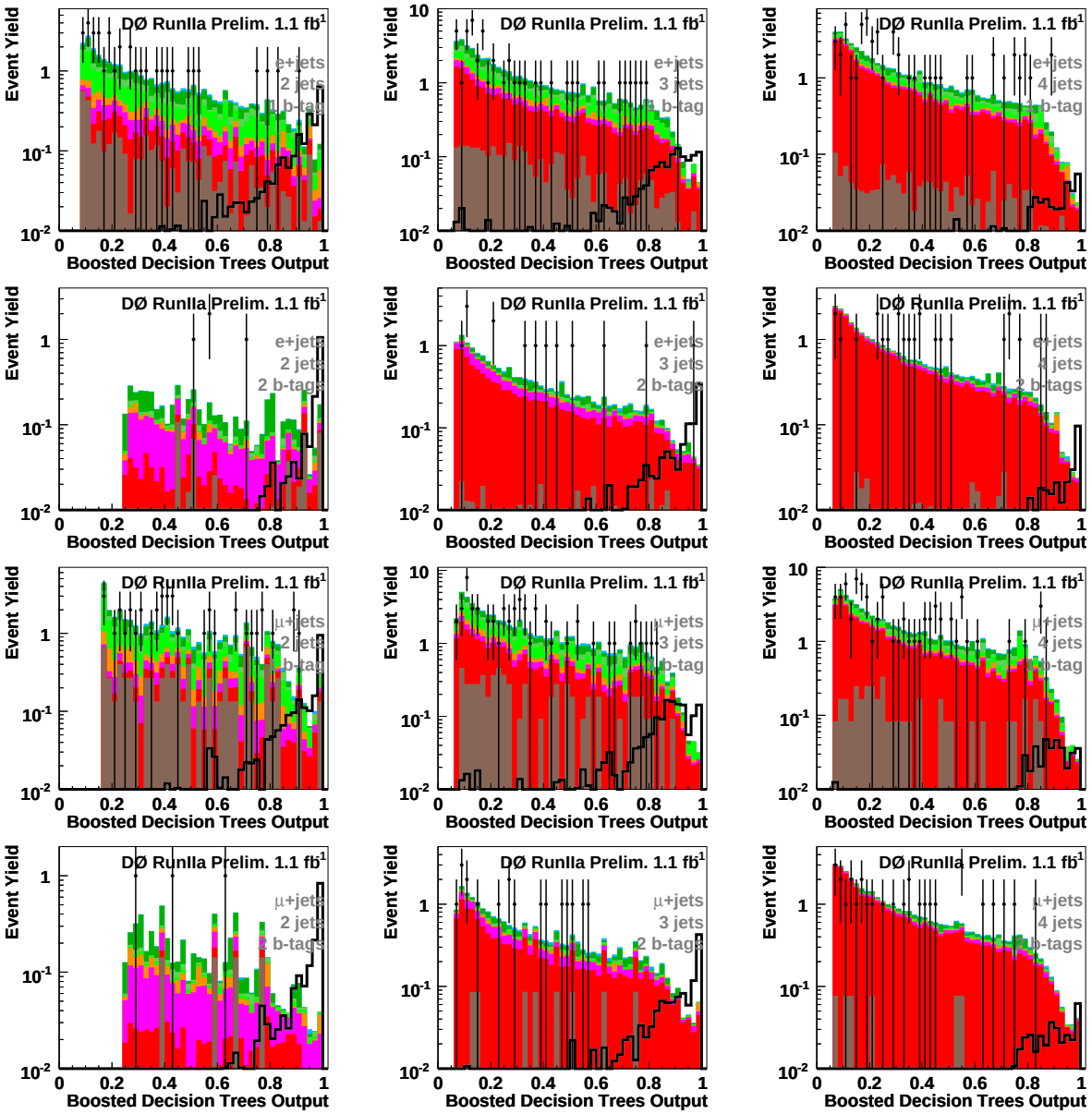

Figure E.12: Distributions of Decision Tree output with $\hat{s}$ cut > 400 GeV for p17 data, background, and W'_L signal with mass 750 GeV. Plots in the four rows, starting from the top row, are from events with electrons with one b-tagged, electrons with both b-tagged, muons with one b-tagged, and muons with both b-tagged respectively. In the three columns, starting from left to right, are events with two jets, three jets, and four jets, respectively.

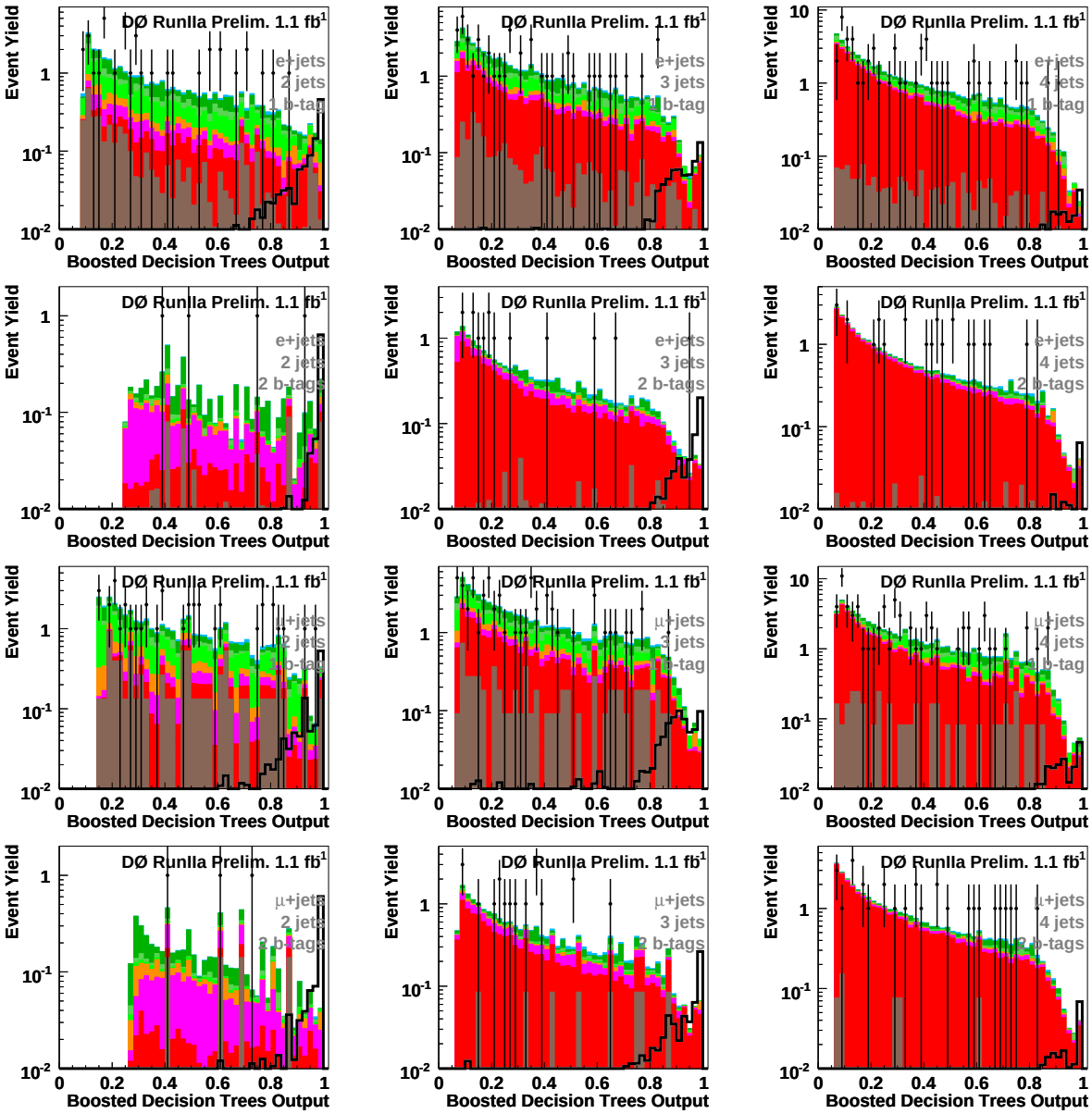

Figure E.13: Distributions of Decision Tree output with $\hat{s}$ cut > ¿ 400 GeV for p17 data, background, and W'_L signal with mass 800 GeV. Plots in the four rows, starting from the top row, are from events with electrons with one b-tagged, electrons with both b-tagged, muons with one b-tagged, and muons with both b-tagged respectively. In the three columns, starting from left to right, are events with two jets, three jets, and four jets, respectively.

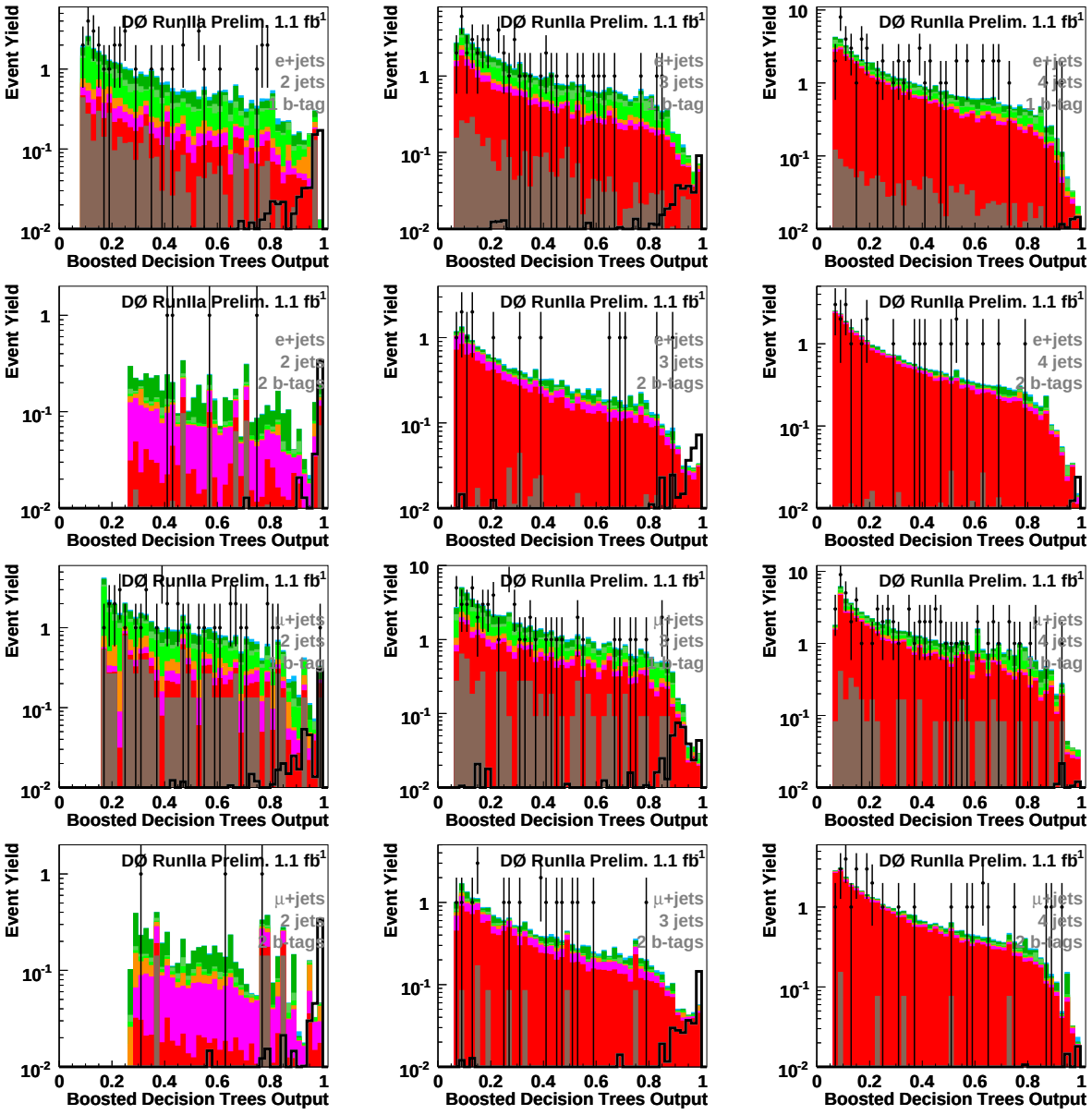

Figure E.14: Distributions of Decision Tree output with $\hat{s}$ cut > 400 GeV for p17 data, background, and W'_L signal with mass 850 GeV. Plots in the four rows, starting from the top row, are from events with electrons with one b-tagged, electrons with both b-tagged, muons with one b-tagged, and muons with both b-tagged respectively. In the three columns, starting from left to right, are events with two jets, three jets, and four jets, respectively.

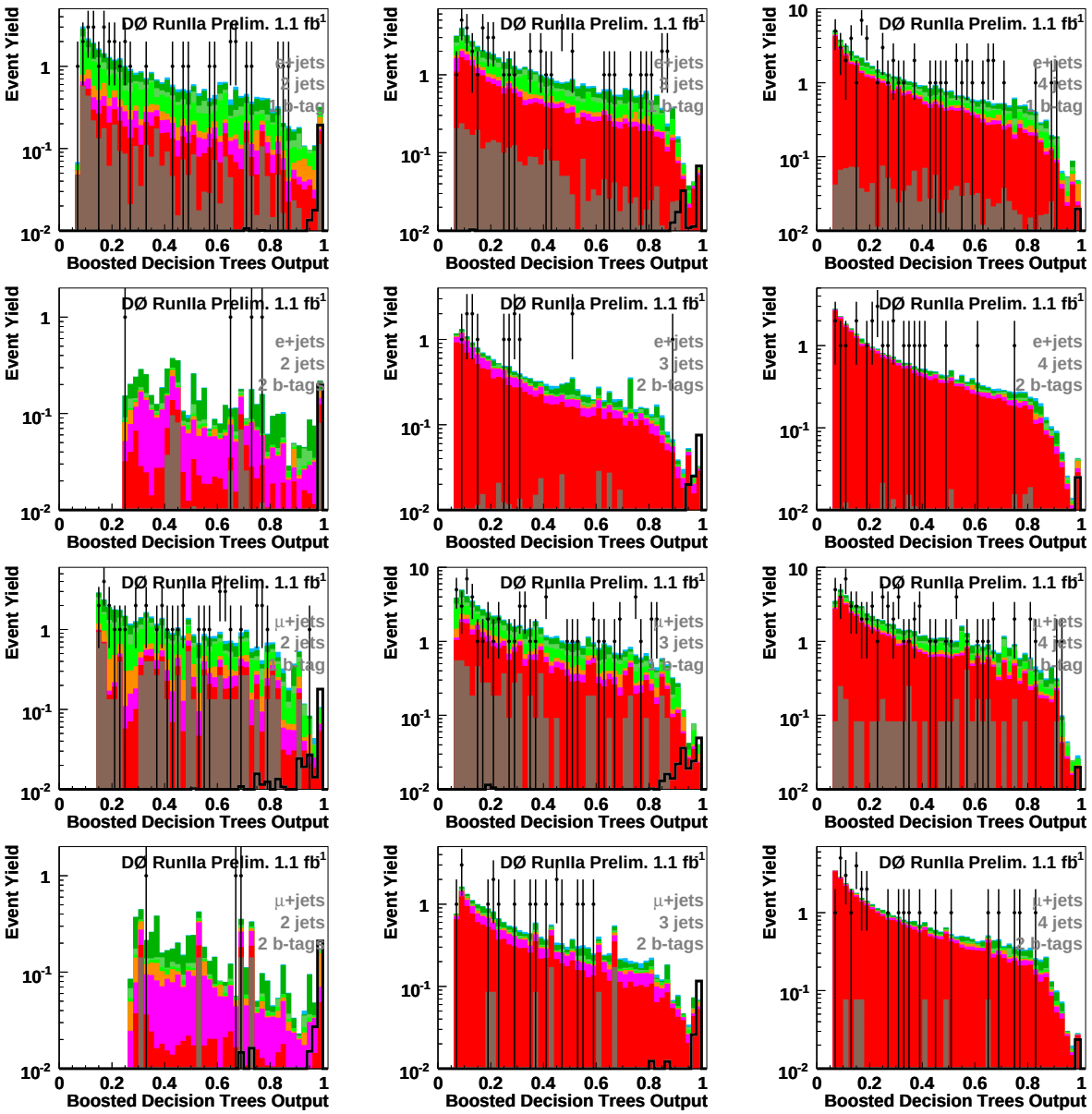

Figure E.15: Distributions of Decision Tree output with $\hat{s}$ cut > 400 GeV for p17 data, background, and W'_L signal with mass 900 GeV. Plots in the four rows, starting from the top row, are from events with electrons with one b-tagged, electrons with both b-tagged, muons with one b-tagged, and muons with both b-tagged respectively. In the three columns, starting from left to right, are events with two jets, three jets, and four jets, respectively.

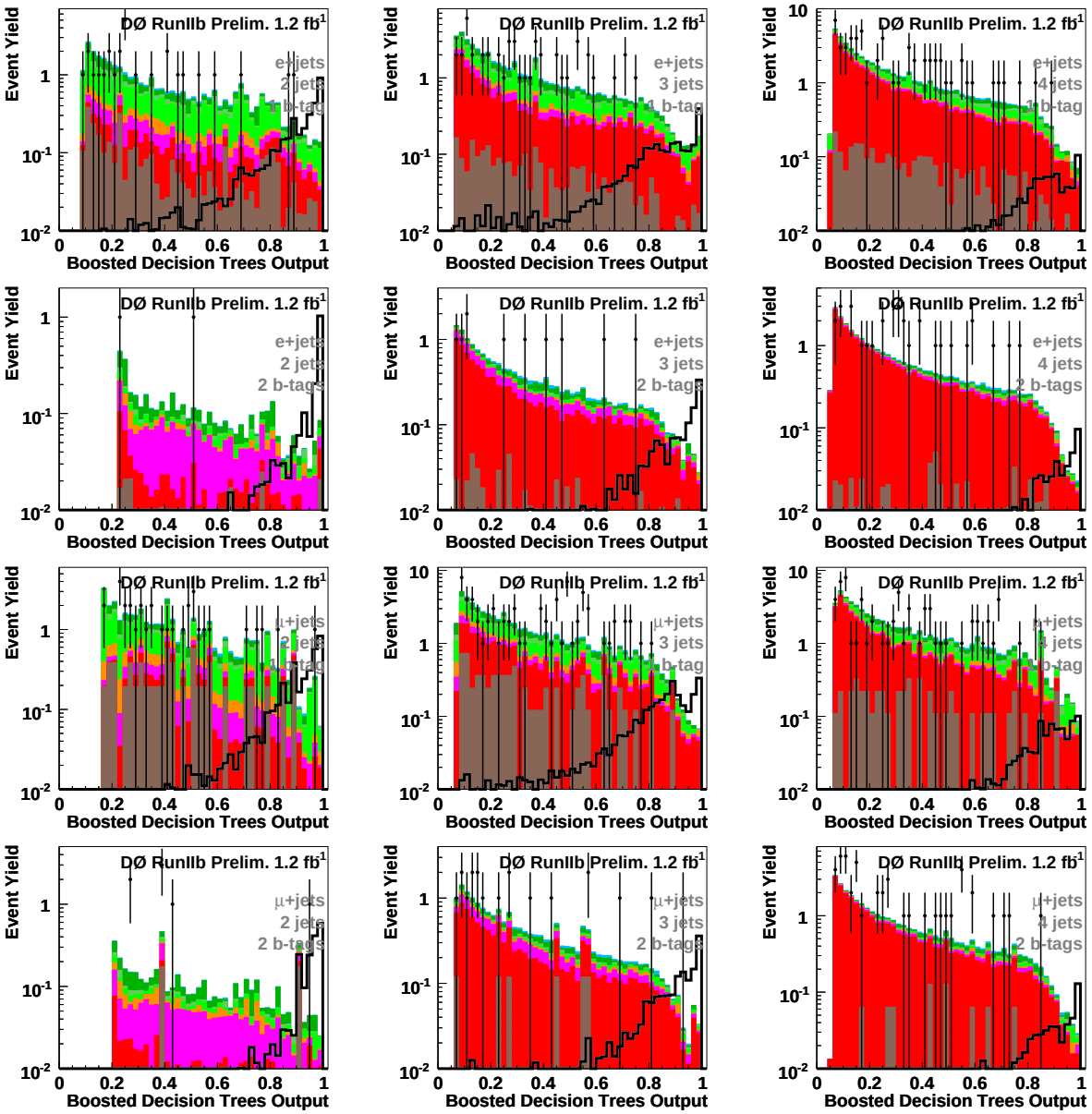

Figure E.16: Distributions of Decision Tree output with $\hat{s}$ cut > 400 GeV for p20 data, background, and W'_L signal with mass 700 GeV. Plots in the four rows, starting from the top row, are from events with electrons with one b-tagged, electrons with both b-tagged, muons with one b-tagged, and muons with both b-tagged respectively. In the three columns, starting from left to right, are events with two jets, three jets, and four jets, respectively.

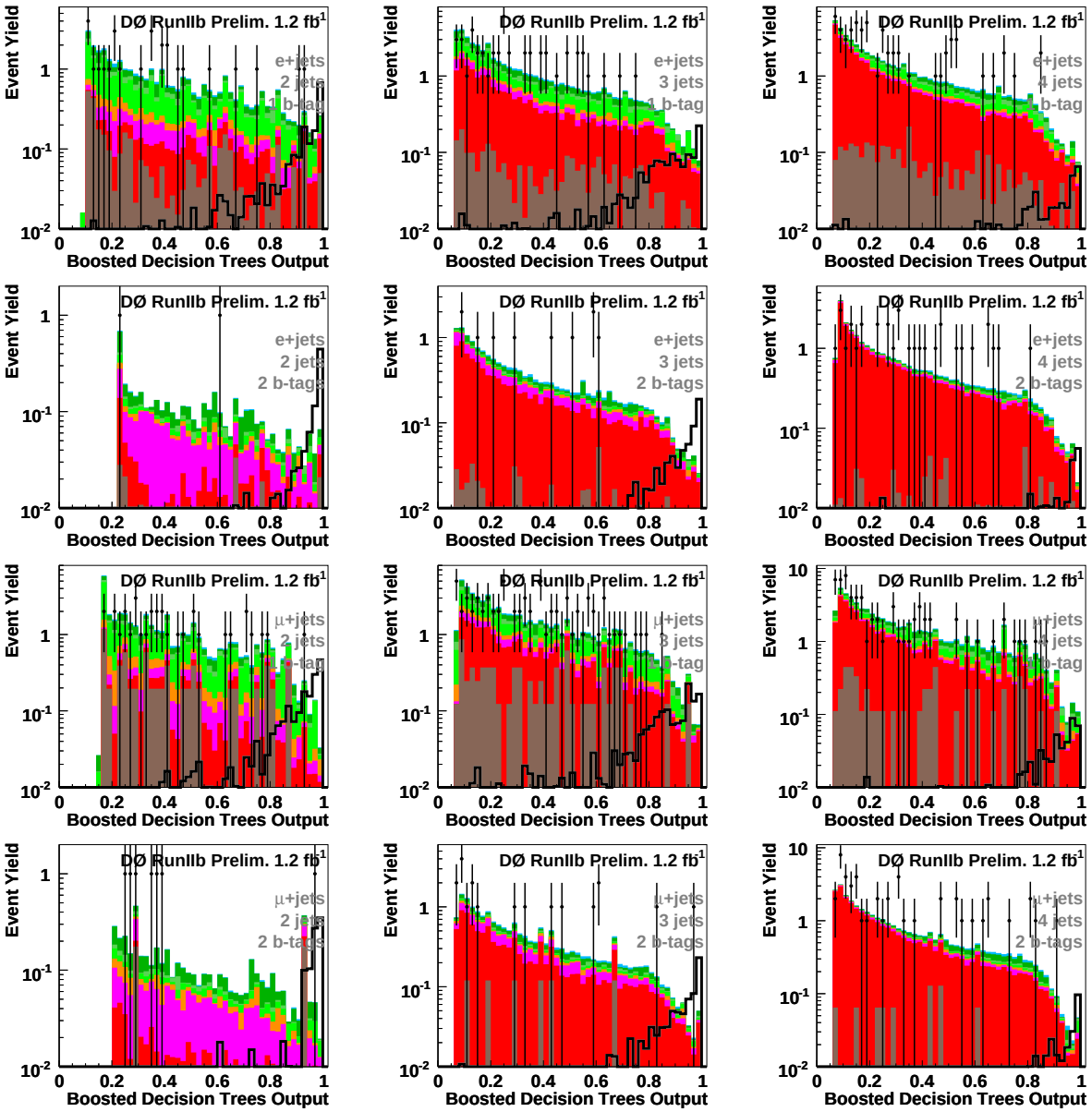

Figure E.17: Distributions of Decision Tree output with $\hat{s}$ cut > 400 GeV for p20 data, background, and W'_L signal with mass 750 GeV. Plots in the four rows, starting from the top row, are from events with electrons with one b-tagged, electrons with both b-tagged, muons with one b-tagged, and muons with both b-tagged respectively. In the three columns, starting from left to right, are events with two jets, three jets, and four jets, respectively.

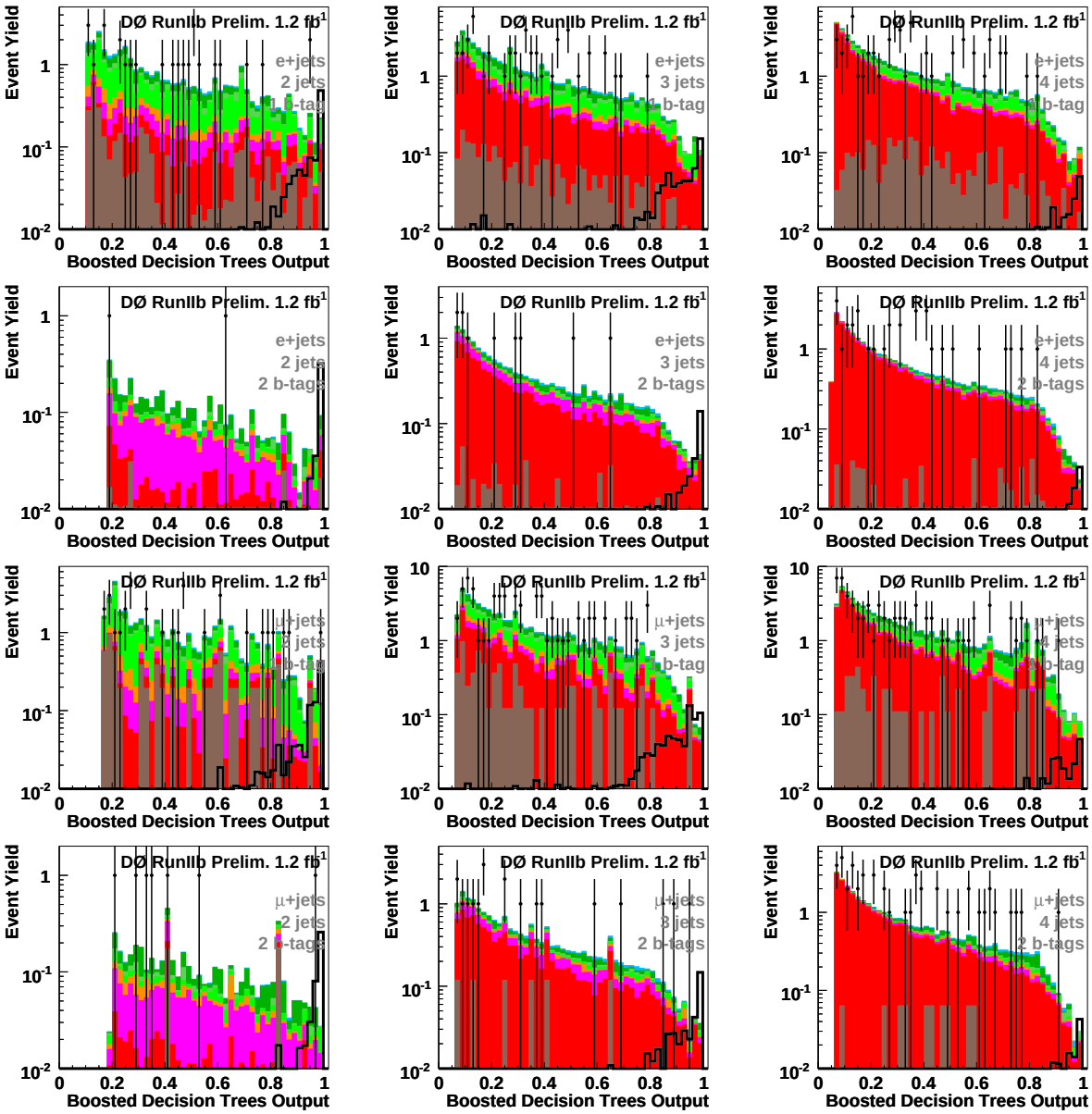

Figure E.18: Distributions of Decision Tree output with $\hat{s}$ cut > 400 GeV for p20 data, background, and W'_L signal with mass 800 GeV. Plots in the four rows, starting from the top row, are from events with electrons with one b-tagged, electrons with both b-tagged, muons with one b-tagged, and muons with both b-tagged respectively. In the three columns, starting from left to right, are events with two jets, three jets, and four jets, respectively.

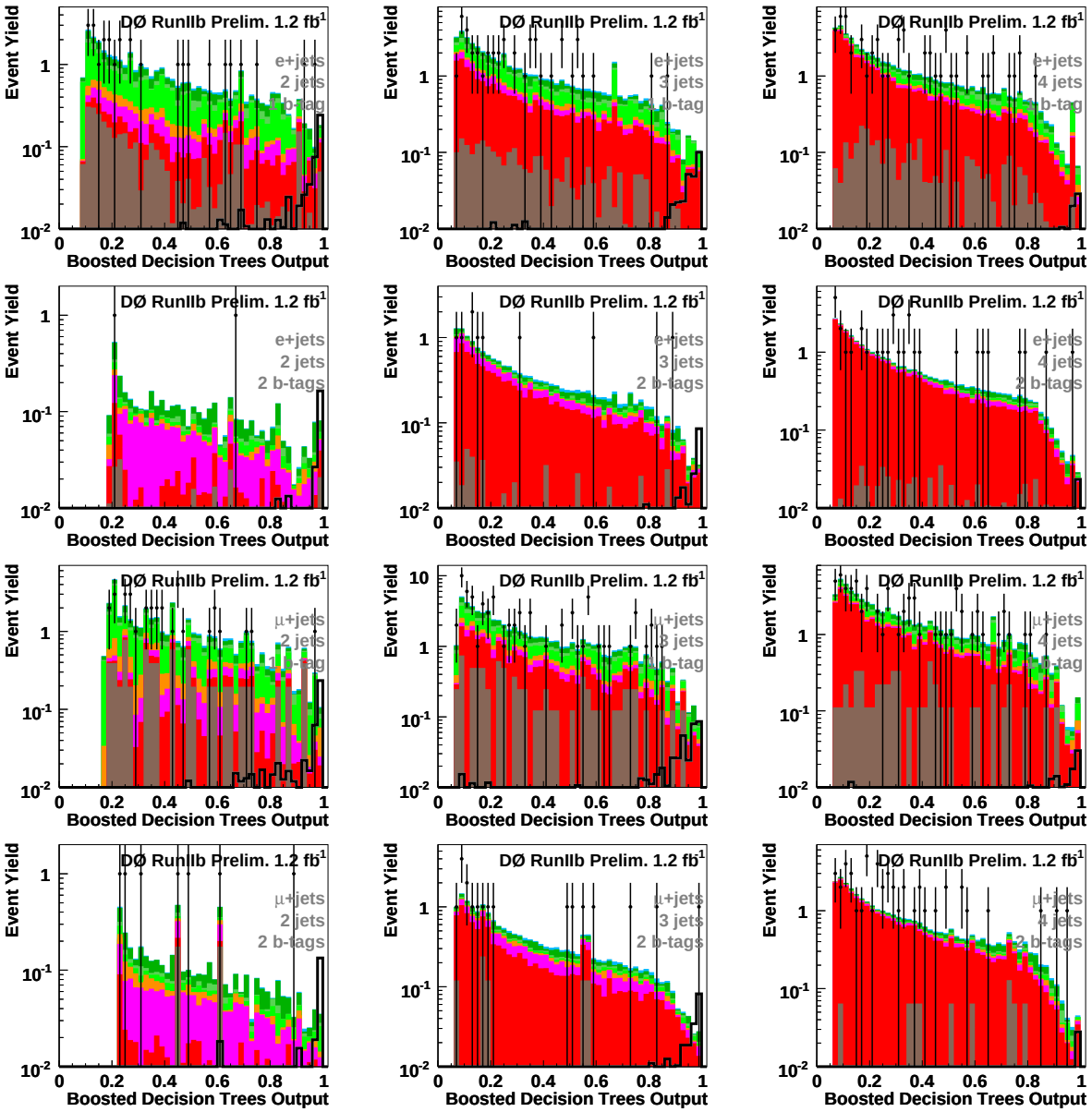

Figure E.19: Distributions of Decision Tree output with $\hat{s}$ cut > 400 GeV for p20 data, background, and W'_L signal with mass 850 GeV. Plots in the four rows, starting from the top row, are from events with electrons with one b-tagged, electrons with both b-tagged, muons with one b-tagged, and muons with both b-tagged respectively. In the three columns, starting from left to right, are events with two jets, three jets, and four jets, respectively.

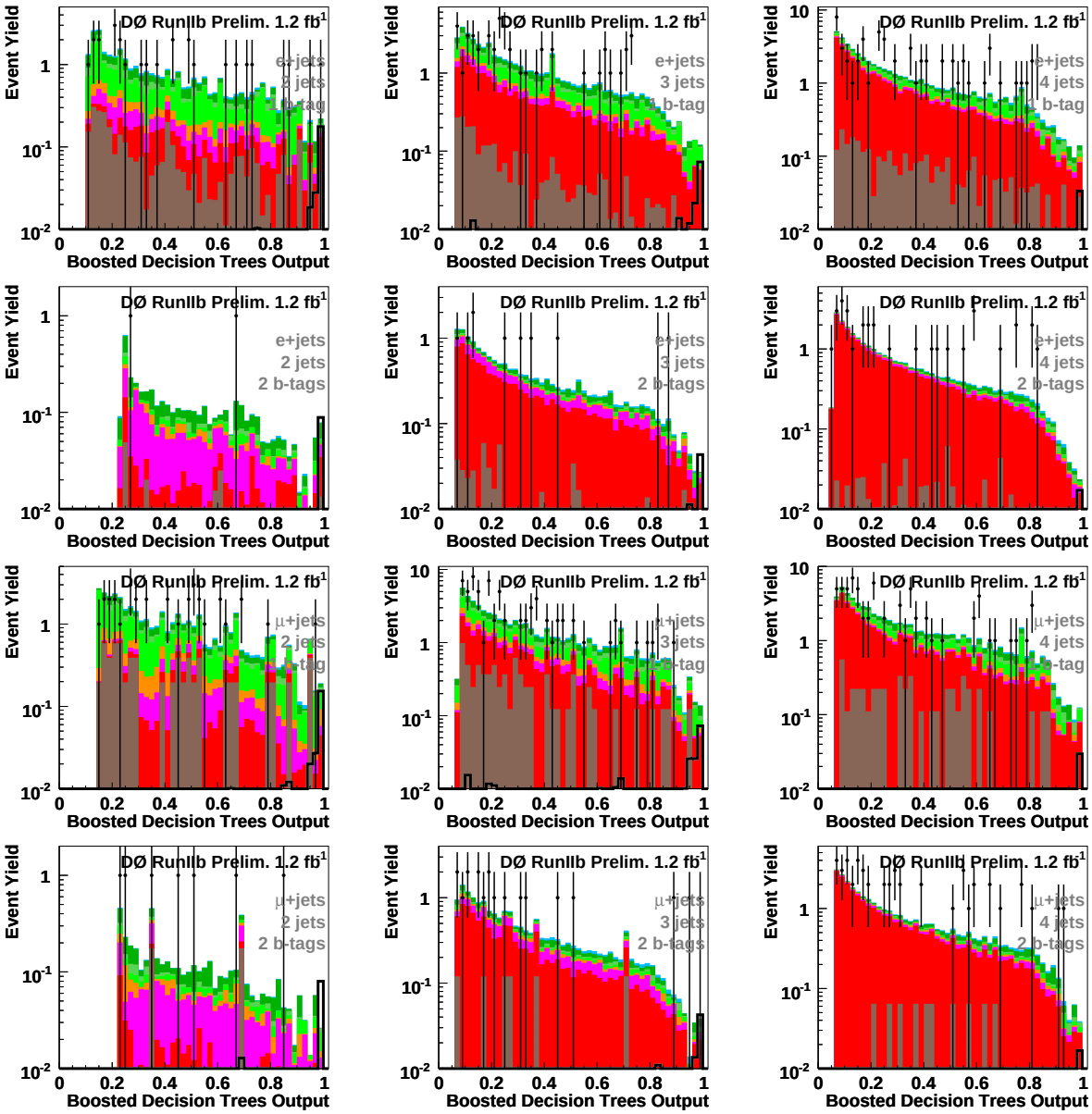

Figure E.20: Distributions of Decision Tree output with $\hat{s}$ cut > 400 GeV for p20 data, background, and W'_L signal with mass 900 GeV. Plots in the four rows, starting from the top row, are from events with electrons with one b-tagged, electrons with both b-tagged, muons with one b-tagged, and muons with both b-tagged respectively. In the three columns, starting from left to right, are events with two jets, three jets, and four jets, respectively.

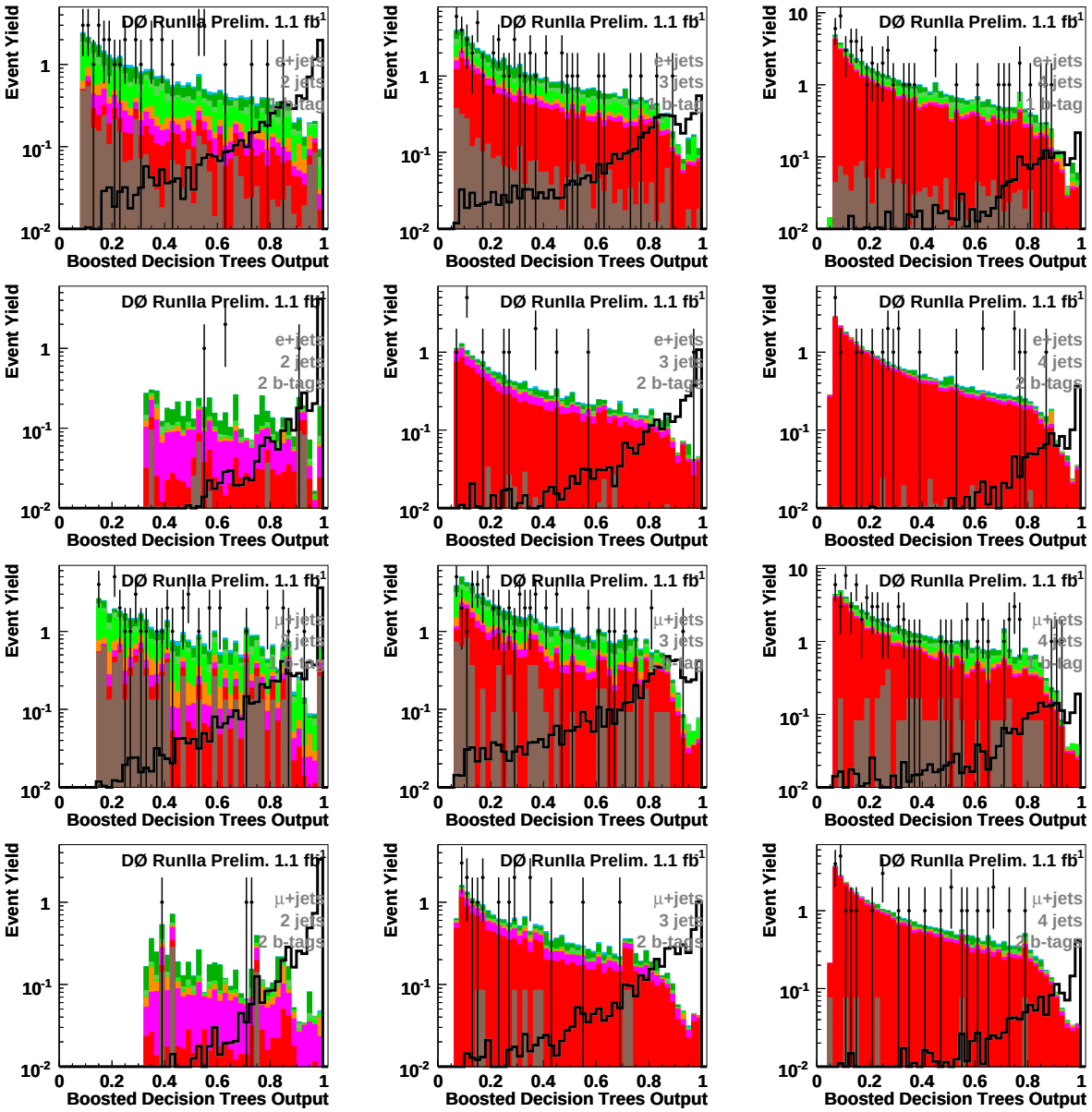

Figure E.21: Distributions of Decision Tree output with $\hat{s}$ cut > 400 GeV for p17 data, background, and W'_{mixed} signal with mass 700 GeV. Plots in the four rows, starting from the top row, are from events with electrons with one b-tagged, electrons with both b-tagged, muons with one b-tagged, and muons with both b-tagged respectively. In the three columns, starting from left to right, are events with two jets, three jets, and four jets, respectively.

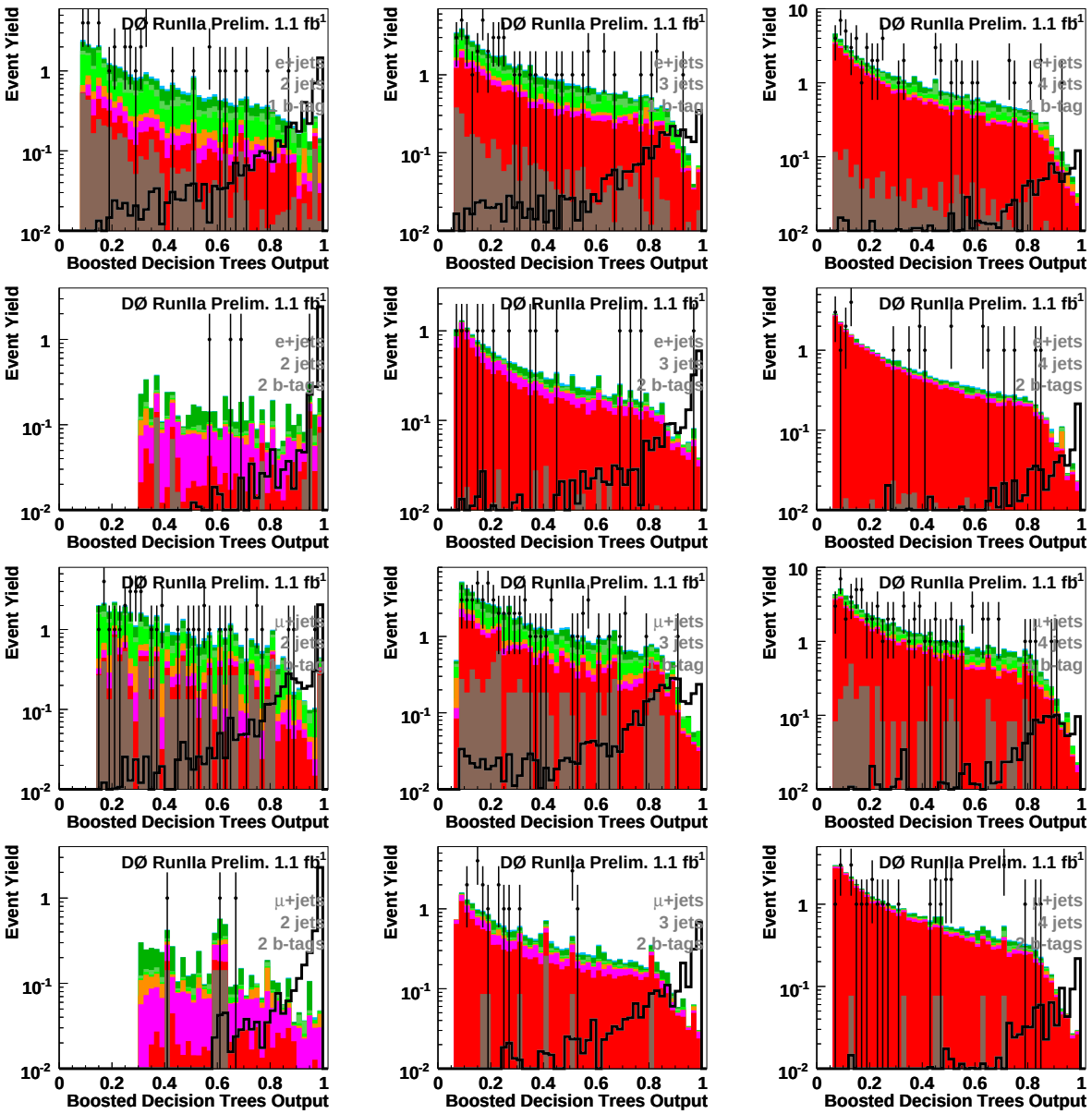

Figure E.22: Distributions of Decision Tree output with $\hat{s}$ cut > 400 GeV for p17 data, background, and W'_{mixed} signal with mass 750 GeV. Plots in the four rows, starting from the top row, are from events with electrons with one b-tagged, electrons with both b-tagged, muons with one b-tagged, and muons with both b-tagged respectively. In the three columns, starting from left to right, are events with two jets, three jets, and four jets, respectively.

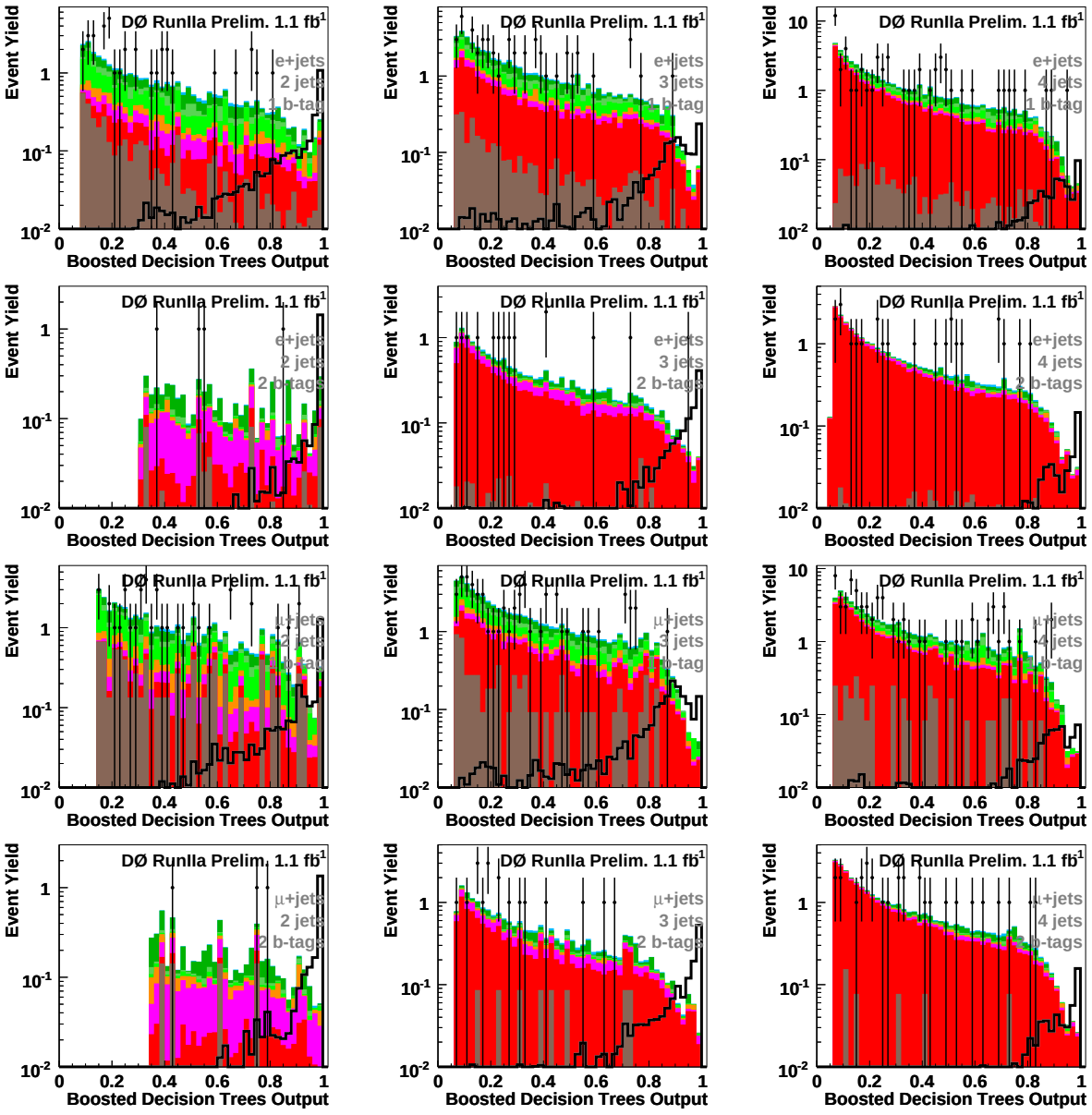

Figure E.23: Distributions of Decision Tree output with $\hat{s}$ cut > 400 GeV for p17 data, background, and W'_{mixed} signal with mass 800 GeV. Plots in the four rows, starting from the top row, are from events with electrons with one b-tagged, electrons with both b-tagged, muons with one b-tagged, and muons with both b-tagged respectively. In the three columns, starting from left to right, are events with two jets, three jets, and four jets, respectively.

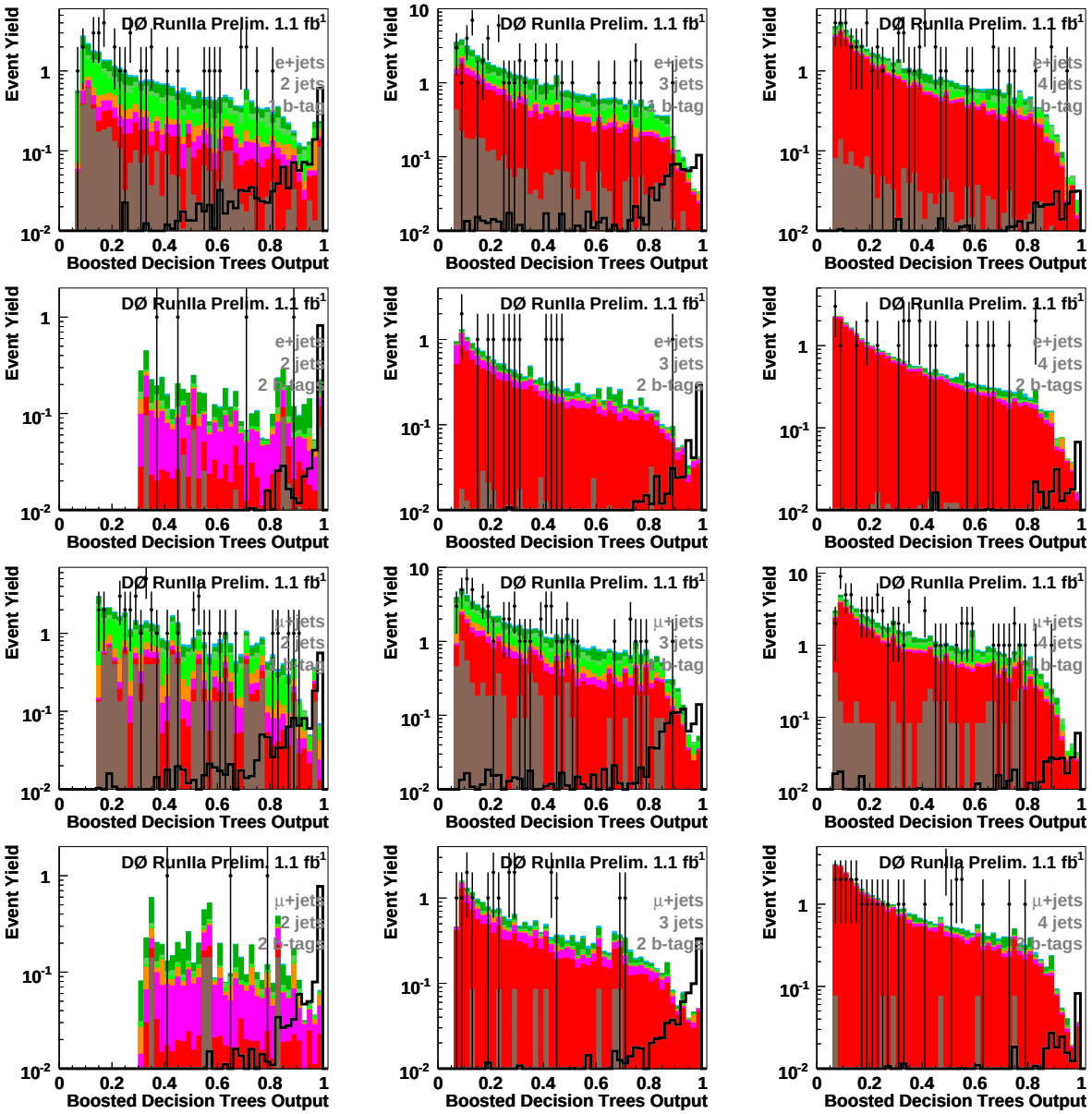

Figure E.24: Distributions of Decision Tree output with $\hat{s}$ cut > 400 GeV for p17 data, background, and W'_{mixed} signal with mass 850 GeV. Plots in the four rows, starting from the top row, are from events with electrons with one b-tagged, electrons with both b-tagged, muons with one b-tagged, and muons with both b-tagged respectively. In the three columns, starting from left to right, are events with two jets, three jets, and four jets, respectively.

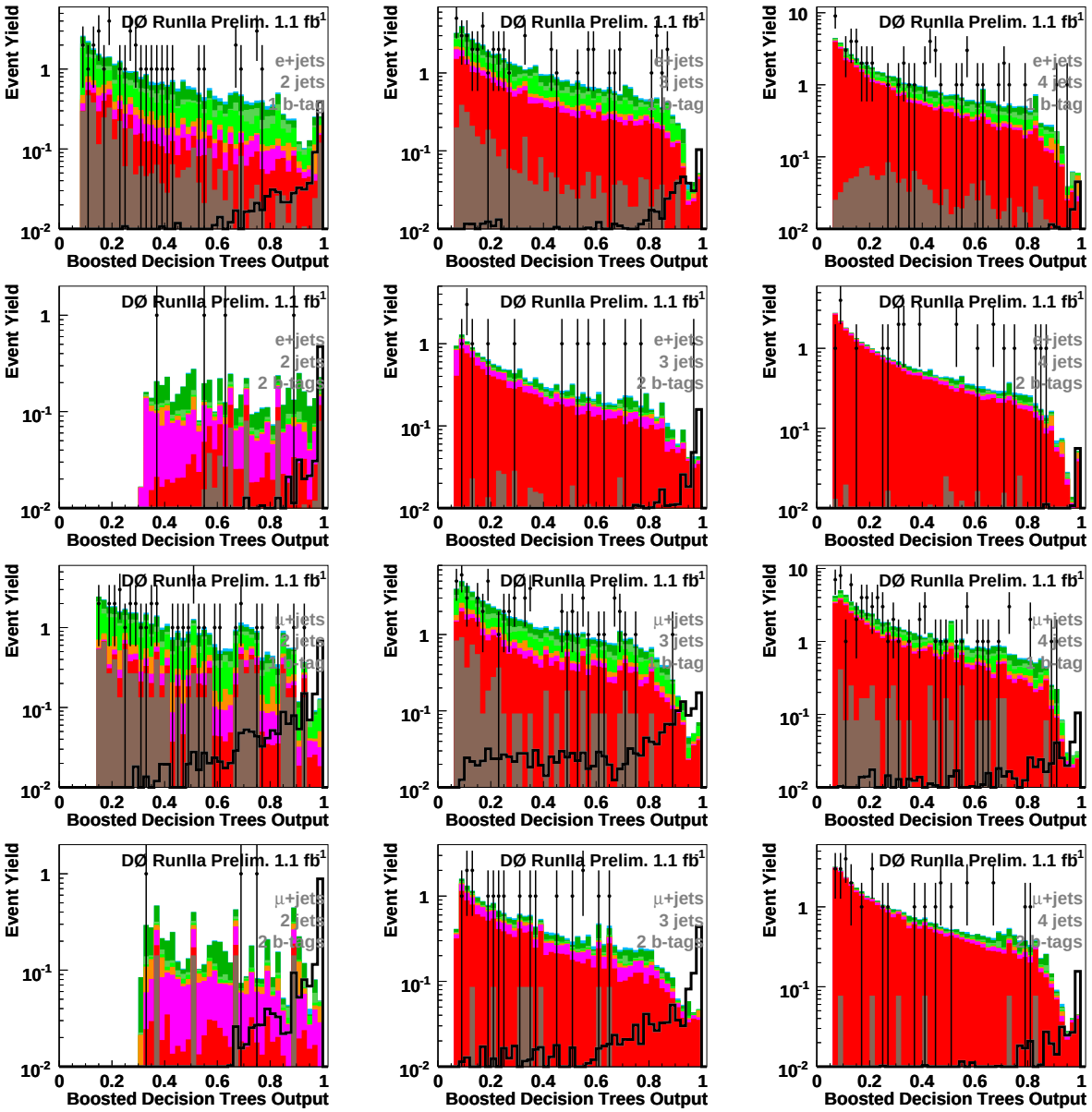

Figure E.25: Distributions of Decision Tree output with $\hat{s}$ cut > 400 GeV for p17 data, background, and W'_{mixed} signal with mass 900 GeV. Plots in the four rows, starting from the top row, are from events with electrons with one b-tagged, electrons with both b-tagged, muons with one b-tagged, and muons with both b-tagged respectively. In the three columns, starting from left to right, are events with two jets, three jets, and four jets, respectively.

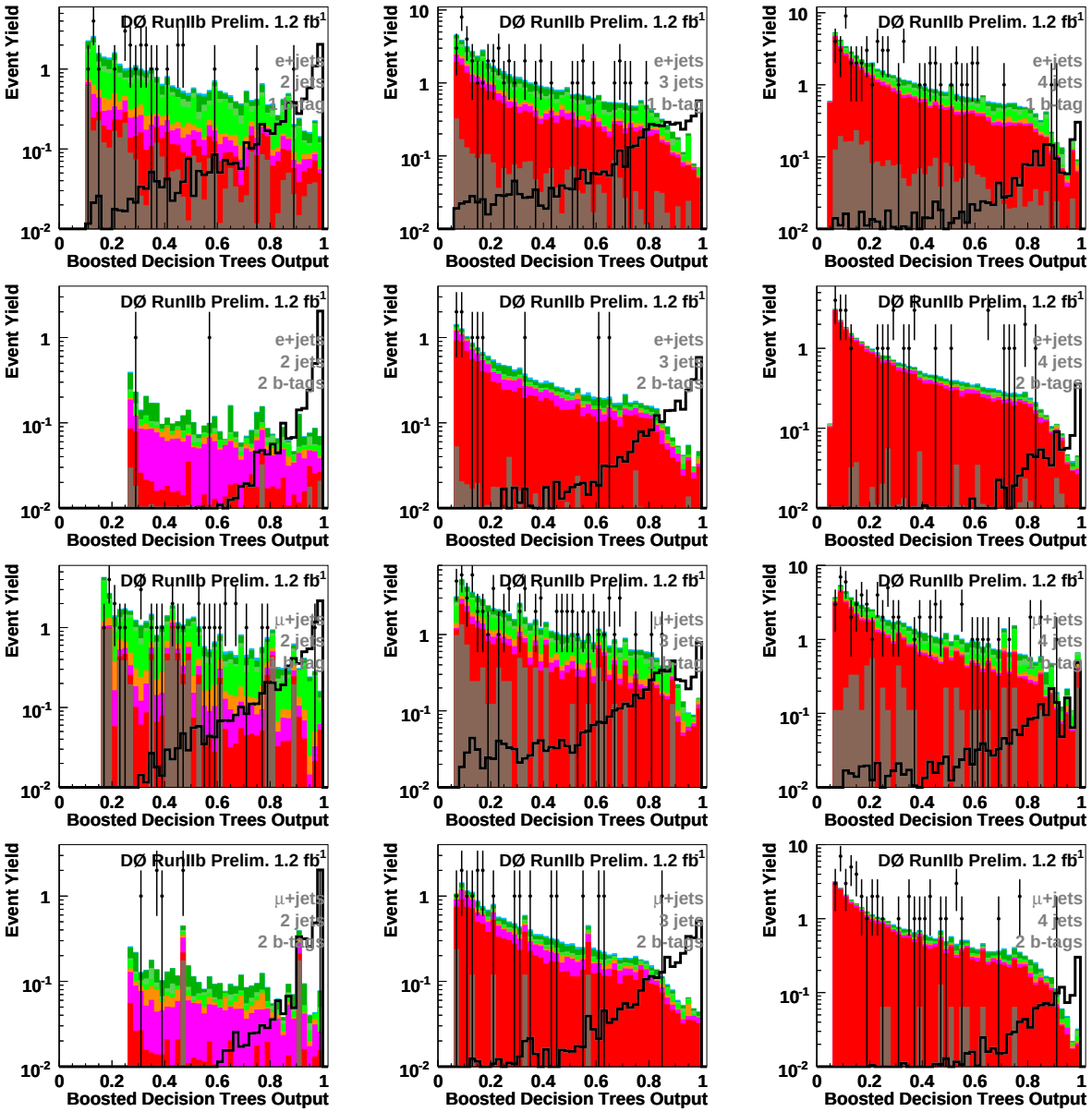

Figure E.26: Distributions of Decision Tree output with $\hat{s}$ cut > 400 GeV for p20 data, background, and W'_{mixed} signal with mass 700 GeV. Plots in the four rows, starting from the top row, are from events with electrons with one b-tagged, electrons with both b-tagged, muons with one b-tagged, and muons with both b-tagged respectively. In the three columns, starting from left to right, are events with two jets, three jets, and four jets, respectively.

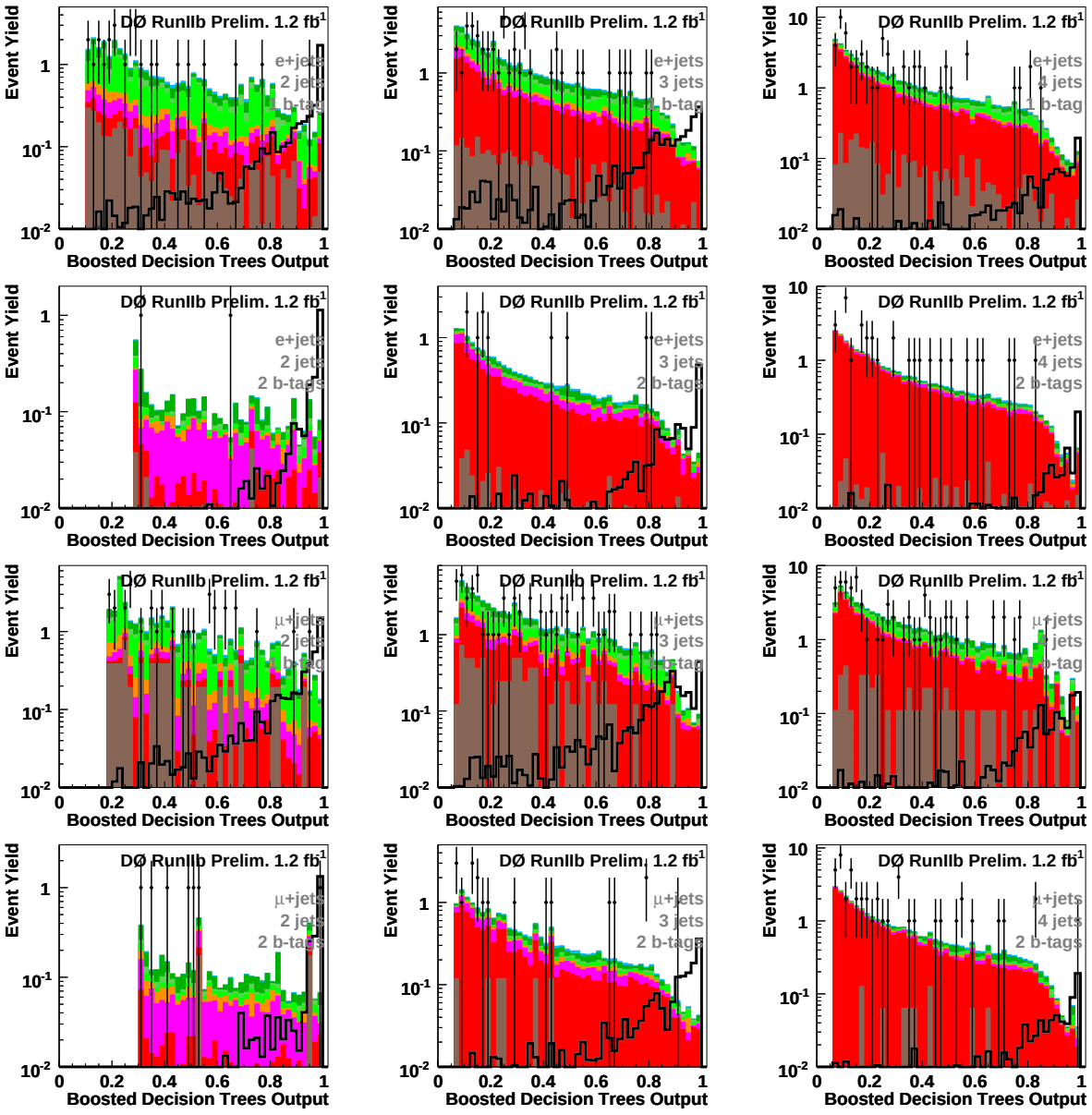

Figure E.27: Distributions of Decision Tree output with $\hat{s}$ cut > 400 GeV for p20 data, background, and W'_{mixed} signal with mass 750 GeV. Plots in the four rows, starting from the top row, are from events with electrons with one b-tagged, electrons with both b-tagged, muons with one b-tagged, and muons with both b-tagged respectively. In the three columns, starting from left to right, are events with two jets, three jets, and four jets, respectively.

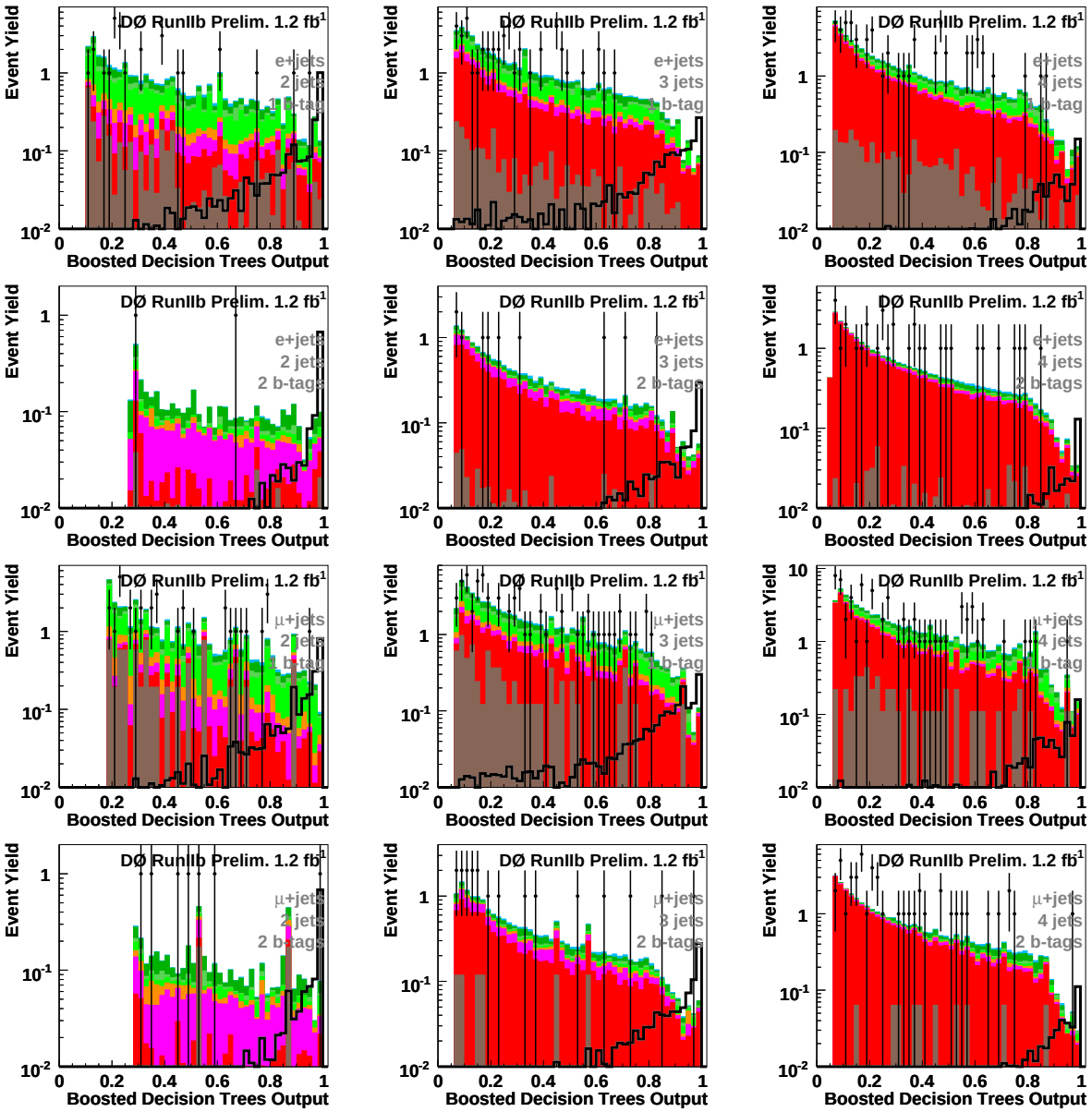

Figure E.28: Distributions of Decision Tree output with $\hat{s}$ cut > 400 GeV for p20 data, background, and W'_{mixed} signal with mass 800 GeV. Plots in the four rows, starting from the top row, are from events with electrons with one b-tagged, electrons with both b-tagged, muons with one b-tagged, and muons with both b-tagged respectively. In the three columns, starting from left to right, are events with two jets, three jets, and four jets, respectively.

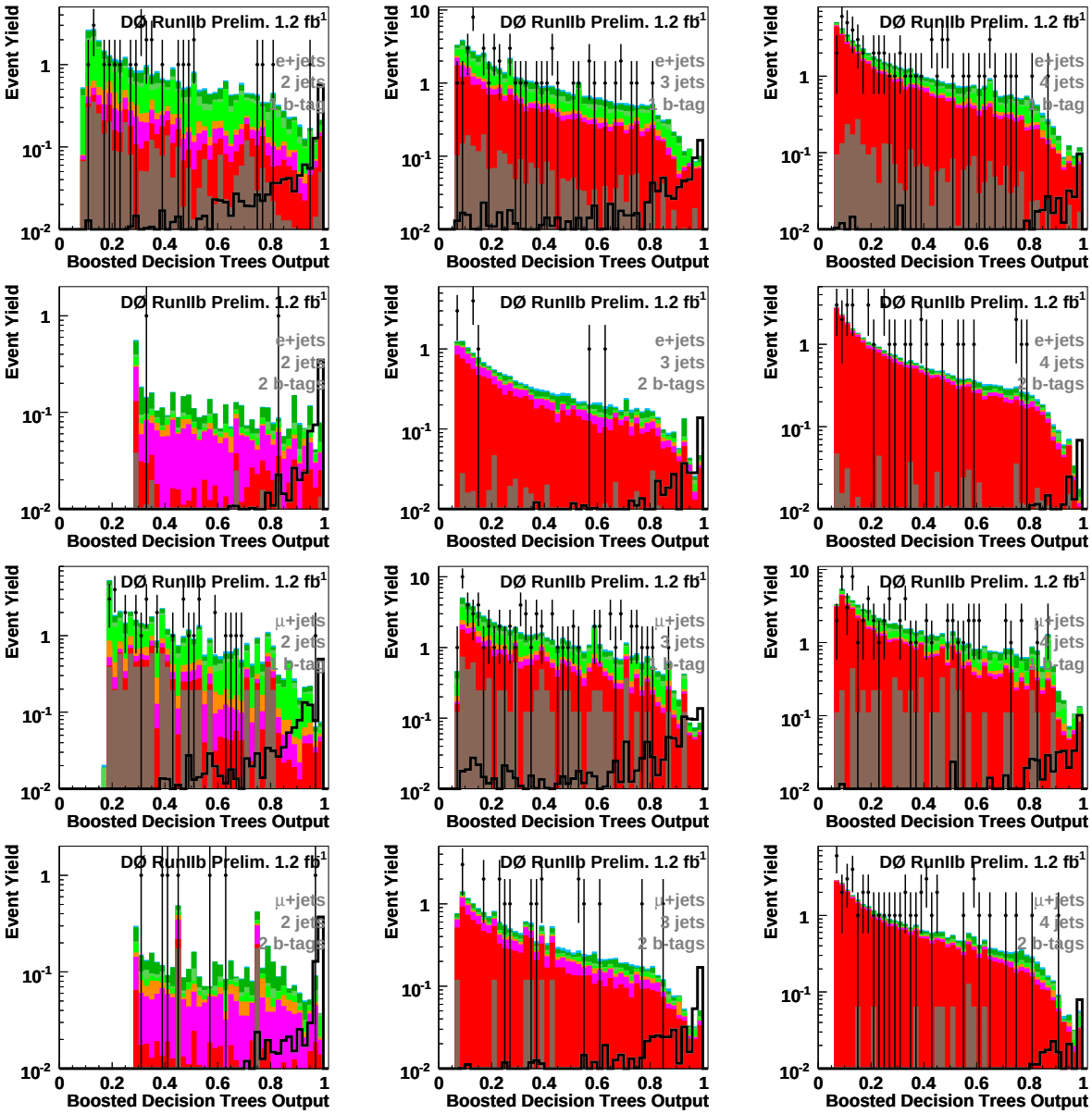

Figure E.29: Distributions of Decision Tree output with $\hat{s}$ cut > 400 GeV for p20 data, background, and W'_{mixed} signal with mass 850 GeV. Plots in the four rows, starting from the top row, are from events with electrons with one b-tagged, electrons with both b-tagged, muons with one b-tagged, and muons with both b-tagged respectively. In the three columns, starting from left to right, are events with two jets, three jets, and four jets, respectively.

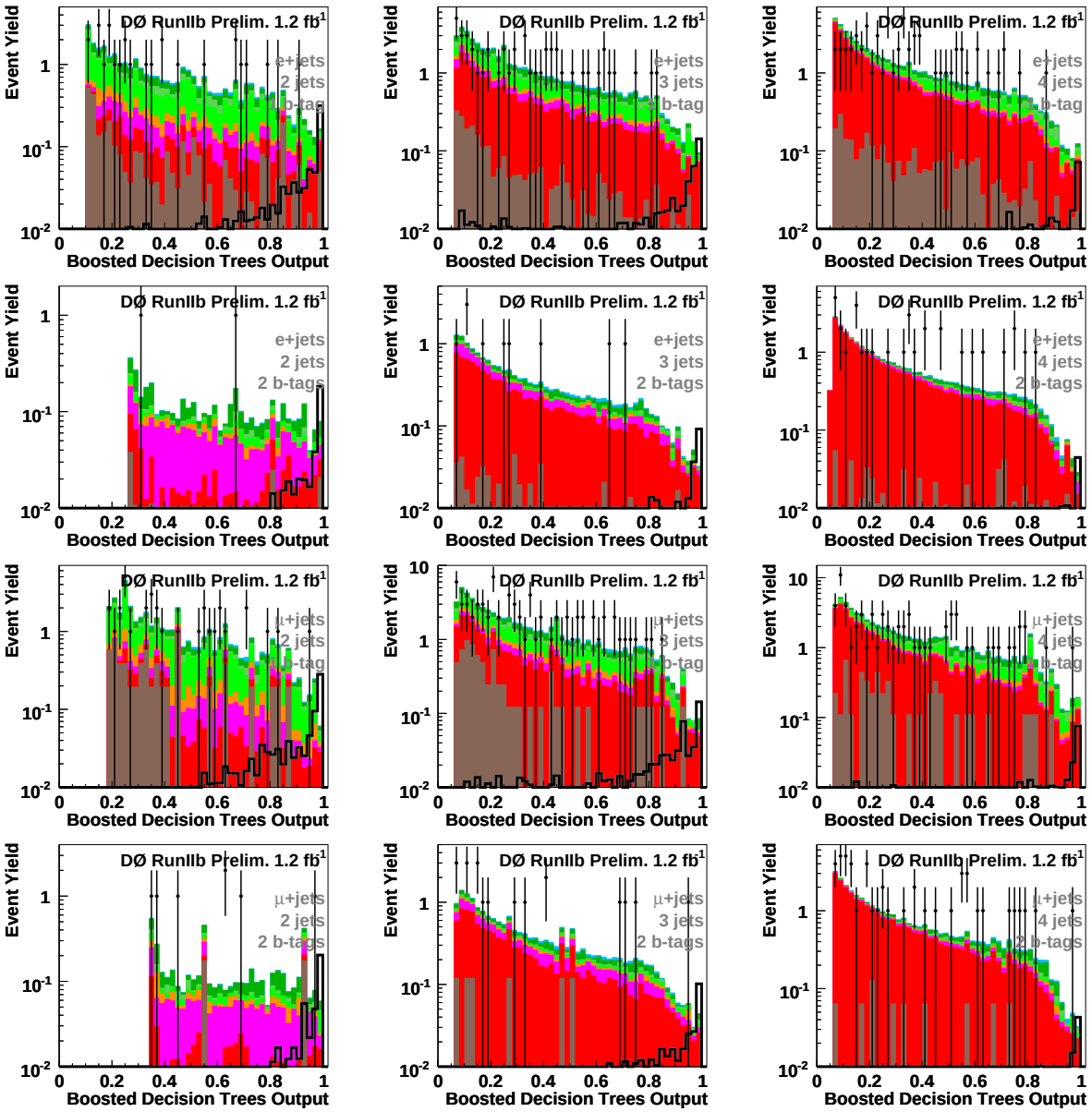

Figure E.30: Distributions of Decision Tree output with $\hat{s}$ cut > 400 GeV for p20 data, background, and W'_{mixed} signal with mass 900 GeV. Plots in the four rows, starting from the top row, are from events with electrons with one b-tagged, electrons with both b-tagged, muons with one b-tagged, and muons with both b-tagged respectively. In the three columns, starting from left to right, are events with two jets, three jets, and four jets, respectively.

Bibliography

[1] W.-M. Yao *et al.*, "The Review of Particle Physics," J. Phys. **G 33**, 1 (2006).

[2] F. Halzen and A. D. Martin, "Quarks & Leptons: An Introductory Course in Modern Particle Physics", John Wiley & Sons, Inc, New York, NY (1984).

[3] CDF Collaboration, "Observation of the Top Quark in $p\bar{p}$ Collisions with the Collider Detector at Fermilab", Phys. Rev. Lett. **74**, 2626 (1995).

[4] DØ Collaboration, "Observation of the Top Quark", Phys. Rev. Lett. **74**, 2632 (1995).

[5] V.M. Abazov *et al.* (DØ Collaboration), "Observation of single top quark production," Phys. Rev. Lett. **103**, 092001 (2009).

[6] T. Aaltonen *et al.* (CDF Collaboration), "First Observation of Electroweak Single Top Quark Production," Phys. Rev. Lett. **103**, 092002 (2009).

[7] E. Brubaker *et al.* Combination of CDF and DØ results on the mass of the top quark. *hep-ex/0603039*, 2006.

[8] N. Kidonakis and R. Vogt, "Next-to-Next-to-Leading Order Soft Gluon Corrections in Top Quark Hadroproduction," Phys. Rev. D **68**, 114014 (2003). The value for $m_{\rm top}$ = 170 GeV is from a private communication.

[9] N. Kidonakis, Single Top Quark Production at the Fermilab Tevatron: Threshold Resummation and Finite-Order Soft Gluon Corrections," Phys. Rev. D **74**, 114012 (2006).

[10] G. Mahlon, Spin Polarization in Single Top Events. *hep-ph/9811219*, 1998.

[11] T. Tait and C.-P. Yuan, *Single top quark production as window to physics beyond the standard model*, Phys. Rev. D **63**, 014018 (2000).

[12] Inquiring Minds Physics at Fermilab Accelerators Homepage, `http://www.fnal.gov/pub/inquiring/physics/accelerators`.

[13] Accelerator Divison Homepage, `http://www-bd.fnal.gov/public`.

[14] V.M. Abazov *et al.* (DØ Collaboration), "The Upgraded DØ Detector", Nucl. Instrum. and Methods A 565, 463-537 (2006).

[15] G. Welsh and G. Bishop "An Introduction to the Kalman Filter", 2006. `http://www.cs.unc.edu/~welch/kalman/kalmanIntro.html`.

[16] H. Greenlee. The DØ Kalman Track Fit", DØ internal note 4303.

[17] A. Khanov, "HTF: histogramming method for finding tracks. The algorithm description.", DØ internal note 3778.

[18] D. Adams, "Finding Tracks", DØ internal note 2958.

[19] A. Schwartzman, C. Tully, "Primary Vertex Reconstruction by Means of Adaptive Vertex Fitting", DØ internal note 4918.

[20] A. Schwartzman and M. Narain, "Probabilistic Primary Vertex Selection", DØ internal note 4042.

[21] J.R. Vlimant *et al.*, "Technical Description of the T42 Algorithm for Calorimeter Noise Suppression", DØ internal note 4146.

[22] J. Hays *et al.*, "Single Electron Efficiencies in p17 Data and Monte-Carlo using d0correct from Release p18.05.00", DØ internal note 5105.

[23] O. Atramentov *et al.*, "Electron and Photon Identification with p20 data" DØ internal notes 5761.

[24] J. Kozminski *et al.*, "The Electron Likelihood in p14," DØ internal note 4449.

[25] J. Vlimant *et al.*, "Technical description of the T42 Algorithm for the calorimeter noise suppression", DØ internal note 4146.

[26] A. Harel, "Jet ID Optimization", DØ internal note 4919.

[27] A. Harel and J. Kvita, "p20 JetID Efficiencies and Scale Factors," DØ internal note 5634.

[28] G. Blazey *et al.*, "Run II Jet Physics", DØ internal note 3750.

[29] E. Busato and B. Andrieu, "Jet Algorithms in the DØ Run II Software: Description and User's Guide", DØ internal note 4457

[30] `http://www-d0.fnal.gov/phys_id/jes/public/plots_v7.1/`.

[31] JES Group, "Jet Energy Scale Determination at DØ Run II", DØ internal note 5382.

[32] G. Otero y Garzón *et al.*, "Taggability in Pass2 p14 Data," DØ internal note 4995.

[33] P. Calfayan *et al.*, "Muon Identification Certification for p17 data", DØ internal note 5157.

[34] S. Cho *et al.*, "Muon ID Certification for p20 data", DØ internal note 5824.

[35] T. Andeen *et al.*, "The DØ experiment's integrated luminosity for Tevatron Run IIa", FERMILAB-TM-2365 (2007)

[36] R. Brun and F. Carminati, 'GEANT: Detector Description and Simulation Tool," CERN Program Library Long Writeup, Report No. W5013 (1993).

[37] Y. Fisyak, J. Womersley, "D0gstar DØ GEANT Simulation of the Total Apparatus Response", DØ internal note 3191.

[38] E.E. Boos *et al.*, "Method for Simulating Electroweak Top-Quark Production Events in the NLO Approximation: SingleTop Generator", Phys. Atom. Nucl. **69**, 1317 (2006).

[39] T. Sjöstrand, L. Lonnblad and S. Mrenna, PYTHIA 6.2: PHYSICS AND MANUAL, LU-TP-01-21, hep-ph/0108264 (2001).

[40] S. Jadach *et al.*, "The Tau Decay Library TAUOLA: version 2.4," Comput. Phys. Commun. **76**, 361 (1993). We used version 2.5.

[41] D.J. Lange, "The EvtGen Particle Decay Simulation Package," Nucl. Instrum. Meth. **A 462**, 152 (2001). We used a DØ version similar to version 00-14-05.

[42] J. Pumplin *et al.*, "New generation of parton distributions with uncertainties from global QCD analysis" JHEP 0207, **012** (2002).

[43] M. L. Mangano *et al.*, ALPGEN, a Generator for Hard Multiparton Processes in Hadronic Collisions, JHEP 0307:001, 2003

[44] S. Höche *et al.*, "Matching Parton Showers and Matrix Elements", hep-ph/0602031.

[45] E. Barberis *et. al.*, "The Matrix Method and its Error Calculation," DØ internal note 4564.

[46] The MCFM (N)NLO calculations of the diboson cross sections and their uncertainties are documented here:
`http://www-clued0.fnal.gov/~nunne/cross-sections/mcfm_cross-sections.html`.
This is MCFM version 3.4.5

[47] B. Tiller and T. Nunnemann, "Measurement of the differential Z0-boson production cross-section as function of transverse momentum", DØ internal note 4660.

[48] `http://www.physics.csbsju.edu/stats/KS-test.html`

[49] S. Muanza, "A Compilation of MCFM v5.1 Cross Section," DØ internal note 5300.

[50] Yvonne Peters *et al.*, "Study of the W+jets heavy flavor scale factor in p17", DØ internal note 5406.

[51] T. Scanlon "A Neural Network b-tagging Tool", DØ internal note 4889.

[52] T. Scanlon "Improvements to the Measurement of b-tagging Performance in p17 Data", DØ internal note 5402.

[53] D. Boline, L. Feligioni, M. Narain, "Update on b-quark jet identification with Secondary Vertex reconstruction using DØ reco version p14-Pass2 Samples", DØ internal note 4796.

[54] R. Demina, A. Khanov, F. Rizatdinova, "b-Tagging with Counting Signed Impact Parameter Method", DØ internal note 4049.

[55] D. Bloch, B. Clement, "Update of the JLIP b-tagger Performance in p14/pass2 with Jes 5.3", DØ internal note 4824.

[56] B. Clement *et al.*,"SystemD or how to get signal, backgrounds and their efficiencies with real data", DØ internal note 4159.

[57] TMinuit, "`http://root.cern/ch/root/html/TMinuit.html`".

[58] M. Anastasoaie, S. Robinson, T. Scanlon, "Performance of the NN b-tagging Tool on p17 Data", DØ internal note 5213.

[59] T. Gadfort *et al.*, "Performance of the DØ NN b-Tagging Tool on p20 Data," DØ Note 5554, (2007).

[60] The Les Houches Accord PDF Interface, `http://hepforge.cedar.ac.uk/lhapdf/`

[61] F. Maltoni and T. Stelzer, "MadEvent: Automatic Event Generation with MadGraph," JHEP **0302**, 027 (2003).

[62] G. Gutierrez, M. Wang, Z. Ye, "Measurement of the Top Quark Mass in the Lepton+Jets Final State of Top Quark Pair Production Using Matrix Element Method on 1.2 fb^{-1} Dzero RunIIb Data," DØ internal note 5585.

[63] Private communication with L. Wang. Parametrization found in the file `/work/cole-clued0/leiwang/wz_epmcs/p170303_sampling/wz_epmcs/src/pmcsana.cpp`

[64] J. Stark, "Understanding and modelling the CAL energy resolution", presentation at the W mass meeting on January 13th, 2006.

[65] P. Haefner and F. Fiedler, "Determination of the Muon Transfer Function for Top Mass Measurements," DØ Note 4818 (2005).

[66] P. Haefner and F. Fiedler, "Muon Transfer Function Parameters for p17 MC," DØ Note 5214, (2006).

[67] P. Shiefferdecker and M. Wang, "Jet Transfer Functions Derived From p17 $t\bar{t}$ Monte Carlo," DØ Note 5136 (2006).

[68] The GNU Scientific Library, `http://www.gnu.org/software/gsl/`

[69] G.P. Lepage, "VEGAS: An Adaptive Multidimensional Integration Program," Cornell Laboratory of Nuclear Sciences report CLNS-80/447, (1980).

[70] S. Jain *et al.*, "Limits using a Bayesian approach in the package 'top_statistics"', DØ internal note 5123.

[71] R. Schwienhorst *et al.*, "Statistical method implemented in the package 'top_statistics"', DØ internal note 5817.

[72] The Tevatron Electroweak Working Group for the CDF and DØ Collaborations, "Combination of CDF and DØ Results on the Mass of the Top Quark," arXiv.org:0808.1089, July 2008.

[73] H. Schellman, "The Longitudinal Shape of the Luminous Region at DØ," DØ internal note 5142; H. Schellman, "Run IIb Longitudinal Beam Shape," DØ internal note 5540.

[74] G. Corcella, I.G. Knowles, G. Marchesini, S. Moretti, K. Odagiri, P. Richardson, M.H. Seymour and B.R. Webber, "HERWIG 6.5 Release Note," JHEP **0101**, 010 (2001).

[75] Y. Peters, M. Begel, K. Hamacher, and D. Wicke, "Reweighting of the Fragmentation Function for the DØ Monte Carlo," DØ internal note 5325.

[76] V.M. Abazov *et al.* (DØ Collaboration), "Evidence for Production of Single Top Quarks," Phys. Rev. D **78**, 012005 (2008).

[77] T. Aaltonen *et al.* (CDF Collaboration), "Measurement of the Single Top Quark Production Cross Section at CDF," Phys. Rev. Lett. **101**, 252001 (2008).

[78] V.M. Abazov *et al.* (DØ Collaboration), "Measurement of the Ratio of the $p\bar{p}\to W + c$-Jet Cross Section to the Inclusive $p\bar{p}\to W$+Jets Cross Section," Phys. Lett. B **666**, 23 (2008).

[79] S. Muanza, talk at the V+Jets meeting, February 5, 2008, `http://www-d0.hef.kun.nl//askArchive.php?base=agenda&categ=a08202&id=a08202s1t1/tran`

[80] M. Voutilainen, "Jet p_T resolution for Run IIa final JES (v7.2) with dijet J4S jet correction." DØ internal note 5499.

[81] The Single Top Working Group, "Observation of Single Top Quark Production in 2.3 fb^{-1} of Data using Boosted Decision Trees," DØ internal note 5811.

[82] D. Gillberg. *Discovery of Single Top Quark Production*. Ph.D Thesis, Simon Fraser University, 2009.

[83] J. Benitez. *Uncovering the Single Top: Observation of Electroweak Top Quark Production*. Ph.D. Thesis. Michigan State University, 2009.

[84] The Single Top Working Group, "Observation of Single Top Quark Production in 2.3 fb^{-1} of Data using Bayesian Neural Networks," DØ internal note 5812.

[85] A. Tanasijczuk. *in preparation*. Ph.D Thesis, Universidad de Buenos Aires, 2010.

[86] The Single Top Working Group, "Combination of three single top quark cross section measurements from 2.3 fb^{-1} of Data using a Bayesian Neural Network", DØ internal note 5814.

[87] The Single Top Working Group, "Measurement of $|V_{tb}|$ Using the Single Top Quark Observation Analyses from 2.3 fb^{-1} of data", DØ internal note 5816.

[88] R. S. Chivukula, E. H. Simmons and J. Terning, Phys. Rev. D **53**, 5258 (1996).

[89] D. B. Kaplan and H. Georgi, Phys. Lett. B **136**, 183 (1984).

[90] H. Georgi and D. B. Kaplan, Phys. Lett. B **145**, 216 (1984).

[91] N. Arkani-Hamed, A. G. Cohen and H. Georgi, Phys. Lett. B **513**, 232 (2001).

[92] D. E. Kaplan and M. Schmaltz, JHEP **0310**, 039 (2003).

[93] M. Schmaltz and D. Tucker-Smith, Ann. Rev. Nucl. Part. Sci. **55**, 229 (2005).

[94] B. Schrempp, Proceedings of the 23rd International Conference on High Energy Physics, Berkeley (World Scientific, Singapore 1987);

U. Baur *et al.*, Phys. Rev. **D35**, 297 (1987);

M. Kuroda *et al.*, Nucl. Phys. **B261**, 432 (1985).

[95] P. Batra, A. Delgado, D.E. Kaplan and T.M.P Tait, JHEP **0402**, 043 (2004).

[96] R.W. Robinett, Phys. Rev. **D26**, 2388 (1982);

R.W. Robinett and J.L. Rosner, Phys. Rev. **D26**, 2396 (1982);

P. Langacker, R. W. Robinett, and J.L. Rosner, Phys. Rev. **D30**, 1470 (1984).

[97] M. Cvetic and P. Langacker, Mod. Phys. Lett. A **11**, 1247 (1996).

[98] J. C. Pati, arXiv:hep-ph/0606089.

[99] M. Green and J. Schwarz, Phys. Lett. **149B**, 117(1984);

D. Gross *et al.*, Phys. Rev. Lett. **54**, 502 (1985);

E. Witten, Phys. Lett. **155B**, 1551 (1985);

P. Candelas *et al.*, Nucl. Phys. **B258**, 46 (1985);

M. Dine *et al.*, Nucl. Phys. **B259**, 549 (1985).

[100] A. Datta, P. J. O'Donnell, Z. H. Lin, X. Zhang and T. Huang, Phys. Lett. B **483**, 203 (2000).

[101] R. Sundrum, arXiv:hep-th/0508134;

C. Csaki, Jay Hubisz, Patrick Meade, arXiv:hep-ph/0510275;

G. Kribs, arXiv:hep-ph/0605325.

[102] E. Malkawi, T. Tait and C. P. Yuan, Phys. Lett. B **385**, 304 (1996).

[103] D. J. Muller and S. Nandi, Phys. Lett. B **383**, 345 (1996).

[104] J. C. Pati and A. Salam, Phys. Rev. D **10**, 275 (1974).

[105] R. N. Mohapatra and J. C. Pati, Phys. Rev. D **11**, 566 (1975).

[106] R. N. Mohapatra and J. C. Pati, Phys. Rev. D **11**, 2558 (1975).

[107] G. Senjanovic and R. N. Mohapatra, Phys. Rev. D **12**, 1502 (1975).

[108] Y. Mimura and S. Nandi, Phys. Lett. B **538**, 406 (2002).

[109] M. Cvetic and J. C. Pati, Phys. Lett. B **135**, 57 (1984).

[110] P. Langacker and S. Uma Sankar, Phys. Rev. D **40**, 1569 (1989).

[111] J. Donoghue and B. Holstein, Phys. Lett. 113B, 383 (1982);

[112] L. Wolfenstein, Phys. Rev. D29, 2130 (1984).

[113] D0 Collaboration, V. Abazov *et al.,* Phys. Rev. D **69**, 111101 (2004).

[114] CDF Collaboration, T. Affolder *et al.,* Phys. Rev. Lett. **87**, 231803 (2001).

[115] E. H. Simmons, Phys. Rev. D **55**, 5494 (1997).

[116] E. Boos, V. Bunichev, L. Dudko and M. Perfilov, Phys. Lett. B **655**, 245 (2007) [arXiv:hep-ph/0610080].

[117] Z. Sullivan, Phys. Rev. D **66**, 075011 (2002).

[118] CDF Collaboration, Phys. Rev. Lett. **103**, 041801 (2009)

[119] V.M. Abazov *et al.*, "Search for W' boson production in the top quark decay channel", Phys. Rev. Lett. **100**, 211803 (2008)

[120] The Central Track Trigger Homepage, `http://www-d0online.fnal.gov/www/groups/cft/CTT/online/ctt_main.html`.

[121] J. Olsen, "DFEA Technical Design Report", DØ internal note 4163.

[122] J. Olsen, "DFEA2 Design Specification", DØ internal note 4676.

[123] G. Wilson, Trigger Algorithms, Simulation and Performance Optimization of the DØ Central Track Trigger. Poster session presented at: IEEE Nuclear Science Symposium; 2006 Dec 13-15; San Diego, CA. `https://plone4.fnal.gov/P1/D0Wiki/tdaq/ctt/meetings/Posters/n30-256.ppt`.

[124] E. Hazen, Hardware aspects of the upgraded DØ Central Track Trigger. Poster session presented at: IEEE Nuclear Science Symposium; 2006 Dec 13-15; San Diego, CA.

[125] Xilinx, Virtex-II FPGA, `http://www.xilinx.com`

[126] R. Mommsen, Trigger Algorithms, Performance measurement of the upgraded DØ Central Track Trigger. Poster session presented at: IEEE Nuclear Science Symposium; 2006 Dec 13-15; San Diego, CA.